GOETHE
UNIVERSITÄT
FRANKFURT AM MAIN

GEORG SPEYER HAUS
INSTITUT FÜR TUMORBIOLOGIE
UND EXPERIMENTELLE THERAPIE

The role of EMT inducer Zeb1 in the invasive tumour stroma during colon cancer progression

Dissertation

zur Erlangung des Doktorgrades

der Naturwissenschaften

vorgelegt beim Fachbereich Biochemie, Chemie und Pharmazie

der Johann Wolfgang Goethe-Universität

in Frankfurt am Main

von

Constantin Menche

aus Groß-Gerau

Frankfurt 2023

(D30)

vom Fachbereich Biochemie, Chemie und Pharmazie (FB 14) der

Johann Wolfgang Goethe-Universität als Dissertation angenommen.

Dekan: Prof. Dr. Clemens Glaubitz

Gutachter: Prof. Dr. Robert Fürst

Prof. Dr. Florian Greten

Datum der Disputation: 17.10.2023

Teile dieser Arbeit werden veröffentlicht (vorläufige Angaben für Autoren und Titel):

Zeb1 governs inflammation and immune checkpoint blockade sensitivity in colorectal cancer by cell-intrinsic modulation of myofibroblast polarization

Constantin Menche[*], Harald Schuhwerk[*], Isabell Armstark, Pooja Gupta, Britta M. Grebbin, Kathrin Fuchs, Ruthger van Roey, Mohammed H. Mosa, Florian R. Greten, Thomas Brabletz, Henner F. Farin[#] and Marc P. Stemmler[#]

[*,#]: equal contribution

Erklärung

Ich erkläre hiermit, dass ich mich bisher keiner Doktorprüfung im Mathematisch-Naturwissenschaftlichen Bereich unterzogen habe.

Frankfurt am Main, den ....
(Unterschrift)

Eidesstattliche Versicherung

Ich erkläre hiermit an Eides statt, dass ich die vorgelegte Dissertation mit dem Titel

"The role of EMT inducer Zeb1 in the invasive tumor stroma during colon cancer progression"

selbstständig angefertigt und mich anderer Hilfsmittel als der in ihr angegebenen nicht bedient habe, insbesondere, dass alle Entlehnungen aus anderen Schriften mit Angabe der betreffenden Schrift gekennzeichnet sind.

Ich versichere, die Grundsätze der guten wissenschaftlichen Praxis beachtet, und nicht die Hilfe einer kommerziellen Promotionsvermittlung in Anspruch genommen zu haben.

Frankfurt am Main, den ....
(Unterschrift)

Declaration of collaborative work

Except where stated otherwise by reference or acknowledgment, the work presented was generated by myself under the supervision of my advisors during my doctoral studies. All contributions from colleagues are explicitly referenced in the thesis. The material listed below was obtained in the context of collaborative research:

Fig. 10: Zeb1$^{fl/fl}$ mice were supplied by Thomas Brabletz (Universität Erlangen), Col1a2-CreERT2 mice were supplied by Florian Greten (Georg-Speyer-Haus). All experimental procedures were performed by myself.

Fig 11: Rosa-mTmG mice were supplied by Thomas Brabletz (Universität Erlangen). All experimental procedures were performed by myself.

Fig 17: Rosa-tdTomato mice were supplied by Florian Greten (Georg-Speyer-Haus). All experimental procedures were performed by myself.

Fig 21 & 34: All experiments using the AOM/DSS model were performed by Harald Schuhwerk (Universität Erlangen). Col6a1-Cre mice were supplied by Dieter Saur (Universität München).

Fig 29: All experiments using the AOM/P53 model were performed by Harald Schuhwerk (Universität Erlangen). Vil-FRT, P53$^{fl/fl}$ mice were supplied by Florian Greten (Georg-Speyer-Haus).

Fig 35: OT1 mice were supplied by Florian Greten (Georg-Speyer-Haus). All experimental procedures were performed by myself.

Fig 36: Plasmid constructs with shRNA were supplied by Thomas Brabletz (Universität Erlangen). All experimental procedures were performed by myself.

Whenever a figure, table or text is identical to a previous publication, it is stated explicitly in the thesis that copyright permission and/or co-author agreement has been obtained.

Table of contents

Zusammenfassung

Eine große Herausforderung bei der Behandlung von Darmkrebs (CRC) ist die starke inter- und intratumorale Heterogenität, die zu diversem Ansprechen auf Behandlungen und häufigen Rückfällen bei initial ansprechenden Patienten führt. Um die zugrundeliegenden Mechanismen besser zu verstehen, wurden kürzlich Tumore anhand ihres transkriptomischen Profils in 4 molekulare Subtypen (consensus molecular subtypes / CMS) eingeteilt [Guinney et al. 2015]. Dabei zeichnet sich der CMS4-Subtyp mit der schlechtesten Prognose und einer Anreicherung von TGFβ- und stromalen Signaturen aus. Diese Signaturen, die durch die Präsenz und Aktivierung von krebsassoziierten Fibroblasten (cancer-associated fibroblasts, CAFs) verursacht sind, betonen die Wichtigkeit des Tumormikromilieu (tumor microenvironment, TME) zusätzlich zu den intrinsischen Eigenschaften der Tumorzellen. Es ist bekannt, dass CAFs das Tumorwachstum durch die Sekretion von Wachstumsfaktoren, den Umbau der extrazellulären Matrix (ECM) oder die Etablierung eines immunsuppressiven TME unterstützen [Sahai et al. 2020]. Eine Verringerung der CAF-Aktivierung durch Hemmung des TGFβ-Signalwegs erlaubte im Mausmodell eine verbesserte Therapieantwort [Tauriello et al. 2018]. Im Pankreaskarzinom wurde in CAFs jedoch ein hohes Maß an transkriptioneller und funktioneller Plastizität beobachtet [Öhlund et al. 2017, Biffi et al. 2021], was die Identifizierung von geeigneten pharmakologischen Zielen zur klinischen Translation erschwert. Eine weitere Signatur, die in CMS4-Tumoren angereichert ist, ist die epitheliale-mesenchymale Transition (EMT). Während zunächst angenommen wurde, dass die metastatische Progression der Tumorzellen für diese Muster verantwortlich ist, wurden in mehreren Studien CAFs als Hauptquelle dieser Signatur identifiziert [Isella et al. 2015, Calon et al. 2015, Li et al. 2017]. EMT wird durch mehrere Master-Transkriptionsfaktoren (Zeb1/2, Snai1/2, Twist1) reguliert, die die Expression epithelialer Schlüsselgene wie E-Cadherin und Cytokeratine hemmen und stattdessen die Expression mesenchymaler Gene wie Vimentin und N-Cadherin induzieren, was zu einer Modulation der Zellpolarität und einer erhöhten Zellmotilität führt [Huang et al. 2012a, Lamouille et al. 2014]. EMT-Transkriptionsfaktoren (EMT-TFs) wurden in Epithelzellen eingehend untersucht, wo sie in der Regel verstärkt an der invasiven Front von Tumoren exprimiert werden und dadurch die Initiierung der Metastasierung vermitteln und Therapieresistenz induzieren können [Chang et al. 2011, Krebs et al. 2017]. EMT-TFs weisen jedoch auch eine heterogene Expression in Stromazellen im gesamten Tumor auf und bis jetzt ist die Funktion dieser Expression in Stromazellen unklar.

In dieser Arbeit wurde die Rolle des EMT-Masterregulators Zeb1 in krebsassoziierten Fibroblasten während der Darmkrebs-Progression untersucht. Dazu wurde in Zusammenarbeit mit der Gruppe von Thomas Brabletz (Uni Erlangen) Mausmodelle analysiert, die entweder die entzündungsgetriebene Tumorinitiation widerspiegeln (AOM/DSS, AOM/P53) [Neufert et al. 2007] oder in Transplantationsmodellen das Voranschreiten des sporadischen CRC nachbilden (subkutan, orthotop)

[Fumagalli et al. 2017]. Die Tumorzell-Transplantation in syngene Mäuse mit Fibroblasten-spezifischer induzierbarer Cre-Expression (*Col1a2-CreERT2*) und einem loxP flankierten *Zeb1* Allel [Brabletz et al. 2017], ermöglichte die Untersuchung von Zeb1 in CAFs während unterschiedlicher Phasen der CRC-Initiierung und -Progression in einem immunkompetenten Hintergrund. *In vivo* Ergebnisse wurden in Mono- und Kokulturen von primären Fibroblasten mit CRISPR/Cas9-manipulierten Tumororganoiden und transgenen T Zellen mechanistisch untersucht.

Verlust von *Zeb1* verändert den Fibroblasten-Subtyp *in vitro*, aber nicht die intestinale Homöostase

Vor Beginn der *in vivo* Experimente wurden primäre Fibroblasten aus induzierbaren konditionalen *Zeb1* Knockout-Mäusen isoliert und charakterisiert. Dazu wurden CAFs adhärent kultiviert und die Abwesenheit von Epithel- oder Immunzellen gezeigt. Die Induktion der *Zeb1*-Rekombination durch lentivirale Transduktion von Cre-Rekombinase führte zu einem Zellzyklus-Arrest und dem Überwachsen von nicht-rekombinierten Zellen. Im Gegensatz dazu konnten rekombinierte Fibroblasten aus konditionellen *Zeb1* Knockout-Mäusen nach Inkubation mit 4-Hydroxy-Tamoxifen dauerhaft expandiert werden. Nach der Rekombination wurde sowohl auf Transkriptom- als auch auf Proteinebene ein Verlust von Myofibroblasten-Markern und ein Anstieg der Expression von Entzündungsgenen beobachtet. Funktionell führte der Verlust von Zeb1 zu einer Verringerung der Kontraktilität - einem Hauptmerkmal von Myofibroblasten - und einem Verlust der typischen spindelartigen Morphologie. Die Rekombination von *Zeb1* in Fibroblasten beeinträchtigte darüber hinaus die Sekretion von Nischensignalen der Fibroblasten in Kokulturen mit Darmorganoiden. Während Organoide in Kokultur mit WT Fibroblasten weiterhin die Zugabe des Wachstumsfaktors Wnt benötigten, konnten Organoide in Kokultur mit *Zeb1*-deletierten Fibroblasten unabhängig von der Zugabe von Wnt wachsen. Diese Ergebnisse deuten auf eine Störung der Fibroblastenaktivierung in Richtung von Myofibroblasten durch Rekombination von *Zeb1* hin, was zu einer Veränderung des Fibroblasten-Subtyps *in vitro* führt. Nach einem vorübergehenden Wachstumsstillstand konnten die rekombinierten Zellen regulär kultiviert werden und der verstärkte Entzündungszustand normalisierte sich. Dies deutet darauf hin, dass unter *in vitro*-Kulturbedingungen die Aktivierung von Kompensationsmechanismen den Verlust von Zeb1 ausgleichen kann.

Obwohl nach Rekombination *in vitro* phänotypische Unterschiede in Fibroblasten festgestellt wurden, konnten bei Mäusen nach einer mehrwöchigen Tamoxifen-Diät-induzierten *Zeb1*-Rekombination keine Auswirkungen auf die intestinale Homöostase beobachtet werden. Dies könnte auf unterschiedliche Eigenschaften von Fibroblasten im Normalgewebe zurückzuführen sein. Während in Adhäsionskultur die ECM-Steifheit die Myofibroblasten-Differenzierung stark fördert, liegt nur ein kleiner Teil der Zellen unter homöostatischen Bedingungen *in vivo* als Myofibroblasten vor. Dies könnte bewirken, dass Fibroblasten weniger stark von Zeb1 abhängig sind. Außerdem wird die

Kontraktilität von Myofibroblasten besonders während Wundheilungsprozessen benötigt, die während der relativ kurzen Dauer der Experimente möglicherweise keine Rolle gespielt hat. Die Veränderungen der von Fibroblasten sekretierten Nischensignale könnten durch andere Zelltypen im Darmgewebe kompensiert worden sein.

Der stromale Zeb1 Verlust bewirkt unterschiedliche Phänotypen in CRC Tumormodellen

In Mausmodellen des kolorektalen Karzinoms waren die Auswirkungen der stromalen *Zeb1*-Rekombination stark vom Tumormodell abhängig: Im entzündungsgetriebenen AOM/DSS Modell führte die Rekombination von *Zeb1* zu einer verstärkten Entzündungsreaktion des Darms und zu einem beschleunigten Wachstum von Adenomen. Im AOM/P53-Modell war das Tumorwachstum und die Invasivität der Tumore reduziert, was auf eine Verzögerung der Tumorentstehung in diesem Modell hinweist. Bei subkutanen Transplantationen (SCT) und orthotopen Transplantationen von Tumor-Organoiden konnten nur geringe Auswirkungen auf das Wachstum des Primärtumors beobachtet werden. Jedoch war im orthotopen Transplantationsmodell die Lebermetastasierung nach *Zeb1*-Rekombination deutlich reduziert. Zusammen deutet dies darauf hin, dass der Effekt eines stromalen Zeb1 Verlusts stark von dem TME des Tumormodells abhängt. Interessanterweise war entweder die aSMA-Färbung reduziert (AOM/P53, SCT, orthotop), die Organisation der Fasern verändert (AOM/DSS) und/oder die Sekretion von extrazellulärer Matrix (ECM) reduziert (AOM/DSS, orthotopic), was auf einen Verlust von Myofibroblasten durch die Deletion von *Zeb1* hindeutet. Außerdem war in allen Modellen mit Ausnahme des immunprivilegierten SCT-Modells die Infiltration von T- und B Zellen im Primärtumor erhöht und die Expression von Immun-Checkpoint Molekülen (PD-L1) verstärkt, was die Aktivierung einer adaptiven Immunantwort und immunregulatorischer Kompensationsmechanismen zeigt. Diese Ergebnisse konnten durch RNA-Sequenzierung bestätigt werden. Im AOM/DSS- und SCT-Modell zeigte die Bulk-RNA-Sequenzierung eine Anreicherung von Entzündungssignaturen und eine verminderte Expression von Zellkontraktilitätsgenen. Darüber hinaus zeigte die Einzelzell-RNA-Sequenzierung im AOM/DSS- und orthotopen Modell den Verlust von Myofibroblasten und ECM-Signaturen, verstärkte Entzündungsmuster in den verbleibenden CAF Populationen und eine insgesamt verminderte Fibroblastenplastizität auf. In der Einzelzell-RNA-Sequenzierung von orthotopen Tumoren zeigte sich außerdem eine verstärkte Aktivierung von T Zellen, B Zellen und Makrophagen.

Insgesamt deuten die Daten aus diesen Modellen in Übereinstimmung mit den *in vitro* Ergebnissen auf eine Hemmung der Myofibroblasten-Differenzierung nach Verlust von *Zeb1* hin. Im Gegensatz zu den *in vitro* Kulturen führten die Entzündungsreize im TME jedoch zu einer anhaltenden entzündlichen Aktivierung der Fibroblasten. Im AOM/DSS Modell scheinen diese inflammatorischen Signale die Entzündung des Darmgewebes weiter zu verstärken und damit, durch Förderung der pro-tumorigenen

Eigenschaften des TME, das Tumorwachstum und die Tumorprogression zu beschleunigen. In den sporadischen Modellen dagegen, führen die pro-inflammatorischen Signale der Fibroblasten zu einer verstärkten anti-Tumor Immunantwort. Im AOM/P53 Modell resultiert dies in einer verzögerten Tumorinitiation und damit verbunden einem verringerten Tumorwachstum und Tumorprogression. Im orthotopen Modell, das ein fortgeschrittenes Stadium widerspiegelt, scheint diese Immunantwort keinen Einfluss mehr auf das Primärwachstum zu haben.

Die Infiltration von Immunzellen wird durch die Expression von Zeb1 in CAFs reguliert

Verschiedene Mechanismen könnten die verstärkte Infiltration von Immunzellen in Tumoren nach stromaler Deletion von *Zeb1* erklären. Die verringerte Anzahl von Myofibroblasten und die Reduktion von ECM in Tumoren mit Zeb1 defizienten CAFs könnten zu einer erhöhten Infiltration durch Verlust der Barriereeigenschaften führen. Außerdem könnte die inflammatorische Aktivierung der Fibroblasten zur Freisetzung von Cytokinen führen, die Immunzellen zum Tumor rekrutieren oder die anti-tumor Effektorfunktion von Immunzellen erhöhen. In Transwell-Kokulturexperimenten mit T Zellen, Fibroblasten und Tumororganoiden stellte eine Schicht aus Zeb1-defizienten Fibroblasten im Vergleich zu Zeb1-profizienten Fibroblasten eine geringere Barriere gegenüber der Migration von T-Zellen dar. Gleichzeitig war die Migration von T Zellen zu Zeb1-defizienten Fibroblasten im Vergleich zu Zeb1-profizienten Fibroblasten erhöht. Obwohl die letztgenannte Beobachtung kein signifikantes Niveau erreichte, deuten diese Experimente darauf hin, dass beide Mechanismen *in vivo* eine Rolle spielen könnten und die relative Abhängigkeit von beiden Mechanismen vom Tumormodell und der TME-Zusammensetzung abhängen könnte.

Zeb1 in Fibroblasten fördert die Entwicklung von Lebermetastasen

Im orthotopen Transplantationsmodell reduzierte die Deletion von *Zeb1* im Stroma die Inzidenz von Lebermetastasen bei Mäusen deutlich. Mehrere Beobachtungen weisen auf die Beteiligung von Immunzellen an diesem Effekt hin: In WT-Mäusen, jedoch nicht in *Zeb1* KO Tieren, sammelten sich Immunzellen häufig am äußeren Rand von Lebermetastasen an. Dies deutet darauf hin, dass Zeb1 in Fibroblasten am Ausschluss von Immunzellen aus Metastasen beteiligt ist, was eine verstärkte anti-Tumor Immunantwort erklären könnte. Dies wurde auch durch eine erhöhte Anzahl von Immunzellansammlungen in den Lebern von stromalen *Zeb1*-KO-Mäusen im Vergleich zu den Lebern von WT-Mäusen unterstützt. Die wenigen KO-Mäuse, die Lebermetastasen entwickelten, zeigten eine ähnliche Anzahl und Größe von Metastasen auf wie WT-Mäuse. Dies deutet auf einen Immun-Escape-Mechanismus hin, durch den Tumorzellen unabhängig von Fibroblasten eine Immunreaktion umgehen können. Während all diese Beobachtungen auf eine wichtige Rolle der immunsuppressiven Funktionen von CAFs bei der Metastasierung hinweisen, wäre es auch möglich, dass CAFs erforderlich sind, um das Gewebe so umzugestalten, dass eine Kolonisierung durch Tumorzellen ermöglicht wird. Um diese

Möglichkeiten zu überprüfen, sind weitere Untersuchungen nötig, die eine Unterscheidung der beiden Mechanismen erlauben. Mögliche Experimente wären die Untersuchung der Leberkolonisation nach Koinjektion von Tumorzellen mit WT- oder KO-Fibroblasten oder der Ausschluss von Immunzellen durch die Analyse von immundefizienten Mäusen.

Veränderung der Fibroblasten-Plastizität als Kombination mit Immun-Checkpoint-Inhibition

Im AOM/DSS-Modell und im orthotopen Transplantationsmodell wurde nach der Rekombination von *Zeb1* in Fibroblasten eine verstärkte Expression von Immun-Checkpoint-Molekülen beobachtet. Dies könnte eine Möglichkeit darstellen, durch Rekombination von *Zeb1* das Ansprechen von Tumoren auf Immun-Checkpoint Therapien zu verbessern. Die Hemmung dieser Immun-Checkpoints führte im orthotopen Modell zu einer Verringerung der Primärtumorgröße und im AOM/DSS-Modell zu einem fast vollständigen Wachstumsstillstand, was die Bedeutung von CAFs als mögliche therapeutische Ziele unterstreicht. Zusammen mit den konservierten Funktionen von ZEB1 in menschlichen Fibroblasten, deutet dies darauf hin, dass die Veränderung von Fibroblasten-Phänotypen durch gezielte Beeinflussung von Zeb1 ein vielversprechender Ansatz für kombinatorische Immunotherapie sein könnte. Da keine nachteiligen Auswirkungen in der intestinalen Homöostase beobachtet wurden und die tumorfördernde Funktion von Zeb1 in Epithelzellen bekannt ist, könnte die pharmakologische Hemmung von Zeb1 sogar zusätzliche positive Auswirkungen im Vergleich zu den Beobachtungen dieser Arbeit haben. Bisher ist jedoch nur ein eher unspezifischer Histon-Deacetylase-Inhibitor zur Verringerung der Zeb1 Expression bekannt. Vor einer klinischen Anwendung wären deshalb spezifischere und wirksamere Ansätze (z.B. mittels PROTACs oder RNAi) erforderlich.

Zusammenfassend deuten die Daten dieser Arbeit darauf hin, dass Zeb1 eine entscheidende Rolle bei der phänotypischen Ausprägung von Myofibroblasten spielt. Das Fehlen von Zeb1 führte zu einer Infiltration von Immunzellen und einem pro-inflammatorischen TME, was je nach untersuchtem Mausmodell eine Förderung oder Hemmung des Tumorwachstums bewirkt. Die durch *Zeb1* Deletion verursachte Immuninfiltration konnte ausgenutzt werden, um in unterschiedlichen Mausmodellen das Ansprechen auf Immun-Checkpoint--Therapien zu verbessern. Eine gezielte Beeinflussung der Zeb1-vermittelten Fibroblasten-Plastizität könnte somit in Kombination mit Immun-Checkpoint-Inhibition von klinischem Vorteil sein.

Summary

One of the major challenges in the treatment of colorectal cancers (CRC) is the high amount of inter- and intratumoural heterogeneity, leading to diverse treatment outcome and frequent relapse in initially responding patients. In order to obtain a better understanding of the underlying mechanisms, tumours have recently been classified into four subtypes (consensus molecular subtypes / CMS) based on their transcriptomic profile [Guinney et al. 2015]. The CMS4 subtype is characterised by the worst prognosis and an enrichment of TGFβ and stromal signatures. These signatures, caused by enrichment and activation of cancer-associated fibroblasts (CAFs), emphasise the importance of the tumour microenvironment (TME) in addition to tumour cell-intrinsic properties. CAFs are known to support tumour growth by secretion of growth factors, remodelling of the extracellular matrix (ECM) or establishment of an immuno-suppressive TME [Sahai et al. 2020]. Reducing CAF activation by inhibiting the TGFβ pathway allowed for improved treatment response in mouse models [Tauriello et al. 2018]. However, in pancreatic cancers, CAFs display a high degree of transcriptional and functional plasticity [Öhlund et al. 2017, Biffi et al. 2021], which complicates the identification of appropriate pharmacological targets for clinical translation. Another signature that was enriched in CMS4 tumours represents the epithelial-mesenchymal-transition (EMT). While metastatic progression of tumour cells was initially thought to be responsible for these patterns, several studies have identified CAFs as the main source of these signatures [Isella et al. 2015, Calon et al. 2015, Li et al. 2017]. EMT is regulated by several master regulator transcription factors (Zeb1/2, Snai1/2, Twist1), which inhibit expression of key epithelial genes such as E-cadherin and cytokeratins and instead induce expression of mesenchymal genes like Vimentin and N-cadherin, resulting in modulation of cell polarity and gain of cell motility [Huang et al. 2012a, Lamouille et al. 2014]. EMT transcription factors (EMT-TFs) have been extensively studied in epithelial cells, where they are usually expressed at the invasive front of tumours and thereby mediate the initiation of metastasis and induce therapy resistance [Chang et al. 2011, Krebs et al. 2017]. However, EMT-TFs also exhibit heterogeneous expression in stromal cells throughout the tumour and until now, the function of sustained expression of these factors in stromal cells remains unclear.

In this work, the role of EMT master regulator Zeb1 in cancer-associated fibroblasts was examined during the progression of colorectal cancers. Therefore, in a collaboration with the group of Thomas Brabletz (University Erlangen), mouse models were analysed that either reflect inflammation driven tumour initiation (AOM/DSS, AOM/P53) [Neufert et al. 2007] or mimic the progression of sporadic CRC in transplantation models (subcutaneous, orthotopic) [Fumagalli et al. 2017]. Tumour cell transplantation into syngeneic mice with fibroblast-specific inducible Cre expression (*Col1a2-CreERT2*) and a loxP-flanked *Zeb1* allele [Brabletz et al. 2017], allowed investigation of Zeb1 in CAFs during multiple stages of CRC initiation and progression in an immuno-competent background. *In vivo* findings

were examined mechanistically in mono- and cocultures of primary fibroblasts with CRISPR/Cas9 engineered tumour organoids and transgenic T cells.

Loss of Zeb1 changes fibroblast subtypes *in vitro* but not intestinal homeostasis

Before starting experiments *in vivo*, primary fibroblasts were isolated from inducible conditional *Zeb1* knockout mice for basic *in vitro* characterization. CAFs were cultured adherently and the absence of epithelial or immune cells was demonstrated. Induction of *Zeb1* recombination using lentiviral transduction of Cre recombinase resulted in cell cycle arrest and overgrowth of non-recombined cells. In contrast, recombined fibroblasts from conditional *Zeb1* animals could be permanently expanded after incubation with 4-hydroxy-tamoxifen. After recombination, a loss of myofibroblastic marker genes and an increase of inflammatory gene expression was observed both on transcriptomic and protein level. Functionally, loss of Zeb1 resulted in a decrease of cell contractility - one major characteristic of myofibroblasts - together with a loss of typical spindle-like morphology. Recombination of *Zeb1* in fibroblasts also affected niche signaling of fibroblasts in cocultures with intestinal organoids. While organoids cocultured with Zeb1 proficient fibroblasts still required addition of the growth factor Wnt, organoids in coculture with *Zeb1* deleted fibroblasts were able to grow independently of the addition of Wnt. Together, these findings indicated a disruption of fibroblast activation towards myofibroblasts after recombination of *Zeb1*, resulting in a change of fibroblast subtype *in vitro*. After a temporary growth arrest, recombined cells could be cultured regularly and the inflammatory state normalised. This suggested that under in vitro culture conditions, activation of compensatory mechanisms can compensate for the loss of Zeb1.

Although phenotypic differences in fibroblasts were found after *in vitro* recombination, no effects on intestinal homeostasis were observed in mice after several weeks of tamoxifen diet-induced *Zeb1* recombination. This could be due to differential properties of fibroblasts in normal tissue. While in adhesion culture ECM stiffness strongly promotes myofibroblast differentiation, only a small fraction of cells exerts a myofibroblast phenotype under homeostatic conditions. This could cause fibroblasts *in vivo* to be less dependent on Zeb1. In addition, myofibroblast contractility is particularly needed during wound healing, which may not have played a role during the relatively short duration of the experiments. The changes in niche signals secreted by fibroblasts might have been compensated by other cell types in the gut.

Stromal *Zeb1* deletion causes different phenotypes in CRC mouse models

In mouse models of colorectal cancer, effects of stromal *Zeb1* recombination were heavily dependent of the tumour model: In the inflammation driven AOM/DSS model, recombination of *Zeb1* induced increased chronic inflammation of the intestine and accelerated adenoma growth. In the AOM/P53 model, tumour growth and invasiveness were slightly reduced, indicating a delay in tumour initiation.

In subcutaneous transplantations (SCT) and orthotopic transplantations of tumour organoids, only minor effects on the primary tumour growth were observed. However, in the orthotopic transplantation model, liver metastasis was drastically reduced after stromal *Zeb1* recombination. Together, this suggests that the effect of stromal Zeb1 is strongly dependent on the TME of the tumour model. Interestingly, either aSMA staining was reduced (AOM/P53, SCT, orthotopic), the organization of fibres was changed (AOM/DSS) and/or the extracellular matrix (ECM) secretion was reduced (AOM/DSS, orthotopic), suggesting a loss of myofibroblasts due to *Zeb1* deletion. Furthermore, in all models except for the immuno-privileged SCT model, immune infiltration of T- and B cells into the primary tumour was increased and expression of immune checkpoint molecules (PD-L1) was enhanced, demonstrating activation of an adaptive immune response and compensatory immunoregulatory mechanism. These results could be confirmed by RNA sequencing. In the AOM/DSS and SCT models, bulk RNA sequencing revealed enrichment of inflammatory signatures and decreased expression of cell contractility genes. In addition, single cell RNA sequencing in the AOM/DSS and orthotopic models revealed loss of myofibroblast and ECM signatures, increased inflammatory patterns in the remaining CAF populations and overall decreased fibroblast plasticity. Single cell RNA sequencing in the orthotopic model also showed increased activation of T cells, B cells and macrophages.

Overall, consistent with *in vitro* findings, data from these models indicated an inhibition of myofibroblast differentiation upon recombination of *Zeb1*. However, in contrast to the *in vitro* cultures, the TME resulted in sustained inflammatory activation of fibroblasts. In the AOM/DSS model, these inflammatory signals appear to further enhance the intestinal inflammation and thereby, by promoting the pro-tumourigenic properties of the TME and consequently accelerate tumour growth and progression. In contrast, in the sporadic models, the pro-inflammatory signals from fibroblasts cause an enhanced anti-tumour immune response. In the AOM/P53 model, this results in delayed tumour initiation and thus slows tumour growth and progression. However, in the orthotopic model that represents an advanced tumour stage, this pro-inflammatory response does not seem to be sufficient to influence primary tumour growth.

Infiltration of immune cells is regulated by expression of Zeb1 in CAFs

Different mechanisms could explain the increased infiltration of immune cells into tumours after stromal deletion of *Zeb1*. The reduced number of myofibroblasts and the reduction of ECM in tumours with Zeb1 deficient CAFs could increase immune cell infiltration by weakening the physical barrier around the tumour. In addition, inflammatory activation of fibroblasts could lead to the release of cytokines that recruit immune cells to the tumour or regulate effector cell function.

In transwell coculture experiments with T cells, fibroblasts and tumour organoids, a monolayer of Zeb1 deficient fibroblasts represented a diminished barrier for T cell migration compared to Zeb1 proficient fibroblasts. At the same time, chemotaxis of T cells towards Zeb1 deficient fibroblasts was increased. Although the latter observation did not reach a significant level, these experiments indicated that both mechanisms might play a role *in vivo* and that the relative dependence of both mechanisms may depend on the tumour model and TME composition.

Zeb1 in fibroblasts promotes development of liver metastasis

In the orthotopic transplantation model, deletion of *Zeb1* in the stroma strikingly reduced incidence of liver metastasis in mice. Several observations indicated the involvement of immune cells in this effect: In WT mice, but not in *Zeb1* KO animals, immune cells frequently accumulated at the outer border of liver metastases. This indicates that Zeb1 is involved in the exclusion of immune cells from metastases, which could explain an enhanced anti-tumour immune response. This was further supported by an increased number of immune cell accumulations in the livers of stromal *Zeb1* KO mice compared to the livers of WT mice. The few KO mice that developed liver metastases exhibited a similar number and size of metastases as WT mice. This could be due to the induction of immune escape mechanisms that render metastatic tumour cells independent of fibroblasts. While all of the above observations indicate an important immuno-suppressive role of CAFs during early metastasis, it is also possible that CAFs are required to generate a pre-metastatic niche that supports colonization. To test these possibilities, further investigation is needed to distinguish both mechanisms. Informative experiments would be co-injection of tumour cells and WT or KO fibroblasts in liver colonisation assays or exclusion of immune cell populations by analysing immuno-deficient mice.

Modulation of fibroblast plasticity as combination therapy with immune checkpoint inhibition

In the AOM/DSS model and the orthotopic transplantation model, increased expression of immune checkpoint molecules was observed after recombination of *Zeb1* in fibroblasts. This could present an opportunity to enhance response to immune-checkpoint therapies by recombination of stromal *Zeb1*. The experiments showed that immune checkpoint inhibition resulted in reduced primary tumour size in the orthotopic model and almost complete growth arrest in the AOM/DSS model, highlighting the importance of CAFs as potential therapeutic targets. Together with the conserved functions of Zeb1 in human fibroblasts, this indicated that manipulation of fibroblast phenotypes by targeting Zeb1 could represent a promising approach for combinatorial therapies. Since no adverse effects occurred in intestinal homeostasis and multiple tumour-promoting functions of Zeb1 are known in epithelial cells, pharmacologic inhibition of Zeb1 might even have additional beneficial effects compared to the observations of this work. However, until now only one rather unspecific histone deacetylase inhibitor

has been shown to reduce expression of Zeb1. More specific and potent approaches (e.g. using PROTACs or RNAi) would therefore be required before clinical application.

In summary, the data in this work indicated that Zeb1 is critically involved in the acquisition of a myofibroblast-like CAF phenotype. The absence of Zeb1 resulted in immune cell infiltration and a pro-inflammatory TME, which could result in promotion or inhibition of tumour growth based on the mouse model. The immune infiltration caused by *Zeb1* deletion could be exploited to enhance response to immune checkpoint blockade therapies in different mouse models. Thus, targeting Zeb1 mediated fibroblast plasticity in combination with immune checkpoint inhibition might be beneficial in a clinical setting.

1. Introduction

1.1 Colorectal cancer

1.1.1 Colorectal cancer represents an important clinical challenge

Malignant transformations are a major health problem and account for approximately 10 million deaths per year worldwide [Bray et al. 2018]. Colorectal cancers (CRC) account for roughly 10 % of all newly diagnosed cancers (approximately 1.100.000 cases per year) and 6 % of cancer related deaths (approximately 550.000 cases per year) making them the second most common cancer in women and the third most common in men [Bray et al. 2018]. Besides aging as a common risk factor for cancers [Siegel et al. 2015], CRC is promoted by characteristics of the 'western lifestyle' including obesity [Kyrgiou et al. 2017], alcohol consumption [Cai et al. 2014], smoking [Botteri et al. 2008] and consumption of red and processed meat [Chan et al. 2011]. This explains why the incidence of CRC is higher in areas with a higher human development index (HDI) [Arnold et al. 2017] and is expected to increase even further. Apart from environmental factors, hereditary diseases and chronic inflammation of the intestine are known to enhance the CRC risk (see below) [Burt 2007, Dulai et al. 2016]. Recently also certain strains of microbiota (e.g. *E. coli* & *P. veronii*) were found to correlate with colorectal cancer incidence and were speculated to influence genomic stability or permeability of cells [Nakatsu et al. 2015, Kwong et al. 2018].

Clinically, CRC are mostly diagnosed by colonoscopy and categorized based on primary tumour size, invasiveness, spreading to surrounding lymph nodes and distant metastasis formation. Patients with early, localized tumours and patients with invasive but not metastasising tumours have high chances to be cured by surgical removal of the primary tumour. This results in relatively high 5-year survival rates in these stages of approximately 90 % and 71 % respectively. Patients with more progressed disease and distant metastases often cannot be cured by surgery and have to be treated by chemo- or radiotherapy. This leads to a dramatic drop of the 5-year survival rate to approximately 14% [Cancer Facts & Figures 2020 (www.cancer.org), CCA Treatment (www.ccalliance.org)]. These numbers highlight the importance of early detection of CRC. Since patients with early-stage CRC or precursor lesions often show only mild symptoms if any, preventive screening programs have been established to detect and remove these lesions before they can progress to invasive tumours. It is mainly attributed to these screening programs that mortality of CRC patients is steadily declining in many countries with high HDI [Ouakrim et al. 2015]. Although this development raises hopes, treatment options for patients with late-stage disease are still lacking. Further studies in clinical and basic research are urgently needed to understand the pathophysiologic mechanisms of CRC and to find treatment options for patients with distant metastases.

1.1.2 Mechanisms of colorectal carcinogenesis

The majority of colorectal cancers (approx. 65 %) occurs sporadic and without any known inherited predisposition. The rest of patients has a familial background of colorectal cancer or risk-enhancing factors like intestinal bowel disease (IBD), a chronic inflammation of the intestine [Dulai et al. 2016]. However, only a small fraction of patients has well defined hereditary syndromes like familial adenomatous polyposis (FAP)(< 1 %), or hereditary non-polyposis colorectal cancer (HNPCC, Lynch syndrome)(1-3 %) [Burt 2007].

Most CRC (approx. 70 - 90 %) follow the classical adenoma-carcinoma sequence [Dekker et al. 2019, TCGA 2012] (Figure 1). These tumours usually start with an inactivating mutation in the *APC* gene resulting in dysregulation and hyperactivation of the Wnt signaling pathway. Mutant cells obtain stem cell properties and start proliferating to form a benign lesion [Sansom 2004]. Subsequent mutations of the *KRAS* and *TP53* gene lead to tumour progression and invasive carcinoma formation. Additional inactivating mutations in the Transforming Growth Factor β (TGFβ) pathway are thought to be the limiting step for the formation of distant metastases and late-stage disease [Fearon & Vogelstein 1990, Drost 2015]. Tumours following this conventional sequence are characterised by chromosomal instability (CIN), which often results in somatic copy number alterations (SCNAs) and loss of heterozygosity (LOH). In contrast to other pathways, conventional tumours do not display microsatellite instability (MSI, see below) and are referred to as microsatellite stable (MSS) and non-hypermutated tumours [TCGA 2012, Dekker et al. 2019]. The molecular reasons for CIN in conventional tumours are unknown but mutations of APC and TP53 have been proposed to play a role [Pino & Chung 2010, Karlsson et al. 2022]. Development of tumours following the conventional sequence is dramatically accelerated in patients with familial adenomatous polyposis. These patients harbour a germline mutation of the *APC* gene and develop large numbers of benign intestinal polyps in early age. The chance of FAP patients to develop CRC from these lesions is close to 100 % [Burt 2007].

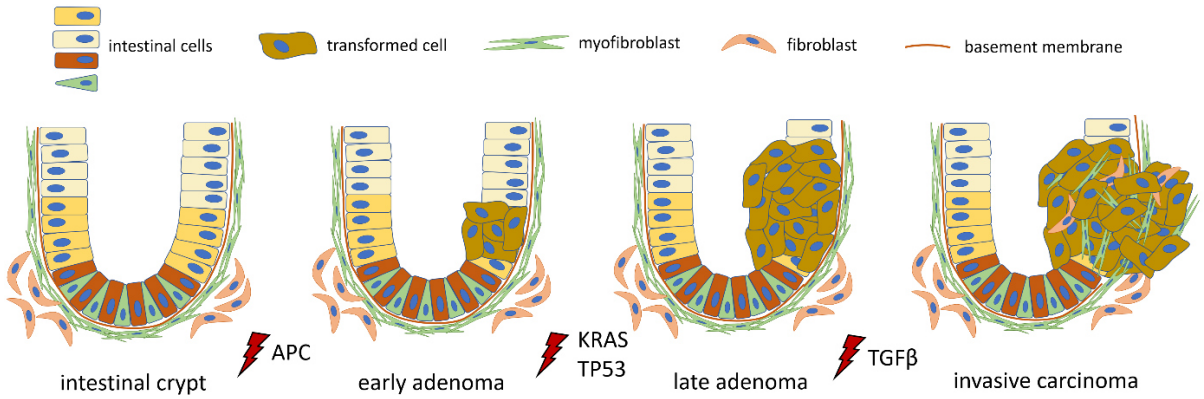

Figure 1: The "adenoma-carcinoma sequence" model of colorectal cancer
Tumour development following the classical adenoma-carcinoma sequence proposed by Fearon & Vogelstein. Intestinal epithelial cells are transformed by acquisition of an *APC* mutation followed by aberrant growth into small polyps (early adenoma). Subsequent mutations of *KRAS* and *TP53* accelerate tumour growth (late adenoma) and acquisition of TGFβ pathway mutations leads to invasive carcinoma growth.

The second group of tumours (approx. 2-7 %) is caused by mutations in genes like *MLH1/3*, *MSH2/3/6* or *PMS2* that comprise the DNA mismatch repair pathway [TCGA 2012, East et al. 2017, Dekker et al. 2019]. During DNA replication, slippage of the DNA polymerase results in errors that are especially frequent in short repetitive regions (so called microsatellites) and that are usually repaired by the cells via the DNA mismatch repair pathway [Boland & Goel 2010]. If this repair pathway is inactivated, e.g. by mutations in the genes mentioned above, these errors occasionally result in small indels and frameshift mutations. These mutations accumulate over time and lead to a tumourigenic hypermutation phenotype combined with alterations in the length of microsatellite regions (microsatellite instability). Most pathways that are commonly mutated in conventional tumours are also affected in hypermutated tumours, although the exact affected genes can vary [TCGA 2012]. Patients with Lynch syndrome harbour germline mutations in the *MLH1*, *MSH2*, *MSH6* or *PMS2* gene and thereby are very likely to develop colorectal cancer with MSI characteristics [Burt 2007].

The third common mechanism of colorectal tumourigenesis is caused by epigenetic dysregulation instead of genomic alterations (approx. 10 - 20 % of patients) [East et al. 2017, Dekker et al. 2019]. The CpG island methylation phenotype (CIMP) leads to hypermethylation and silencing of cancer related genes and tumourigenesis. Tumours with the CIMP phenotype usually progress from serrated polyps and harbour mutations in the *KRAS* or *BRAF* gene. Depending on the methylation status of DNA mismatch repair genes like *MLH1*, *CIMP* driven tumours can exhibit both, the MSI or the CIN phenotype [TCGA 2012, Kim & Kim 2018, Dekker et al. 2019] (Figure 2 A).

Both pathways, the mutation driven and the epigenetically driven tumourigenesis can be accelerated in patients with chronic inflammatory diseases like Ulcerative colitis. Injury of intestinal tissue and failure to restore the epithelial barrier function can cause chronic inflammation and lead to exaggerated regenerative responses resulting in increased proliferation and stem cell characteristics. Combined with the continuous release of inflammatory cytokines and growth factors, this microenvironment can increase the mutation rate and cause epigenetic dysregulation [Grivennikov 2013]. Together, chronic inflammation increased the CRC risk approximately about 60% [Herrinton et al. 2012].

1.1.3 Clinical and molecular classification of colorectal cancers

Irrespective of the mechanism of tumourigenesis, CRC are clinically categorized based on the anatomic location and histological features. However, clinical staging only shows limited predictive value for the treatment response [De Rosa et al. 2015]. To improve understanding of the underlying mechanisms, multiple studies were performed that tried to link tumour properties to specific mutations [Drost et al. 2015, Matano et al. 2015] but while often the same pathways are activated in CRC, many genes responsible for this activation are affected in less than 10 % of tumours [TCGA 2012], which

complicates application of targeted therapies [Ke & Shen 2017]. In addition, CRC often displays high levels of intratumoural heterogeneity, where regional differences in driver and bystander mutations can act as a reservoir of resistance conferring alterations in case of therapies [Braisse et al. 2001, Venkatesan et al. 2017, Molinari et al. 2018]. To include this heterogeneity in classifications, tumours were categorized based on expression profiles and next generation sequencing [Sadanandam et al. 2013, Marisa et al. 2013, Calon et al. 2015, Bramsen et al. 2017]. Recently, a consortium of research groups combined multiple classification system into a consensus molecular subtype (CMS) classifier [Guinney et al. 2015] (Figure 2 B). Four different CMS groups were defined based on transcriptomic data of large numbers of patients from multiple cohorts:

The 14 % of tumours in the CMS1 subtype represented the majority of hypermutated MSI tumours in the datasets. These tumours had lower CIN and fewer SCNAs compared to the other CMS groups combined with a general hypermethylation status (CIMP high). CMS1 tumours were enriched for BRAF mutations and for immune-infiltration and immune-evasion signatures. Accordingly, CMS1 was termed the MSI immune subtype. Early stage CMS1 tumours showed favourable prognosis, however in line with previous findings, patients in this group showed worse survival after relapse [Gavin et al. 2012]. This can be explained by good response to ICB in early stage cancers, which is lost in patients with tumour relapse due to development of immune escape mechanisms and therapy resistance.

37 % of the tumours were assigned to the CMS2 subtype. These tumours were enriched for CIN and SCNAs and represented the conventional adenoma to carcinoma axis [Fearon & Vogelstein 1990]. These 'canonical' tumours showed high Wnt and MYC levels and enrichment for differentiation signatures. Patients with CMS2 tumours showed enhanced survival after relapse. The 13 % of tumours assigned to the 'metabolic' CMS3 subtype showed a mixed MSI and CIMP status together with enrichment for *KRAS* mutations. They were characterized by an enrichment of metabolic signatures indicating dysregulation previously reported for other cancer entities [Son et al. 2013, Brunelli et al. 2014]. Approximately one quarter (23 %) of tumours was assigned to the 'mesenchymal' CMS4 subtype. This subtype was enriched for stromal signatures, angiogenesis and matrix remodelling together with signatures of the epithelial-to-mesenchymal-transition EMT and TGFβ signaling. Patients assigned to this subtype more often had late-stage disease compared to other subtypes and had a worse overall prognosis [Guinney et al. 2015].

14 % of the examined tumours could not clearly be assigned to one subtype. This could be explained either by high intra-tumour heterogeneity or low sequencing quality data of these tumours. Interestingly, only few mutations showed clear enrichment in one subtype or had an effect on patient prognosis, highlighting the importance of other factors than classical driver mutations [Guinney et al.

2015]. The clinical relevance of CMS classification is currently examined in clinical trials [Mooi et al. 2018, Stintzing et al. 2019, Rebersek 2020].

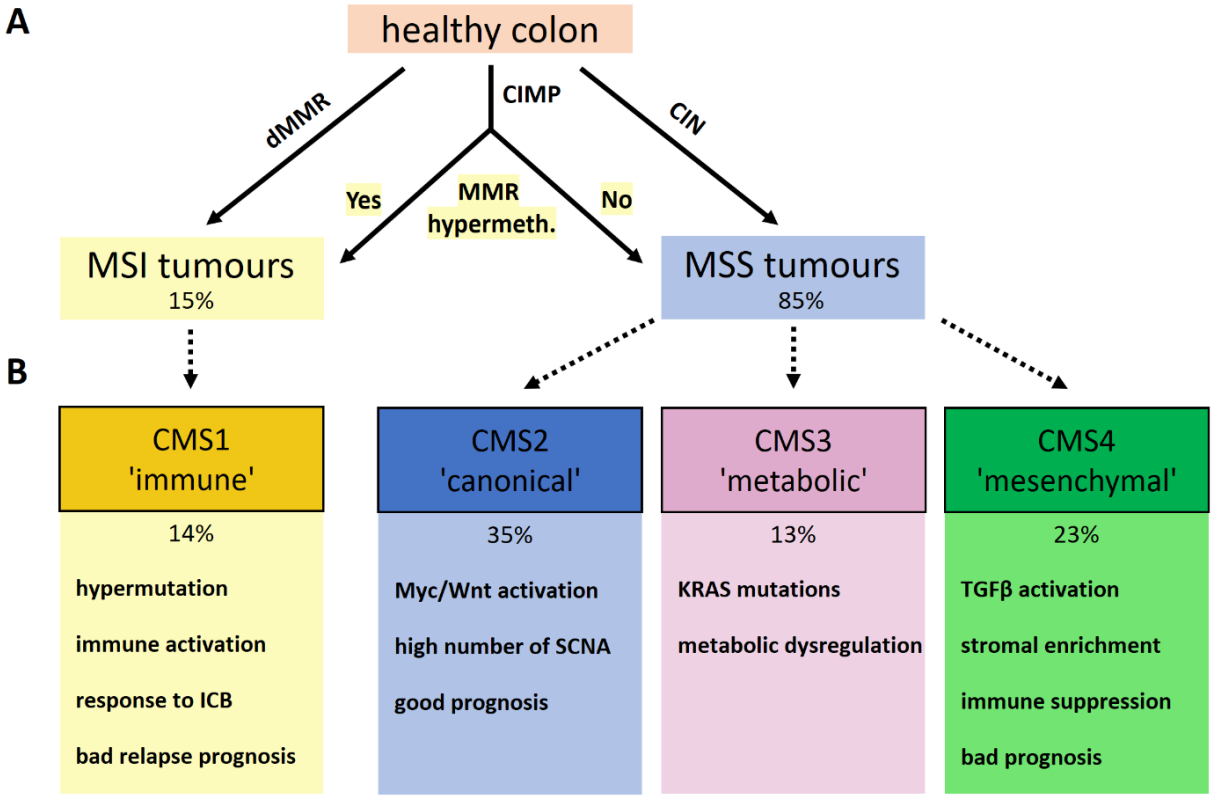

Figure 2: Potential routes of tumourigenesis and molecular classification of human CRC
A Mechanisms of colorectal cancer development based on genetic and epigenetic molecular features. dMMR: deficient mismatch repair, CIMP: CpG island methylation phenotype, CIN; chromosomal instability, MSI: microsatellite instable, MSS: microsatellite stable. **B** Classification of colorectal cancers into consensus molecular subtypes (CMS) and features of the respective subtypes. Percentages are based on Guinney et al. 2015. Missing 15% could not be assigned clearly to one subtype. SCNA: somatic copy number alterations, ICB: immune checkpoint blockade.

1.1.4 Intestinal organoids as a model for the gastrointestinal epithelium

In healthy individuals, intestinal epithelial cells are continuously replaced by new cells that are shed into the lumen of the gut after only 3-4 days [Date et al. 2015]. This regeneration is driven by adult intestinal stem cells which are located in the crypt bases between the intestinal villi interspaced between differentiated cells (Paneth cells in the small intestine and specialized goblet cells in the colon) [Sato et al. 2011, Rothenberg et al. 2012]. Proliferation of these stem cells results in proliferating progenitor cells called transit-amplifying cells that further differentiate while ascending towards the villus tip (Figure 3 A). The balance between stem cell self-renewal and differentiation is maintained by a gradient of autocrine and paracrine growth factors (e.g. from the Wnt-, bone morphogenic protein (BMP)- or Notch-pathway) that are secreted by epithelial, stromal or immune cells [Meran et al. 2017].

About ten years ago, this architecture could be reproduced *in vitro* by culturing mouse or human intestinal stem cells in an artificial extracellular matrix (Matrigel®) [Sato et al. 2009, Sato et al. 2011].

Addition of appropriate growth factors led to formation of three-dimensional (3D) structures termed organoids that self-organized to recapitulate the crypt-villus axis and that could be propagated infinitely. Compared to cell lines, organoids offer the advantages of prolonged untransformed growth and the potential to differentiate into all epithelial intestinal cell lineages. This results in a high degree of heterogeneity, which can be used to examine interactions between different cell types, and allows detection of phenotypes driven by differentiated cells [Kretzschmar 2020].

Organoids can be generated from fragments of healthy tissue (as small as single adult stem cells) or malignant tissue (like cancer biopsies) or can be differentiated from induced pluripotent stem cells [Sato et al. 2009, Sato et al. 2011, McCauley et al. 2017]. Organoids derived from adult tissues closely mimic the morphology of epithelial cells within the organ context including heterogeneity of cell types and growth factor dependencies [Drost et al. 2015, Matano et al. 2015] (Figure 3 B). Additionally, a variety of genetic methods has been adapted, including CRISPR/Cas9, transduction and transfection, allowing versatile genetic engineering of organoids [Schwank et al. 2013, Schwank et al. 2013a, Koo et al. 2013, Menche & Farin. 2021]. This makes organoids a valuable tool in cancer research, where they have been used to model the stepwise acquisition of driver gene mutations [Drost et al. 2015, Matano et al. 2015] or to study different aspects of tumour progression in transplantation models (see below). Also, efficient cryopreservation protocols allow for long-term storage of patient derived tumour organoids (PDTOs). Such "living biobanks" facilitate phenotypic analyses, e.g. drug screens to predict therapy responses in patients [Van de Wetering et al. 2015, Fujii et al. 2016].

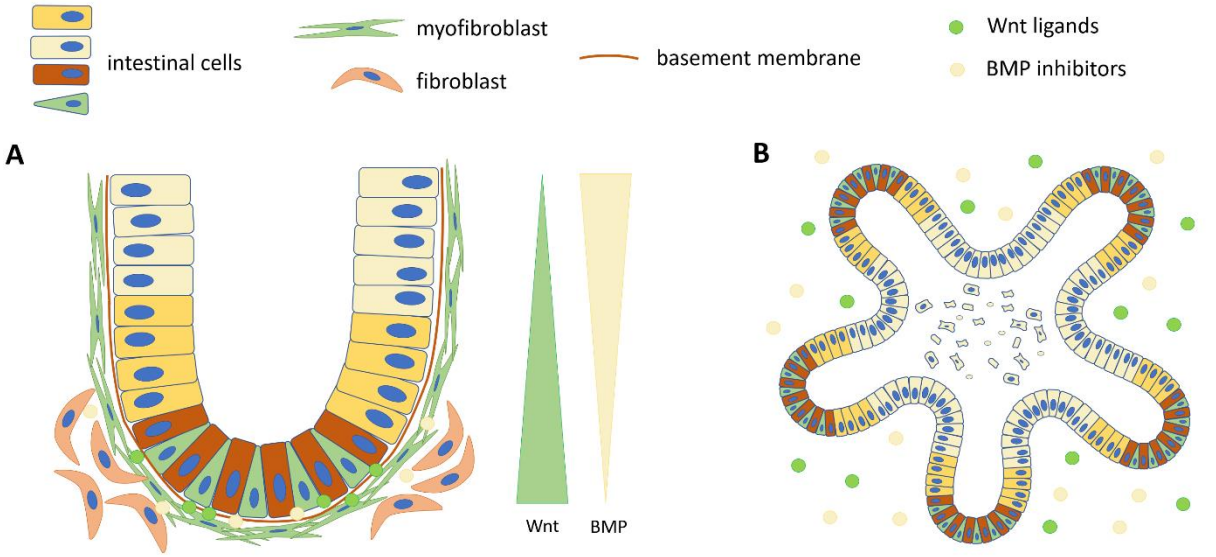

Figure 3: Recapitulation of the stem cell niche in intestinal organoids
A Tissue architecture in the intestinal stem cell niche. Stem cells (green) are interspaced between Paneth cells (small intestine) or specialized goblet cells (colon)(red). Proliferation of stem cells in the crypt bottom produces proliferative progenitor cells (dark yellow) that are displaced towards the villus tip and differentiate into the effector lineages (light yellow). Gradients of growth factors are established by cytokine secretion from epithelial and stromal cells and regulate these differentiation processes. **B** Section through an intestinal organoid recapitulating the intestinal niche and villus architecture. Differentiated cells are shed into the organoid lumen. The stromal contribution to the intestinal niche is replaced by exogenous addition of growth factors.

1.1.5 Overview of current mouse models of colorectal cancer

In order to recapitulate the pathophysiology of tumour growth *in vivo*, animal models of colorectal tumourigenesis have been established. Since no single mouse model can recapitulate the whole process from tumour initiation to metastatic disease, a variety of models has been established that focus on different stages of CRC. Two major types of *in vivo* models have been established: Autochthonous models, in which tumours are initiated *de novo* in the surrounding tissue context, recapitulate tumourigenesis in the mouse intestine and allow to address tumour initiation and primary tumour development. In contrast, transplantation models usually bypass the steps of tumour initiation but allow to examine late-stage cancer phenotypes (Table 1) [Bürtin et al. 2020].

One common approach to induce tumourigenesis in mice is the repeated exposure to carcinogenic reagents. The most frequently used reagent is Azoxymethane (AOM) a DNA methylating agent which, when administered orally, induces DNA damage and thereby leads to introduction of mutations in the intestinal tract. Accumulation of these mutations leads to formation of intestinal adenomas starting from week 24 [Papanikolaou et al. 2000] qualifying this system as a model of early-stage colorectal carcinogenesis. AOM is often combined with the administration of dextran sodium sulfate (DSS) to speed up tumour development [Tanaka et al. 2003, Neufert et al. 2007]. DSS disrupts the epithelial monolayer of the intestine, leading to entry of microbiota into the colonic mucosa and to subsequent inflammatory response in the mouse intestine [Eichele & Kharbanda 2017]. Exposure of mice to DSS alone can be used to model chronic inflammation of the gut and in combination with AOM is used to model inflammation induced tumourigenesis in the intestine [Neufert et al. 2007]. Using these models, the influence of factors like diet composition or microbiome were examined on colorectal carcinogenesis [Velázquez et al. 2016, Sun et al. 2018]. However, the AOM/DSS models cannot fully represent the human disease. While humans often only harbour single tumours mainly in the colon, mice exposed to AOM develop a multitude of adenomas in the colon and the small intestine. Due to this high tumour burden, mice have to be sacrificed before developing invasive tumours, which prevents examination of late-stage disease [Rosenberg et al. 2008, Bürtin et al. 2020]. Additionally, the effect of AOM and DSS heavily depends on the genetic background of the mouse strain, the intestinal microbiome and the concentrations used [Prashant et al. 2003, Suzuki et al. 2005, Zackular et al. 2015]. Also, AOM driven tumours only partially reflect the genetics of human tumours and the heterogeneity introduced by random mutagenesis leads to high experimental variability [De Filippo et al. 1998, Erdman et al. 1998, Bürtin et al. 2020].

Another approach to induce colorectal tumourigenesis in mice is the targeted introduction of driver gene mutations. The first genetic mouse model of CRC was the APC^{Min} model where mutation of one allele of the *APC* gene and loss of heterogeneity (LOH) leads to the formation of intestinal adenomas

after approximately 120 days [Moser et al. 1990]. The APC^{Min} model reflects tumour development following the classical adenoma-carcinoma sequence but due to development of multiple small intestinal tumours and the long latency, it is not suited to study of invasive or metastatic disease. Because of embryonic lethality of homozygous APC^{Min} mutation [Moser et al. 1995], APC^{Min} mice are combined with administration of AOM to accelerate tumour development [Møllersen et al. 2004]. Subsequently, crossing of mutated mouse strains and targeted mutagenesis were applied to combine mutations in different driver genes (e.g. *Tp53*, *Kras, Pik3ca* or *Smad4*) to model different aspects of tumourigenesis which resulted in invasive growth in some of the models [Takaku et al. 1998, Halberg et al. 1999, Sansom et al. 2006, Hadac et al. 2015]. Recent studies have been able to link combinations of driver gene mutations to the development of cancers representing specific CMS subtypes [Kucherlapati et al. 2010, Jackstadt et al. 2019, Maitra et al. 2019] and combination of AOM administration with conditional deletion of *Tp53* has led to formation of invasive and metastatic tumours [Schwitalla et al. 2013]. To limit the cancerogenic effects to the intestine, tumourigenic mutations are usually driven by promoters with expression restricted to intestinal stem cells [Saam et al. 1999, el Marjou et al. 2004] or colonic cells [Tetteh et al. 2016]. However, similar to the AOM/DSS model mice with conditional activation of driver genes often develop multiple tumours instead of single lesions and the burden of primary tumours prevents examination of metastatic progression [Bürtin et al. 2020].

To accelerate tumour formation and reduce mutational heterogeneity, transplantation models of colorectal cancer have been established. Early approaches used cancer cell lines that were transplanted subcutaneously into the flank of mice. While this leads to robust tumour formation after approximately 20 days [Radulovic et al. 1999], these tumours can neither reflect the morphology of human cancers nor recapitulate stromal influences. This is especially true for the transplantation of human cell lines that have to be transplanted in immuno-deficient mice and therefore lack the ability to model influences of immune cells [Bürtin 2020]. Recapitulation of tumour morphology improves dramatically when tumour fragments or organoids are transplanted instead of cell lines. In these, preservation of cell type heterogeneity enables tumour morphologies that closely resemble parental tumour tissue [Burgenske et al. 2014, Fujii et al. 2016, Mullins et al. 2019] or mimics histological features observed during CRC progression [Drost et al. 2015]. Although subcutaneous transplantation enables analysis of defined invasive tumours, mice usually lack formation of distant metastases and the immuno-privileged nature of the skin prevents analysis of immune-cell driven phenotypes.

To overcome these hurdles, orthotopic transplantation models of CRC have been established in which tumour cells are administered directly into the intestine. This allows to study the influence of the native tissue microenvironment and also leads to spontaneous metastasis to liver, lungs and peritoneum,

which are common sites of metastasis in patients [Riihimäki et al. 2016]. In general, three different ways of cell delivery to the intestine have been published: The first technique uses (endoscopy-based) submucosal injection of tumour cells [Zigmond et al. 2011, Zaytseva et al. 2014] or tumour organoids [de Sousa e Melo et al. 2017, Roper et al. 2018]. This method offers the advantage of not being very labour intensive combined with a minimally invasive procedure for the animal. On the downside, the exact location and amount of the injected cells cannot be determined. The second technique uses engraftment of tumour cells [Kishimoto et al. 2013] or organoids [O'Rourke et al. 2017] into pre-damaged mucosa of mice. While this model can reflect a broad spectrum from early tumour growth to metastasis, it also takes considerably longer to develop distant metastases (>20 weeks compared to approximately 6 weeks in the organoid models) and stochastic engraftment of cells leads to high variability between mice. In addition, pre-damaging of the colonic mucosa can increase mortality of mice and induces an inflammatory response that might influence tumour development. To reduce DSS induced mortality, predamaging of the colonic mucosa can be done using a brush instead of DSS [Sugimoto et al. 2018, Kim et al. 2022]. The third technique uses surgery to transplant cells [Klose et al. 2016] or organoids [Fumagalli et al. 2017, Fumagalli et al. 2018] into the caecum wall. By embedding the cells in a Matrigel® or collagen matrix, number and location of transplanted cells can be reliably adjusted. While the first two techniques reflect tumour engraftment and late stages of tumour initiation, the surgical approach has an advantage to study metastasis.

In summary, a vast spectrum of mouse models of CRC has been established and by choosing appropriate models for different stages of tumour development, specific questions can reliably be addressed. The use of organoid transplantations over cell lines is recommended to closely recapitulate cancer morphologies and phenotypes [Bürtin 2020].

Table 1: Comparison between available mouse models of colorectal cancer.

Model	Focus	Advantages & limitations
Subcutaneous transplantation	**- primary tumour**	**- very fast & easy to perform** **- convenient monitoring** **- does not accurately recapitulate TME** **- no invasion / metastasis**
AOM/DSS	**- initiation** **- primary tumour**	**- autochthonous tumour initiation** **- reflects inflammation driven carcinogenesis** **- multifocal, long latency and generally no metastasis** **- heterogeneous DSS response & lethality**
AOM/P53	**- initiation** **- primary tumour** **- invasion**	**- autochthonous tumour initiation & invasion** **- multifocal, long latency** **- rarely metastasis due to primary tumour burden**
Orthotopic transplantation	**- late stage tumours** **- invasion** **- metastasis**	**- fast distant organ metastasis** **- only one primary tumour at defined location** **- inappropriate model for tumour initiation** **- labour intensive and reduced monitoring**

1.2 The tumour microenvironment in colorectal cancers

In solid cancers, the malignant tumour cells are surrounded by a multitude of other cell types and elements of the extracellular matrix, which in total is termed the tumour microenvironment (TME). Each of the individual elements of the microenvironment influences tumour cells and other elements of the TME and thereby contributes to regulation of tumour progression and growth. In CRC, enrichment of TME signatures correlates with worst overall prognosis in CMS4 patients [Guinney et al. 2015]. The most important elements of the TME are the extracellular matrix (ECM), blood vessels, immune cells and cancer-associated fibroblasts (CAFs) [Giraldo et al. 2019]. Recent advances in single cell sequencing technology allowed to characterise the TME in great detail, uncovering subpopulations of stromal cells in various tumour entities. Conserved and context specific subpopulations were observed and further research is required to decipher the functions and crosstalk of these populations [Elyada et al. 2019, Wu et al. 2021, Khaliq et al. 2022].

1.2.1 Extracellular matrix

The extracellular matrix consists of multiple different protein and glycan fibres including collagens, fibronectins, laminins and glycosaminoglycans. The composition and structure of these molecules is actively remodelled by cells secreting additional fibres or proteases (especially CAFs and tumour cells) and can serve as a barrier or as a reservoir for cytokines and growth factors [Winkler et al. 2020, Sheppard 2005] In cancers, changes in fibre composition of the ECM influence tissue stiffness and thereby affect invasiveness and therapy resistance of cancer cells [Liu et al. 2020, Henke et al. 2020].

1.2.2 Tumour vasculature

Due to dysregulated proliferation, tumour growth depends on continuous supply of oxygen and nutrients. In areas that are not vascularized, hypoxic conditions can induce secretion of proangiogenic factors like vascular endothelial growth factor (VEGF) or fibroblast growth factor (FGF) leading to formation or expansion of blood vessels and vascularization of the tumour [Carmeliet et al. 2000]. In addition to the enhanced nutrient supply, tumour blood vessels can express adhesive or repulsive surface molecules and chemokines and modulate the immune cell recruitment to the tumour [Huang et al. 2018]. Access to blood vessels also represents a limiting step in the formation of distant metastases [Pereira et al. 2018].

1.2.3 Tumour infiltrating immune cells

Immune cells play various roles in the regulation of tumour growth and progression. On one hand, immune cells (especially cytotoxic $CD8^+$ T cells and NK cells) can recognize transformed tumour cells and exert anti-tumour immune responses leading to killing of malignant cells [Giraldo et al. 2019]. This requires tumour cells to develop evasion mechanisms to avoid immune cell detection or reactivity. Immune-escape mechanisms can include downregulation or mutation of MHC class I molecules

[Maleno et al. 2004, Shukla et al 2015] or expression of immune-inhibitory ligands like PD-L1 or CTLA-4 [Contardi et al. 2005, Ohaengbulam et al. 2014]. On the other hand, inflammatory processes can lead to the release of cytokines, which promote proliferation, angiogenesis and tumour growth [Condeelis et al. 2006, Smyth et al. 2006, Grivennikov et al. 2010]. Additionally, tumour cells can induce suppressive phenotypes of immune-populations (e.g. regulatory T cells or myeloid-derived suppressor cells) which attenuate anti-tumour responses of other immune cell populations [Gallimore et al. 2008, Gabrilovich & Nagaraj 2009].

Generally, the sustained infiltration of immune cells into the tumour is associated with better prognosis in patients [Galon et al. 2006]. This led to development of the "Immunoscore", which can predict the risk of relapse based on the localization of CD3 and CD8 T cells with a better prognostic value compared to classical TNM classification [Galon & Lanzi 2020]. However, the composition of immune cells and their activation status are critical for the interaction with tumour cells or other components of the TME [Grivennikov et al. 2010, Giraldo et al. 2019]. Different approaches have been used to include the patient's or foreign immune cells in anti-cancer therapies. Most prominent examples are immune checkpoint blockade (ICB) therapies [Darvin et al. 2018] or adoptive cell transfer of tumour-reactive immune cells [Rohaan et al. 2019]. ICB therapies aim at immune-inhibitory ligands (e.g. PD-L1 or CTLA-4) that are expressed by cancer cells and dampen host immune responses as a mechanism of tumour immune evasion. Antibody-mediated blockade of these ligands then re-enables the patient's immune system to exhibit anti-tumour immune responses [Darvin et al. 2018]. For many cancer entities, ICB therapy has proven a promising treatment during the last years [Havel et al. 2019]. Likely due to the increased amount of tumour-infiltrating immune cells and generation of neoantigens [Boland & Goel 2010, Giannakis et al. 2016], ICB therapy has been most efficient in tumours with high mutational burden [Le et al. 2017, Samstein et al. 2019, Chan et al. 2019]. Accordingly, the approximately 5 % of late-stage CRC patients that harbour MSI tumours show consistent response to ICB [Kalyan et al. 2018, Marmorino et al. 2020]. However, the majority of CRC patients harbours MSS tumours, which show low immunogenicity and often display an immune-excluded or immune-deserted phenotype [Picard et al. 2020, Marmorino et al. 2020]. These patients rarely benefit from immune checkpoint blockade therapy [Le et al. 2015].

1.2.4 Cancer-associated fibroblasts

Fibroblasts are usually defined based on their location and origin and do not express lineage markers of epithelial (CD326), endothelial (CD31) or immune (CD45) cells [Sahai et al. 2020]. Fibroblasts are involved in many physiologic and pathophysiologic processes including organization of extracellular matrix, secretion of niche factors, wound healing and regulation of inflammation [Kalluri 2016, Ziani et al. 2018, Karpus et al. 2019]. In proximity of cancer cells, fibroblasts can become activated by secreted

growth factors (like TGFβ) resulting in a change of gene expression and phenotypic plasticity [Kuzet & Gaggioli 2016]. So far, two major subtypes of CAFs have been identified that appear in multiple different cancer entities: contractile myofibroblasts (myCAFs) and inflammatory fibroblasts (iCAFs) [Öhlund et al. 2017, Li et al. 2017, Lambrechts et al. 2018]. While myCAFs can be identified by strong expression of alpha smooth muscle actin (aSMA) in addition to common fibroblast markers, no single unique marker could be identified for inflammatory fibroblasts [Biffi et al. 2021]. Also, fibroblast subtypes are believed to be highly plastic and intermediate states might further complicate isolation and characterization of specific subpopulations [Biffi et al. 2019, Liu et al. 2019]. Recent reports indicate pro-tumourigenic properties of myofibroblasts including the exclusion of immune cells and secretion of growth factors or ECM components whereas inflammatory CAFs have been found to recruit and modulate immune cells by secretion of cytokines and chemokines (e.g. IL6, CXCL1 and CXCL12) and to induce EMT in epithelial cells [Öhlund et al. 2017, Tauriello et al. 2018, Biffi et al. 2019, Mosa et al. 2020]. However, also tumour-suppressive properties of CAFs have been described [Rhim et al. 2014, Özdemir et al. 2014] and the origin of CAFs might also play a role in determining CAF markers and functions [Raz et al 2018].

The clinical relevance of CAFs is highlighted by tumours of the CMS4 subgroup, which are enriched for stromal and TGFβ signatures [Guinney et al. 2015]. In addition, further stratification of patients has highlighted CAFs as markers of bad prognosis and promising targets for new therapeutic approaches [Isella et al. 2015, Calon et al. 2015, Li et al. 2017]. Recent single cell sequencing has identified diverse CAF subpopulations, yet their exact functions have to be further examined which could offer opportunities for future stroma-directed therapies [Li et al. 2017, Bartoschek et al. 2018, Su et al. 2018, Costa et al. 2018, Givel et al. 2018, Elyada et al. 2019].

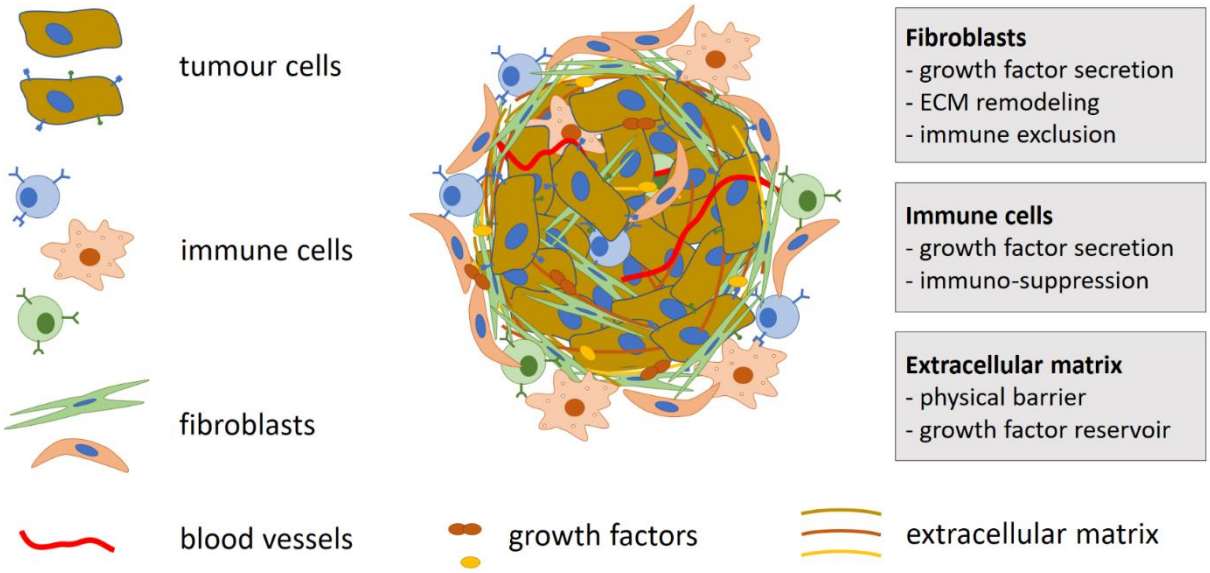

Figure 4: Elements of the tumour microenvironment and their tumour-promoting functions
Elements of the tumour microenvironment. Tumour cells are interspersed by extracellular matrix fibres, blood vessels and fibroblasts. Immune cells mainly accumulate on the outside of the tumour where fibroblasts and extracellular matrix present a barrier for immune cell infiltration. Epithelial cells can upregulate immune-checkpoint molecules to inhibit anti-tumour immune responses.

1.3 Regulation of the epithelial-mesenchymal-transition in cancers

The epithelial-to-mesenchymal transition (EMT) is a developmental program that allows epithelial cells to reduce expression of cell-cell adhesion molecules and lose apical-basal cell polarity in order to acquire features of mesenchymal cells including increased motility and cell protrusions and acquisition of stem cell features [Mani et al. 2008, Thiery et al. 2009, Lamouille et al. 2014]. This process can be initiated either by activation of extracellular signaling pathways (e.g. TGFβ, Notch or Wnt [Song 2007, Heuberger & Birchmeier 2010, Scheel et al. 2011, Palagani et al. 2012]) or by intracellular stimuli like Hypoxia and metabolic stress [Zhang et al. 2013, Puisieux et al. 2014]. Presence of these cues activates the EMT transcription factors (EMT-TFs) Zeb1/2, Snai1/2 and/ or Twist1 which inhibit expression of key epithelial genes (E-cadherin, claudins, cytokeratins) and induce expression of mesenchymal genes (N-cadherin, Vimentin) [Yilmaz & Christofori 2009, Huang et al. 2012a]. This leads to destabilization of cell-cell junctions, remodelling of the ECM and restructuring of the cytoskeleton [Lamouille et al. 2014]. During this process, cells transition plastically through multiple intermediate stages, which possess features of both epithelial and mesenchymal cells. These hybrid states are called partial EMT (pEMT) and it has been observed that EMT can be reversible by a process called mesenchymal-epithelial-transition (MET) [Huang et al. 2012a, Lamouille et al. 2014, Pei et al. 2019]. While EMT is required in physiologic processes like gastrulation and wound healing, it also plays an important role in development of several disorders like fibrosis and cancer [Kim et al. 2017, Haensel et al. 2018].

In cancers, a varying degree of motility of tumour cells is required depending on the stage and environment of the tumour. Especially in late stage cancers, cells along the invasive front undergo EMT to invade into adjacent tissues and to dissociate from the primary tumour mass to intravasate into the vasculature [Brabletz et al. 2001, Spaderna et al. 2006]. Afterwards, cells have to switch back to an epithelial status in order to colonize distant organs and to form metastases [Tsai et al. 2012, Beerling et al. 2016]. This back and forth between epithelial and mesenchymal traits is achieved by a tightly regulated balance between EMT and MET processes [Nieto et al. 2016, Lu & Kang. 2019]. In addition to this highly dynamic regulation, the effect of EMT was shown to be highly context and model dependent. Many models show a strong increase of metastasis upon upregulation of EMT-TFs [Tran et al. 2014, Krebs et al. 2017, Xu et al. 2017], however in some cases, EMT seems to be dispensable for metastasis [Zheng et al. 2015, Fischer et al. 2015]. A clear association of EMT with pro- or anti-tumourigenic functions is complicated by the pleiotropic functions of EMT-TFs that can also affect tumour progression independently. For example, Twist1 enhances p53 degradation [Piccinin et al. 2012], Snai1 increases tumourigenesis of keratinocytes by inducing proliferation and resistance to genotoxic stress [De Craene et al. 2014] and Snai2 confers resistance to the EGF pathway inhibitor gefitinib [Chang et al. 2011]. Additionally, activation of EMT-TFs can lead to acquisition of stem cell features in differentiated cells, increasing malignant potential of these cells and connecting EMT with the concept of cancer stem cells [Scheel & Weinberg 2011].

As the focus of this work mainly lies on Zeb1, the following paragraph will provide a more detailed view of this EMT-TF only.

1.4 Pathophysiologic functions of the EMT-TF Zeb1

Zinc finger E-box binding homeobox 1 (Zeb1) is a large protein of 1124 amino acids in humans that contains seven zinc finger and one homeobox domains [www.uniprot.org]. The zinc fingers are split into two clusters (N- and C- terminal of the homeobox domain), which bind to E-box-like (CACCT(G)) DNA sequences [Drápela et al. 2020]. After binding of DNA, various co-factors including CtBP or YAP1 interact with Zeb1 to enhance or inhibit expression of the target genes [Postigo et al. 1999, Postigo et al. 2003a, Sánchez-Tilló et al. 2010, Roche et al. 2013, Lehmann et al. 2016].

The function of Zeb1 is regulated by members of the miR-200 family (miR-200a, miR-200b, miR-200c, miR-141 and miR-429) and miR-205. These miRNAs bind to several conserved regions in the *Zeb1* 3'-UTR and mediate post-transcriptional repression [Gregory et al. 2007, Korpal et al. 2008]. At the same time, Zeb1 transcriptionally represses expression of these miRNAs resulting in a double-negative-

feedback loop and the Zeb1/miR-200 axis thereby constitutes a molecular switch between epithelial and mesenchymal states [Burk et al 2008, Bracken et al. 2008, Brabletz & Brabletz 2010].

In cancers, expression of Zeb1 has been associated with multiple factors that favour tumour progression and metastasis. The most prominent role is the direct repression of cell-cell junction proteins, which facilitates dissociation of tumour cells from the primary tumour as a first step during metastasis [Aigner et al. 2007]. In addition, cells expressing Zeb1 have been shown to overcome senescence [Liu et al. 2008, Ohashi et al. 2010] and the presence of Zeb1 or the absence of miR-200 family members has been linked to increased stemness in pancreatic or colorectal cancer cells respectively [Wellner et al. 2009, Lu et al. 2014]. Together, these growth benefits result in increased therapy resistance (chemotherapy or targeted (e.g. EGFR inhibitors)) of Zeb1 expressing cells in various tumour entities [Witta et al. 2006, Wellner et al. 2009, Arumugam et al. 2009, Haddad et al. 2009, Tryndyak et al. 2010, Guo et al. 2017].

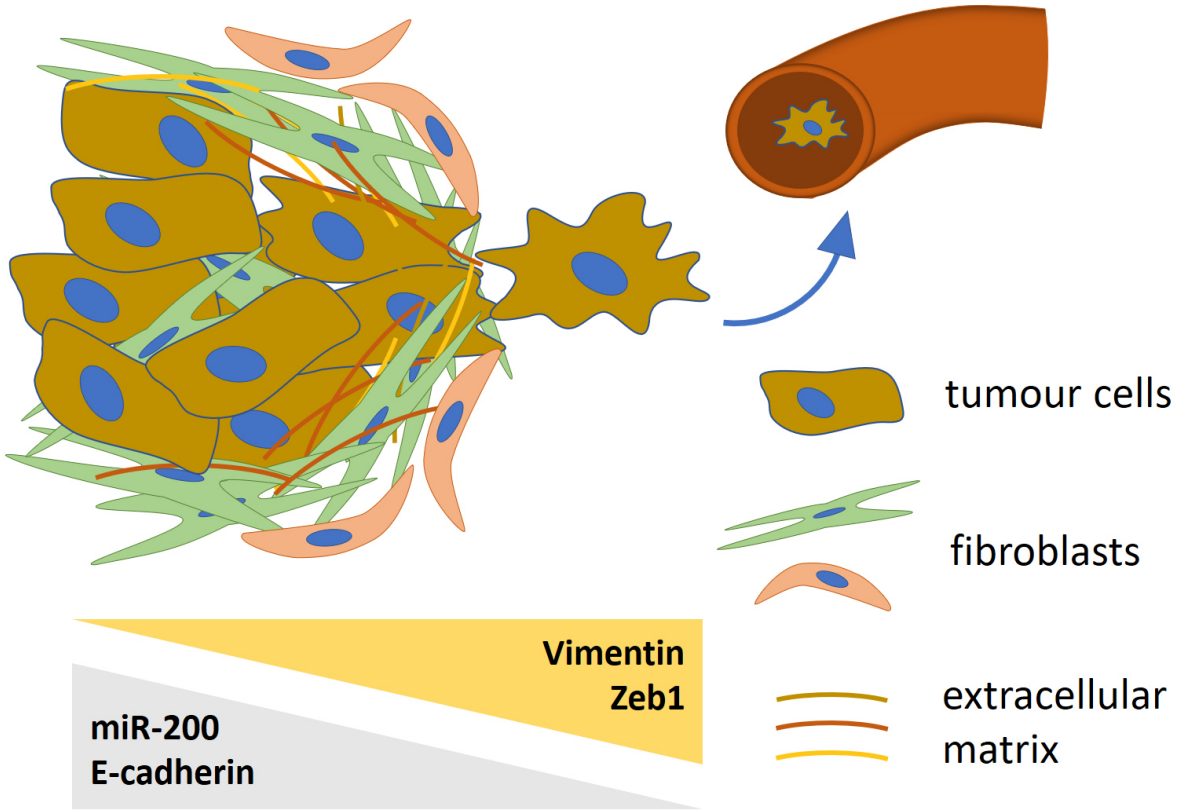

Figure 5: The Zeb1/miR-200 axis regulates EMT during invasion and metastasis
Classical model of EMT during cancer metastasis. Cells at the invasive front of the tumour undergo EMT and invade into adjacent tissue followed by intravasation for distant organ metastasis. During the EMT process, EMT transcription factors and mesenchymal genes (here exemplified by *Zeb1* and *Vimentin*) are upregulated while inducers of differentiation and epithelial cell markers (here exemplified by the miR-200 family and E-cadherin) are downregulated. Hybrid states can exist during EMT.

1.5 Aims of this study

High expression of Zeb1 or low expression of the miR-200 family correlates with bad prognosis in many tumour entities [Lu et al. 2014, Zhang et al 2015, Krebs et al 2017, Katsura et al. 2017]. This is in concordance with the worse prognosis of CRC patients with CMS4 tumours that show an enrichment of mesenchymal and EMT signatures. [Guinney et al. 2015]. In contrast to the classical model of epithelial cells undergoing EMT during metastasis, stromal cells were found as major contributors of this enrichment of EMT signatures in CRC [Isella et al. 2015, Li et al. 2017]. While epithelial Zeb1 expression is usually restricted to the invasive front in experimental CRC models (Figure 6 red circle), stromal expression of Zeb1 can be observed throughout the tumour (Figure 6 red triangles) and is highly heterogeneous in neighbouring cells. In epithelial cells, Zeb1 has been associated with several tumour-promoting functions (see above). However, in stromal cells little is known about the functions of Zeb1, the difference between Zeb1 positive and negative cells and how it possibly affects tumour growth and progression. In pancreatic cancer, high expressing of Zeb1 in cancer-associated fibroblasts correlated with worse prognosis of patients [Bronsert et al. 2014].

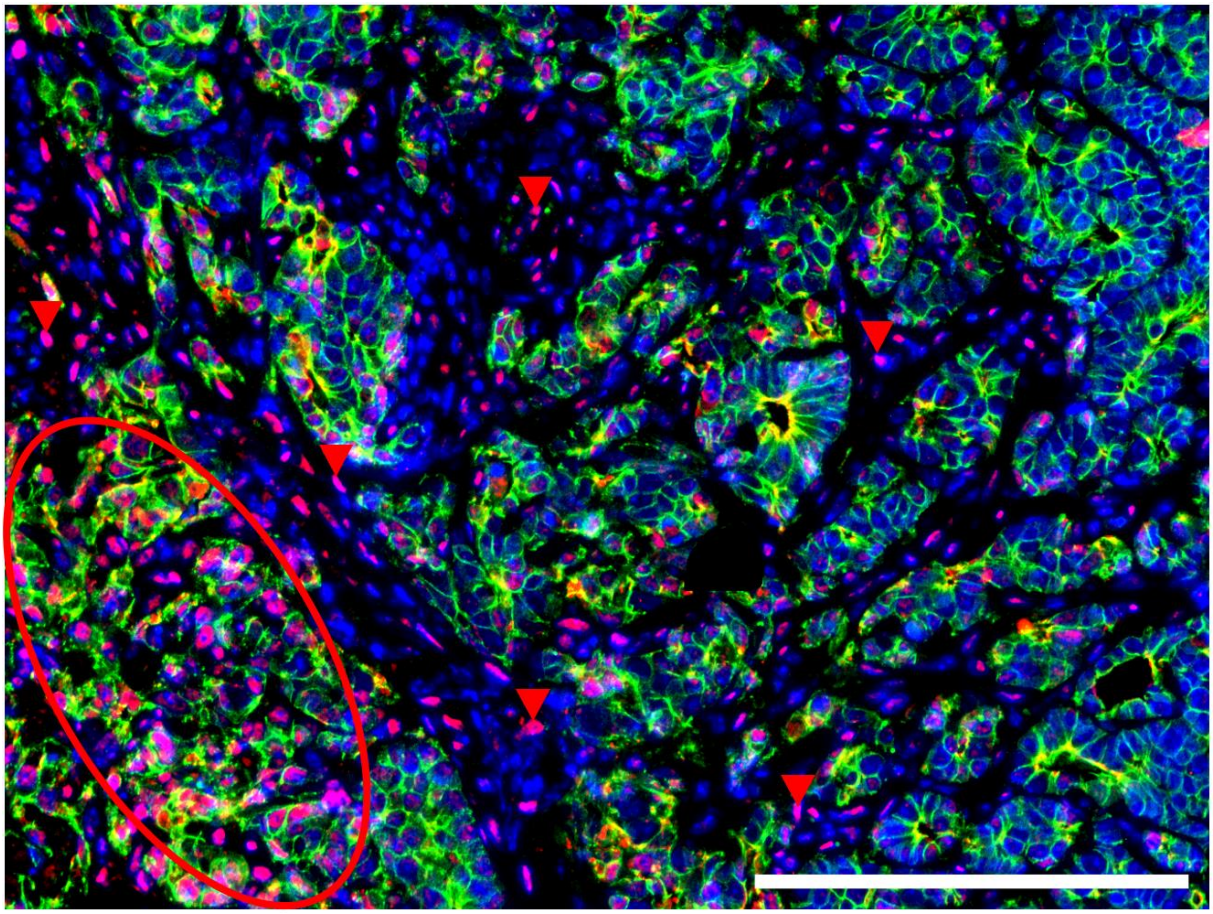

Figure 6: Expression of Zeb1 in tumour cells and the surrounding stroma
Immunofluorescent image of a mouse orthotopic tumour stained for Zeb1 (red), E-cadherin (green) and DAPI (blue). Some epithelial cells at the invasive front (upper left) express Zeb1 (red circle) while the majority of epithelial cells does not express Zeb1. Stromal cells show heterogeneous Zeb1 expression throughout the tumour. While some express high levels (some examples shown with red triangles), others don't express Zeb1 at all. Scalebar represents 200 µm.

In this work, the role of stromal Zeb1 during progression and metastasis of colorectal cancer should be examined. The work was conducted in collaboration between the groups of Henner Farin with the group of Thomas Brabletz as part of the DFG research group FOR2438 (Cell plasticity in colorectal carcinogenesis). The involvement of Zeb1 in regulating fibroblast-intrinsic properties was examined *in vitro* using conditional KO fibroblasts in mono- and cocultures, where reduced phenotypic plasticity was observed. Effects of this Zeb1 mediated modulation of fibroblast subtypes on intestinal carcinogenesis were then investigated in mouse models of CRC initiation and metastasis, indicating increased formation of an immuno-suppressive TME by stromal Zeb1. The therapeutic potential of this finding was examined by combination of stromal Zeb1 modulation with immune checkpoint inhibition.

2. Material and methods

2.1 Mice

All mouse works were approved by the Regierungspräsidium Darmstadt (V 54 - 19 c 20/15 - F123/1004; V 54 - 19 c 20/15 - F123/1031; V 54 - 19 c 20/15 - F123/1040 and V 54 - 19 c 20/15 - F123/2001). Mice were bred and housed in the internal mouse facility of the Georg-Speyer-Haus.

2.1.1 Mouse strains

For the generation of conditional *Zeb1* KO mice, *BL6/(Col1a2-cre/ERT,-ALPP)7Cpd/J* mice [Zheng et al. 2002] were crossed with *FVB.Cg-Zeb1*$^{tm1.2Mpst}$ mice [Brabletz et al. 2017]. After several round of backcrossing with FvB mice, this resulted in *FVB.Cg-Tg(Col1a2-cre/ERT,-ALPP)7Cpd-Zeb1tm1.2Mpst* mice, further termed '*Col1a2*$^{Tg/+}$*; Zeb1*$^{fl/fl}$ ' (or variations hereof based on allele status). Other mice mentioned in this work are *C57BL/6-Tg(TcraTcrb)1100Mjb/J* [Hogquist et al. 1994], further termed '*OT1*', *B6.Cg-Gt(ROSA)26Sor*$^{tm4(ACTB-tdTomato,-EGFP)Luo}$*/J* [Muzumdar et al. 2007] further termed '*Rosa mTmG*', *B6.Cg-Gt(ROSA)26Sor*$^{tm14(CAG-tdTomato)Hze}$*/J* [Madisen et al. 2010] further termed '*Rosa tdTomato*' and *B6.129S4-Kras*^{tm4Tyj}*/J* further termed 'KrasG12D' [Jackson et al. 2001]. All experiments were performed with age-matched littermates of both sexes that were randomly assigned to experimental or control groups if not predetermined by genotype. Activity of CreERT transgenes for recombination of conditional knockout mice was induced by food containing 400 mg/kg Tamoxifen (custom order based on Altromin, 1824P).

2.1.2 Genotyping of mice

For isolation of mouse genomic DNA, ear biopsies were incubated in 50 µL Proteinase K Buffer (table 2, Tris: Carl Roth, A411.2; NaCl: AppliChem, A1371; EDTA: Carl Roth, X986.2; SDS: Carl Roth, 4360.2) with 2,5 µL Proteinase K (Merck, 3115828001) at 60 °C. After 16 hours, 450 µL of distilled water (Life technologies, 10977035) were added and the gDNA was used for genotyping. Genotyping was performed by PCR amplification of transgene specific regions. Therefore, the PCR reaction mix was prepared according to table 3 (Taq Polymerase: Promega, M7805; dNTPs: VWR, TQAC135). Thermocycler (T3000, Biometra) programs for the different genes are listed in tables 4 and 5. Primer sequences used for each gene are listed in table 6. PCR results were analysed by gel electrophoresis (see below). For *Zeb1*, the wildtype band was expected at 230 bp and the band of the floxed allele at 295 bp. After recombination, a band of 367 bp was expected, which should only occur after *in vitro* recombination of cells and not during genotyping of mice before treatment. For *Col1a2-CreERT* genotyping, the DNA control band was expected at 290 bp and a transgene specific band was expected at 186 bp.

Table 2: Proteinase K Buffer

Compound	Concentration
Tris/HCl pH 8,5	100 mM
NaCl	200 mM
EDTA	0,5 mM
SDS	0,2%

Table 3: Genotyping PCR reaction mix

Compound	Amount
5x Buffer	5 µL
$MgCl_2$ 25 mM	1,5 µL
dNTPs 10mM each	0,5 µL
Primers 10mM	0,5 µL each
Go-Taq	0,2 µL
genomic DNA	2 µL
H_2O	to 25 µL

Table 4: PCR program for *Zeb1* genotyping

Temperature [°C]	Duration [s]	Cycles
95	60	
95	30	35
60	90	
72	95	
72	300	
4	hold	

Table 5: PCR program for *Cre* genotyping

Temperature [°C]	Duration [s]	Cycles
95	60	
95	45	40
58	45	
72	60	
72	300	
4	hold	

Table 6: Primer sequences for mouse genotyping (all 5' -> 3')

Name	Sequence
Zeb1 floxed forward	CGTGATGGAGCCAGAATCTGACCCC
Zeb1 floxed reverse	GGCCTGTCTTTCTCAGCAGTGTGG
Zeb1 deleted reverse	GCCATCTCACCAGCCCTTACTGTGC
Col1a2 DNA Control forward	AACACACACTGGAGGACTGGCTAGG
Col1a2 DNA Control reverse	CAATGGTAGGCTCACTCTGGGAGATGATA
Col1a2 forward	CAGGAGGTTTCGACTAAGTTGG
Col1a2 reverse	CATGTCCATCAGGTTCTTGC

2.1.3 Subcutaneous transplantation of organoids

For subcutaneous transplantation of tumour organoids, four wells of densely grown organoids per mouse were collected 4 - 5 days after splitting. Organoids were sheared mechanically and washed similar as during regular splitting (see below). Resulting fragments were resuspended in a mixture of 50 % BME (AMSBIO, 3533-010-02) and 50% ENA medium (see below) with 10 µM Y-27632 (Biotrend, Y-5301) and stored on ice until further use. The right flank of the mice was shaved and disinfected before subcutaneous injection of 100 µL organoid cell suspension with a 500 µL insulin syringe (BD

Micro-Fine, 324824). Tumour size was measured 1 - 3 times weekly with a calliper. Tumours were assumed ellipsoid and the estimated volume was calculated with the formula $V = \frac{\pi}{6} \times {D_1}^2 \times D_2$ where D_1 is the length of the shorter axis and D_2 is the length of the longer axis of the tumour. Mice were sacrificed by cervical dislocation when the tumour volume reached 1500 mm³ and the tumours were collected and fixed in 4 % PFA (VWR, 361367L) at 4 °C. After 16 hours, fixed tumours were stored in 70 % ethanol until further use for histological analysis. For bulk sequencing, tumour fragments were frozen without prior fixation and stored at -80 °C until further use (see below).

2.1.4 Orthotopic transplantation of organoids

Orthotopic transplantation was adapted from a published protocol [Fumagalli et al. 2018]. Densely grown organoids were split (see below) 1:1 into a mix of high concentration collagen (Corning, 354249) with 20 % collagen neutralization buffer (table 7, MEM alpha: ThermoFisher Scientific, 12000014; $NaHCO_3$: Carl Roth, 8551.1; HEPES: ThermoFisher Scientific, 15630056) and cultured in ENA medium with 10 µM Y-27632 for two days. Mice were sedated by intraperitoneal injection of 10 µL per 1 g of bodyweight of PBS + 12 mg/mL Ketamine (Zoetis, Ketaset) + 1,6 mg/mL Xylazine (WDT). Collagen drops containing tumour organoids were transplanted into the caecum (see reference for details). Analgesic treatment of mice was performed by subcutaneous injection of 4 µL / 1 g bodyweight of 50 mg/mL Metamizol (bela-pharm, Novaminsulfon) and subsequent supplementation of 13,2 µl per 1 g bodyweight of 500 mg/mL Metamizol in the drinking water for 2 days. Mice were monitored three times a week by palpation of tumours and sacrificed by cervical dislocation when the estimated tumour size exceeded 1 cm in any direction or other health issues occurred. Parts of the caecum containing primary tumours, liver and lungs of mice were collected for histology and fixed in 4 % PFA at 4 °C over night. Tissues were stored in 70 % ethanol until further use In case of immune checkpoint blockade, anti-PD-L1 (Hölzel, BE0101) or matched control antibodies (Hölzel, BE0090) were resuspended in dilution buffer (Hölzel, IP0070) at a concentration of 2 mg/mL. Mice were injected intraperitoneally at days 14, 21 and 28 with 5 µL per 1 g bodyweight of antibody solution. After treatment, only tumours collected after day 28 were included in analysis of primary tumour size to ensure sufficient treatment.

Table 7: Collagen neutralization buffer

Compound	Amount
MEM alpha	2,5 g
$NaHCO_3$	1 g
H_2O	45 mL
HEPES 1M, pH 7,5	5 mL

2.2 Patient samples

Primary patient samples used in this work were obtained with written informed consent from the cancer biobank of the University Cancer Center Frankfurt (UCT). Study design was approved by the Ethics committee of the University Hospital Frankfurt (#274-18).

2.3 Cell culture

2.3.1 Initiation of primary colonic mouse fibroblast and organoid cultures:

For establishment of primary colonic mouse cultures, the colon of mice was collected, cut open longitudinally and cleaned with cold 1x PBS (ThermoFisher Scientific, 10010023). The colon was then cut into small fragments of approximately 5 mm² and incubated in PBS with 10 mM EDTA (ThermoFisher Scientific, 15575020). After 10 minutes of incubation, fragments were pipetted several times, supernatant was discarded and fresh EDTA solution was added. After another 25 minutes of incubation, fragments were pipetted again and the supernatant containing epithelial crypts was collected for establishment of organoid cultures. Colon fragments were further incubated in EDTA solution for another 30 minutes with pipetting and replacement of EDTA solution after 15 minutes. After the last washing step, fragments were resuspended in 2D cell culture medium (table 8, DMEM: ThermoFisher Scientific, 31966-047; FCS: Sigma Aldrich, F7524; Pen/Strep: ThermoFisher Scientific, 15140-122) and seeded in cell culture dishes (Greiner, 628160, 664160, 639160), which were previously coated with 0,1 % gelatine (Sigma, G2500) for at least 10 minutes. After several days, multi-layered fibroblast cultures grew from these fragments onto the dish and were split for further propagation and expansion (see 2D cell culture). For establishment of colon organoid cultures, supernatant from the second washing step was passed through filters with 100 µm pore size (Greiner, 542000) and epithelial crypts were pelleted by centrifugation for 5 min at 300 x g and 4 °C. Supernatant was removed and crypts were seeded at high density in 25 µl of BME in suspension culture plates (Greiner, 657185, 665102, 662102, 677102). Crypts were cultured in WENRA medium (see below) with 10 µM Y-27632. After several days, colonic crypts grew as intestinal organoids and were split for further propagation and expansion (see 3D Organoid culture).

For isolation of tumour organoids from primary orthotopic tumours, mice were sacrificed by cervical dislocation 5 - 6 weeks after orthotopic transplantation, tumours were cut free from surrounding tissue and collected in PBS. Tumours were cut into small fragments and digested for 30 minutes in RPMI medium (ThermoFisher Scientific, 11875093) with 10 % FCS, 0,1 % Collagenase I (ThermoFisher Scientific, 17018029), 0,2 % Dispase II (Merck, D4693) and 2 U/mL DNase I (New England Biolabs, M0303L). Digestion was stopped by addition of washing medium (see below) and passed through a 40

µm filter (Greiner, 542040). After centrifugation at 300 x g for 5 min at 4 °C, cells were seeded at high density in BME and cultured in ENA medium with 10 µM Y-27632.

Table 8: 2D cell culture medium

Substance	Amount
DMEM (1x)	500 mL
FCS	60 mL
Pen/Strep (100x)	5 mL

2.3.2 Initiation of human primary fibroblast cultures from patient samples

For initiation of primary fibroblast cultures, colorectal cancer resection samples were cut into small fragments, washed once with washing medium and two times with PBS. Subsequently, fragments were incubated in PBS with 4 mM EDTA for 30 minutes and pipetted several times to remove debris. Remaining fragments were seeded in cell culture dishes previously coated with 0,1% gelatine in 2D cell culture medium. After several days, outgrowing cells were propagated as described below.

2.3.3 2D Cell culture:

Stable cell lines (HEK293T) and primary fibroblasts were cultured as 2-dimensional (2D) monolayer cultures. Cells were grown until confluent and split in ratios between 1:2 and 1:20 depending on growth speed of the line. For splitting, cells were washed once with cold PBS and dissociated by incubation with Trypsin (ThermoFisher Scientific, 12605-010) for 5 minutes at 37 °C. Dissociation was stopped by addition of 2D cell culture medium and cells were pelleted by centrifugation for 5 min at 300 x g and 4 °C. After aspiration of the supernatant, cells were resuspended in 1 mL of medium and seeded in desired ratios into cell culture treated dishes in fresh 2D cell culture medium. For culture of primary fibroblasts, cell culture dishes were coated with PBS + 0,1% gelatine for at least 10 minutes at room temperature before use. Recombination of floxed alleles *in vitro* was achieved by incubation with 1 µM 4-Hydroxytamoxifen (Enzo Life Sciences, ALX-550-361-Moo1) for several days.

For cryopreservation, cells were collected after trypsinization, resuspended in commercial freezing medium (ThermoFisher Scientific, 12648010) and cooled to -80 °C at a rate of 1 °C per minute. After several hours at -80 °C, cells were transferred to liquid nitrogen for long-term storage. For reconstitution, cells were thawed for few minutes at 37 °C, washed once with 2D cell culture medium and seeded as described for splitting.

For transduction of monolayer cultures, cells were split similar to normal passaging and freshly thawed viral vectors were added either directly to the freshly seeded cells in suspension or after 1 day of

culture to allow for cell attachment before transduction. In case of low virus titres, 10 µg/mL Polybrene (Merck, TR-1003-G) were added to improve infection rates.

Activity of inducible shRNA constructs in primary human fibroblasts was induced by incubation with 1 µg / mL Doxycycline (Merck, D9891-1G).

2.3.4 Lentivirus production in HEK293T cells:

For production of lentiviral vectors, a mixture of 16,6 µg VSV-G plasmid, 50 µg PAX2 plasmid, 60 µg lentiviral plasmid (containing the packaging signal) and 250 µl of polyethyleneimine solution (1 mg/mL, pH 7,4) was prepared in DMEM + 1x Pen/Strep. After incubation of this mix for 30 minutes at room temperature, HEK293T cells were transfected in suspension by addition of the mixture to cells freshly split in a ratio of 1:3. After 4-6 hours, supernatant containing the transfection mix was replaced by fresh 2D cell culture medium. After three days of incubation, the supernatant was collected and passed through 0,45 µm SFCA filters (Corning, 431220). Viral vectors were pelleted by centrifugation for 1 hour at 20000g x g and 4 °C and resuspended in +++ medium (Adv. DMEM/F12: ThermoFisher Scientific, 12634028; GlutaMAX: ThermoFisher Scientific, 35050061). Aliquots of this suspension were stored at -80 °C and used for transduction of primary fibroblast or organoid cultures.

Table 9: +++ medium

Substance	Amount
Adv. DMEM/F12	500 mL
HEPES 1M pH 7,5	5 mL
Pen/Strep (100x)	5 mL
GlutaMAX (100x)	5 mL

2.3.5 Collagen contraction assay

For the collagen contraction assay, 1 mg/mL collagen I solution was prepared according to table 10 (Collagen I: ThermoFisher Scientific, A1048301; 10x PBS: ThermoFisher Scientific, 14200-067; NaOH: AppliChem, A3910) and kept on ice until further use. Fibroblasts were detached from culture plates like during regular splitting and 100.000 mouse fibroblasts or 50.000 human fibroblasts were seeded in 500 µL collagen I solution in a 24-well suspension culture plate. After polymerization of collagen for 45 minutes at 37 °C, 1 mL of +++ medium was added and the collagen disc was detached from the bottom of the plate. Directly after detaching the disc and after 24 hours, the plate was scanned (Canon, CanoScan 8800F) and the area of the floating collagen disk was measured by ImageJ (Fiji v2.5.0) [Schindelin et al. 2012, Schindelin et al. 2015, Rueden et al. 2017].

Table 10: Collagen I solution

Substance	Amount
+++ medium	375 µL
Collagen I 3mg/mL	200 µL
10x PBS	21 µL
1M NaOH (add last)	5 µL

2.3.4 3D Organoid culture:

After initiation, mouse colonic organoids were expanded and propagated in 3-dimensional (3D) extracellular matrix domes in suspension culture plates and split in ratios between 1:2 and 1:16. For splitting, the domes containing organoids were collected in cold washing medium (table 11, BSA: ThermoFisher Scientific, 15260-037) and organoids were dissociated by mechanical shearing. Therefore, a 10 µL pipette tip was placed on top of a 1000 µL pipette tip and the organoid suspension was pipetted multiple times after placing the tip at the bottom of a 6 mL eppendorf tube. As soon as no more large organoid fragments were visible to the eye, tubes were filled with additional washing medium and cells were pelleted by centrifugation for 5 minutes at 300 x g and 4 °C. The supernatant was discarded and the cell pellet was resuspended in a small volume of washing medium (20% of seeding volume). Fresh BME was added to the suspension (85% of seeding volume) and the mixture was seeded into domes of 12,5 to 25 µl in suspension culture plates. Domes were solidified by incubation for 30 minutes at 37 °C and organoid growth medium was added on top after solidification. During the first days of culture after splitting, 10 µM Y-27632 was added to the medium to prevent anoikis and medium was changed at least every three days. WT mouse colon organoids were cultured in WENRA medium (table 12, B27: ThermoFisher Scientific, 17504-044; n-Acetylcysteine: Merck, A9165; human EGF: Peprotech, AF-100-15; A 83-01: Tocris, 2939/10). Tumour organoids harbouring mutations in the *Apc* gene were cultured in ENA medium (table 13). Conditioned media for organoid cultures (Wnt3a, Noggin, R-spondin1) were produced in house in 293F cells under serum free conditions.

Organoids were cryopreserved by pelleting cells similar to splitting and resuspending cells in commercial freezing medium. Several hours after cooling the suspension to -80 °C at a rate of 1 °C per minute, cells were transferred to liquid nitrogen for long-term storage. Reconstitution was performed by thawing organoids for several minutes at 37 °C, washing once with washing medium and then proceeding like after normal dissociation during splitting.

Table 11: washing medium

Substance	Amount
DMEM (1x)	500 mL
7,5% BSA	2,65 mM
Pen/Strep	5 mL

Table 12: WENRA medium

Substance	Amount
+++ medium	30 mL
Wnt3a-CM	10 mL
Noggin-CM	5 mL
R-spondin1-CM	5 mL
B27 (50x)	1 mL
n-Acetylcysteine 500 mM	125 µL
human EGF 500 µg/mL	5 µL
A 83-01 500 µM	50 µL

Table 13: ENA medium

Substance	Amount
+++ medium	45 mL
Noggin-CM	5 mL
B27 (50x)	1 mL
n-Acetylcysteine 500 mM	125 µL
human EGF 500 µg/mL	5 µL
A 83-01 500 µM	50 µL

2.3.5 Genetic modification of organoids:

For transduction of 3D organoid cultures, organoids were pelleted similar to splitting and resuspended in Accutase (ThermoFisher Scientific, A1110501) for dissociation into single cells. Cells were incubated at 37 °C and checked every 3 - 4 minutes under the microscope to prevent over-digestion. Upon reaching single cell state for most organoid cells, dissociation was stopped by addition of washing medium and cells were pelleted again by centrifugation for 5 minutes at 550 x g and 4 °C. Single cells were resuspended in organoid growth medium supplemented with 10 µM Y-27632 and 10 µg/mL Polybrene. This cell suspension was mixed with viral vectors and spinfected for 1 hour at 1000 x g and 32 °C. After spinfection, cells were incubated for 4 hours at 37 °C. Subsequently, cells were washed once with washing medium and seeded in BME similar to splitting. For selection of successfully transduced cells, Purocymcin (InvivoGen, ant-pr-1) or Blasticidin (Santa Cruz Biotechnology, sc-495389) were added in ranges from 0,5 - 2 µg/mL as soon as organoids grown from single cells started developing a lumen.

For electroporation, organoids were supplemented with 1,25 % dimethyl sulfoxide (DMSO, Merck, D4540). After 1 day of incubation, organoids were dissociated into single cells similar to organoid transduction and single cells were resuspended in Opti-Mem medium (ThermoFisher Scientific, 31985062). Directly before electroporation, single cell suspensions were mixed with 10 µg of plasmids for electroporation (see list below) and transferred into an electroporation cuvette (NepaGene, EC-

002S). Cells were electroporated in a NEPA21 electroporator (NepaGene) with settings according to table 14 and washed once with washing medium. Subsequently, cells were pelleted and seeded like during regular splitting. After electroporation, cells were cultured in regular organoid medium with 1,25 % DMSO and 10 µM Y-27632. After 24 hours, DMSO was removed from the medium. For electroporation of WT colon organoids, 3 µM Chir-99021 (Reprocell, 04-0004) was added 24 hours before and three days after electroporation.

Selection of mutated organoids was performed by addition of small molecules or growth factor deprivation. For selection of *Tp53* mutated organoids, 5 - 20 µM nutlin-3 (Biomol, Cay10004372) was added to the medium. For selection of *Kras* mutant organoids, 0,5 µM Gefitinib (Selleck Chemicals, S1025) was added to hEGF deprived medium. For selection of *Tgfbr2* mutant organoids, 5 ng/mL hTGFβ (Peprotech, 100-21) was added to A 83-01 deprived medium. Selection of *Apc* mutant organoids was performed by deprivation of medium from Wnt3a- and R-spondin1-conditioned media.

To obtain clonal organoid cultures, organoids were dissociated into single cells with Accutase (see above) and seeded sparsely in BME. After few days of cultures, single organoids were picked from the BME with a 200 µL pipette, dissociated by shearing and seeded in a 25 µL drop of BME. After splitting at least once more, gDNA of clonal cultures was obtained following manufacturer's instructions of the DNeasy Blood & Tissue Kit (Qiagen, 69504). The region of interest was amplified by PCR using the reaction mix, primers and programs listed in tables 15 - 17 (Phusion DNA Polymerase: ThermoFisher Scientific, F530L) and the PCR products were sent for Sanger sequencing (Eurofins Genomics, LightRun Tube). Modified allele frequencies were determined by analysis with the Inference of CRISPR Edits (ICE) Assay (Synthego, [Conant et al. 2022]).

Table 14: Electroporation settings

Parameter	Poring	Transfer
Voltage	175 V	20 V
Pulse length	5 ms	50 ms
Pulse interval	50 ms	50 ms
Number of pulses	2	5
Decay rate	10 %	40 %
Polarity	+	+/-

Table 15: Genotyping reaction mix

Compound	Amount
5x HF Buffer	4 µL
dNTPs (10 mM each)	0,4 µL
Primers (10 µM)	1 µL each
DMSO	1 µL
Phusion Polymerase	0,2 µL
DNA	50 ng
H_2O	to 20 µL

Table 16: Genotyping PCR program

Temperature	Duration	Cycles
98 °C	300 s	
98 °C	20 s	45
57 °C	20 s	
72 °C	15 s	
72 °C	300 s	
4 °C	hold	

Table 17: Genotyping primers

Name	Sequence
Tp53-Geno-forward	AACACAGTCCTGAGGGTTCTTC
Tp53-Geno-reverse	AGAAAAAGAGGCATTGAAAGGTCA
Tgfbr2-Geno-forward	AAACTTCCCGTTTCCGCTCT
Tgfbr2-Geno-reverse	CCTGAGAGGGCGAGGAGTAA
KrasG12D-Geno-forward	TGTCTTTCCCCAGCACAGT
KrasG12D-Geno-reverse	CTGCATAGTACGCTATACCCTGT
KrasG12D-Geno-LoxP	GCAGGTCGAGGGACCTAATA
Apc-Geno-forward	CCCAAATTTCATTTTGTGTGA
Apc-Geno-reverse	TCCCACCTCCACTTTCAATAA

2.3.6 Cocultures

For coculture of organoids with colon fibroblasts, organoids were dissociated by shearing and fibroblasts were dissociated from cell culture plates like during regular splitting. For medium deprivation experiments, organoids were split in a 1:8 ratio and resuspended in a small amount of washing medium. Per well, 15.000 fibroblasts were added to the suspension, mixed by pipetting

several times and then seeded as for regular organoid culture in 25 µL of BME in 24-well plates. In contrast to organoid monocultures, no Y-27632 was added to cocultures during the first days after splitting. Cultures were imaged and split 1:4 every 4 - 5 days and the number of organoids was counted manually using Fiji. Every second passage, 10.000 fibroblasts were added during splitting (in the resuspended pellet after the washing step) to maintain organoid to fibroblast ratios. Cultures were considered dead when no multicellular structures were found at the end of a passage.

OT1 T cells were stimulated for 3 days before use in cocultures. Therefore, the spleen of *OT1* mice was collected in PBS and mashed through a 100 µm filter using the back of a syringe (B Braun, 4616057V). Filter and cells were washed with 40 mL of PBS and cells were pelleted by centrifugation at 640 x g and 4 °C for 3 minutes. Cells were resuspended in 1 mL ACK Lysis buffer (ThermoFisher Scientific, A1049201) and incubated at room temperature. Generally, T cells were pipetted very slowly and resuspended by flicking of the tube instead of pipetting whenever possible. After 6 minutes, 9 mL DMEM + 10 % FCS were added and cells were pelleted again. Cells were resuspended in OT1 medium (table 18, 2-Mercaptoethanol: ThermoFisher Scientific, 31350-010; NEAA: ThermoFisher Scientific, 11140-50) with 2 µg/mL SIINFEKL (OVA) peptide (AnaSpec, AS-60193-1) and 10 U/mL human IL-2 (PeproTech, 200-02) and seeded at a density of $5x10^6$ cells per mL and well in 24-well cell culture plates (Corning, 3524). After 4 hours of incubation at 37 °C and 5 % CO_2, cells were washed once with PBS and seeded as before but without addition of SIINFEKL peptide. After another 24 hours, cells were collected, two times the amount of fresh medium from initial seeding (without SIINFEKL peptide) was added and cells were seeded in 3 times the wells of the initial seeding. After another 48 hours of culture, the cells were considered mainly CD8 T cells and were used for experiments after washing once with PBS.

Table 18: OT1 medium

Substance	Amount
RPMI	500 mL
FCS (heat inactivated)	60 mL
GlutaMAX (100x)	5 mL
Pen/Strep (100x)	5 mL
2-Mercaptoethanol (50 mM)	500 µL
NEAA (100x)	5 mL
HEPES (100x)	5 mL

For organoid killing assays, organoids were transduced with a luciferase reporter plasmid and an expression plasmid of the chicken ovalbumin protein recognized by *OT1* T cells (see plasmids below).

Isogenic organoids transduced with luciferase but without ovalbumin were used as controls for unspecific T cell killing. Due to the lack of BL6/J fibroblasts with the floxed allele of *Zeb1*, fibroblasts from FvB background were used in all cocultures. Three different setups were tested: For myCAF killing, 50.000 fibroblasts were seeded in a 48-well tissue culture plate (Corning, 3548) in 2D cell culture medium on top of a 0,1% gelatine coating. After 24 hours, medium was aspirated and organoids were seeded in a ratio of 1:8 (48-well equivalent to 25 µL of BME) on top of the fibroblast layer in ENA medium with 5 % BME. After another 24 hours, 30.000 stimulated T cells were added on top of the fibroblasts and organoids in ENA medium. After 2 days of culture, surviving organoids were quantified by measurement of luciferase activity. For iCAF killing, 25.000 fibroblasts were seeded in a flat drop of 25 µl BME in a 48-well suspension culture plate in 2D cell culture medium. After 24 hours, medium was aspirated and organoids were seeded in a ratio of 1:8 (48-well equivalent to 25 µL of BME) on top of the fibroblast-containing drop in ENA medium. After another 24 hours of culture, 30.000 T cells were added on top of the organoids in ENA medium. Surviving organoids were quantified after 3 days of culture by measurement of luciferase activity.

For T cell migration assays, 100.000 fibroblasts were seeded in a 12-well adhesion plate on top of a gelatine layer in 2D cell culture medium. After 24 hours, medium was replaced with 1,5 mL of +++ medium, a transwell with 3 µm pore size (Corning, CLS3462-48EA) was placed in the well and 30.000 T cells were added to the transwell with 1µL of anti-CD45-APC antibody (ThermoFisher Scientific, 17-9459-42). After 48 hours, the whole lower compartment per well was imaged (Cytation C10, Agilent) and the number of T cells was quantified by APC fluorescence using Gen5 software (v3.12).

For the T cell permeability assay, 8µm transwell inserts (Greiner, 665638) were coated with 0,1 % gelatine and 200.000 fibroblasts were seeded on top of the coating in 2D cell culture medium. After 48 hours, medium was aspirated and 30.000 T cells were added on top of the fibroblast layer in ENA medium with 1:2000 anti-CD45-APC antibody. After 24 hours, five representative images of T cells in the lower compartment were taken per well (Evos FL, ThermoFisher Scientific) and the relative number of T cells per condition was measured by quantification of the APC fluorescent area above a certain threshold (Fiji).

For measurement of luciferase activity, OneGlo Ex Substrate was reconstituted in OneGlo Ex Buffer (Promega, E8120) and diluted 1:10 with Luciferase assay buffer (table 19, Triton X 100: Carl Roth, 3051.2). Medium was aspirated and 100 µl of diluted OneGlo Ex substrate were added per well. After few minutes, contents of the well were mixed by pipetting up and down several times and transferred to a white 96-well measurement plate (ThermoFisher Scientific, 7571). Luciferase signal was measured by a plate reader (Spectramax ID3, Molecular Devices) according to manufacturer's protocol.

Table 19: Luciferase assay buffer

Substance	Concentration
H_2O	-
NaCl	50 mM
Tris HCl pH 7,4	50 mM
Triton X 100	1 %

2.4 Laboratory methods

2.4.1 Plasmids

The plasmids hCas9, gRNA_GFP-T2, lentiCas9-Blast, Cre-IRES-Puro, and pLVX-puro-cOVA were kind gifts from George Church [Mali et al. 2013, Addgene plasmids #41815 and #41820], Feng Zhang [Sanjana et al. 2014, Addgene plasmid #52962] ,Darrell Kotton [Somers et al. 2010, Addgene plasmid #30205] and Maria Castro [Addgene plasmid #135073] respectively. The plasmid pAC1 Cre was purchased from ATCC (39532). Design of cloning primers was aided by SnapGene (v4.1.9) and Primer-BLAST [Ye et al. 2012]. The Luciferase-GFP expression plasmid was cloned previously [Schnalzger et al. 2019].

The lentiviral expression plasmid for the notch intracellular domain (NICD) was cloned by replacing the Cas9 sequence from lentiCas9-Blast with the NICD sequence. The NICD sequence was amplified from whole colon cDNA by PCR with Phusion DNA polymerase (PCR reaction mix in table 15, PCR program and primers used in tables 20 and 22). Cas9 sequence was cut from lentiCas9-Blast by digestion with XbaI (New England Biolabs, R0145S) and BamHI-HF (New England Biolabs, R3136S) for 1 hour at 37 °C (reaction setup in table 21, CutSmart: New Englang Biolabs, B7204). NICD sequence was inserted into the lentiCas9-Blast backbone by In-Fusion cloning according to the manufacturer's instructions (Takara Bio, 638910).

Table 20: NICD amplification PCR program

Temperature	Duration	Cycles
98 °C	300 s	
98 °C	20 s	40
61 °C	20 s	
72 °C	120 s	
72 °C	300 s	
4 °C	hold	

Table 21: Digestion reaction mix

Substance	Amount
CutSmart Buffer (10x)	2 µL
Plasmid DNA	1 µg
Restriction enzyme	1 µL each
H_2O	to 20 µL

The plasmid expressing a sgRNA targeting the mouse *Apc* gene was a kind gift of Hans Clevers [Schwank et al. 2013a]. Plasmids containing sgRNAs targeting *Tp53* and *Tgfbr2* were cloned by inverse PCR. Reverse primers were created by adding a common cloning sequence (table 22, bold) to the reverse complement of the sgRNA sequence (table 22, italic). The forward primer was the same for all sgRNAs and was 5'-phosphorylated to enable subsequent ligation. PCR was performed with gRNA_GFP-T2 as template with the program and reaction mix from tables 23 and 24. PCR products were digested with *Dpn*I (protocol as above; New England Biolabs, R0176S) to cut template strands and ligated using T4 ligase (New England Biolabs, M0202S).

Table 22: Primer & sgRNA sequences

Name	Sequence (homologous regions for In-Fusion cloning in red)
NICD-InFusion-forward	CAGGACCGGTTCTAGAGCGCTGCCACCATGAAGCGCCGGCGGCAGCATG
NICD-InFusion-reverse	TTGTTGCGCCGGATCCTGCCGGTGCACCCACGGTG
mAPC-gRNA	TATGGAACCTGTCTGCACACTGCAC
mTgfbr2-gRNA	GGCCGCTGCATATCGTCCTG
mTgfbr2-gRNA-primer	*CAGGACGATATGCAGCGGCC***GGTGTTTCGTCCTTTCCACAAGAT**
mTp53-gRNA	GACACTCGGAGGGCTTCACT
mTp53-gRNA-primer	*AGTGAAGCCCTCCGAGTGTC***GGTGTTTCGTCCTTTCCACAAGAT**
sgRNA-common	5'P-GTTTTAGAGCTAGAAATAGCAAG

Table 23: sgRNA cloning program

Temperature	Duration	Cycles
98 °C	300 s	
98 °C	50 s	20
61 °C	30 s	
72 °C	120 s	
72 °C	300 s	
4 °C	hold	

Table 24: sgRNA cloning reaction mix

Compound	Amount
5x HF Buffer	5 µL
dNTPs (10 mM each)	0,5 µL
Primers (10 µM)	1 µL each
DMSO	1 µL
Phusion Polymerase	0,3 µL
gRNA_GFP-T2 template	100 ng
H_2O	to 25 µL

Lentiviral plasmids with shRNA targeting *ZEB1* or *GFP* were a kind gift of Thomas Brabletz. The respective shRNA sequences are listed in table 25.

Table 25: shRNA sequences

Name	Sequence
shGFP	ccggCCCGCTACCTGTTCCATGGCCAttcaagagaTGGCCATGGAACAGGTAGCTTTTTGGAAA
shZEB1	ccggCCCAGATGATGAATGCGAGTCGttcaagagaTGACTCGCATTCATCATCTTTTTTGGAAA

Newly cloned plasmids were transformed into Stellar competent cells (Takara Bio, 636763). All established plasmids were retransformed into *DH10β* competent bacteria for further amplification. For transformation of newly cloned plasmids, bacteria were thawed on ice and 2 µL of cloning mix were added to the bacteria. After incubation on ice for 25 minutes, bacteria were heat-shocked for 45 seconds at 42 °C and incubated on ice for another 2 minutes. Subsequently, 900 µL of LB medium were added and the suspension was incubated under constant shaking for 1 hour at 37 °C. Cultures were then pelleted by centrifugation at 1300 x g for 3 minutes and plated in a volume of 50 µL on LB Agar plates with 200 µg/mL Ampicillin (Merck, A9518) or 50 µg/mL Kanamycin (Merck, 60615) depending on the respective plasmids. After incubation at 37 °C for 16 hours, bacteria were stored at 4 °C until further use.

Plasmid DNA was isolated from bacteria using NucleoSpin Plasmid (Macherey-Nagel, 740588.250) or NucleoBond Xtra Maxi (Macherey-Nagel, 740414.50) kits according to the manufacturer's instructions.

2.4.2 Gelelectrophoresis

For DNA gelelectrophoresis, 1 - 2 % solutions of Agarose (Avantor, 2340773) in 1x TAE buffer (50x stock in table 26, acetic acid: Carl Roth, 3738.5) were heated until fully dissolved, mixed with 0,01 % Ethidiumbromide (Carl Roth, 2218.2) and poured into a gel casting tray (Peqlab, PerfectBlue Mini M). After solidification for minimum 30 minutes, the gel was transferred into the electrophoresis chamber, loaded with samples mixed 1:5 with 6x Loading dye (ThermoFisher Scientific, R0611) and run for approximately 30 minutes at a constant voltage of 140 V (Pharmacia LKB GPS 200/400). As reference, 7 µl of DNA marker (ThermoFisher Scientific, SM1331) were added to an empty lane. Gels were imaged at a fluorescent imager (Bio-Rad, 170-8170). If necessary, DNA was isolated from the agarose gel using the NucleoSpin Gel and PCR Clean-up kit (Macherey-Nagel, 740609.250) according to the manufacturer's instructions.

Table 26: 50x TAE buffer

Substance	Concentration
EDTA	50 mM
Tris	2 M
Acetic acid	1 M

2.4.3 Western Blot

For western blotting, cells were lysed using radioimmunoprecipitation- (RIPA-) buffer (table 27, Nomidet P-40: Fluka, 74385; Sodium deoxycholate: Merck, 30970; Sodiumfluoride: Merck, F916049) with 0,1 % protease inhibitor cocktail (Merck, 539134). Lysates were centrifuged at 20.800 x g for 5 minutes at room temperature and the supernatant was used for further analysis. Protein concentration in lysates was measured using bradford-assay (Bio-Rad, 500-0006). For analysis of Actin or Zeb1, 12% or 8% acrylamide resolving gels were prepared in a casting stand (Bio-Rad Mini-PROTEAN system) according to tables 28 and 29 (acrylamide: Carl Roth, 3029.3; ammonium persulfate: Carl Roth, 9592.2; TEMED: Carl Roth 2367.3) and a 5% stacking gel (table 30) was added on top. After solidification of gels, samples were mixed 1:3 with 4x loading buffer (Carl Roth, K929.1), incubated at 95 °C for 5 minutes and separated by electrophoresis at a constant voltage of 120 V (Power Pac 300, Bio-Rad) in SDS running buffer (table 31, glycine: AppliChem, A4554). As reference, 5 µl of Protein ladder (NewEngland Biolabs, P7712S) were added in an empty lane.

Table 27: Ingredients of RIPA buffer

Substance	Amount
Tris-HCl 1M	25 mL
Nomidet P-40	5 mL
Sodium deoxycholate	2,5 g
SDS	0,5 g
NaCl 5 M	15 mL
EDTA 0,5 M	2 mL
NaF	1,05 g
H_2O	to 500 mL

Table 28: Ingredients of 8% resolving gel

Compound	Amount
H_2O	4.6 mL
30 % acrylamide	2,7 mL
Tris 1,5 M pH 8.8	2,5 mL
SDS 10%	0,1 mL
Ammonium persulfate 10%	0,1 mL
TEMED	0,006 mL

Table 29: Ingredients of 12% resolving gel

Compound	Amount
H_2O	3,3 mL
30 % acrylamide	4 mL
Tris 1,5 M pH 8.8	2,5 mL
SDS 10%	0,1 mL
Ammonium persulfate 10%	0,1 mL
TEMED	0,004 mL

Table 30: Ingredients of 5% stacking gel

Compound	Amount
H_2O	2,1 mL
30 % acrylamide	0,5 mL
Tris 1 M pH 6.8	0,38 mL
SDS 10 %	0,03 mL
Ammonium persulfate 10%	0,03 mL
TEMED	0,003 mL

After separation, proteins were transferred onto a nitrocellulose membrane by semi-dry blotting (transfer buffer in table 32, Methanol: Carl Roth, 4627) for 60 minutes (Actin) or 150 minutes (Zeb1) at a constant current of 50 mA per gel. The membrane was dried for 5 minutes at room temperature and the total protein was stained using Revert 700 (LI-COR, 926-11011). The membrane was blocked for 1 hour with 5 % milkpowder (Carl Roth, T145.3) in TBS + 0,1 % Tween 20 (TBST, Tween 20: AppliChem, A1389). Primary antibodies (Zeb1: Merck, HPA027524, 1:500; Actin: Merck A2066, 1:10.000) were added in a 50 mL tube (Corning, 352070) in blocking buffer. After incubation at 4 °C over night, membranes were washed 3 times with TBST and secondary antibody (LI-COR, 926-32211) was added 1:10.000 in blocking buffer for 1 hour at room temperature. Again, membranes were washed 3 times with TBST and antibodies were detected using an Odyssey infrared imaging system (LI-COR, 9120 with Image Studio v5.2).

Table 31: Ingredients of 10x SDS running buffer

Substance	Amount
Tris-HCl	121,1 g
Glycine	576 g
SDS 20 %	200 mL
H_2O	to 4 L

Table 32: Ingredients of transfer buffer

Compound	Amount
Tris-HCl	5,82 g
Glycine	2,93 g
SDS 10 %	3,75 mL
Methanol	200 mL
H_2O	to 1 L

2.4.4 RNA isolation and quantitative real-time PCR

For isolation of RNA from various samples, the NucleoSpin RNA kit (Macherey-Nagel, 740955.250) was used according to the manufacturer's instructions. For cDNA synthesis, 500 ng RNA were mixed with 4,5 µL of distilled water and 0,5 µL of 50 µM random hexamer primers (ThermoFisher Scientific, SO142) and incubated for 5 minutes at 70 °C. Then, 20,375 µL distilled water, 15 µL of 5x Buffer (Promega, M531A), 3,125 µL of dNTP mix (10 mM each), 0,75 µL RNAsin (Promega, N2511) and 0,75 µL reverse transcriptase (Promega, M3681) were added and the mix was incubated for 60 minutes at 45 °C and

for another 15 minutes at 70 °C. Resulting cDNA was dilluted 1:1 with distilled water and stored at -20 °C until further use for qRT-PCR.

For qRT-PCR, 2 µl of cDNA were mixed with 12,5 µL Power SYBR Green Master Mix (ThermoFisher Scientific, 4367659), 9,5 µL distilled water and 1 µl of qRT-PCR primer mix (5 µM each primer). Amplification was monitored using StepOnePlus real-time PCR system (ThermoFisher Scientific, software v2.3) and a standard amplification protocol. Relative expression was calculated as $2^{-\Delta\Delta Ct}$ compared to expression of *Hprt* and biological reference groups. qRT-PCR Primers are listed in table 33.

Table 33: Sequences of qRT-PCR primers

Name	Sequence
mHprt-FW	AAGCTTGCTGGTGAAAAGGA
mHprt-RW	TTGCGCTCATCTTAGGCTTT
mZeb1-FW	CGAGCATTTAGACACAAGCGAG
mZeb1-RW	CGGAATCTGAATTTGCTTCTACC
mPdgfrb-FW	TCCCACATTCCTTGCCCTTC
mPdgfrb-RW	GCACAGGGTCCACGTAGATG
mTnc-FW	TTGGGAACTCGTTGTGGCTT
mTnc-RW	GAGGTTGGACTGGCTAGGTG
mTagln-FW	CGGCCTTTAAACCCCTCACC
mTagln-RW	GACTGCACTTCTCGGCTCAT
mActa2-FW	AGGGCTGTTTTCCCATCCAT
mActa2-RW	GGCCCATTCCAACCATTACTC
mIL6-FW	ATGGTACTCCAGAAGACCAGAGG
mIL6-RW	GTATGAACAACGATGATGATGCACTT
mLif-FW	CTTTCCATGGCAACGGGAC
mLif-RW	AGGGAGGCGCTCAGGTATG
mCxcl1-FW	ACTGCACCCAAACCGAAGTC
mCxcl1-RW	TGGGGACACCTTTTAGCATCTT
mIcam1-FW	GCAGTCCGCTGTGCTTTGA
mIcam1-RW	CTCCGGAAACGAATACACGGT
hHPRT-FW	GCTGAGGATTTGGAAAGGGT
hHPRT-RW	CATCTCGAGCAAGACGTTCA
hZEB1-FW	GGCATACACCTACTCAACTACGG
hZEB1-RW	TGGGCGGTGTAGAATCAGAGTC

2.4.5 Histological analysis of tissue sections

For immunohistochemical analysis of tumours, tissues were dehydrated using histokinette, embedded in paraffin and cut into 3 µm sections. These sections were mounted on slides, deparaffinized and rehydrated in distilled water. Slides were stained using Bond-Max (Leica) and Bond Polymer Refine Detection system (Leica, DS9800) according to the manufacturer's instructions. Stained sections were embedded in DPX mountant (Merck, 06522) and imaged using an Aperio CS2 digital pathology slide scanner (Leica). Positive cells were quantified using macros for Aperio ImageScope (v12.4.0.7018). Antibodies used for immunohistochemical staining of tumour sections are listed in table 34. Masson-Goldner stainings were performed with the Masson-Goldner's Trichrome staining kit (Carl Roth, 3459.1) according to the manufacturer's instructions.

Table 34: Antibodies for immunohistochemical stainings of tissue sections

Target	Manufacturer	Reference number
Ki67	Cell Signaling Technology	9129
Vimentin	Abcam	ab92547
cl. Casp. 3	Cell Signaling Technology	9661S
CD4	Cell Signaling Technology	25229S
CD8a	Synaptic Systems	361003
FoxP3	R&D Systems	MAB8214
PD-L1	Cell Signaling Technology	13684S
B220	ThermoFisher Scientific	14-0452-82

2.4.6 Immunofluorescent staining of tissue sections

For immunofluorescent staining of tumour sections, deparaffinized sections were incubated in citrate based antigen unmasking solution (Vector Laboratories, H-3300) in a pressure cooker at maximum heat for 20 minutes and allowed to cool down slowly. Subsequently, slides were washed once with PBS and blocked for 30 minutes with 20 % goat serum (Merck, G9023) in PBS+0,1 % Tween 20. Primary antibodies (table 35) were added 1:200 in blocking buffer and slides were incubated for 1 hour at room temperature with occasional shaking. Slides were washed 3 times with PBS and secondary antibodies (table 35) were added 1:500 in blocking buffer with 2 drops/mL DAPI (ThermoFisher Scientific, R37606). After incubation for 30 minutes at room temperature, slides were washed 3 times with PBS and embedded in ProLong Gold Antifade mountant (ThermoFisher Scientific, P36935). Slides were imaged at the Evos microscope at 20x magnification and analysed using Cell Profiler (v3.1.5, McQuin et al. 2018) and ImageJ.

Table 35: Antibodies for immunofluorescent stainings of tissue sections

Target	Manufacturer	Reference number
Zeb1	Bethyl	IHC-00419
E-Cadherin	BD Biosciences	610181
aSMA	ThermoFisher Scientific	14-9760-82
Pdgfra	Abcam	ab203491
Mouse IgG	ThermoFisher Scientific	A-21202
Rabbit IgG	ThermoFisher Scientific	A-31573

For staining of freshly frozen sections, mouse tissue was collected and submerged in Tissue-Tek O.C.T. compound (Sakura, SA62550) in cryo molds. Tissues were stored on dry ice or -20 °C until solidification of matrix and cut into sections with a cryostat (Leica). Freshly cut sections were mounted on slides, blocked for 30 minutes with 20% goat serum in PBS + 0,1% Tween 20 and incubated for one hour with 1:100 Epcam-APC antibody (eBioscience, 17-5791-80) in blocking solution with 2 drops/mL DAPI. After washing with PBS 3 times, slides were embedded in ProLong Gold Antifade mountant and imaged at Evos microscope.

2.4.7 Immunofluorescent staining of cell cultures

For staining of cell cultures, supernatant was removed and cells were fixed by incubation with 4 % PFA for 20 minutes at room temperature. Cells were permeabilized by incubation with PBS+0,1% Tween 20 + 0,1 % Triton X 100 for 10 minutes at room temperature and blocked by incubation with 2 % BSA (Merck, A7030). Primary antibodies (listed in table 36) were added in blocking buffer for one hour in dilutions from 1:100 to 1:500. After washing 3 times with PBS, secondary antibodies were added in dilutions from 1:100 to 1:500 with 2 drops/mL DAPI. Cells were washed another 3 times with PBS and stored for imaging in PBS + 0,1 % Sodium azide (Merck, S-2002). Cells were imaged at Evos microscope and analysed using ImageJ.

Table 36: Antibodies for immunofluorescent staining of cell cultures

Target	Manufacturer	Reference number
Zeb1	Bethyl	IHC-00419
Epcam-APC	eBioscience	17-5891-80
aSMA	ThermoFisher Scientific	14-9760-82
Pdgfra	Abcam	ab203491
CD31-APC	eBioscience	17-0311-82
CD45-Biotin	eBioscience	13-0451-82
Vimentin	Abcam	ab24525
Ki67-660	eBioscience	50-5698-80
Mouse IgG	ThermoFisher Scientific	A-21202
Rabbit IgG	ThermoFisher Scientific	A-31573
Chicken IgG	ThermoFisher Scientific	SA1-72000
Streptavidin-PE	ThermoFisher Scientific	S11225

2.5 Bioinformatics

Bioinformatics in this work were performed using R Studio (v2022.02.0) with Rtools (v4.0.1.0) and R (v4.1.2) [R Core Team 2021]. Used plugins and their versions are listed in table 37.

Table 37: Versions of R plugins

Plugin	Version	References
DESeq2	1.32.0	Love et al. 2014
xlsx	0.6.5	Dragulescu & Arendt 2020
apeglm	1.14.0	Zhu et al. 2019
Seurat	4.1.0	Satija et al. 2015, Butler et al. 2018, Stuart et al. 2019, Hao et al. 2021
sctransform	0.3.3	Hafemeister et al. 2019
ggplot2	3.3.5	Wickham 2016
dplyr	1.0.8	Wickham, Francois, Herny & Müller 2022
ggpubr	0.4.0	Kassambara 2020
tidyr	1.2.0	Wickham & Girlich 2022
glmGamPoi	1.4.0	Ahlmann-Eltze & Huber 2020

2.5.1 Bulk RNA sequencing analysis

For bulk RNA sequencing analysis, an approximately 1 mm wide section of frozen tissue was cut from primary tumours after subcutaneous transplantation of AKP tumour organoids. RNA was isolated from

the tumour and concentrations were measured using Qubit RNA HS Assay kit (ThermoFisher Scientific, Q32852) following manufacturer's instructions. For each tumour, 50 µL of 50 ng/µL RNA solution were sent for RNA sequencing at the High Throughput Sequencing Core Facility in Heidelberg.

Raw reads were aligned to a reference genome (Genome Reference Consortium Mouse Build 38) using Spliced Transcripts Alignment to a Reference (STAR) (v2.7.3, [Dobin et al. 2012]) and differential gene expression was analysed using DESeq2 with the code provided in attachments. Differentially regulated genes were used for gene set enrichment analysis (GSEA, see below).

2.5.2 Single cell RNA sequencing analysis

For single cell RNA sequencing analysis, primary orthotopic tumours were cut free from surrounding tissue and dissociated into single cells by incubation in RPMI medium with 10% FCS, 0,1% collagenase I, 0,2 % dispase II and 2 U/mL DNase I for 30 minutes at 37 °C. Digestion was stopped by addition of PBS + 2 % FCS and the cell suspension was passed through a 70 µm filter (Greiner, 542070). After pelletation, cells were resuspended in 1 mL of ACK lysis buffer and incubated for 5 minutes at room temperature. PBS + 2 % FCS + 2mM EDTA (sorting buffer) were added to stop the reaction and cells were passed through a 40 µm filter. Cells were resuspended in sorting buffer at a density of 10.000 cells per µL and incubated with 5 µg/mL Fc Block (BD Biosciences, 553142) for 15 minutes on ice. Subsequently, 1 µL of antibodies against CD45 (BioLegend, 103113), CD31 (ThermoFisher Scientific, 12-0311-82), Epcam (ThermoFisher Scientific 48-5791-82), and PDGFRa (ThermoFisher Scientific, 17-1401-81) were added per 100 µL of cell suspension together with 1 µL of eFluor780 (ThermoFisher Scientific, 65-0865-14) per 500 µL of cell suspension. After incubation for 20 minutes on ice, cells were analysed by flow cytometry (FACSAria Fusion with FACS Diva v8.0.1, BD Biosciences). For each analysed tumour, 80 EpCAM+ cells, 148 CD45+ cells and 148 CD31- CD45- EpCAM- cells (gating shown in Figure 7) were sorted into a 384-well capture plate and sent for commercial sequencing (Single cell discoveries, Sort Seq [Muraro et al. 2016]). Flow cytometry marker expression of index sorted cells was obtained by FlowJo (v10.8.1) with plugin "IndexSort".

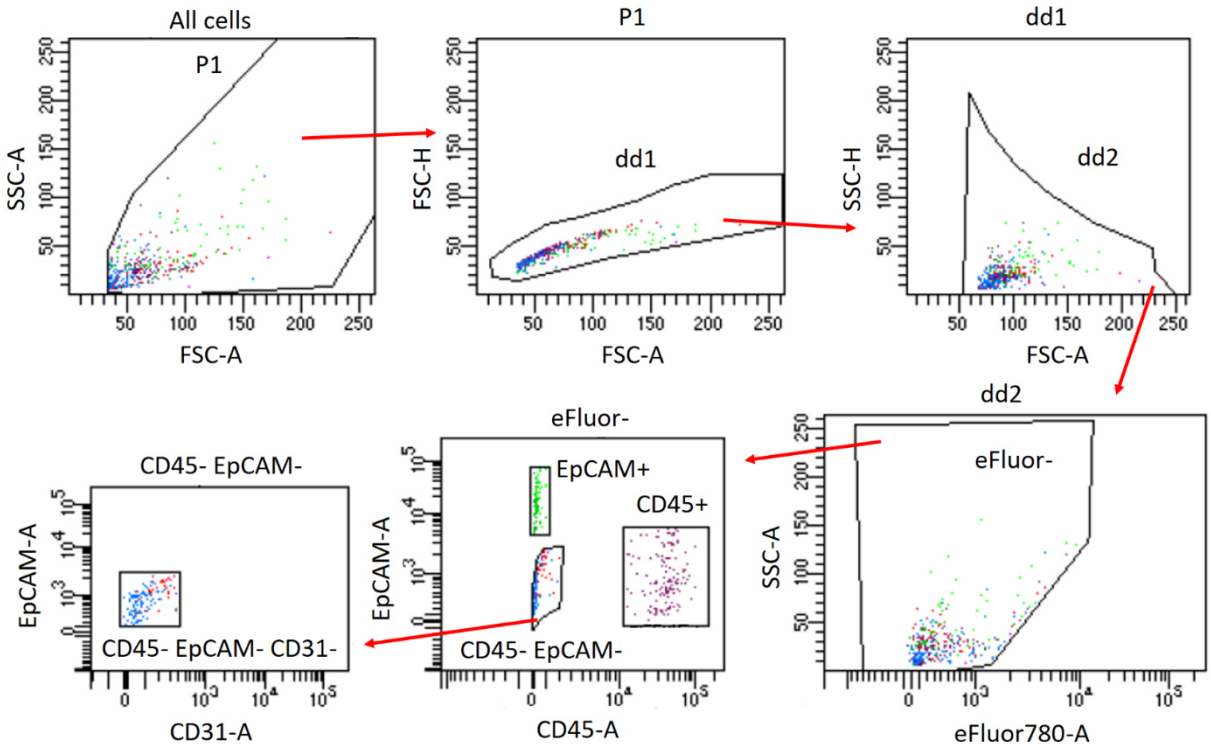

Figure 7: Gating strategy for sorting of tumor/stromal cell populations from orthotopic tumours
AKP tumour organoids were transplanted orthotopically into *Col1a2-CreERT2$^{Tg/+}$;Zeb1$^{fl/fl}$* (KO) or *Col1a2-CreERT2$^{+/+}$;Zeb1$^{fl/fl}$* (WT) mice. Four tumours per genotype were collected and sorted by flow cytometry. Figure shows exemplary gating strategy to remove debris (P1) and deplete cell doublets (dd1 & dd2). After depletion of dead cells, remaining eFluor- cells were analysed for expression of CD45 and EpCAM. CD31 positive cells were depleted from double negative (CD45- EpCAM-) cells to enrich for fibroblasts.

Raw reads provided by the company were aligned to the reference genome (Genome Reference Consortium Mouse Build 39 with ERCC RNA spike-in reference (ThermoFisher Scientific, 4456740)) by STAR (v2.7.3) with multimappers distributed based on expectation maximization (option "EM"). Obtained read counts were analysed using Seurat with the code provided in attachments. In brief, five quality control metrics were calculated per cell (Figure 8 A). For filtering, cells were assigned to one of three cell types (CD45+: immune cells, EpCAM+: epithelial cells, CD31- CD45- EpCAM-: fibroblasts) based on index sorting data. For each of the cell types, separate filtering rules were applied due to big differences in quality control metrics between cell types (thresholds shown in Figure 8 B). After applying these filtering rules, 1285 cells remained for further analysis (cells before and after filtering shown in Figure 8 C). After filtering, differentially expressed genes were calculated based on Wilcoxon rank sum test between KO and WT cells of the same cluster and used for GSEA.

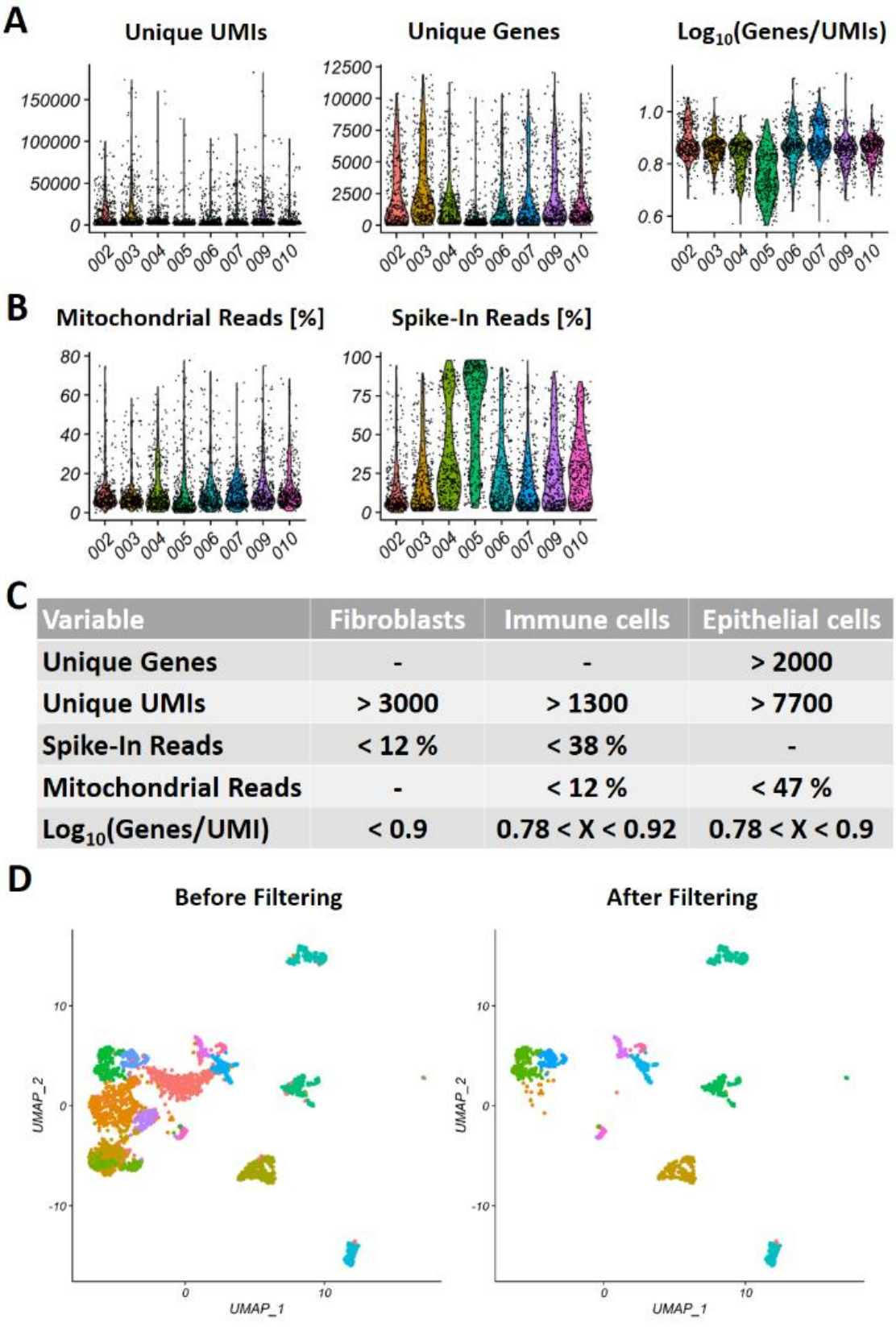

C

Variable	Fibroblasts	Immune cells	Epithelial cells
Unique Genes	-	-	> 2000
Unique UMIs	> 3000	> 1300	> 7700
Spike-In Reads	< 12 %	< 38 %	-
Mitochondrial Reads	-	< 12 %	< 47 %
Log_{10}(Genes/UMI)	< 0.9	0.78 < X < 0.92	0.78 < X < 0.9

Figure 8: Filtering rules for cells after single cell sequencing

AKP tumour organoids were transplanted orthotopically into *Col1a2-CreERT2$^{Tg/+}$;Zeb1$^{fl/fl}$* (KO) or *Col1a2-CreERT2$^{+/+}$;Zeb1$^{fl/fl}$* (WT) mice. Four tumours per genotype were sent for single cell sequencing. **A** Number of Unique UMIs (**left**), number of unique genes (**middle**) or log_{10}(genes/UMIs)(**right**) for each tumour before filtering of cells. UMI: unique molecular identifier. **B** Percentage of mitochondrial reads (**left**) and spike-in quality control reads (**right**) for each tumour before filtering of cells. **C** Filtering rules for cells of the different lineages (fibroblasts, immune cells, epithelial cells) based on variables plotted in A and B. **D** UMAP representation of cells before (**left**) and after (**right**) filtering of low quality cells according to rules in C.

2.5.3 Gene set enrichment analysis

For gene set enrichment analysis, GSEA software (Broad Institute, v4.2.3, [Mootha et al. 2003, Subramanian et al. 2005]) was used with curated gene sets from MSigDB (v7.5.1, [Ashburner et al. 2000, Liberzon et al. 2015, The Gene Ontology Consortium 2020]. Log_2 fold changes of differentially expressed genes were used as preranked datasets and collapsed to human orthologues using the MSigDB chip file v7.5.1.

2.6 Statistics

Statistics were calculated using GraphPad Prism (v9.4.0.673). Comparisons between genotypes (contraction assays, histological quantifications, tumour quantifications, qRT-PCR analysis) were analysed by student's t-Test. Comparisons of IHC scores (data from AG Brabletz) was performed using Mann-Whitney rank test. For comparison of more than two groups, ordinary one-way ANOVA was used (OT1 barrier function assay, analysis of ICB treatment). Statistics of metastasis and tumour stages between genotypes were calculated by Fisher's exact test. Survival curves of mice were compared using the Log-rank (Mantel-Cox) test.

3. Results

3.1 Myofibroblast features are reduced after deletion of *Zeb1* in fibroblasts

The EMT transcription factor Zeb1 is involved in the regulation of many processes during homeostasis and tumour development. Its role has been studied extensively in epithelial cells (see above) but the function of Zeb1 in fibroblasts and especially CAFs is not understood yet. To be able to address this question, primary colon fibroblast cultures were established. Colon fragments of healthy mice were partially digested to remove the majority of epithelial cells and the residual pieces were placed in tissue culture plates (Figure 9 top left). After several days, the pieces attached to the substrate followed by outgrowth of a coherent layer of cells. Immunofluorescence staining revealed the presence of $CD31^+$ endothelial cells, $aSMA^+$ fibroblasts and $CD45^+$ immune cells at early time points. Absence of epithelial cells was evidenced by the lack of EpCAM signal where only tiny fragments of $EpCAM^+$ cells could be found floating in the culture, which most likely represented fragments of apoptotic cells (Figure 9 top). After passaging these cultures twice, a homogeneous monolayer of cells was obtained that consisted solely of fibroblasts showing clear fibrillar aSMA staining and lacking any of the other lineage markers (Figure 9 bottom). These results show that the applied culture conditions are suitable for the isolation and selective expansion of primary fibroblasts.

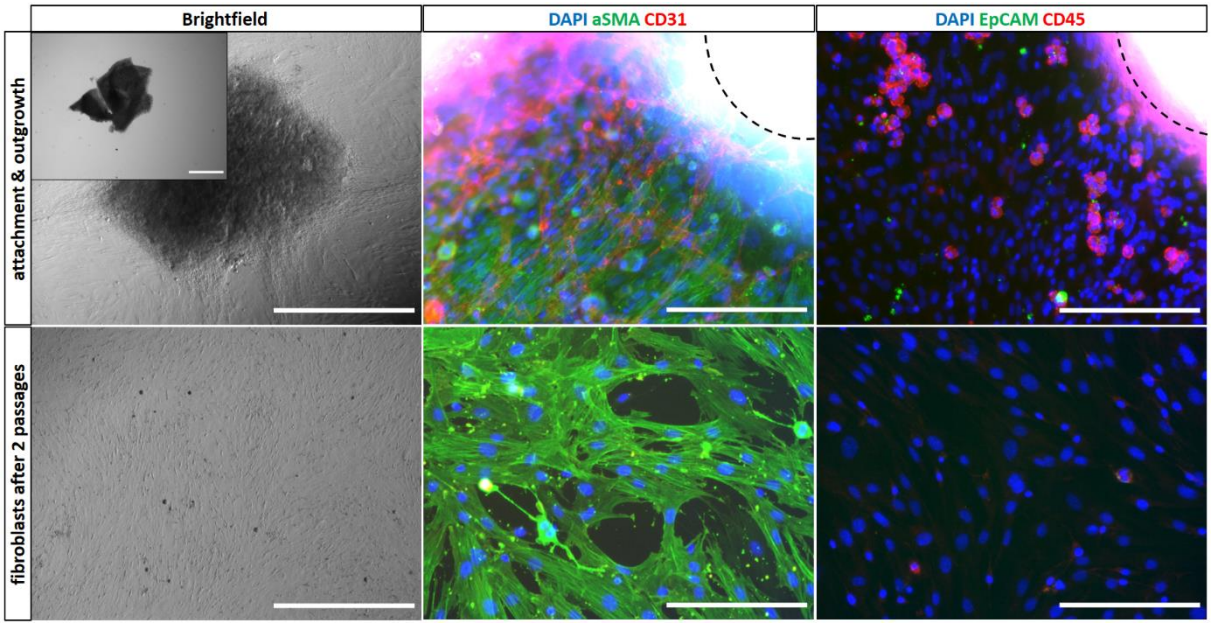

Figure 9: Primary fibroblasts form homogeneous cultures after few passages.
Fragments of the mouse intestine were cultured in cell culture dishes (**small image top left**) until multiple layers of cells grew onto the dish (**top left**). Immunofluorescence images (**middle**: DAPI, aSMA, CD31; **right**: DAPI Epcam, CD45) of these primary cultures revealed the presence of various cell lineages. After two passages, a homogeneous monolayer was obtained (**bottom left**), which did no longer contain cells of epithelial or immune lineages (**bottom middle** and **right**). Scalebars represent 1000 µm for brightfield images and 200 µm for immunofluorescence images.

To examine whether the loss of Zeb1 has an effect on primary stromal cells, colonic fibroblasts were isolated from *Col1a2-CreERT2*$^{Tg/+}$*; Zeb1*$^{fl/fl}$ mice. In these, induction of Cre recombinase activity leads to excision of exon 6 of *Zeb1* resulting in protein truncation and ablation of Zeb1 activity [Brabletz et al. 2017] (Figure 10 A and B). To determine how Zeb1 loss affects cell growth and viability, recombination was induced in a fraction of cells by lentiviral delivery of Cre recombinase and the expression of Zeb1 and Ki67 were evaluated by quantification of immunofluorescence stainings. Initially, more than 60 % of fibroblasts showed successful recombination of *Zeb1*. The rate of proliferative (Ki67^{+}) in recombined (Zeb1^{-}) cells was around 10 % compared to approximately 62 % of non-recombined cells. After passaging, more than 90 % of cells were non-recombined with about 40 % of proliferating cells, while recombined cells constituted less than 10 % and proliferative recombined cells only 2 - 3 % of all cells (Figure 10 C). This indicated a growth disadvantage of recombined cells, which could be caused by cell cycle arrest or induction of apoptosis.

To generate lines with homogeneous loss of Zeb1, expression of the *Col1a2-CreERT2* transgene was used to induce quantitative recombination by incubation with 4-hydroxy-tamoxifen (4OHT). Following this approach, most likely due to the absence of non-recombined cells that compete with Zeb1 deficient fibroblasts, successful recombination could be achieved in four independent cell lines. Recombination was confirmed by genomic PCR that showed complete loss of exon 6 (Figure 10 D). In addition, complete loss of Zeb1 protein expression in KO fibroblasts was observed by Western blot analysis of whole cell lysates (Figure 10 E).

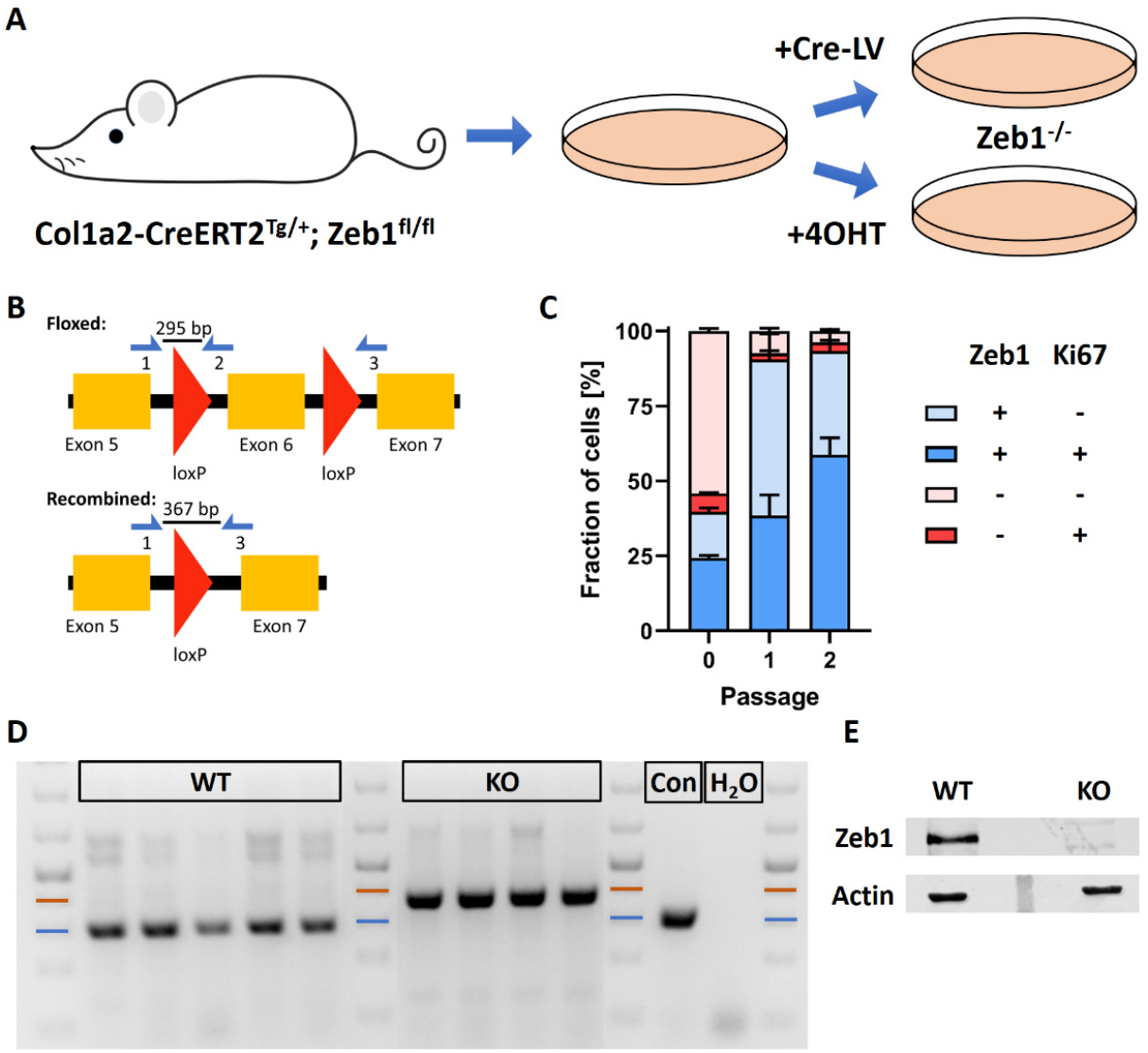

Figure 10: Recombination of *Zeb1* in mouse colon fibroblasts

A Strategies for depletion of Zeb1 *in vitro*. After isolation of primary colon fibroblasts from *Col1a2-CreERT*$^{Tg/+}$*; Zeb1*$^{fl/fl}$ mice, *Zeb1* was recombined either by lentiviral transduction of Cre recombinase (Cre-LV) or by incubation with 4-hydroxy-tamoxifen (4OHT). **B** Strategy for genomic confirmation of *Zeb1* deletion. Recombination of the loxP sites leads to excision of Exon 6 and removes the binding site of primer 2 resulting in a 72 bp difference in PCR fragment size. **C** Percentage of Ki67 and Zeb1 positive cells after transduction of primary fibroblasts with Cre lentivirus. Cells were fixed few days after transduction or passaging and Ki67 and Zeb1 status were analysed by immunofluorescent stainings (Mean ± SD of 3 independent transductions in the same fibroblast line). **D** Primary fibroblasts from *Col1a2-CreERT2*$^{Tg/+}$*;Zeb1*$^{fl/fl}$ (KO) or *Col1a2-CreERT2*$^{+/+}$*;Zeb1*$^{fl/fl}$ (WT) mice were incubated with 4OHT. Image shows gelelectrophoretic analysis of PCR fragments from *Zeb1* genotyping. Lines mark 300 (blue) and 400 (orange) bp size respectively. Genomic DNA from a mouse expressing the floxed allele of *Zeb1* was used as control. **E** Analysis of Zeb1 levels in one exemplary WT and KO line by western blot.

To examine the phenotypic consequences after loss of Zeb1, immunofluorescence stainings of general fibroblast markers were analysed. The stainings confirmed a complete loss of Zeb1 expression in KO cells compared to strong nuclear staining in WT cells. Additionally, while no changes could be observed in Vimentin staining, KO fibroblasts showed a changed pattern of aSMA expression. In WT fibroblasts, aSMA was concentrated in fibrillar structures reflecting the cytoskeletal organisation. In *Zeb1* KO fibroblasts, fibrillar aSMA staining was lost and only basal cytoplasmic expression could be observed

resulting in a weaker overall expression of aSMA. In addition, expression of PDGFRa, a marker of inflammatory CAFs [Elyada et al. 2019], was increased in *Zeb1* KO fibroblasts compared to WT cells (Figure 11 A).

Apart from changes of marker expression, the initial outgrowth of KO fibroblasts from colonic tissue fragments (see Figure 9) was analysed using a *Rosa26-mTmG* reporter transgene. This transgene consists of a membrane-targeted tdTomato (mT) gene flanked by loxP sites and followed by a membrane-targeted EGFP (mG) gene. Before recombination, tdTomato is expressed and the stop codon at the end of the open reading frame prevents expression of EGFP. Recombination excises the tdTomato fragment and allows EGFP expression, which marks cells with Cre activity by green fluorescence (Figure 11 B). Fibroblasts from colonic fragments of Cre negative animals (*Rosa26-mTmG*$^{Tg/+}$; *Col6a1-Cre*$^{+/+}$; *Zeb1*$^{fl/fl}$) did not show GFP expression and nuclear expression of Zeb1 was observed in the vast majority of cells. In contrast, approximately 50 % of the cells from Cre positive animals (*Rosa26-mTmG*$^{Tg/+}$; *Col6a1-Cre*$^{Tg/+}$; *Zeb1*$^{fl/fl}$) displayed green fluorescence together with loss of Zeb1 expression. Interestingly, most of the recombined fibroblasts displayed smaller nucleus size and less cytoplasmic area compared to non-recombined fibroblasts in the same culture (Figure 11 C). Together, these findings indicated that loss of Zeb1 in fibroblasts induces changes in the cytoskeleton.

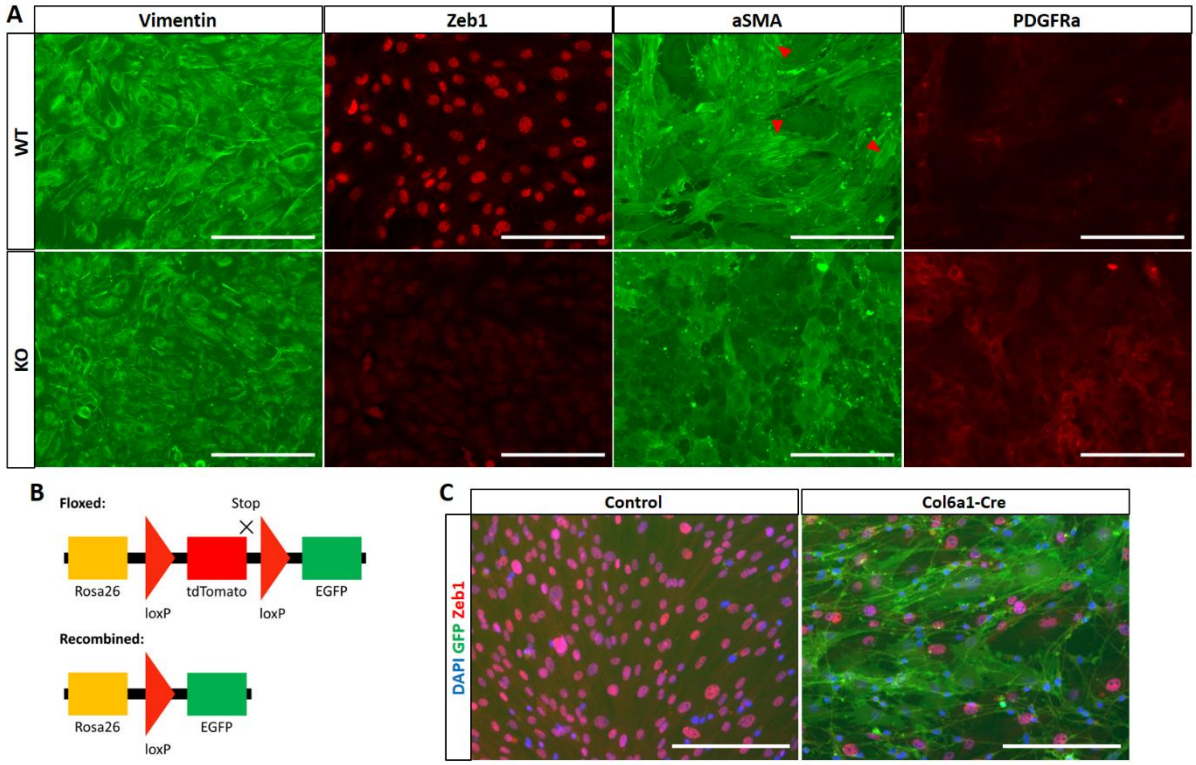

Figure 11: Fibroblast morphology changes upon depletion of Zeb1

A Colon fibroblasts from *Col1a2-CreERT2$^{Tg/+}$;Zeb1$^{fl/fl}$* (KO) or *Col1a2-CreERT2$^{+/+}$;Zeb1$^{fl/fl}$* (WT) mice were incubated with 4-hydroxy-tamoxifen and cultured for several passages. Cells were fixed and stained for fibroblast markers (Vimentin, aSMA, PDGFRa) and Zeb1 (representative images of 5 WT and 4 KO fibroblast lines, red arrowheads point towards good visible fibrillar structures). **B** Structure of the mTmG reporter transgene. Before recombination, expression of EGFP is prevented by the stop codon of tdTomato. Cre activity leads to excision of tdTomato and subsequent EGFP expression. **C** Colon from *Col6a1-Cre$^{Tg/+}$; Zeb1$^{fl/fl}$; Rosa26^{mTmG}* (Col6a1-Cre) or *Col6a1-Cre$^{+/+}$; Zeb1$^{fl/fl}$; Rosa26^{mTmG}* (Control) mice were cut into fragments and transferred into cell culture dishes. After few days, cells growing from the fragment to the plate were fixed and stained for Zeb1. GFP signal (green) indicates Cre activity by recombination of the mTmG reporter transgene. Scalebars represent 200 µm.

To examine whether the observed changes of marker expression and cytoskeletal differentiation are associated with changes on a functional level, collagen contraction assay was performed. For this assay, equal numbers of *Zeb1* WT or KO fibroblasts were seeded in a collagen drop, which was detached from the plate after polymerisation. Subsequently, fibroblast mediated contraction was measured by monitoring the area of the collagen disc to quantify contractility of the cells. While *Zeb1* WT fibroblasts reduced the area covered by the collagen drop by about 64 % after 24 hours, *Zeb1* KO fibroblasts only led to a reduction of approximately 13 % after the same time (Figure 12). This hinted towards loss of myofibroblastic features in fibroblasts after *Zeb1* deletion on a functional level.

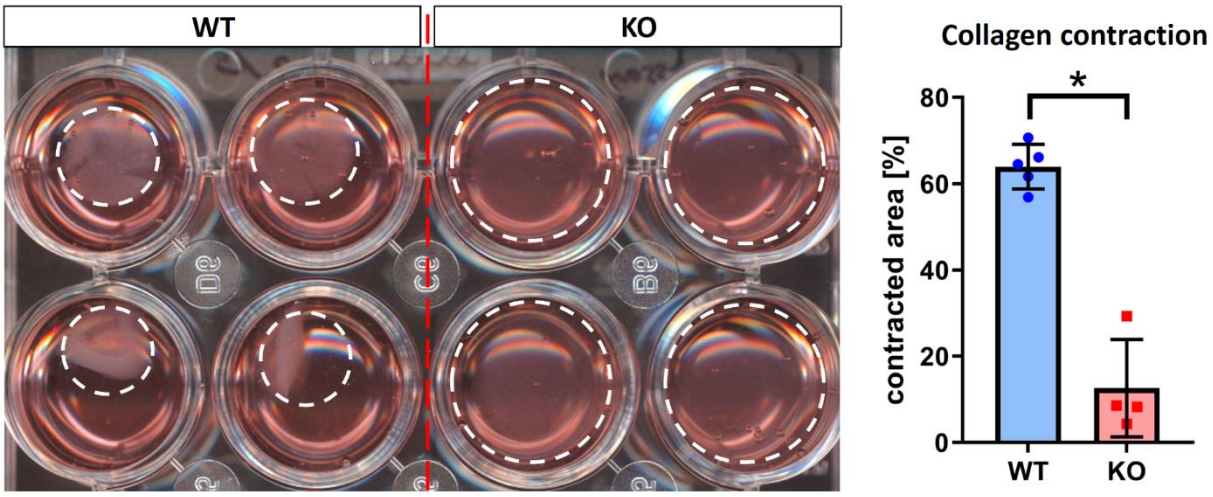

Figure 12: *Zeb1* KO Fibroblasts are less contractile
WT or KO fibroblasts were seeded in a collagen disc that was detached after polymerization. After 24 hours, the area of the collagen disc was measured (**left,** white lines, 24-well plate). The relative contraction compared to the initial area is shown (**right**)(Mean ±SD of 5 WT and 4 KO independent fibroblast lines, * = p < 0.05)

Since the results indicated that Zeb1 loss induces a phenotypic switch of myofibroblasts, gene expression analysis was performed to examine the expression markers of distinct fibroblast subtypes. To study the immediate consequences and avoid possible compensatory adaptations of the fibroblasts to overcome the observed growth arrest (see Figure 10), a model of acute loss of Zeb1 was chosen. Colon fibroblasts from *Zeb1*$^{fl/fl}$ mice were transduced with a Cre lentivirus and after few days, expression of different myofibroblast markers [Öhlund et al. 2017, Elyada et al. 2019] and inflammatory genes were analysed in addition to mRNA levels of *Zeb1*. Lentiviral delivery of Cre resulted in a 75 % reduction of *Zeb1* expression confirming the efficiency of recombination. Additionally, expression of several myofibroblast markers (*Pdgfrb*, *Tnc*, *Tagln*, *Acta2*) was decreased between 24 and 53 %. In contrast, the expression of inflammatory genes (*Il6*, *Lif*, *Cxcl1*, *Icam1*) was increased around between 118 and 200 % (Figure 13). In line with previous findings, these results indicated that loss of Zeb1 induced a shift from a myofibroblast to an inflammatory fibroblast subtype.

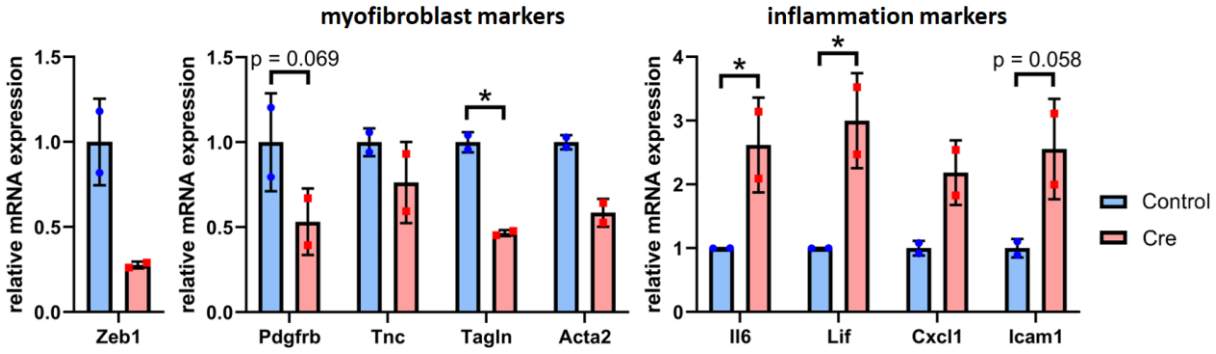

Figure 13: *Zeb1* KO fibroblasts express higher levels of inflammatory markers
Primary *Zeb1*$^{fl/fl}$ fibroblasts were transduced with Cre or GFP (Control) lentivirus to induce recombination. Transcriptomic effects of acute loss of Zeb1 were analysed by quantitative real-time PCR (Mean ±SD of 2 independent fibroblast lines, *: p< 0.05).

Fibroblasts are involved in the regulation of multiple processes in homeostasis and tumour development and recent analyses have identified diverse populations [Kobayashi et al. 2019]. To examine whether the observed change in differentiation also affects homeostatic functions of fibroblasts, coculture experiments with colon organoids were performed. First, the minimal growth factor requirements of mouse colon organoids were determined by removing every individual growth factor from the culture medium and monitoring organoid growth over several passages. The five components Wnt3a, hEGF, Noggin, R-spondin-1 and the TGFβ-inhibitor A-83-01 were found indispensable to maintain growth of organoid monocultures as withdrawal of either factor disrupted organoid expansion. When WT mouse colon fibroblasts were seeded together with organoids in the Matrigel®, hEGF, Noggin and A-83-01 could be removed from the medium without affecting organoid growth. Additionally, organoids cocultured with WT fibroblasts survived withdrawal of Wnt3a for two additional passages compared to the monoculture condition. When the same experiment was performed with *Zeb1* KO fibroblasts, withdrawal of Wnt3a no longer led to an arrest of organoid growth (Figure 14). Taken together, the coculture experiments indicated a changed growth factor secretion profile upon *Zeb1* deletion in the fibroblasts.

In summary, the *in vitro* experiments indicated that loss of Zeb1 in fibroblasts led to a shift of fibroblast subtypes from myofibroblasts to inflammatory fibroblasts. This affected both marker protein expression and transcriptomic profile. On a functional level, the KO of *Zeb1* in fibroblasts affected contractility and fibroblast niche functions in organoid cocultures.

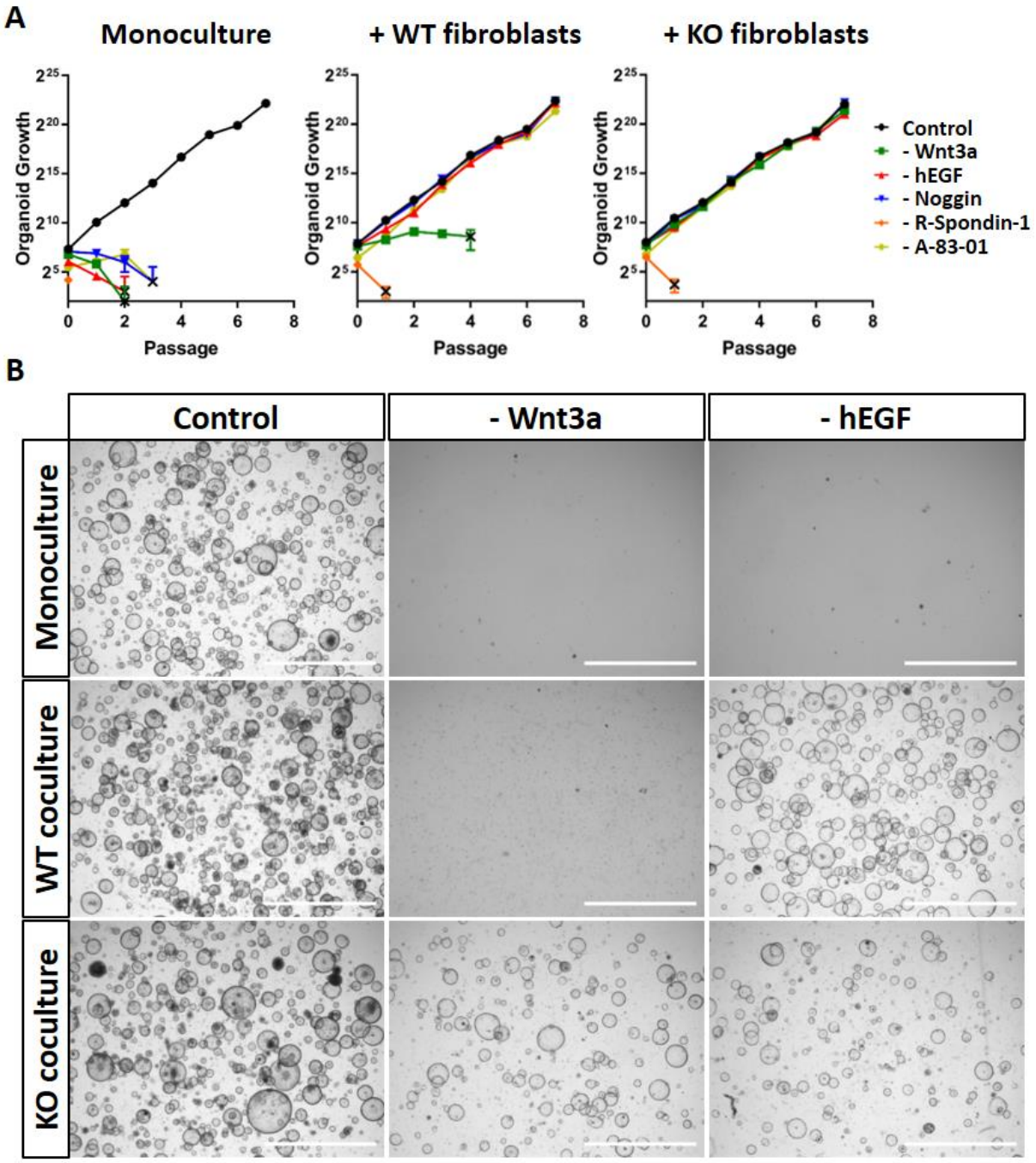

Figure 14: *Zeb1* KO fibroblasts show distinct niche functions in coculture with colon organoids
Mouse colon organoids were cultured either in control medium containing 5 components or medium with each factor removed individually from the medium. **A** The total number of organoids after each passage was estimated based on organoids present at time of splitting and splitting factor of previous passages. Organoids were cultured as monoculture (**left**), coculture with WT fibroblasts (**middle**) or coculture with *Zeb1* KO fibroblasts (**right**)(Mean ± SD of 2 independent fibroblast lines or monoculture controls for each condition). **B** Representative images of mono- and cocultures of mouse colon organoids with WT or *Zeb1* KO fibroblasts in different media conditions. Images of monocultures in '- Wnt3a' and '- hEGF' medium are from passage 2. Image of coculture with WT fibroblasts in '- Wnt3a' medium is from passage 4. All other images are from passage 7. Scalebars represent 2 mm.

3.2 Generation and characterization of tumour organoid lines

CAF phenotypes can impact tumour-promoting and -restricting properties of the TME (see above). Since observations from *in vitro* experiments indicated a modulation of CAF plasticity by Zeb1,

consequences of stromal Zeb1 loss were examined in mouse models of CRC. Together with the group of Thomas Brabletz, models for sporadic or inflammation driven tumourigenesis were analysed. To study the functional consequences on the TME, all experiments were performed in immuno-competent mice. For organoid transplantation, a library of syngeneic tumour organoids was generated first.

After isolation of colon organoids from FvB mice harbouring a floxed *KrasG12D* allele [Jackson et al. 2001], oncogenic mutations were induced using either CRISPR/Cas9 technology, Cre recombinase or lentiviral transduction. Organoid lines with different combinations of driver mutations were generated and transplanted subcutaneously into FvB mice for characterization (Figure 15. A). Mutations that were introduced into the organoids have been described as driver mutations of human cancers (*APC*, *TP53* and *TGFBR2* loss of functions, *KRAS* gain of function and Notch activation) [TCGA 2012] and have previously been used in transplantation models of CRC [Drost et al. 2015, Matano et al. 2015]. Oncogenic mutations were added in a stepwise manner and each mutation was confirmed by Sanger sequencing (*Apc*, *Tp53*, *Tgfbr2*), genomic PCR (*Kras*) or acquisition of antibiotic resistance (NICD). To avoid prolonged times of genomic instability [Eischen 2016, Karlsson et al. 2022], mutations of *Tp53* were added last. The abbreviations for the different lines reflect the genotype and the order of mutagenesis (Figure 15 B). Initially, five tumour organoid lines were chosen for further analysis (ATN, ATP, AKT, AKP and AKTP). Morphologic comparison of these tumour organoid lines revealed only minor differences *in vitro*. The thicker epithelium in $KRAS^{G12D}$ mutant organoids could be attributed to the differentiation induced by activation of the MAPK pathway (Figure 15 C) [Uhlitz et al. 2021].

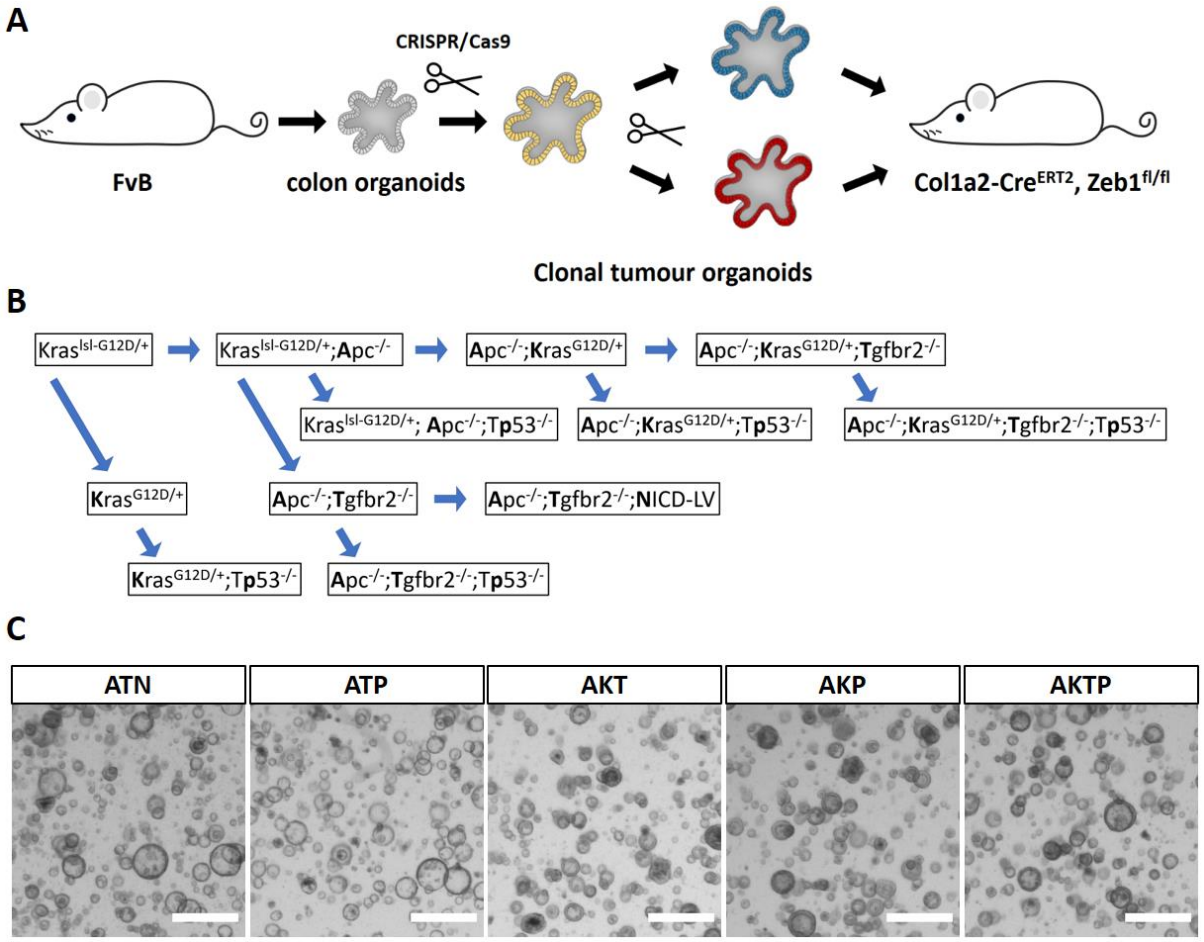

Figure 15: Generation of syngeneic mouse tumour organoid lines

A Generation of mouse colon tumour organoid lines. Colon organoids were isolated from *Kras*$^{lsl\text{-}G12D/+}$ FvB mice, modified using CRISPR/Cas9, Cre transfection or lentiviral transduction in a stepwise process and then transplanted into conditional *Col1a2-CreERT2*$^{Tg/+}$*;Zeb1*$^{fl/fl}$ (KO) or *Col1a2-CreERT2*$^{+/+}$*;Zeb1*$^{fl/fl}$ (WT) mice. **B** Sequential generation of tumour organoid lines. Mutations were added individually to the predecessor lines, always starting with an *Apc* mutation and ending with a *Tp53* mutation when present in the final line. Bold letters indicate abbreviation used for the combination of mutations. **C** Representative images of organoid morphologies from different genotypes 48 hours after regular splitting. Scalebars represent 500 µm.

To test how the driver mutations affect tumour growth and histology *in vivo*, subcutaneous transplantation of the five organoid lines was performed (ATN, ATP, AKT, AKP and AKTP), of which ATN failed to generate tumours. Histological analysis revealed clear morphological differences between the organoid lines, reflecting the influence of certain driver mutations on the tumour growth. While AKT and ATP tumours formed low grade and well differentiated tumours, transplantation of AKP and AKTP organoids led to gradually more undifferentiated tumours reflecting more progressed states [Fleming et al. 2012]. Additionally, differences in stromal Zeb1 expression were observed by immunofluorescence staining suggesting distinct signals from tumour cells that modulate the composition of the TME (Figure 16 A). Quantification of expression levels of Ki67, Vimentin and stromal Zeb1 revealed high levels of proliferation and a high fraction of stromal cells in AKP tumours. Together with the high levels of stromal Zeb1, this indicated that AKP tumours were most informative for the

subsequent analyses (Figure 16 B). Robust tumour growth and medium growth speed further qualified AKP tumours as a suitable model to capture tumour suppressive and promoting phenotypes (Figure 16 C). To confirm the importance of all introduced mutations, subcutaneous transplantations with organoids that lacked one of the three mutations of the AKP line (AK, AP and KP) were performed. The fact that none of the double mutant lines showed tumour growth (Figure 16 D) demonstrated that the AKP line contained a minimal number of drivers, providing a sensitive model to investigate stromal influences.

In summary, a library of syngeneic tumour organoid lines was generated, of which AKP organoids exhibited the highest stromal content and stromal Zeb1 expression in subcutaneous tumours.

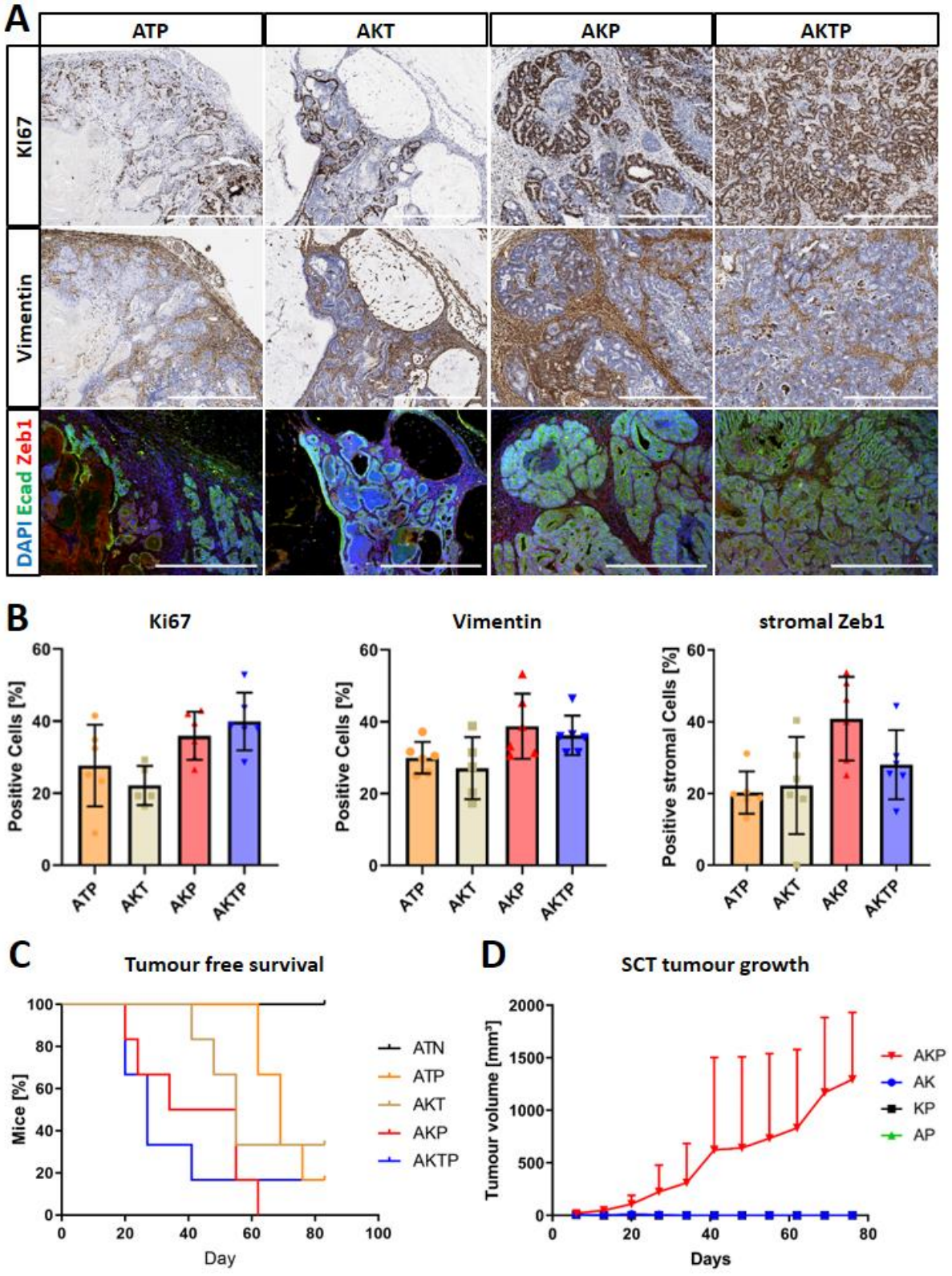

Figure 16: Profound differences of tumour growth and histology after SCT of tumour organoid lines
Colon tumour organoids with different genotypes were transplanted subcutaneously into WT FvB mice. Tumour growth was monitored by non-invasive measurement of the flank and at endpoint (line dependent), tumours were collected for histological analysis. **A** Representative images of FFPE tumour sections from different genotypes stained for Ki67 (**top**), Vimentin (**middle**) or DAPI, E-cadherin and Zeb1 (**bottom**). Scalebars represent 500 µm. **B** Quantification of stainings shown in A (Mean ± SD of ≥ 5 tumours of each genotype). **C** Tumour free survival (tumour volume < 200 mm³) of mice after subcutaneous transplantation of colon tumour organoids with different genotypes (6 mice per organoid line). **D** Tumour volume after subcutaneous transplantation of colon tumour organoids with different genotypes in mice (Mean ± SD of 6 mice per genotype).

3.3 Stromal loss of Zeb1 reveals minor changes in the normal colon

Before performing transplantation experiments with tumour organoid lines in conditional knockout mice, specificity of the *Col1a2-CreERT* transgene was tested using *Rosa26R*$^{CAG\text{-}tdTomato}$ reporter mice. These mice harbour a floxed reporter construct in the *Rosa26* locus and cells containing Cre activity are marked by expression of tdTomato, resulting in red fluorescence [Madisen et al. 2010]. After feeding *Col1a2Cre*^{ERT2}*;Rosa26R*$^{CAG\text{-}tdTomato}$ mice with tamoxifen food for two weeks, strong red fluorescence could be observed in colon fibroblasts but not in epithelial cells. Also, control mice harbouring the reporter transgene but not the *Col1a2-CreERT* transgene did not show any red fluorescent cells (Figure 17 A top). Additionally, skin fragments from these mice were analysed to confirm specific recombination in a subcutaneous setting. As in the colon, red fluorescence was found specifically in fibroblasts from Cre-expressing mice but not in fibroblasts from control mice (Figure 17 A bottom).

After confirmation of Cre specificity, general effects of stromal loss of Zeb1 in the intestine were examined. After tamoxifen diet for two weeks, colons from *Col1a2-CreERT2*$^{+/+}$*;Zeb1*$^{fl/fl}$ (WT) and *Col1a2-CreERT2*$^{Tg/+}$*;Zeb1*$^{fl/fl}$ (KO) mice were isolated and analysed using immunohistochemistry. Staining for Ki67 or Vimentin did not reveal differences in general morphology or crypt architecture between the two groups (Figure 17 B). In mice of both genotypes, proliferative (Ki67^{+}) cells were located from the bottom of the crypts to approximately half way towards the villus tip and Vimentin expression was similarly restricted to regions of the submucosa. This indicated no major effects of stromal Zeb1 loss on intestinal homeostasis.

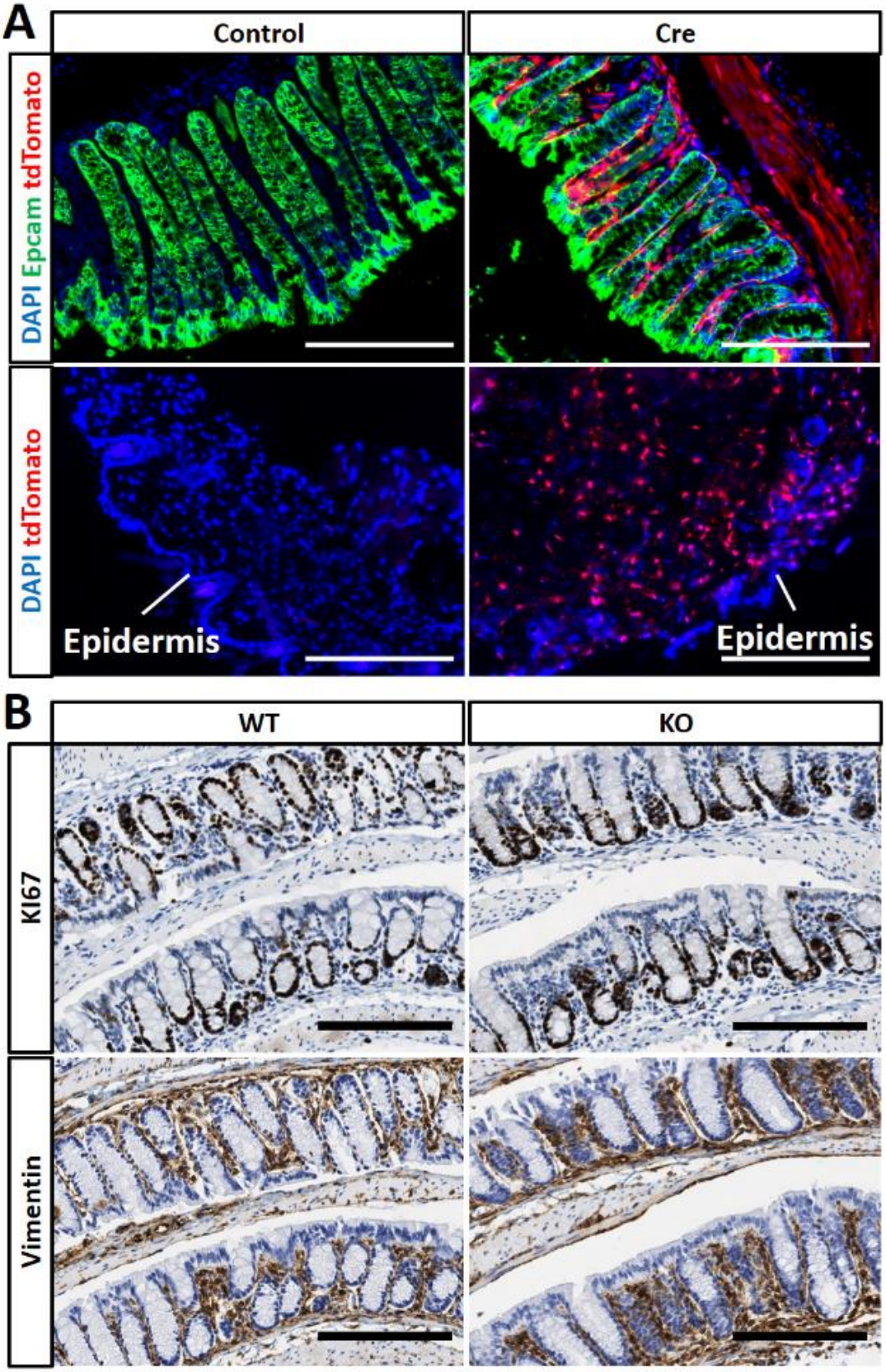

Figure 17: Loss of stromal Zeb1 does not affect intestinal homeostasis

A *Rosa26R-CAG-tdTomato*$^{Tg/+}$ (Control) or *Col1a2-CreERT2*$^{Tg/+}$*;Rosa26R-CAG-tdTomato*$^{Tg/+}$ (Cre) mice were fed with tamoxifen diet for 2 weeks. Tissues were collected and tdTomato expression was analysed in immunofluorescent stainings of freshly frozen sections from colon (DAPI & Epcam, **top**) or skin (DAPI, **bottom**). Scalebars represent 200 µm. **B** *Col1a2-CreERT2*$^{+/+}$*;Zeb1*$^{fl/fl}$ (WT) or *Col1a2-CreERT2*$^{Tg/+}$*;Zeb1*$^{fl/fl}$ (KO) mice were fed with tamoxifen diet for 2 weeks. Colons were collected and expression of Ki67 (**top**) or Vimentin (**bottom**) was analysed on immunohistochemical stainings of FFPE sections. Scalebars represent 200 µm.

3.4 Stromal changes upon Zeb1 loss in CAFs show a moderate impact on subcutaneous tumour growth

As a model of sporadic colorectal cancer, AKP tumour organoids were transplanted subcutaneously into *Col1a2-CreERT2$^{+/+}$;Zeb1$^{fl/fl}$* (WT) and *Col1a2-CreERT2$^{Tg/+}$;Zeb1$^{fl/fl}$* (KO) mice. Fibroblast specific depletion of Zeb1 was induced by tamoxifen food starting from day 4 after transplantation. Tumour size was monitored until first mice reached termination criteria on day 34 and tumours were collected for analysis latest at day 55 after transplantation (Figure 18 A).

Successful recombination of stromal *Zeb1* was confirmed by immunofluorescence staining. Epithelial cells were excluded from the analysis based on E-cadherin staining (Figure 18 B) and quantification of Zeb1 expression in E-cadherin$^-$ cells revealed a reduction of Zeb1$^+$ cells from more than 30 % in WT tumours to below 10 % in KO tumours (Figure 18 C). The few remaining Zeb1$^+$ cells in KO mice could either be non-recombined fibroblasts or other cell types expressing Zeb1.

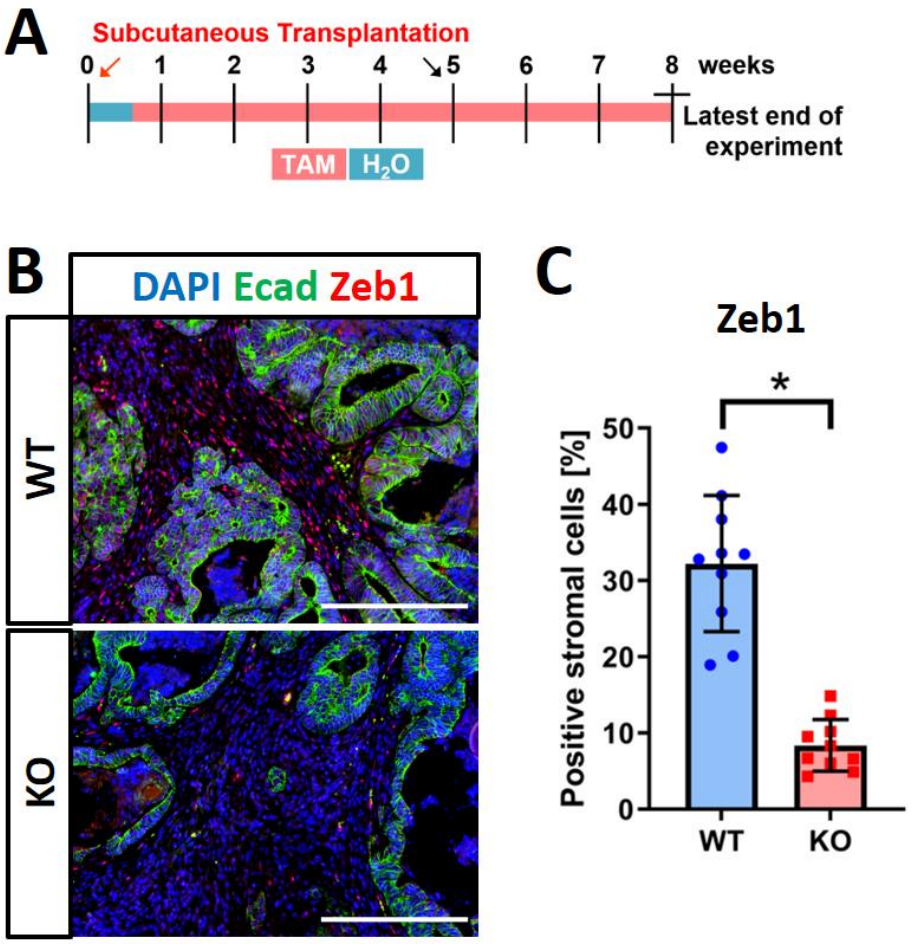

Figure 18: Stromal expression of Zeb1 is ablated in subcutaneous tumours after tamoxifen diet
A Experimental setup of subcutaneous transplantations in *Col1a2-CreERT2$^{+/+}$;Zeb1$^{fl/fl}$* (WT) or *Col1a2-CreERT2$^{Tg/+}$;Zeb1$^{fl/fl}$* (KO) mice. Mice were injected with AKP tumour organoids and fed tamoxifen food from day 4 after injection. Tumour sizes were compared until day 34 (black arrow) when first mice reached abortion criteria and had to be removed from the experiment. At day 55 the last mice reached abortion criteria and the experiment was ended. **B** FFPE tumour sections were stained for DAPI, E-cadherin and Zeb1. Scalebars represent 200 µm. **C** Non-necrotic, E-cadherin negative areas were considered stromal areas and Zeb1 expression in these areas was quantified using Cell Profiler software. (Mean ± SD of 10 tumours per genotype, * = $p < 0.05$)

Fibroblast specific deletion of *Zeb1* led to a comparable tumour size after subcutaneous transplantation of AKP tumour organoids (Figure 19 A). Immunohistological analysis revealed that the proliferation and cell death were unchanged between the two genotypes (Figure 19 B and C). In addition, the number of Vim positive fibroblasts and the infiltration of CD4, CD8 and FoxP3 positive T cells and the PD-L1 expression was not significantly changed (Figure 19 D-H).

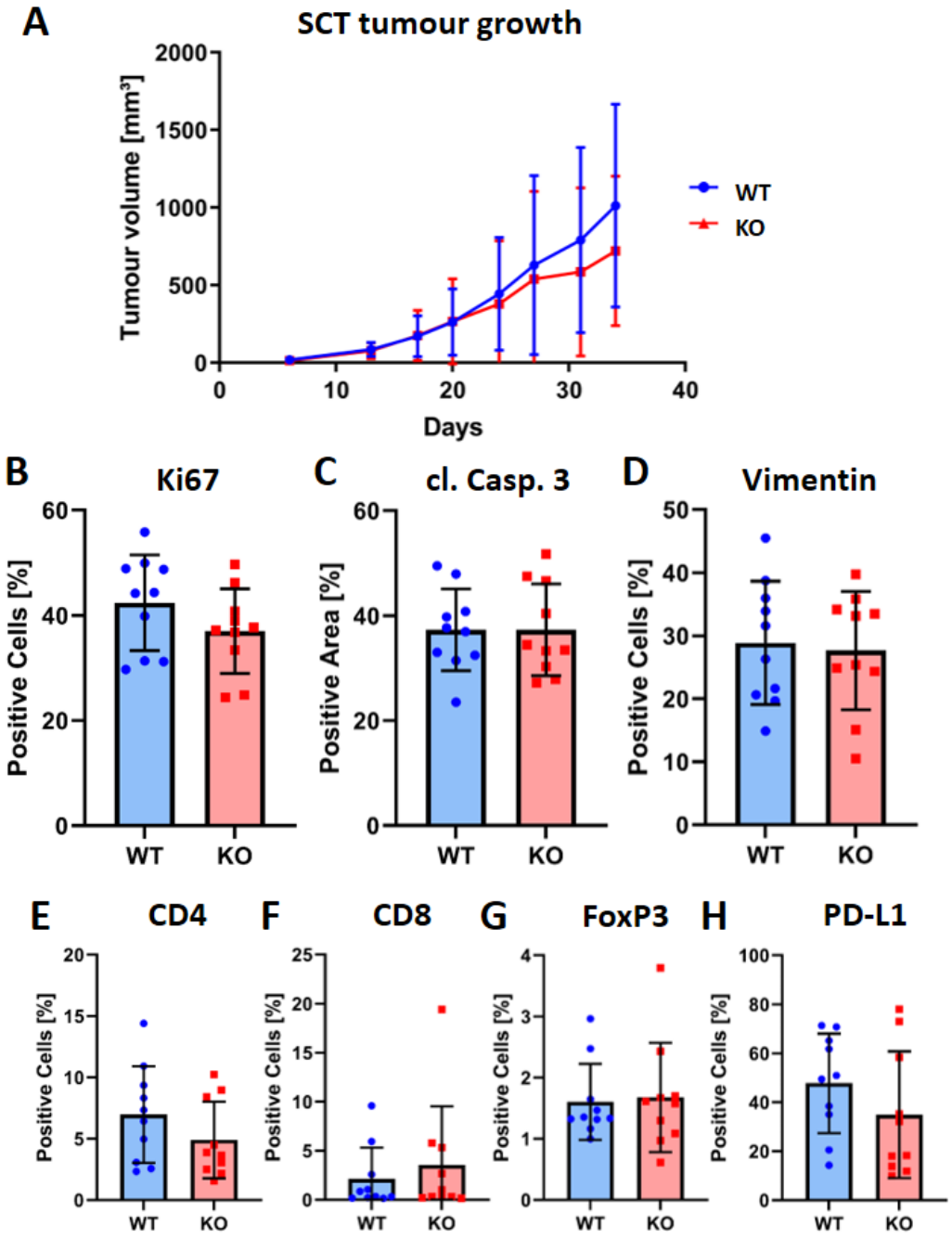

Figure 19: The morphology of subcutaneous tumours is unchanged upon stromal *Zeb1* deletion
AKP tumour organoids were transplanted subcutaneously into *Col1a2-CreERT2*$^{+/+}$*;Zeb1*$^{fl/fl}$ (WT) or *Col1a2-CreERT2*$^{Tg/+}$*;Zeb1*$^{fl/fl}$ (KO) mice. Mice were fed with tamoxifen diet from day 4 after transplantation and tumours were collected at day 55 (latest) for analysis. **A** Tumour volumes after subcutaneous transplantation of AKP tumour organoids were compared until day 34 (Mean ± SD of 10 mice per genotype). **B-H** Tumours from subcutaneous transplantation of AKP tumour organoids were collected at endpoint and FFPE sections were stained immunohistochemically for Ki67 (B), cl. Casp. 3 (C), Vimentin (D), CD4 (E), CD8 (F), FoxP3 (G) or PD-L1 (H). Expression was quantified using ImageScope software (Mean ± SD of 10 mice per genotype). Statistical analysis showed no significant differences.

In contrast to epithelial and immune cells, clear phenotypic differences could be observed between cancer-associated fibroblasts from WT and KO mice. While CAFs from WT tumours showed strong and homogeneous expression of aSMA, a fraction of fibroblasts in KO tumours displayed loss of aSMA staining together with PDGFRa expression (Figure 20 B). This effect was especially pronounced in areas with an accumulation of fibroblasts where fibroblasts in close contact to epithelial cells maintained aSMA expression while fibroblasts further away from epithelial cells stained positive for PDGFRa instead (Figure 20 A). To confirm these findings also on a transcriptomic level, bulk RNA-sequencing from KO vs WT tumours was performed. In line with histological analyses, few genes were differentially regulated between KO and WT tumours (Figure 20 C, n = 5 each). Gene set enrichment analysis (GSEA) revealed strong reduction of genes involved in actin-mediated cell contractility and increased inflammatory gene expression (Figure 20 D), confirming the fibroblast subtype changes observed upon *Zeb1* deletion *in vitro*. However, apparently these changes had no major consequences on the tumour growth and immunity of SCT models.

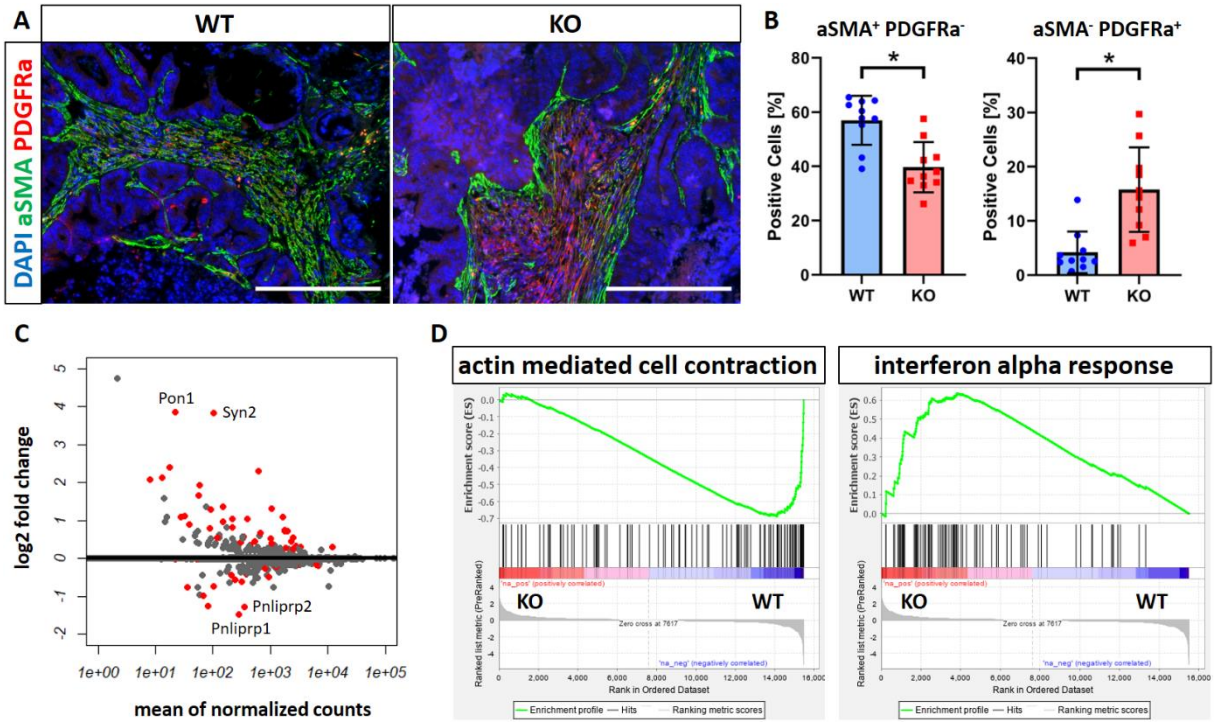

Figure 20: Stromal *Zeb1* deletion changes fibroblast subtypes in subcutaneous tumours
Tumours from subcutaneous transplantation of AKP tumour organoids into *Col1a2-CreERT2$^{+/+}$;Zeb1$^{fl/fl}$* (WT) or *Col1a2-CreERT2$^{Tg/+}$;Zeb1$^{fl/fl}$* (KO) mice were collected for analysis latest at day 55. **A** FFPE tumour sections were stained for DAPI, aSMA and PDGFRa. Scalebars represent 200 µm. **B** Fractions of aSMA^{+} PDGFRa^{-} and aSMA^{-} PDGFRa^{+} areas were determined on stained FFPE sections using Cell Profiler software (Mean ± SD of 10 tumours per genotype, * = $p < 0.05$). **C+D** Bulk RNA of 5 subcutaneous tumours per genotype was collected, sent for RNA sequencing and analysed using DESeq2 R package. **C** MA plot of shrunken differentially expressed genes of tumours from KO compared to WT mice. Red colour indicates adjusted p-Value < 0.1. Top 2 significantly up- and downregulated genes are labelled. **D** Gene set enrichment analysis based on differentially expressed genes of tumours from KO versus WT mice.

3.5 Expression of Zeb1 in fibroblasts attenuates tumour growth in an inflammation driven model of colorectal cancer

The TME of the gut plays an important role for initiation and progression and chronic inflammation is a common CRC risk factor [Grivennikov 2013]. The observation from *in vitro* and subcutaneous experiments indicated increased inflammatory signaling in fibroblasts after *Zeb1* deletion. To investigate whether this changed TME influences CRC initiation and progression, a model of inflammation driven tumourigenesis was examined in *Col6a1-Cre$^{+/+}$;Zeb1$^{fl/fl}$* (WT) or *Col6a1-Cre$^{Tg/+}$;Zeb1$^{fl/fl}$* (KO) mice. Therefore, the group of Thomas Brabletz used the AOM/DSS mouse model where mutagenic AOM treatment is combined with administration of DSS in the drinking water to induce colonic inflammation during weeks 1, 4 and 7. Tumour development was monitored by weekly endoscopy and tumours were collected after latest 16 weeks (Figure 21 A).

In KO mice, the tumour number and the tumour size were increased compared to WT mice (Figure 21 B). Histological analysis revealed increased proliferation and reduced apoptosis in tumours of KO mice (Figure 21 C). In addition, increased infiltration of CD4 T cells and B cells into tumours of KO mice was observed. This was accompanied by enhanced expression of the immuno-regulatory marker PD-L1 and the marker of regulatory T cells FoxP3, indicating an inflammatory microenvironment and upregulation of tumour escape mechanisms to prevent anti-tumour immune responses (Figure 21 D).

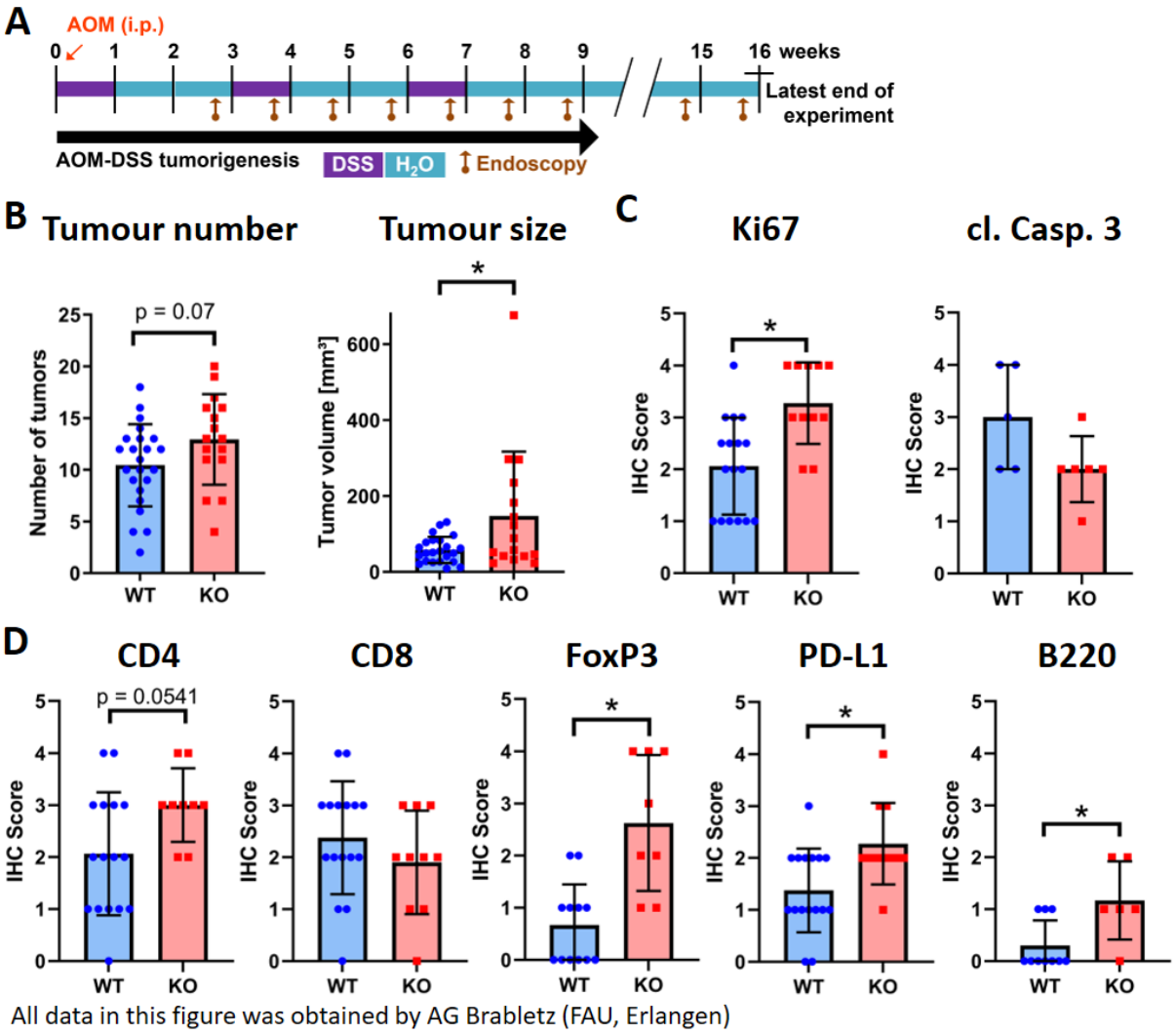

Figure 21: Stromal *Zeb1* deletion enhances tumour growth in inflammatory CRC model
A *Col6a1-Cre$^{+/+}$;Zeb1$^{fl/fl}$* (WT) or *Col6a1-Cre$^{Tg/+}$;Zeb1$^{fl/fl}$* (KO) mice were injected with AOM intraperitoneally to induce mutagenesis. In week 1, 4 and 7 after AOM treatment, mice were fed with DSS in the water. Tumour progression was monitored by weekly endoscopy and tissues were collected for analysis after 16 weeks (latest). **B** The number of tumours per mouse (**left**) and the size of the tumours (**right**) were analysed on histological sections (Mean ± SD of ≥ 16 tumours per genotype, * = $p < 0.05$). **C+D** FFPE sections of primary tumours were stained immunohistochemically and positive cells were scored based on visual inspection (Mean ± SD of ≥ 8 tumours per genotype, * = $p < 0.05$). All data in this figure was obtained by the group of Thomas Brabletz (FAU, Erlangen).

3.6 Stromal Zeb1 promotes metastasis in an orthotopic model of CRC

Subcutaneous transplantations can only partially reflect the situation in human patients. This is due to reduced immuno-surveillance of the skin and differences in the tissue architecture compared to the intestine. To examine the role of Zeb1 in the context of sporadic cancer development in a more clinically relevant model, an orthotopic transplantation of organoids was established [Fumagalli et al. 2017]. For this model, tumour organoids were dissociated into small fragments and seeded in collagen gels. After two days of recovery, the collagen gels were transplanted beneath the outer muscle layer of the mouse caecum (Figure 22 A). This resulted in macroscopic primary tumours after five to seven weeks together with spontaneous metastasis in a fraction of mice (Figure 22 B).

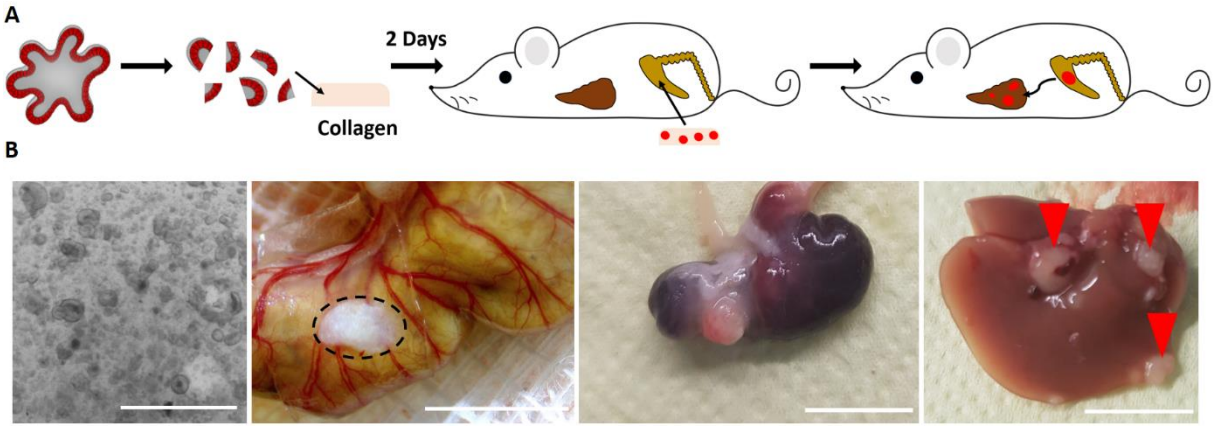

Figure 22: An orthotopic transplantation model for colorectal cancer metastasis
A Orthotopic transplantation of mouse colon tumour organoids. Organoids were cultured for 5 days in Matrigel®, dissociated into fragments and seeded in collagen gels. Organoid fragments were allowed to recover in collagen for 2 days and transplanted into the caecum of immunocompetent mice. After 5 - 6 weeks mice developed metastases in liver and lungs. **B** Exemplary images of orthotopic mouse model: Collagen drop containing AKP tumour organoids (**left**). Collagen gel below outer muscle layer of the caecum during transplantation process (**middle left,** transplant outlined). Primary tumour in the caecum (**middle right**) or liver metastases (**right**) 6 weeks after orthotopic transplantation of AKP mouse colon tumour organoids. Scalebars represents 1 mm for microscopic image of organoids in collagen (left), 5 mm for image of freshly transplanted collagen pad (middle left) and 1 cm for endpoint pictures (middle right & right).

Similar to SCT, tumour organoids were transplanted into *Col1a2-CreERT2*$^{+/+}$*;Zeb1*$^{fl/fl}$ (WT) and *Col1a2-CreERT2*$^{Tg/+}$*;Zeb1*$^{fl/fl}$ (KO) mice and fibroblast specific deletion of *Zeb1* was induced by tamoxifen diet. Deletion was induced starting from day 20 after transplantation to allow for undisturbed initial engraftment of the transplants (Figure 23 A). After seven weeks, mice were sacrificed and tissues were collected for analysis. Successful recombination of stromal *Zeb1* was confirmed by immunofluorescence staining of primary tumour sections (Figure 23 B) and automated quantification revealed loss of Zeb1 expression in the majority of stromal cells (Figure 23 C). Primary tumour growth was monitored by palpation and stromal deletion of *Zeb1* did not result in changes in tumour free survival of the mice (Figure 23 D). Tumour engraftment and size of primary tumours at endpoint were also similar between WT and KO mice (Figure 23 E).

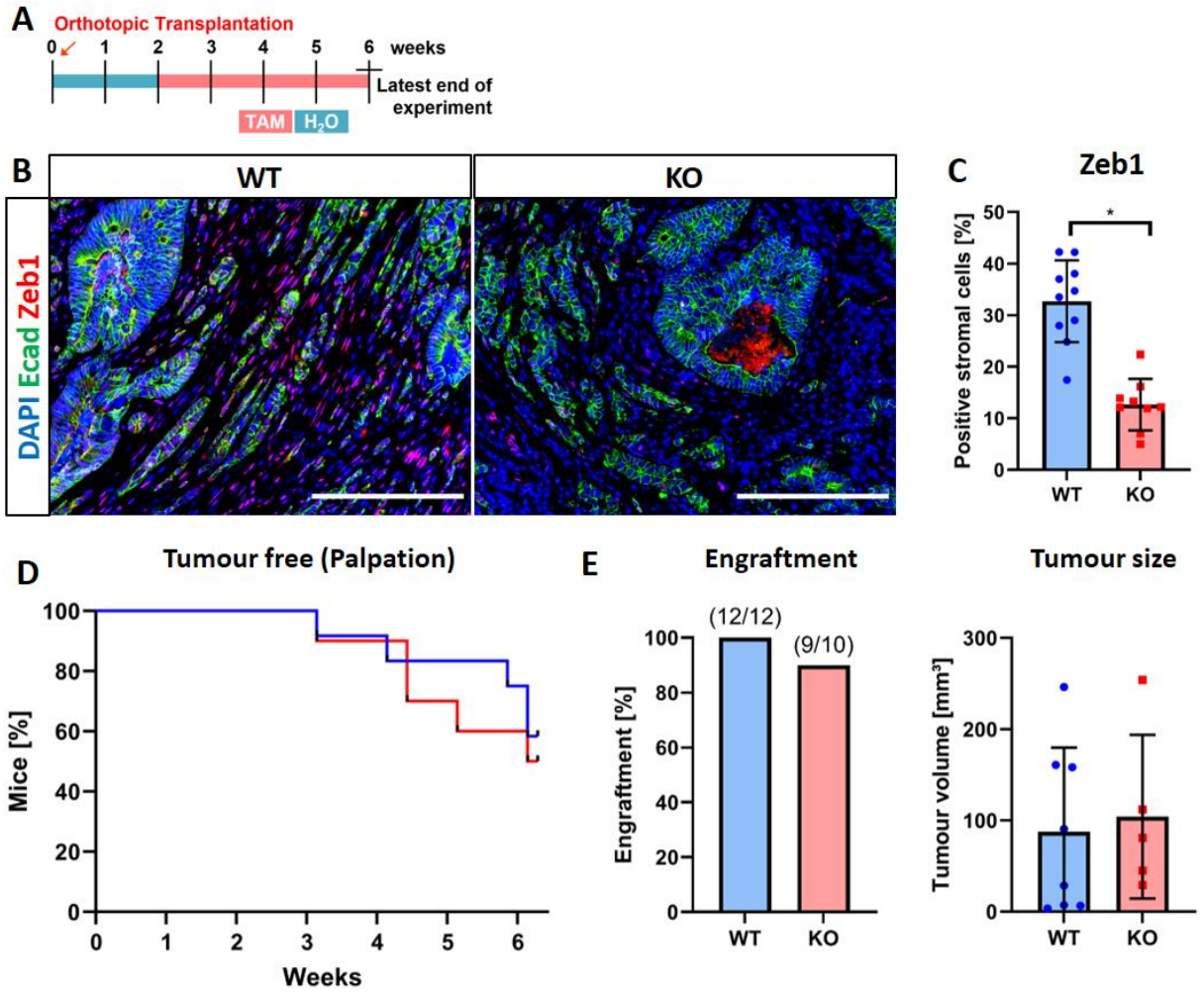

Figure 23: Primary tumour growth is not affected by stromal loss of Zeb1

A Mouse AKP tumour organoids were transplanted orthotopically into *Col1a2-CreERT2$^{+/+}$;Zeb1$^{fl/fl}$* (WT) or *Col1a2-CreERT2$^{Tg/+}$;Zeb1$^{fl/fl}$* (KO) mice. Starting from day 20 after orthotopic transplantation, mice were fed with tamoxifen diet. All mice were sacrificed after 6 weeks (latest) and tissues were collected for analysis. **B** FFPE sections of orthotopic tumours were stained for DAPI, E-cadherin and Zeb1. Scalebars represent 200 µm. **C** Non-necrotic, E-cadherin negative areas were considered stromal areas and Zeb1 expression in these areas was quantified using Cell Profiler software (Mean ± SD of ≥ 9 tumours per genotype, * = $p < 0.05$). **D** Mice were monitored by palpation and were considered tumour free, if no tumour could be detected. **E** Engraftment rate of primary tumours was determined at endpoint (**left**, numbers above bars indicate absolute number of mice) and the size of the primary tumours was estimated based on serial histological sections of the tumours (**right**, Mean ± SD of ≥ 5 tumours per genotype). 4 Tumours per genotype were excluded from size estimation because no serial histology was available.

Next, histological analysis of primary tumours was performed. Similar to subcutaneous tumours, general morphology did not differ between WT and KO tumours (Figure 24 A top). Proliferation (Ki67$^+$ cells) and apoptosis (cl. Caspase 3$^+$ areas) were unchanged (Figure 24 B). Again, a shift in fibroblast subtype markers was observed from aSMA expressing fibroblasts in WT tumours to PDGFRa expressing fibroblasts in KO tumours (Figure 24 C). In addition, orthotopic tumours displayed no significant changes of the immune microenvironment (Figure 24 D).

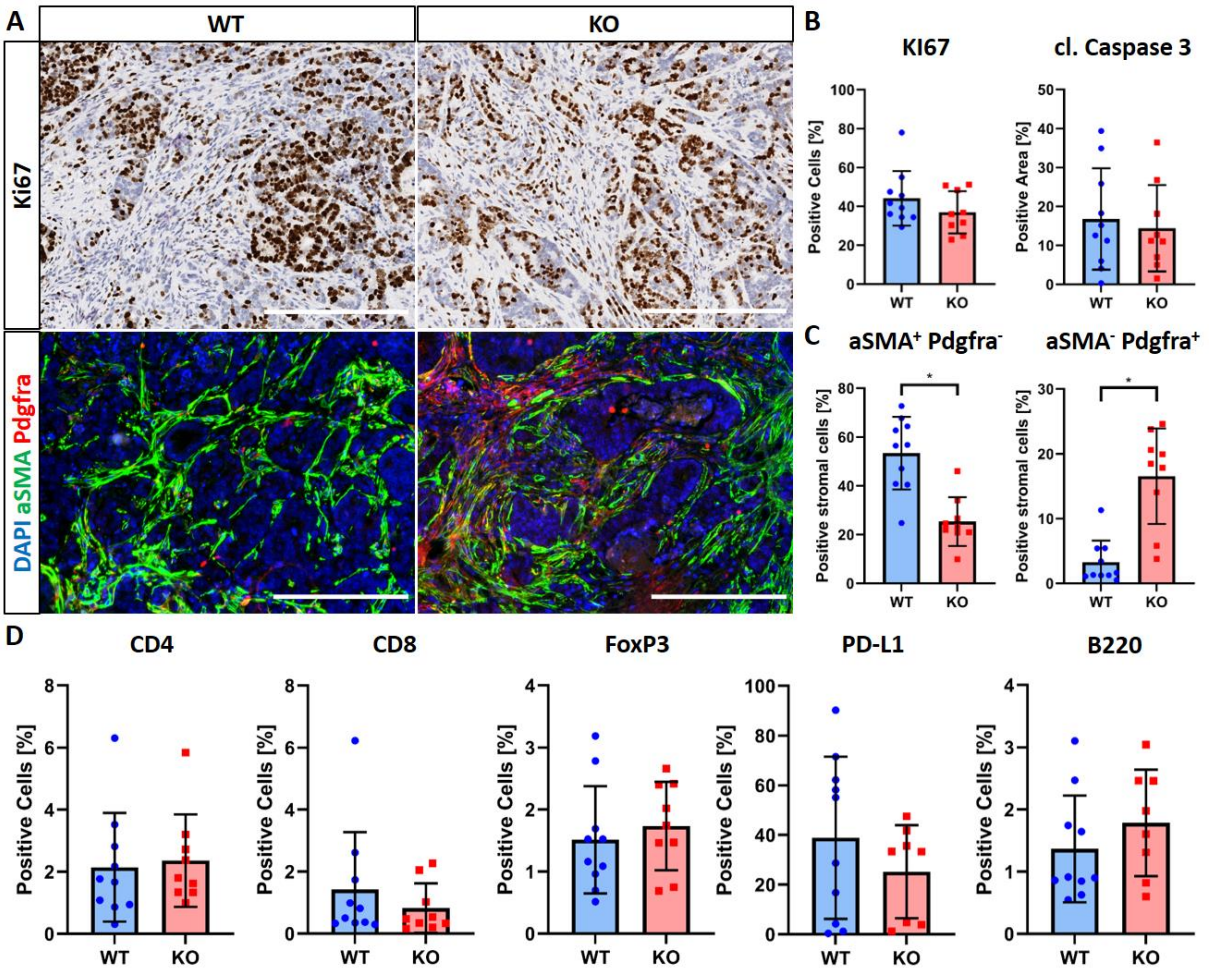

Figure 24: Deletion of stromal *Zeb1* affects fibroblast subtypes in orthotopic tumours

Primary tumours from AKP tumour organoids transplanted orthotopically into *Col1a2-CreERT2$^{+/+}$;Zeb1$^{fl/fl}$* (WT) or *Col1a2-CreERT2$^{Tg/+}$;Zeb1$^{fl/fl}$* (KO) mice were collected for analysis after latest 42 days. **A** FFPE sections were stained with Ki67 (**top**) or DAPI, aSMA and Pdgfra (**bottom**). Scalebars represent 400 µm for immunohistochemical and 200 µm for immunofluorescent images. **B+D** Immunohistochemically stained FFPE sections were quantified by ImageScope software (Mean ± SD of ≥ 9 tumours per genotype). **C** Fractions of aSMA$^+$ PDGFRa$^-$ and aSMA$^-$ PDGFRa$^+$ areas were determined on stained FFPE sections using Cell Profiler software (Mean ± SD of ≥ 9 tumours per genotype, * = $p < 0.05$).

After analysis of primary tumours, the liver tissues were analysed to study spontaneous metastasis after orthotopic transplantation. Despite the unchanged primary tumour growth (see Figure 23), the incidence of liver metastasis was strongly decreased from 67 % in WT animals to 22 % in KO animals. Interestingly, KO mice that contained liver metastases displayed a similar number and area of metastases as WT mice (Figure 25 A), suggesting an escape mechanism in these *Zeb1* KO animals.

Successful recombination of *Zeb1* in fibroblasts in metastases was also observed in the liver by immunofluorescence analysis (Figure 25 B). Tissue infiltration of T and B cells was quantified in the whole liver of WT and KO animals. While a slight increase in the number of B cells was found in the livers of KO mice, no differences between the two genotypes could be observed for the number of CD4$^+$ or CD8$^+$ T cells (Figure 25 C). Metastases were histologically unchanged upon stromal loss of Zeb1

(Figure 25 D). Interestingly, accumulations of CD4 T cells were found around metastases of WT animals (Figure 25 D, red arrows) but not of KO animals.

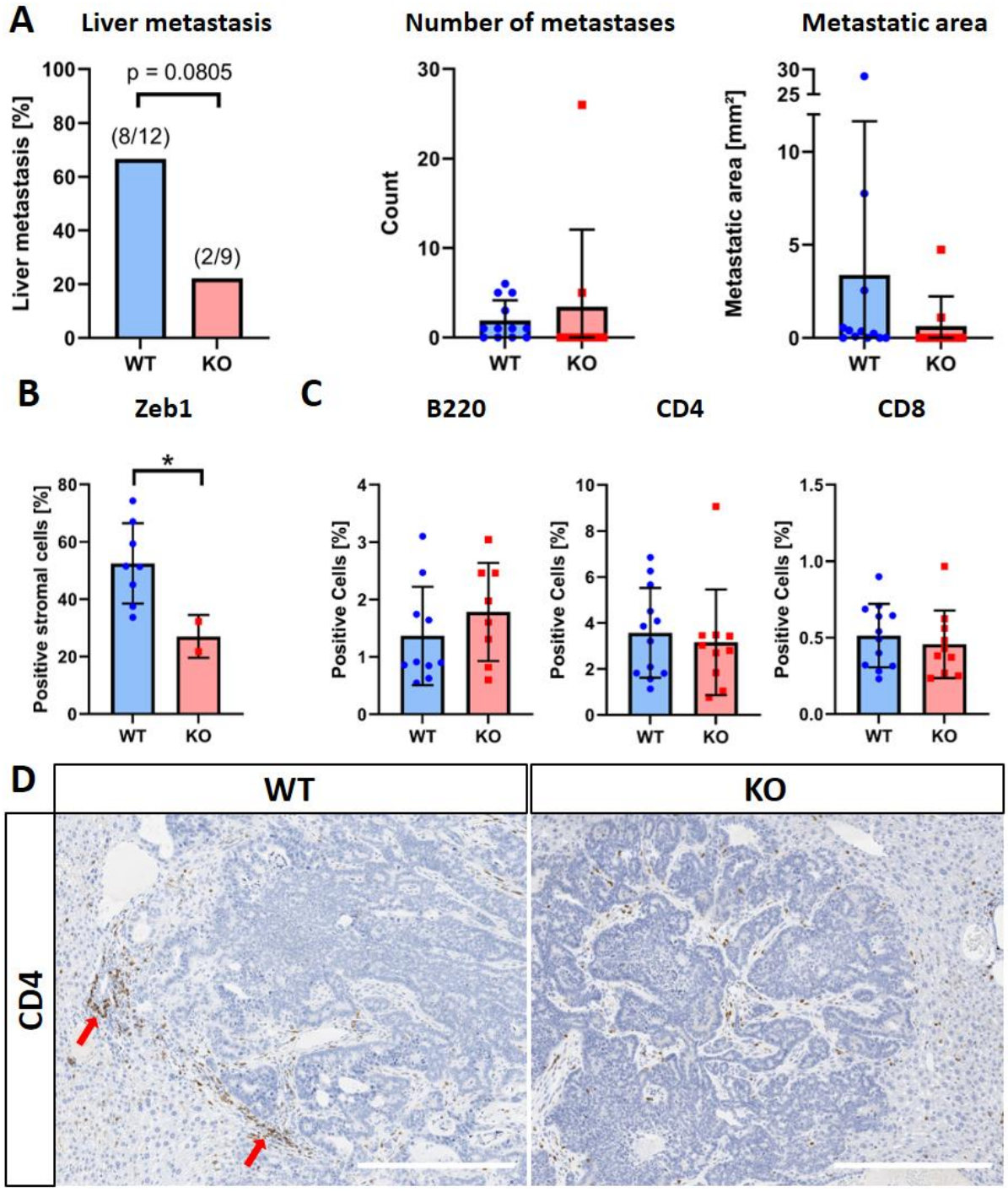

Figure 25: Liver metastasis is reduced after deletion of *Zeb1* in fibroblasts

Livers from *Col1a2-CreERT2$^{+/+}$;Zeb1$^{fl/fl}$* (WT) or *Col1a2-CreERT2$^{Tg/+}$;Zeb1$^{fl/fl}$* (KO) mice after orthotopic transplantation of AKP tumour organoids were collected for analysis after latest 42 days. **A** The number of mice with liver metastasis (**left**, numbers above bars indicate absolute numbers of mice, p-Value from Fisher's exact test), the number of liver metastases per mouse (**middle**) and the sum of the metastatic area per mouse (**right**) were analysed using serial sections of the livers. Number and area of metastases were not significant due to high variability between mice. **B** FFPE sections of the livers containing metastases were stained for DAPI, E-cadherin and Zeb1. Non-liver and E-cadherin negative areas were considered stromal areas and Zeb1 expression in these areas was quantified using Cell Profiler software (Mean ± SD of 8 WT and 2 KO mice, * = $p < 0.05$). **C** FFPE sections of the whole livers were stained immunohistochemically and analysed using ImageScope software (Mean ± SD of ≥ 8 mice per genotype). **D** Representative images of FFPE sections containing liver metastases stained for CD4. Red arrows indicate areas with accumulation of immune cells. Scalebars represent 400 µm.

For more insights into the effects of stromal *Zeb1* deletion, primary orthotopic tumours were analysed by single cell RNA-sequencing. Therefore, four tumours from WT mice and four tumours from KO mice were digested into single cells and sorted by flow cytometry. For each tumour, 80 EpCAM$^+$ epithelial cells, 148 CD45$^+$ immune cells and 148 CD45$^-$, EpCAM$^-$, CD31$^-$ fibroblasts were sorted and sent for RNA-sequencing following the SORT-seq protocol (Figure 26 A) [Muraro et al. 2016]. Sequencing data was filtered based on specific rules for each cell type (see methods) and 1285 cells passed filtering. Unbiased transcriptomic clustering of these cells resulted in 20 clusters (Figure 26 B). Every cluster consisted of similar numbers of cells from WT and KO mice (Figure 26 C).

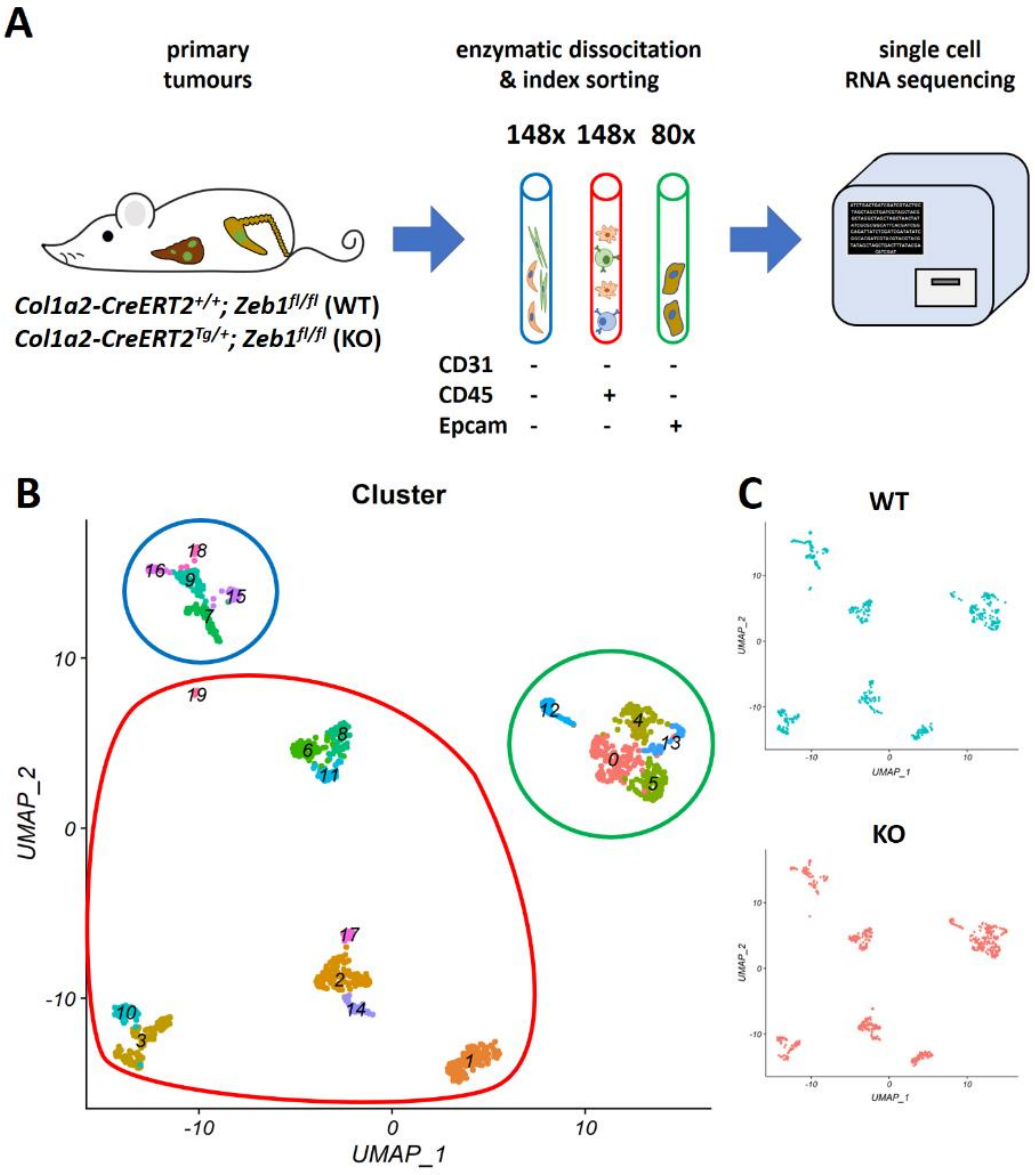

Figure 26: Single cell RNA sequencing of orthotopic tumours after *Zeb1* deletion in CAFs
Four primary tumours of *Col1a2-CreERT2$^{+/+}$;Zeb1$^{fl/fl}$* (WT) or *Col1a2-CreERT2$^{Tg/+}$;Zeb1$^{fl/fl}$* (KO) mice after orthotopic transplantation of AKP tumour organoids were collected for analysis after 42 days. **A** Tumours were dissociated enzymatically into single cells. Epithelial and immune cells were enriched by positive selection for Epcam and CD45 respectively and fibroblasts were enriched by negative selection of Epcam, CD45 and CD31. For each tumour, indicated numbers of each cell type were sorted by flow cytometry and sent for single cell RNA sequencing. **B** Reads from single cell RNA sequencing were filtered based on quality control metrics (see methods) and cells were unbiasedly clustered into 20 different clusters. C Every cluster included cells from WT (**top**) and KO (**bottom**) mice.

To confirm cell type specificity of the sorting procedure, expression of markers from index sorting were compared to transcriptomic expression of corresponding genes. Expression of CD45 (gene name *Ptprc*) was highly similar between flow cytometry and transcriptomic data and clusters 1, 2, 3, 6, 7, 10, 11, 14, 17 and 19 were assigned as immune cells according to elevated expression compared to other clusters (Figure 27 A left). Similarly, expression of Epcam was highly concordant between flow cytometry and transcriptomic data and clusters 0, 4, 5, 12 and 13 were assigned as epithelial cells (Figure 27 A right). Remaining clusters 7, 9, 15, 16, and 18 were assigned as fibroblasts lacking expression of CD45 or Epcam.

Further classification was based on marker gene expression. Cluster 1 was assigned as B cells and cluster 2 as macrophages based on expression of *Cd79b* and *Ccl9* respectively. Clusters 3 and 10 were assigned as T cells based on expression of *Cd3e* and *Ctla4*. Clusters 6, 8, 11, 14, 17 and 19 were assigned as myeloid cells based on expression of *Itgax* and *Cd14*. Fibroblast populations were further divided into subpopulations based on published marker genes [Elyada et al. 2019]. Cluster 7 was assigned as inflammatory CAFs (iCAFs, *Clec3b*$^+$, *Pdgfra*$^+$), cluster 9 was assigned as myofibroblastic CAFs (myCAFs, *Tnc*$^+$, *Tagln*$^+$) and cluster 15 was assigned as antigen presenting CAFs (apCAFs, *Saa3*$^+$, *Nkain4*$^+$). Cluster 16 did express relatively high levels of myCAF marker genes, but was assigned as CAFs producing ECM fibres based on elevated expression of collagens (ECM-CAFs, *Col4a1*$^+$, *Col4a2*$^+$) [Chakravarthy et al. 2018]. Cluster 18 was related to myCAFs but could not clearly be assigned to any known subpopulation. Gene set enrichment implicated involvement of these CAFs in wound healing (data no shown) (Figure 27 B + C). Of note, while apCAFs clustered equally distant from myCAFs and iCAFs, ECM-CAFs appeared to be rather similar to myCAFs (see Figure 26).

Additionally, expression of *Zeb1* in the different cell types was analysed. Apart from all fibroblast clusters, where *Zeb1* was expressed broadly, only two immune cell clusters and one epithelial cell cluster expressed relevant levels of *Zeb1* (Figure 27 D). Expression of Zeb1 in immune cell populations could explain the residual Zeb1 signal observed in immunohistochemical stainings of recombined tumours (see Figure 18 and Figure 23).

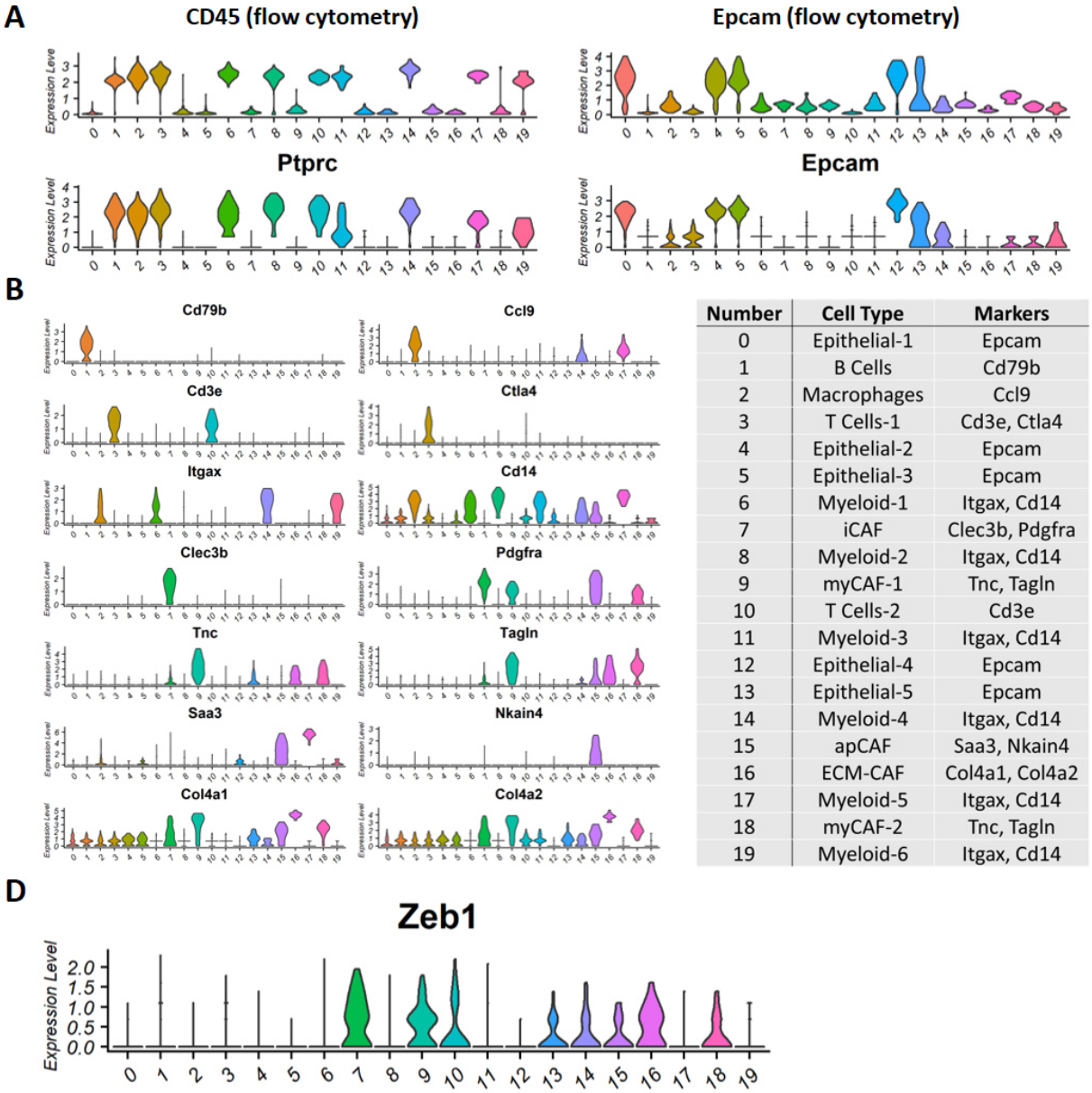

Number	Cell Type	Markers
0	Epithelial-1	Epcam
1	B Cells	Cd79b
2	Macrophages	Ccl9
3	T Cells-1	Cd3e, Ctla4
4	Epithelial-2	Epcam
5	Epithelial-3	Epcam
6	Myeloid-1	Itgax, Cd14
7	iCAF	Clec3b, Pdgfra
8	Myeloid-2	Itgax, Cd14
9	myCAF-1	Tnc, Tagln
10	T Cells-2	Cd3e
11	Myeloid-3	Itgax, Cd14
12	Epithelial-4	Epcam
13	Epithelial-5	Epcam
14	Myeloid-4	Itgax, Cd14
15	apCAF	Saa3, Nkain4
16	ECM-CAF	Col4a1, Col4a2
17	Myeloid-5	Itgax, Cd14
18	myCAF-2	Tnc, Tagln
19	Myeloid-6	Itgax, Cd14

Figure 27: Various CAF subtypes exist in orthotopic tumours
Four primary tumours of *Col1a2-CreERT2$^{+/+}$;Zeb1$^{fl/fl}$* (WT) or *Col1a2-CreERT2$^{Tg/+}$;Zeb1$^{fl/fl}$* (KO) mice after orthotopic transplantation of AKP tumour organoids were sent for single cell RNA sequencing and cells were clustered unbiasedly into 20 clusters. **A** For each cluster, expression of CD45 (**left**, gene name *Ptprc*) and Epcam (**right**) was compared between flow cytometry marker expression (**top**) and mRNA expression levels (**bottom**). **B** Expression of common and published cell type markers was compared between cell clusters. **C** Clusters were assigned to cell types based on marker expression. **D** Expression of *Zeb1* was compared between cell clusters.

To examine functional changes in cell populations induced by stromal loss of Zeb1, gene set enrichment analysis was performed. Therefore, signatures of CAF subtype specific functions (MSigDB, [Subramanian et al. 2005, Libezon et al. 2015]) were analysed in different fibroblast clusters. In concordance with previous findings from the *in vitro* experiments (see Figure 10 and Figure 11), signatures of the actin cytoskeleton and of the G2M checkpoint were reduced in myCAFs from KO tumours (Figure 28 A). In ECM-CAFs of KO tumours, expression of ECM related signatures was reduced and signatures related to immune cell chemotaxis were enriched instead (Figure 28 B). In apCAFs, increased expression of signatures related to antigen processing and presentation and lymphocyte

chemotaxis was observed in KO mice (Figure 28 C). In iCAFs, no relevant enrichments could be found in KO versus WT tumours (data not shown).

For immune cells, enrichment of signatures related to immune cell activation and immune activity could be observed in various clusters of tumours in stromal *Zeb1* KO mice including macrophages, B cells and T cells (Figure 28 D-F). Due to the low number of cells per cluster and the high similarity between clusters, epithelial cell clusters could not clearly be assigned to specific cell types and were not analysed in more detail.

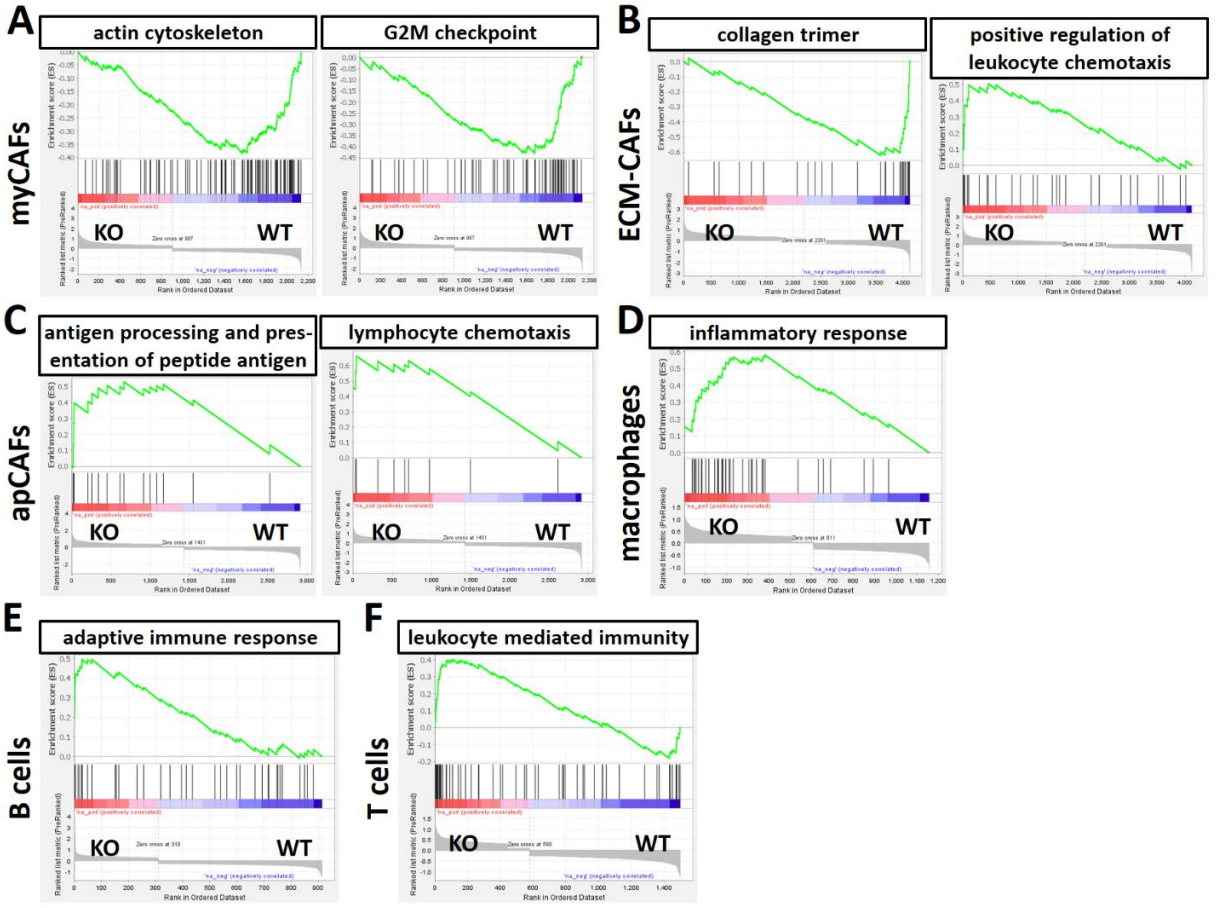

Figure 28: Stromal Zeb1 depletion induces a shift from ECM- to apCAFs and generalized immune activation

Four primary tumours of *Col1a2-CreERT2$^{+/+}$;Zeb1$^{fl/fl}$* (WT) or *Col1a2-CreERT2$^{Tg/+}$;Zeb1$^{fl/fl}$* (KO) mice after orthotopic transplantation of AKP tumour organoids were sent for single cell RNA sequencing. Fibroblast or immune cell clusters were compared between KO an WT mice. **A-C & F-H** Gene set enrichment analysis of indicated gene sets was performed for myCAFs (cluster 9, **A**), ECM-CAFs (cluster 16, **B**) or apCAFs (cluster 16, **C**) and for macrophages (cluster 2, **D**), B cells (cluster 1, **E**) or T cells (cluster 3, **F**).

In summary, loss of stromal Zeb1 in orthotopic tumours led to a shift in fibroblast subtype markers similar to the changes observed in subcutaneous tumours. Whereas primary tumour growth was not affected, stromal *Zeb1* deletion led to reduced metastasis in KO mice. Single cell sequencing identified ECM-CAFs and apCAFs as the most strongly dysregulated CAF populations and changes in diverse

immune cell populations suggesting increased anti-tumour immunity upon *Zeb1* deletion in fibroblasts may cause better control of metastasis.

3.7 Stromal *Zeb1* KO reduces tumour size in AOM/P53 Model of sporadic CRC

To address whether *Zeb1* deletion can also block tumour progression in an autochthonous model, the group of Thomas Brabletz also analysed the AOM/P53 model of sporadic colorectal cancer. In this model, repeated injections of mutagenic AOM in mice with an intestinal epithelial cell specific deletion of *P53* (*Vil-Flp*$^{Tg/+}$*;P53*$^{FRT/FRT}$) result in development of intestinal tumours after several weeks (Figure 29 A). This model was performed in mice with floxed *Zeb1* and constitutively expressing Cre under the *Col6a1* promoter (KO, *Col6a1-Cre*$^{Tg/+}$*;Zeb1*$^{fl/fl}$*;Vil-Flp*$^{Tg/+}$*;P53*$^{FRT/FRT}$) or the respective Cre-negative controls (WT, *Col6a1-Cre*$^{+/+}$*;Zeb1*$^{fl/fl}$*;Vil-Flp*$^{Tg/+}$*;P53*$^{FRT/FRT}$).

Stromal *Zeb1* deletion reduced number and size of primary tumours in the AOM/P53 model compared to WT mice (Figure 29 B). At the same time, tumours of KO mice were less invasive as revealed by clinical grading of tumour sections (Figure 29 C). Similar to the AOM/DSS model (see Figure 21), infiltration of various immune cell populations into the tumours of KO mice was increased. However, in contrast to the AOM/DSS model, upregulation of the immune regulatory molecule PD-L1 was observed in stromal instead of epithelial cells (Figure 29 D). These results indicate that CAFs influence tumour progression by modulation of the immune TME and participate in establishment of an immuno-suppressive environment.

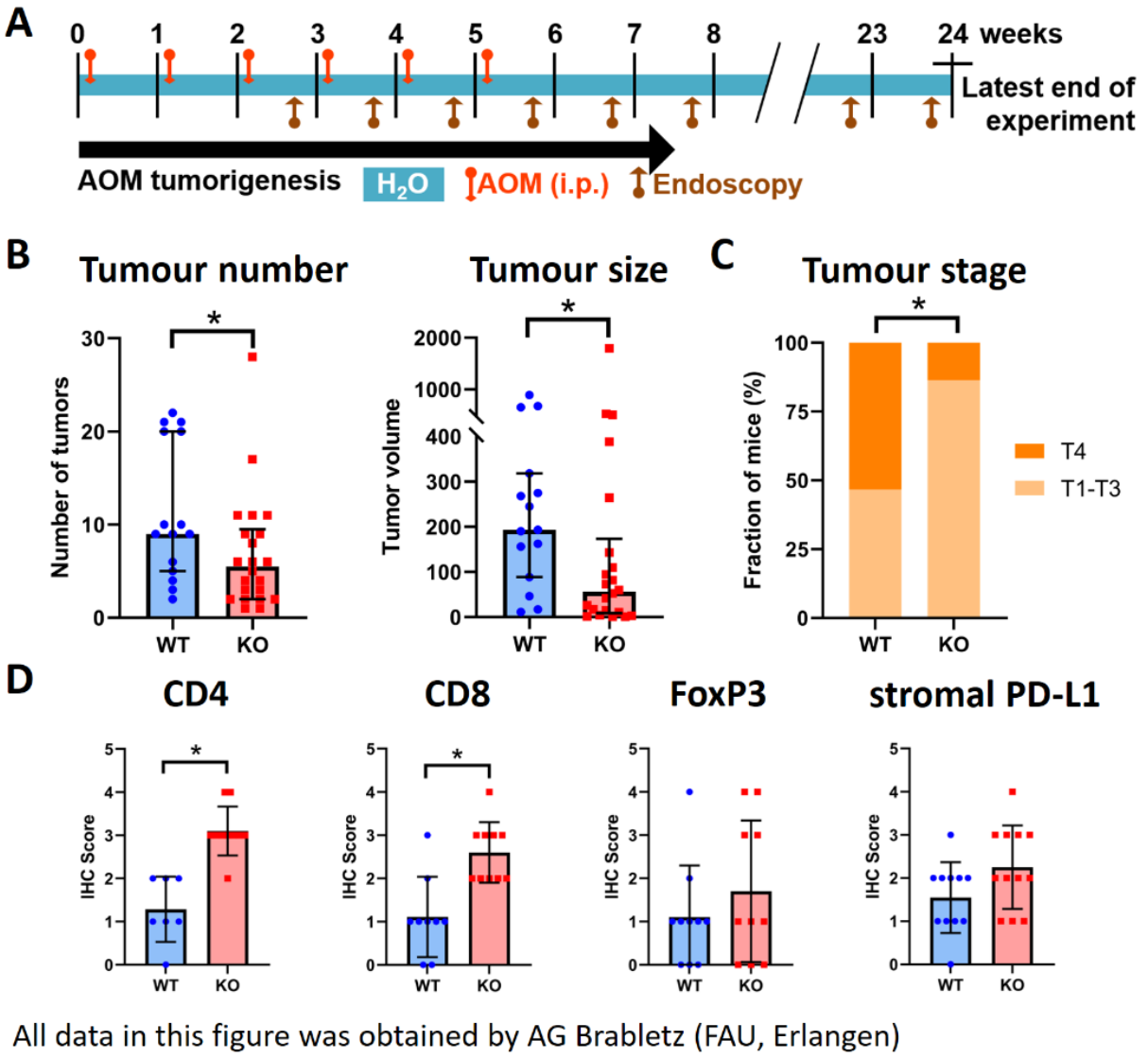

Figure 29: Loss of stromal Zeb1 reduces primary tumour size in AOM/P53 model

A *Col6a1-Cre$^{+/+}$;Vil-Flp$^{Tg/+}$;Zeb1$^{fl/fl}$;P53$^{FRT/FRT}$* (WT) or *Col6a1-Cre$^{Tg/+}$;Vil-Flp$^{Tg/+}$;Zeb1$^{fl/fl}$;P53$^{FRT/FRT}$* (KO) mice were injected weekly with AOM intraperitoneally for 6 weeks to induce mutagenesis. Tumour progression was monitored by weekly endoscopy and tissues were collected for analysis after 24 weeks (latest). **B** The number of tumours per mouse (**left**) and the size of the tumours (**right**) were analysed by histological sections (Mean ± SD of ≥ 15 tumours per genotype). **C** Tumours were graded into 4 categories (T1-3: adenoma and locally invasive carcinoma, T4: fully invasive carcinoma) based on histological sections (Fractions ≥ 10 tumours per genotype). **D** FFPE sections of primary tumours were stained immunohistochemically and percentage of positive cells was estimated by visual inspection (Mean ± SD of ≥ 7 tumours per genotype, * = $p < 0.05$). All data in this figure was obtained by the group of Thomas Brabletz (FAU, Erlangen).

3.8 *In vivo* evolution enhances immune effects of stromal *Zeb1* deletion

In both, the AOM/DSS model and the AOM/P53 model, stromal loss of Zeb showed the strongest effects related to infiltration of immune cells into the tumours (see Figure 21 and Figure 29). This could not be observed after subcutaneous and orthotopic transplantation of AKP tumour organoids (see Figure 19 and Figure 24). A key difference between the models could be the number of mutations present in the tumour cells that can induce anti-tumour immune reactions and shape the tumour-immune crosstalk. In the AOM/DSS model, injection of AOM not only leads to mutation of driver genes,

but also to random mutations without direct effects on tumour growth [Pan et al. 2017]. In the AOM/P53 model, accumulation of random mutations might be even more pronounced due to chromosomal instability caused by artificial mutation of *Tp53* and prolonged duration of the model. In the orthotopic model, CRISPR/Cas9 mediated targeted mutagenesis of organoids result in very defined alterations and absence of bystander mutations. In addition, the short duration of the transplantation model prevents accumulation of random mutations *in vivo*. To obtain transplantation models that more closely represent the situation in patients, tumour organoids were subjected to an *in vivo* evolution step.

AKP tumour organoids were transplanted orthotopically into WT FvB mice. After five weeks of tumour growth, mice were sacrificed and new organoid lines (termed AKP*) were established from primary tumours. Polyclonal cultures of AKP* tumour organoids were then transplanted orthotopically into conditional KO mice to examine effects of stromal Zeb1 (Figure 30 A). Mice received tamoxifen diet from day four to ensure complete *Zeb1* recombination and tissues were collected for analysis latest 34 days after transplantation (Figure 30 B).

Similar to AKP tumours (compare Figure 23), stromal loss of Zeb1 in AKP* tumours did not affect engraftment rate, primary tumour size or tumour free survival (Figure 30 C + D). In contrast to AKP tumours, AKP* tumours displayed very high levels of epithelial Zeb1 expression and stromal cells were more evenly distributed throughout the tumours, which prevented quantification of stromal Zeb1 expression levels (Figure 30 E).

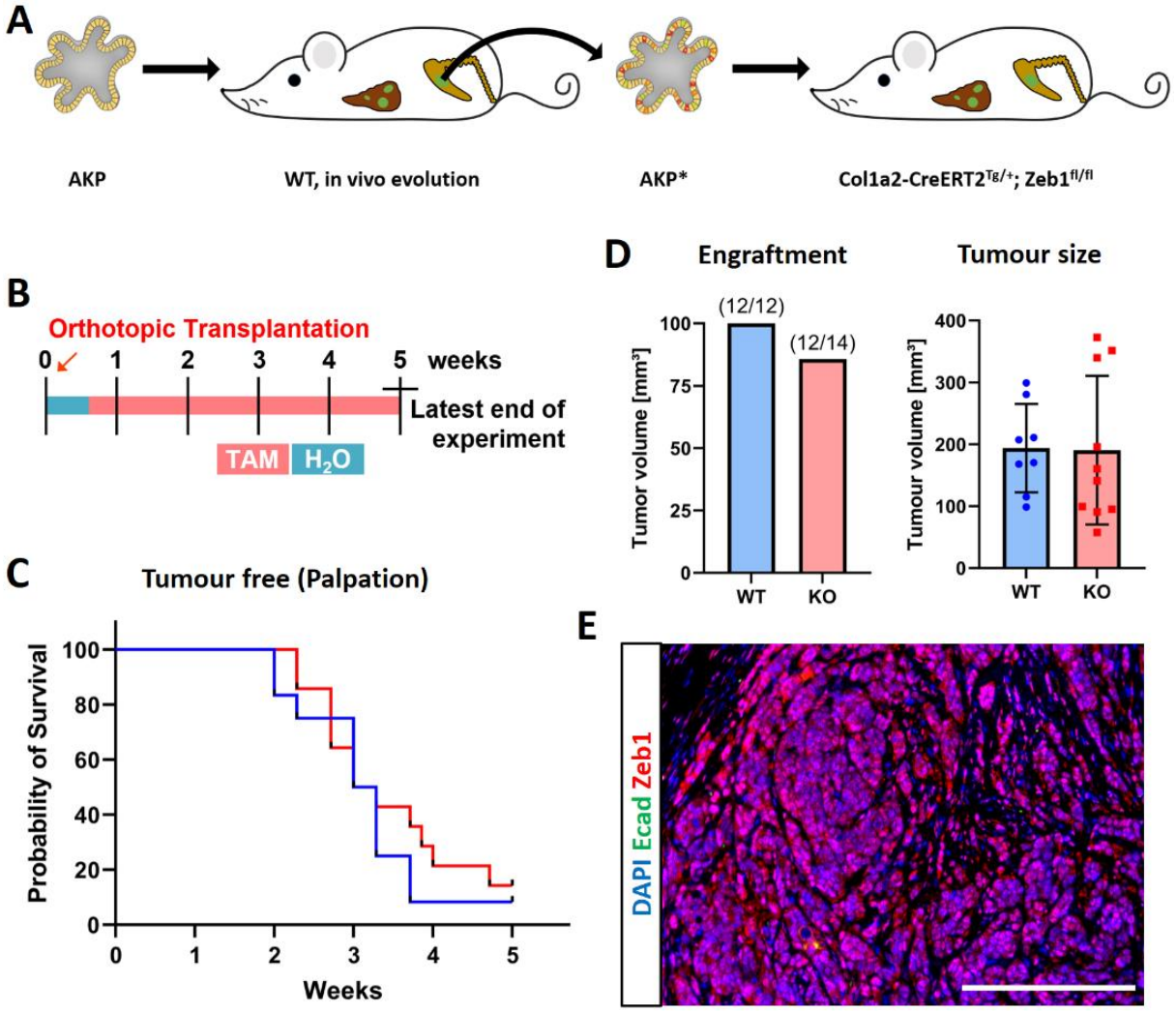

Figure 30: Organoid retransplantation to induce *in vivo* tumour evolution

A *In vivo* evolution and orthotopic retransplantation of AKP* organoids. Mouse colon organoids (AKP) were orthotopically transplanted in WT mice. After *in vivo* growth for 7 weeks, new organoid lines (AKP*) were established from primary tumours of these mice. Subsequently, AKP* organoids were orthotopically transplanted in conditional KO mice. **B** Experimental procedure of orthotopic retransplantation of AKP* mouse tumour organoids. AKP* organoids were transplanted orthotopically into *Col1a2-CreERT2$^{+/+}$;Zeb1$^{fl/fl}$* (WT) or *Col1a2-CreERT2$^{Tg/+}$;Zeb1$^{fl/fl}$* (KO) mice. Starting from day 4 after transplantation, mice were fed with tamoxifen diet. All mice were sacrificed after 35 days (latest) and tissues were collected for analysis. Mice were injected intraperitoneally with control antibodies for the ICB experiment. **C** Mice were monitored by palpation and were considered tumour free, if no tumour could be made out by touch. **D** Engraftment rate of primary tumours was determined at endpoint (**left**, numbers above bars indicate absolute number of mice) and the size of the primary tumours was estimated based on serial histological sections of the tumours (**right**, Mean ± SD of ≥ 8 tumours per genotype). For tumour size, only tumours that were collected more than 28 days after transplantation were included in this analysis. **E** FFPE sections of primary tumours were stained for DAPI, E-cadherin and Zeb1. Scalebar represents 200 µm.

Histological analysis of primary AKP* tumours revealed a decrease in Ki67 and cleaved Caspase 3 expression in KO compared to WT mice (Figure 31 A). Due to the changed morphology of AKP* tumours, devoid of larger accumulations of stromal cells, reliable quantification of stromal subtype markers was not possible (Figure 31 B). However, reduced collagen covered area and collagen intensity hinted towards the same effects as observed in AKP tumours (Figure 31 C). In contrast to AKP tumours (compare Figure 24), stromal deletion of *Zeb1* resulted in increased infiltration of immune cells

including CD8 T cells and B cells into AKP* tumours. In addition, upregulation of immune checkpoint marker PD-L1 was observed upon Zeb1 loss, indicating increased immunogenicity of tumours after retransplantation (Figure 31 D).

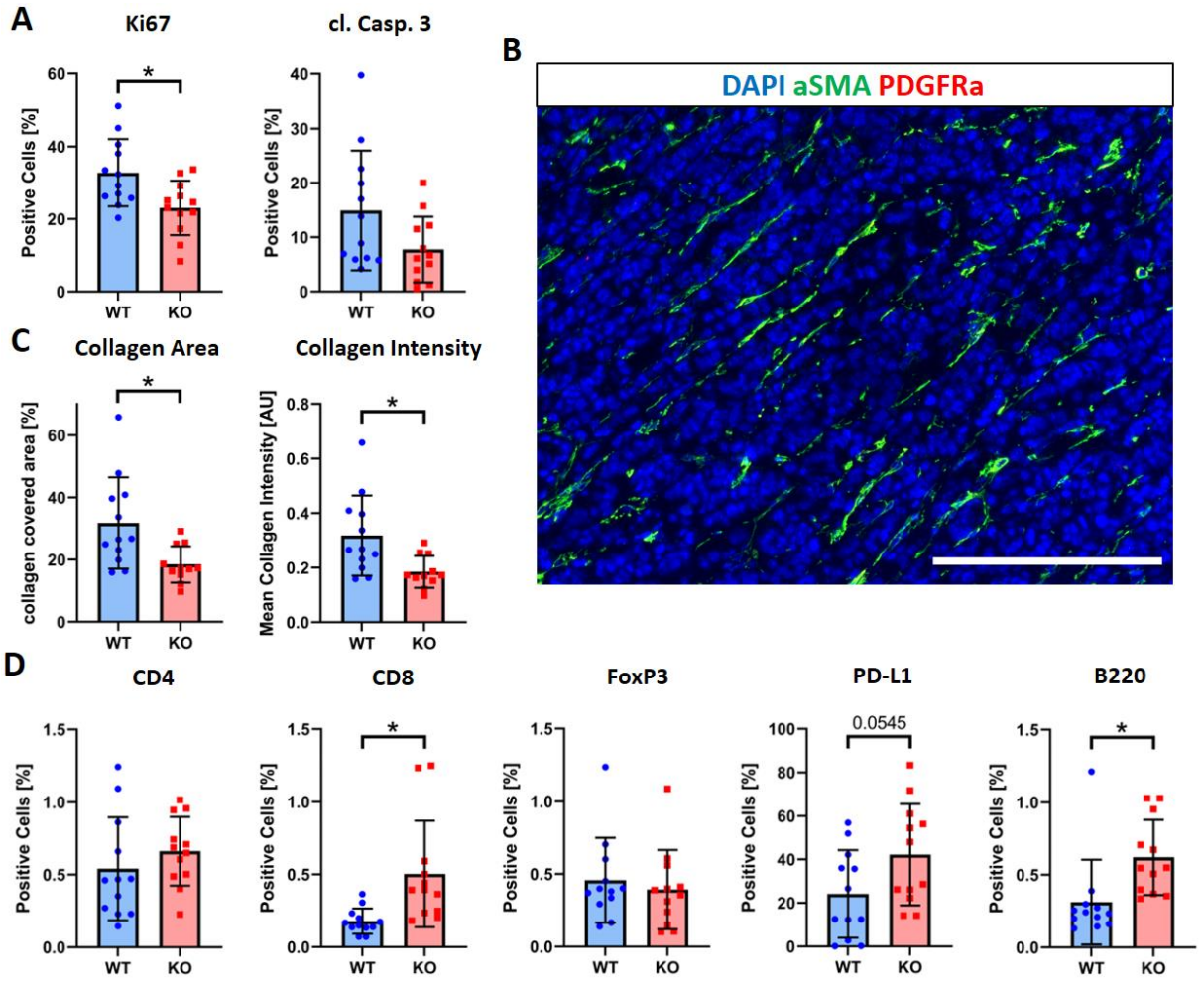

Figure 31: *In vivo* evolution enhances immune infiltration in primary orthotopic tumours
AKP* tumour organoids were transplanted orthotopically into *Col1a2-CreERT2$^{+/+}$;Zeb1$^{fl/fl}$* (WT) or *Col1a2-CreERT2$^{Tg/+}$;Zeb1$^{fl/fl}$* (KO) mice and tissues were collected at day 35 (latest) for analysis. Mice were injected intraperitoneally with control antibodies for the ICB experiment. **A+D** FFPE sections of primary tumours were stained immunohistochemically and marker expression was analysed using ImageScope software (Mean ± SD of ≥ 11 tumours per genotype, * = $p < 0.05$). **B** FFPE sections of primary tumours were stained for DAPI, aSMA and PDGFRa. Scalebar represents 200 µm. **C** FFPE sections of primary tumours were stained with Masson-Goldner-Trichrome staining. Collagen covered area (**left**) or mean collagen intensity (**right**) were analysed using cell profiler software (Mean ± SD of ≥ 11 mice per genotype).

Quantification of metastasis after orthotopic transplantation of AKP* tumour organoids revealed reduced liver metastasis in mice with stromal deletion of *Zeb1*. While all WT mice developed liver metastasis, 25 % of KO mice did not develop distant organ metastasis. In addition, the number of metastases per mouse was reduced and the size of these metastases showed a slight trend towards reduction in KO mice with only few mice displaying large metastases (Figure 32 A). While some big metastases did not show signs of anti-tumour immune activity, many others, especially small ones, were surrounded by lots of immune cells, indicating ongoing adaptive immune response (Figure 32 B

top right). These accumulations could also be found in the livers of many mice without metastatic cells in close proximity (examples shown in Figure 32 B bottom). Independent of the presence of metastases, all livers were scored according to the presence of immune cell accumulations. The number of immune cell accumulation was higher in livers of KO compared to WT mice (Figure 32 C).

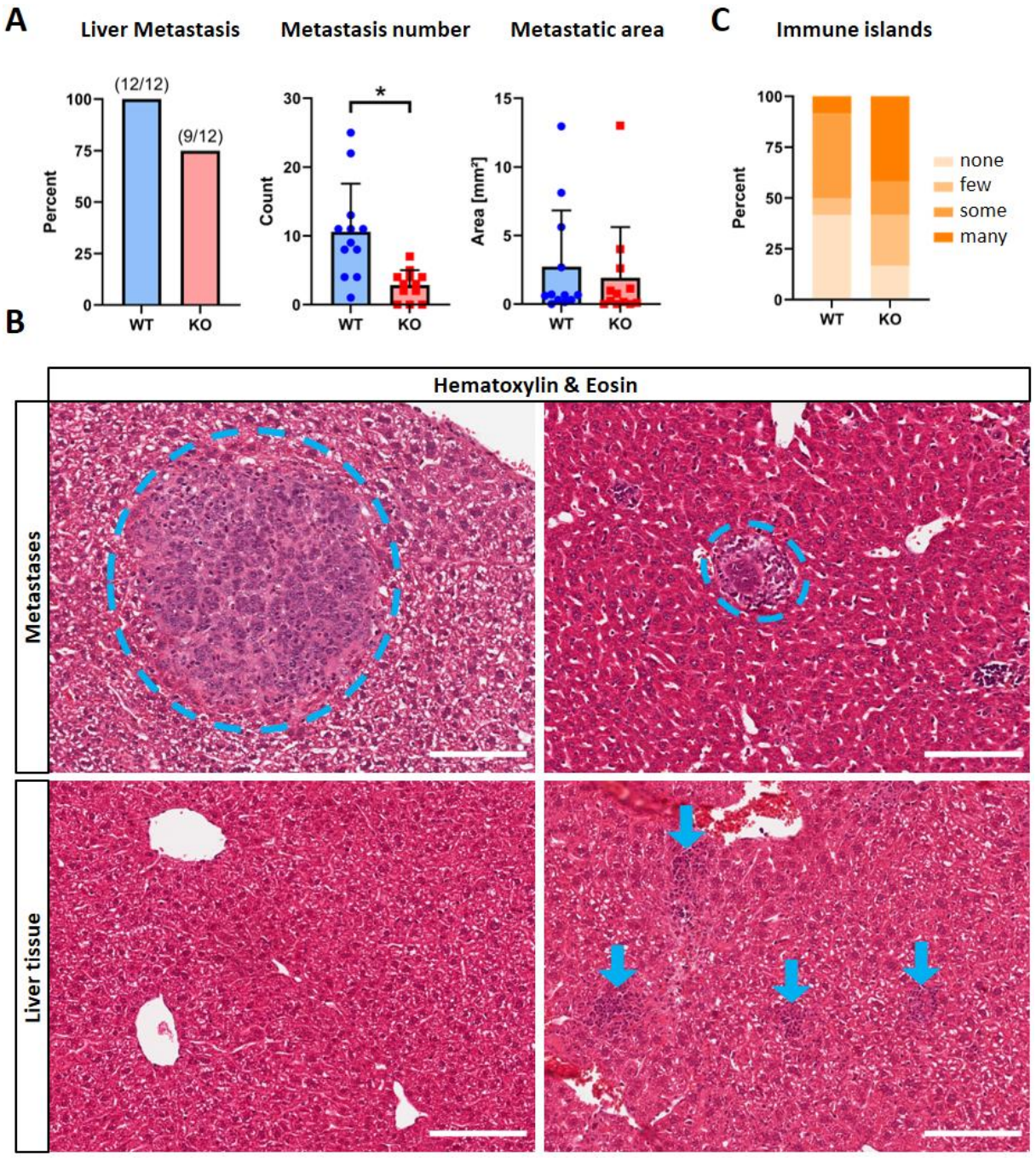

Figure 32: Liver metastases are reduced after orthotopic retransplantation

AKP* tumour organoids were transplanted orthotopically into *Col1a2-CreERT2$^{+/+}$;Zeb1$^{fl/fl}$* (WT) or *Col1a2-CreERT2$^{Tg/+}$;Zeb1$^{fl/fl}$* (KO) mice and livers were collected at day 35 (latest) for analysis. Mice were injected intraperitoneally with control antibodies for the ICB experiment. **A** The number of mice with liver metastasis (**left**, numbers above bars indicate absolute numbers of mice), the number of liver metastases per mouse (**middle**) and the sum of the metastatic area per mouse (**right**) were analysed using serial sections of the livers (* = $p < 0.05$). **B** FFPE sections of livers were stained with hematoxylin and eosin. Metastases are marked with a blue circle (**top**) and immune cell accumulations are marked with blue arrows (**bottom**). Scalebars represent 200 µm. **C** Each mouse was classified into one of four categories based on the presence of immune cell accumulations in representative slides of the liver (Means of ≥ 9 mice per genotype).

In summary, orthotopic retransplantation of AKP* tumour organoids resulted in increased immune infiltration and immune checkpoint upregulation after Zeb1 loss in CAFs. While primary tumour growth was not affected by stromal *Zeb1* deletion, liver metastasis was reduced in KO mice, matching observations from AKP tumours.

3.9 Response to immune checkpoint blockade therapy is enhanced in stromal *Zeb1* KO mice

Increased infiltration of immune cells into tumours is generally considered a sign of good prognosis in CRC. In addition, enhanced T cell recruitment is considered one of the main reasons why immune checkpoint blockade therapy works better in MSI compared to MSS tumours. To test whether this pro-inflammatory effect of stromal loss of Zeb1 could be used to enhance ICB therapy responses, orthotopic transplantation was combined with intraperitoneal injection of anti-PD-L1 antibody. Mice were fed with tamoxifen diet from day 4 after transplantation and injected intraperitoneally with ICB or control antibody once a week starting from day 14 after transplantation (Figure 33 A). While treatment with control antibody did not change tumour free survival of mice, treatment with anti-PD-L1 antibody increased median tumour free survival from 19 days in WT mice to 26 days in KO mice (Figure 33 B). This was confirmed by reduced primary tumour size in stromal *Zeb1* KO mice (Figure 33 C). Immune checkpoint inhibition did not cause further reduction of liver metastases in KO mice (data not shown). Histologically, immune checkpoint inhibition further increased infiltration of T- and B cells into tumours, indicating elevated immune activation. At the same time, expression of PD-L1 was reduced in treated mice, which might be due to a loss of survival advantage of PD-L1^{+} cells in presence of ICB antibodies or due to competition of ICB and immunohistochemical antibodies. Interestingly, increased presence of FoxP3^{+} regulatory T cells was observed in treated mice of both genotypes, indicating activation of alternative mechanisms to induce an immuno-suppressive TME (Figure 33 E).

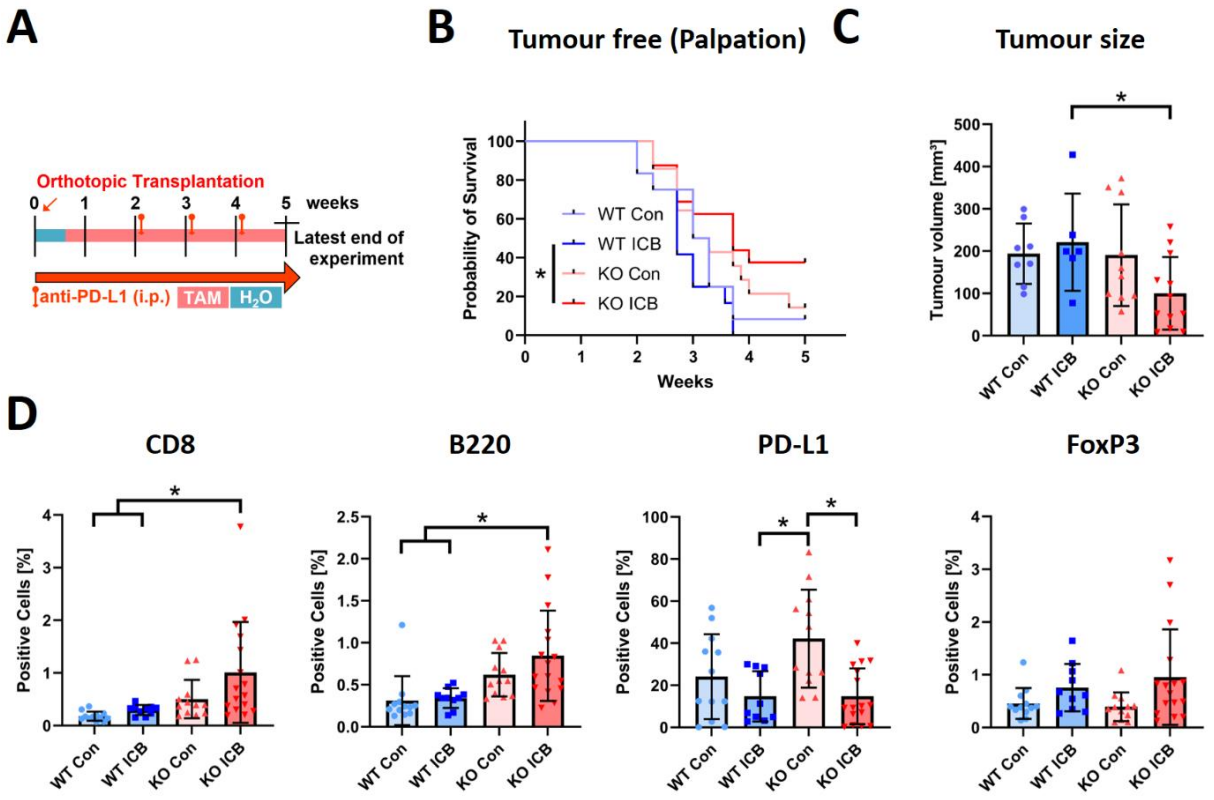

Figure 33: Response to immune checkpoint inhibition is enhanced by stromal loss of Zeb1

A Experimental procedure of orthotopic retransplantation of AKP* mouse tumour organoids with immune checkpoint inhibition. AKP* organoids were transplanted orthotopically into *Col1a2-CreERT2$^{+/+}$;Zeb1$^{fl/fl}$* (WT) or *Col1a2-CreERT2$^{Tg/+}$;Zeb1$^{fl/fl}$* (KO) mice. Starting from day 4 after transplantation, mice were fed with tamoxifen diet. Starting from day 14 after transplantation, mice were injected intraperitoneally with anti-PD-L1 antibody ('ICB') or matched non-targeting IgG control antibody ('Con') once a week. All mice were sacrificed after 35 days (latest) and tissues were collected for analysis. **B** Mice were monitored by palpation and were considered tumour free, if no tumour could be made out by touch (* = $p < 0.05$). **C** The Size of primary tumours was estimated based on serial histological sections of the tumours (Mean ± SD of ≥ 6 tumours per condition). Only tumours that were collected more than 28 days after transplantation were included in this analysis. **D** FFPE sections of primary tumours were stained immunohistochemically and marker expression was analysed using ImageScope software (Mean ± SD of ≥ 10 tumours per genotype, * = $p < 0.05$, all other conditions $p > 0.05$).

In addition to the orthotopic transplantation model, the group of Thomas Brabletz also tested inhibition of PD-L1 and CTLA-4 in the inflammation driven AOM/DSS model. Due to the slower progression of the model, the duration of treatment could be prolonged to 6 weeks, with intraperitoneal injections twice a week starting from week 10. Therapy response over time was monitored by endoscopy (Figure 34 A). While control treated mice did not show reduced tumour growth upon treatment, strong treatment responses could be observed in mice treated with ICB antibodies (Figure 34 B). This resulted in similar tumour sizes in treated and control mice, indicating that KO tumours grew faster before treatment and seized to grow during treatment (Figure 34 C).

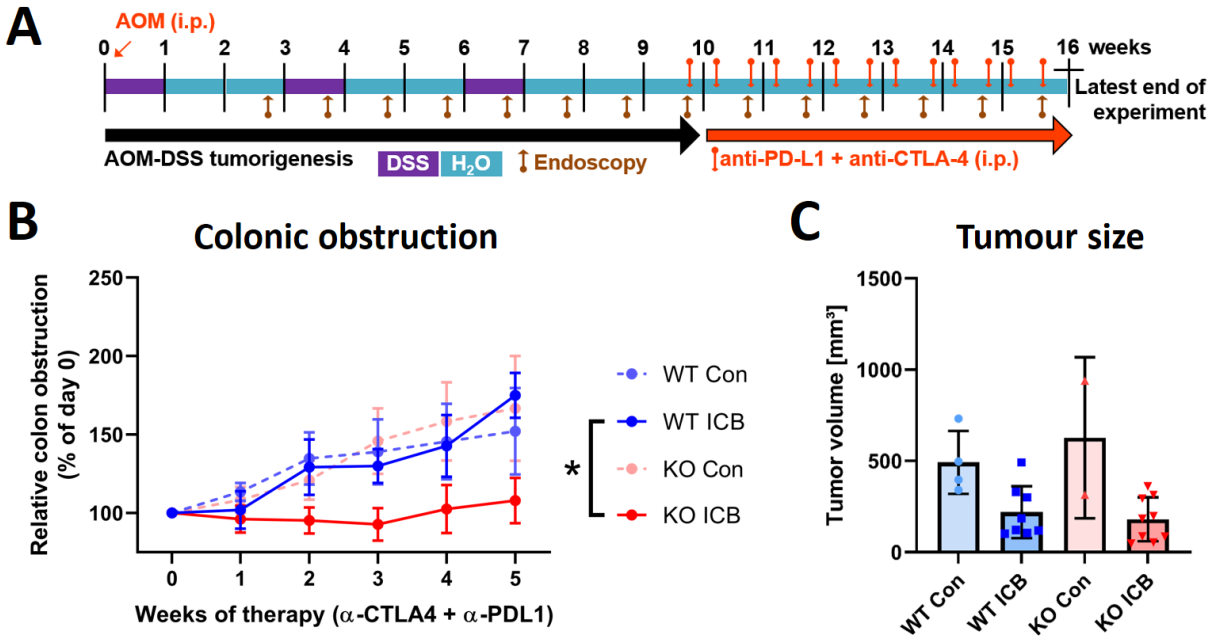

All data in this figure was collected by AG Brabletz (FAU, Erlangen)

Figure 34: Stromal *Zeb1* deletion enhances ICB response in inflammation driven tumours
A *Col6a1-Cre$^{+/+}$;Zeb1$^{fl/fl}$* (WT) or *Col6a1-Cre$^{Tg/+}$;Zeb1$^{fl/fl}$* (KO) mice were injected with AOM intraperitoneally to induce mutagenesis. In week 1, 4 and 7 after AOM treatment, mice were fed with DSS in the water. Mice were injected intraperitoneally with anti-PD-L1 and anti-CTLA-4 antibody ('ICB') or matched non-targeting IgG control antibody ('Con') twice a week. Tumour progression was monitored by weekly endoscopy and tissues were collected for analysis after 16 weeks (latest). **B** The relative colonic obstruction was monitored by endoscopy once a week (Mean ± SD of ≥ 2 control tumours & ≥ 8 experimental tumours per genotype, * = $p < 0.05$). **C** The tumour volume at endpoint was determined by analysis of histological sections (Mean ± SD of ≥ 2 control tumours & ≥ 8 experimental tumours per genotype). All data in this figure was obtained by the group of Thomas Brabletz (FAU, Erlangen).

In summary, the increased infiltration of immune cells into tumours after stromal deletion of *Zeb1* led to increased effects of immune checkpoint inhibition. This resulted in increased survival and reduced tumour size independent of the model. Modulation of Zeb1 therefore represents an attractive strategy to improve response to ICB. In the AOM/DSS model, this resulted in almost complete growth arrest from the start of the treatment while more moderate effects were obtained in the more aggressive transplantation model.

3.10 Loss of stromal Zeb1 enhances T cell activation and reduces fibroblast barrier function *in vitro*

To analyse how stromal Zeb1 modulates infiltration of immune cells into tumours and anti-tumour immune responses, an *in vitro* coculture model including T cells, tumour organoids and primary fibroblasts was established. T cell responses against tumour organoids were examined by combining transgenic T cells from *OT1* mice [Hogquist et al. 1994] with tumour organoids expressing the ova-peptide (SIINFEKL) that is specifically recognized by *OT1* T cells. Since CAFs can influence immune cells

by various mechanisms, different coculture configurations were tested to examine specific interactions between CAFs and T cells.

Isogenic (*BL6/J*) tumour organoids were transduced to express SIINFEKL peptide and Luciferase to monitor cell viability (Figure 35 A).

Transwell migration assays were performed to study T cell infiltration. Therefore, a confluent layer of fibroblasts was seeded in the bottom of the well and T cells were added inside of a transwell insert. The number of migrated T cells was determined after anti-CD45-APC antibody staining in the lower compartment after 48 hours (Figure 35 B). Enhanced attraction of T cells could be observed when fibroblasts were present in the well compared to control wells without fibroblasts. This effect was stronger with *Zeb1* KO fibroblasts compared to WT ones, although statistical significance was not reached because of heterogeneous results between fibroblast lines.

To test whether loss of Zeb1 might reduce the ability of fibroblasts to physically prevent T cell migration, a confluent layer of fibroblasts was seeded in a transwell insert with 8 µm pore size and T cells were added on top of the fibroblasts. T cells that had penetrated the layer of fibroblasts and moved to the lower compartment were quantified after 24 hours (Figure 35 C). While a layer of WT fibroblasts reduced the number of T cells in the lower compartment by 70 %, a layer of KO fibroblasts only led to a reduction of 35 %.

In addition to T cell recruitment, the killing activity of T cells in the presence of fibroblasts was examined. Tumour organoids were seeded on top of a confluent fibroblast layer representing the myCAF phenotype (Figure 35 D) or on top of fibroblasts in a layer of BME representing the iCAF phenotype (Figure 35 E). T cells were added and surviving organoids were quantified after 2 (myCAF) or 3 (iCAF) days by luciferase measurement. In both settings, no difference could be observed between killing efficiency without fibroblasts or with WT or KO fibroblasts, arguing against a strong direct influence of Zeb1 in CAFs on T cell mediated cytotoxicity.

In summary, loss of Zeb1 in fibroblasts slightly enhanced the attraction of T cells towards fibroblasts and reduced the physical hindrance of T cell migration by fibroblasts without directly affecting T cell killing activity.

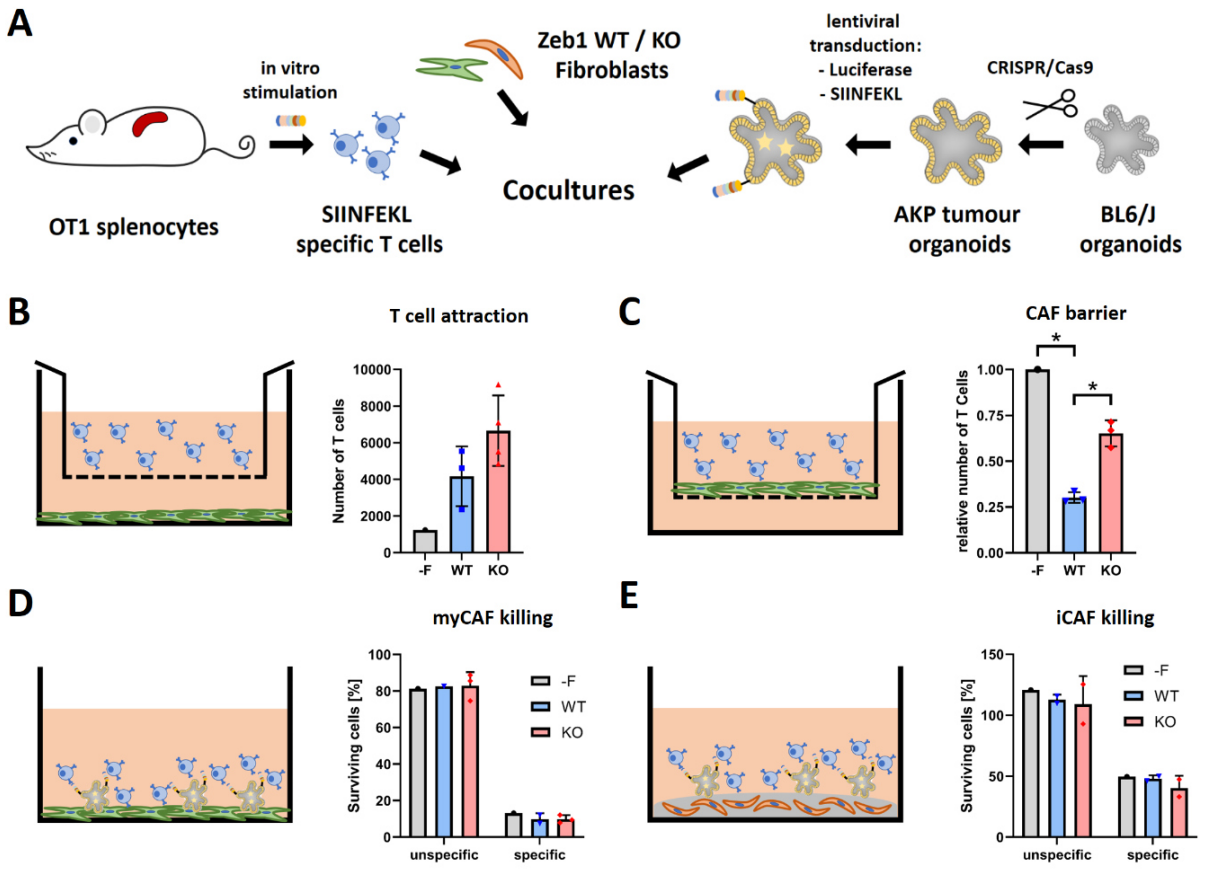

Figure 35: Stromal *Zeb1* deletion increases T cell recruitment but not cytotoxicity in coculture assays
A SIINFEKL specific T cells were obtained by *in vitro* stimulation of splenocytes from *OT1* mice. Organoids from matched BL6/J background were engineered to harbour oncogenic mutations in *Apc*, *Tp53* and *Kras* (AKP) and transduced with SIINFEKL peptide and luciferase. T cells and organoids were combined with *Zeb1* WT or KO fibroblasts in various coculture setups. **B** A confluent layer of fibroblasts was seeded. T cells were added in a transwell on top of the fibroblasts (**left**) and the number of T cells migrating to the lower compartment was quantified by microscopic imaging after 48 hours (**right**, Mean ± SD of 1-3 fibroblast lines per condition). **C** A confluent layer of fibroblasts was seeded in a transwell. T cells were added on top of the fibroblasts (**left**) and the number of T cells migrating to the lower compartment was quantified after 24 hours (**right**, Mean ± SD of 1-3 fibroblast lines per condition). **D** Tumour organoids were seeded on top of a confluent layer of fibroblasts. T cells were added 1 day after seeding of organoids (**left**) and surviving organoids were quantified by luciferase activity (**right**, Mean ± SD of 1-3 fibroblast lines per condition). **E** Fibroblasts were seeded in a layer of BME. After polymerization of BME, tumour organoids were seeded on top of this layer and T cells were added 1 day after seeding of organoids (**left**). Surviving organoids were quantified by luciferase activity (**right**, Mean ± SD of 1-3 fibroblast lines per condition). Experiments in D and E were performed with alternating cell numbers and durations and always yielded similar results.

3.11 Loss of Zeb1 has similar effects on human fibroblasts *in vitro*

Previous observations in this work have all been made in mouse models or *in vitro* using murine cells. To confirm relevance of these findings in a human setting, human primary fibroblasts were isolated from colorectal cancer biopsies and expression of *ZEB1* was reduced by transduction with short hairpin RNA (shRNA) targeting *ZEB1* or control shRNA. Following stable selection, expression of *ZEB1* was reduced by 30% (Figure 36 A). In a collagen contraction assay, this resulted in a reduction of the contracted area from 60 % with control shRNA to 38 % with *ZEB1* shRNA (Figure 36 B). In addition, immunofluorescent staining revealed changes in the aSMA expression similar to observations from murine cells. In fibroblasts expressing control shRNA, aSMA staining was concentrated in fibrillar

structures in almost every cell. In contrast, in the majority of fibroblasts expressing *ZEB1* shRNA, aSMA expression was reduced (Figure 36 C), demonstrating that ZEB1 regulates myofibroblast contractility in a conserved manner.

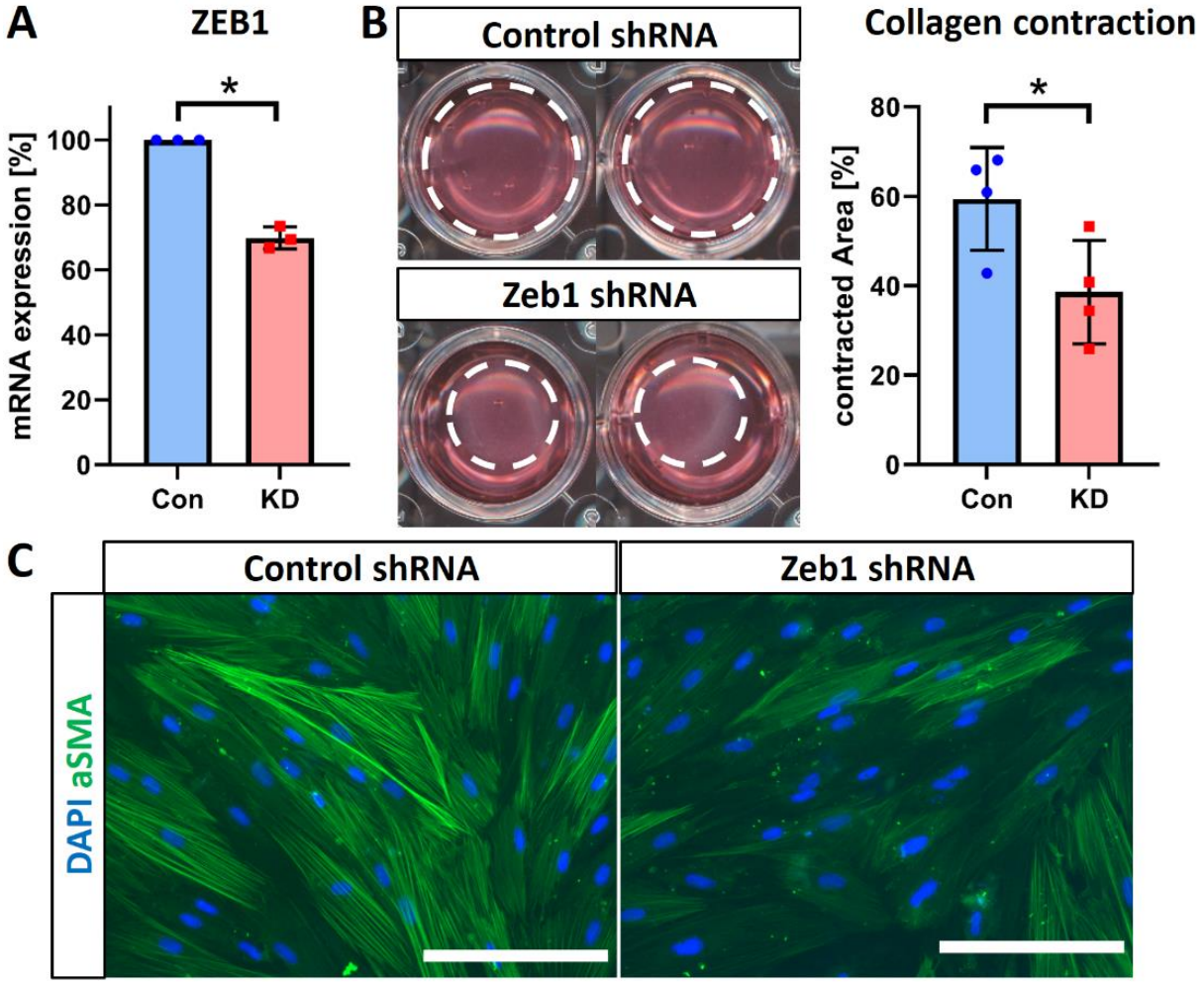

Figure 36: Knockdown of ZEB1 recapitulates effects in human fibroblasts

Human cancer-associated fibroblasts were transduced with shRNA against *ZEB1* ('KD') or untargeting control ('Con'). **A** Relative mRNA expression of *ZEB1* was determined using qRT-PCR (Mean ±SD of 3 independent fibroblast lines per condition, * = $p < 0.05$). **B** Control or KD fibroblasts were seeded in a collagen disc that was detached after polymerization. After 24 hours, the area of the collagen disc was measured (**left,** white lines). The relative contraction compared to the initial area is shown (**right**)(Mean ±SD of 4 independent fibroblast lines per condition, * = $p < 0.05$). **C** After several days in culture, fibroblasts were fixed and stained for DAPI and aSMA. Scalebars represent 200 µm.

4. Discussion

In this section, the aforementioned results will be grouped into comprehensive sections focusing on overlapping and diverging aspects between experiments and mouse models. First, direct and fibroblast-intrinsic effects of *Zeb1* recombination are discussed together with consequences for cells in close proximity. Then, these effects will be put in the context of primary tumours with special focus on the presence of fibroblast subtypes, immune cell infiltration and the model dependent effects on tumour growth. Afterwards, effects of Zeb1 loss on tumour progression are discussed regarding invasion and metastasis in the progressed mouse models and finally, possibilities and advantages of Zeb1 modulation are put in the context of clinical applications and future directions.

4.1 Zeb1 mediated myofibroblast activation is dispensable for intestinal homeostasis

Under homeostatic conditions, fibroblasts are involved in maintaining tissue architecture mainly by modulation of the ECM and secretion of growth and differentiation factors [Dang et al. 2021]. Although changes in phenotypic features of fibroblasts in mono- and coculture were observed in this work, loss of stromal Zeb1 did not affect intestinal homeostasis and colonic tissue architecture in mice (Figure 17). These observations can be grouped into two major effects: induction of quiescence and altered niche signaling. The following paragraphs try to explain where these effects might come from and why they do not translate into effects in intestinal homeostasis.

4.1.1 Induction of quiescence in fibroblasts after loss of Zeb1

Lentiviral deletion of *Zeb1* in fibroblasts resulted in a growth arrest of recombined cells, which were subsequently overgrown by non-recombined cells. However, recombination of *Zeb1* in fibroblasts using an inducible Cre recombinase resulted in homogeneously recombined and expandable fibroblast lines (Figure 10). This was likely due to the more homogeneous Cre expression in cells isolated from transgenic mice compared to the approximately 40 % of successfully transduced cells in the lentiviral approach. Due to this, growth disadvantages by recombination of *Zeb1* equally affected all cells and did not lead to overgrowth of non-recombined ones. Moreover, inflammatory responses due to viral transduction as another stress factor may have further exacerbated the growth disadvantage of recombined cells [Yan & Chen 2012]. Together, this indicated a phase of quiescence or cell cycle arrest caused by recombination of *Zeb1*. Quiescence could be caused directly by Cre toxicity [Loonstra et al. 2001], stabilization of P53 by loss of Zeb1 with associated cell cycle arrest [Lavin and Gueven 2006, Fu et al. 2019] or involvement of Zeb1 in the regulation of cell cycle checkpoints [Fouani et al. 2020]. Another possible explanation for the quiescence would be reduced activation of the fibroblasts. Two-dimensional culture of fibroblasts has been shown to induce myofibroblast activation, which can be

reversed to a quiescent state by embedding them in a softer extracellular matrix [Jesnowski 2005, Olsen et al. 2010, Huang et al. 2012, Avery et al. 2017]. In this inactivated state, fibroblasts also show slightly increased expression of inflammation markers compared to myofibroblasts [Öhlund et al. 2017, Mosa et al. 2020], which would fit with the observed transcriptional changes after acute recombination (Figure 13). Since *Zeb1* KO fibroblasts that have overcome the initial quiescence still show changes in actin expression (Figure 11) and typical myofibroblast functions (Figure 12) compared to WT fibroblasts, changes in the activation state of fibroblasts appear to represent the primary phenotype following Zeb1 loss that may induce quiescence secondarily.

Various mechanisms have been reported to result in fibroblast activation including ECM stiffness, TGFβ pathway activation and inflammatory stimuli [Sahai et al. 2020]. In addition, fibroblast plasticity was shown to be balanced by external stimuli like inflammatory IL-1 signaling and myofibroblastic TGFβ signaling [Biffi et al. 2019]. Cells can induce an inflammatory response after lentiviral transduction due to the recognition of lentiviral particles [Yan & Chen 2012]. This response was enhanced in *Zeb1* KO compared to WT fibroblasts (Figure 13), indicating that loss of Zeb1 specifically affects myofibroblastic activation and does not inhibit fibroblast activation in general. This is in line with recent studies reporting elevated expression of Zeb1 in myofibroblasts compared to other subtypes [Kinchen et al. 2018, Elyada et al. 2019]. Single cell sequencing data from this work did not confirm this observation (Figure 27), but low cell numbers of fibroblast clusters and low detection rates of *Zeb1* reads in all cells might have led to a distorted view of the actual situation. However, the modest changes of subtype markers compared to previous studies [Öhlund et al. 2017, Mosa et al. 2020] and the residual presence of myofibroblasts in mice with almost complete recombination of stromal *Zeb1* (e.g. Figure 18) indicate that other mechanisms of myofibroblast activation can compensate for the loss of Zeb1. Since Zeb1 is involved in multiple pathways that can lead to myofibroblast activation (e.g. TGFβ pathway [Postigo 2003, Joseph et al. 2014] or YAP signaling [Liu et al. 2015, Lehmann et al. 2016]) and other EMT-TFs may play partially redundant roles in CAFs, the mechanism by which loss of Zeb1 affects myofibroblast activation requires further investigation.

In vivo, most fibroblasts are thought to reside in a quiescent state until being activated by stimuli like intestinal injury, where myofibroblast contraction mediates wound closure [Rieder et al. 2007, Kalluri 2016, Dang et al. 2021]. A reduced contractility after Zeb1 loss may be sufficient to allow healing of smaller injuries.

4.1.2 Niche signaling of fibroblasts changes upon *Zeb1* recombination

Direct coculture with *Zeb1* deleted fibroblasts led to enhanced survival of primary colonic organoids after withdrawal of Wnt ligands from the medium (Figure 14). While it is commonly accepted that fibroblasts can secrete growth factors and thereby support growth of other cell types, exact secreted

molecules and marker genes that might identify responsible fibroblast populations are currently under discussion [Sahai et al. 2020]. Myofibroblasts have been reported to support intestinal growth by secretion of Wnt ligands both *in vitro* and *in vivo* [Lahar et al. 2011, Farin et al. 2012, Shoshkes-Carmel et al. 2018]. However, recently Wnt secretion was also reported for fibroblasts expressing PDGFRa [Yang et al. 2022], which is generally considered a marker of inflammatory fibroblasts [Elyada et al. 2019]. At the same time, fibroblasts have been reported to secrete hepatocyte growth factor [Pallangyo et al. 2015] or activate YAP signaling by secretion of Prostaglandin E2 [Roulis et al. 2020], which both can lead to activation of the Wnt pathway [Monga et al. 2002, Apte et al. 2006, Deng et al. 2018]. In addition, fibroblasts can secrete Wnt inhibitors to block juxtacrine Wnt signaling between epithelial cells [Nik et al. 2013, Valcz et al. 2014].

One additional consideration is the subtype plasticity of fibroblasts in direct coculture. Generally, fibroblasts in a coculture in soft extracellular matrix resemble inflammatory fibroblasts. However, close proximity to epithelial cells was shown to induce a myofibroblast phenotype [Öhlund et al. 2017, Mosa et al. 2020]. With the present information, it can be hypothesized that the recombination of *Zeb1* changes the ratio of fibroblast phenotypes in coculture and this results in altered cytokine secretion conferring Wnt independence of epithelial cells. Single cell RNA sequencing would be necessary to determine the spectrum of fibroblast phenotypes and to gain insights into their respective secretion profiles to identify responsible mediators.

Despite the observed effects in vitro, no influence on intestinal homeostasis was observed after several weeks of *Zeb1* recombination. This might again be due to differential activation states of fibroblasts in tumours compared to normal tissue. While the coculture experiments were performed with tumour organoids that efficiently activate fibroblasts, untransformed epithelial cells may not secrete the responsible mediators. Thus, the lack of homeostatic phenotypes might be explained by the resting fibroblast state. In addition, secretion of Wnt ligands by other cell types (e.g. macrophages) might regulate a sufficient level of activation in the WT [Cosin-Roger et al. 2019]. A stable activity of the Wnt pathway could be regulated by feedback mechanisms, as observed in several developmental contexts [Giráldez et al. 2002, Gerlitz & Basler 2002, Mah et al. 2016].

In summary, the data collected in this work indicates that Zeb1 is crucial for the activation of fibroblasts towards myofibroblasts. However, compensatory mechanisms allow for maintenance of myofibroblast function and tissue maintenance during intestinal homeostasis.

4.2 The TME determines the functional consequences of stromal Zeb1 loss

The effect of Zeb1 in fibroblasts on colorectal cancer was analysed using multiple mouse models of sporadic and inflammation driven tumourigenesis. Effects observed after recombination of *Zeb1* varied depending on the model, demonstrating a critical dependence on the cellular context. In this paragraph, the observations will be discussed with respect to the involvement of fibroblast subtypes, immune cells and primary cancer growth.

4.2.1 Zeb1 dependent presence of fibroblast subtypes in the TME

The most direct effects that were observed following recombination of *Zeb1* in fibroblasts were changes in the phenotype of cancer-associated fibroblasts. As already observed *in vitro* (Figure 11), fibroblasts in subcutaneous tumours displayed changes in marker expression after recombination. Both, the immunofluorescent staining for fibroblast markers and the transcriptional changes in bulk RNA sequencing indicated a shift from myofibroblasts towards more inflammatory fibroblasts (Figure 20), confirming previous observations. The pronounced effect in areas with large accumulations of fibroblasts with maintenance of myofibroblastic marker expression along the contact areas with epithelial cells confirmed the previous report of myofibroblast induction in close proximity to tumour cells [Öhlund et al. 2017].

In the AOM/DSS model, the tumour microenvironment differs significantly from models of sporadic cancers. Due to the autochthonous setting and the relatively slow development of the tumours, high numbers of fibroblasts are present in the tumour microenvironment (some examples are shown in [Tanaka et al. 2003, Meira et al. 2008, Ishikawa and Herschman 2010, Grill et al. 2018]). The abundance of fibroblasts and the resulting distance to epithelial cells may lead to a reduced induction of myofibroblast activation compared to more progressed tumours (e.g. Figure 31). In combination with the repeated administration of DSS, this promotes an enrichment of inflammatory fibroblasts in the TME of AOM/DSS tumours [Kinchen et al. 2018]. Of note, inflammatory fibroblast populations in the AOM/DSS model were found to be different from ones published in pancreatic cancer and sporadic cancer models [Öhlund et al. 2017, Elyada et al. 2019, Vega et al. 2022]. This could be caused by chronic inflammation of the tissue, resulting in adaptation of fibroblast populations, or by stage dependent changes in the TME of adenoma-like AOM/DSS tumours compared to carcinoma-like tumours of other models [Zhu et al. 2021]. Due to the low abundance of myofibroblasts and highly inflammatory nature of the tumour microenvironment, only minor changes in fibroblast subpopulations were observed in the AOM/DSS model. However, one population of myofibroblast-like fibroblasts was lost after *Zeb1* recombination (data not shown). This is in line with the hypothesis that Zeb1 is necessary for myofibroblast activation and not for fibroblast activation in general (see above).

In single cell sequencing data of orthotopic tumours from AKP organoids, fibroblast clusters from pancreatic cancers could clearly be recapitulated as described for other models of sporadic cancer [Öhlund et al. 2017, Elyada et al. 2019, Vega et al. 2022]. Differential analysis of WT and stromal *Zeb1* KO mice indicated enhanced apCAF and reduced ECM-CAF functions in KO mice (Figure 28). apCAFs expressed relatively high levels of Pdgfra (Figure 27), which is in line with the changes observed in immunofluorescent stainings of fibroblast markers in orthotopic tumours (Figure 24). In tumours from orthotopic transplantation of AKP* organoids, strong intermixing of epithelial cells and fibroblasts prevented quantification of fibroblast subtypes and a similar shift can only be hypothesized (Figure 31).

Although the tumour microenvironment in the AOM/P53 model has not been characterised extensively, initial reports indicated the induction of an inflammatory tumour microenvironment after tumour initiation due to loss of P53 [Schwitalla et al. 2013]. In this work, loss of Zeb1 in stromal cells led to a reduction of $aSMA^+$ fibroblasts (data not shown), further supporting a generalized requirement for myofibroblast formation.

In summary, coherent findings in the TME of 4 different tumour models, as well as a strong phenotype in *in vitro* cultures support the primary function of Zeb1 in the induction of a myofibroblast phenotype. Detailed analysis by single cell RNA sequencing indicated a shift towards apCAFs, which could be explained by a disturbed balance of TGFβ and IL-1 signaling [Biffi et al. 2019]. Recently, simultaneous activation of TGFβ and IL-1 signaling was shown to induce the apCAF phenotype [Huang et al. 2022]. The ablation of Zeb1 as downstream mediator of TGFβ [Postigo 2003, Joseph et al. 2014] appeared to be sufficient to prevent myofibroblast differentiation but to still allow apCAF activation in the inflammatory environment of tumours. This hypothesis could not be confirmed in the AOM/DSS model, since no apCAFs were found in these tumours. This might be due to a potential mesothelial origin of apCAFs, which might limit the presence of apCAFs to more invasive late stage tumours that come in contact with the mesothelial cell layer [Huang et al. 2022]. *In vitro*, strong myofibroblast induction by matrix stiffness and the lack of inflammatory signaling might still lead to predominant myofibroblast polarization. Differences between the models analysed in this work might be a result of varying levels of inflammatory signaling in the TME. However, it should be examined to which extent this is caused by the use of an inducible versus a constitutively active Cre in the different models (orthotopic: Col1a2-CreERT2 and AOM/DSS: Col6a1-Cre).

4.2.2 Influence on the tumour immune microenvironment

In terms of immune infiltration, two aspects have to be distinguished: base line differences between the models and the model specific influence of stromal *Zeb1* deletion.

In WT mice, tumours following subcutaneous or orthotopic transplantation of AKP tumour organoids (Figure 19, Figure 24) contained higher numbers of infiltrating immune cells compared to tumours from transplantation of AKP* tumour organoids or models including AOM exposure (Figure 21, Figure 29, Figure 31). This observation can be explained by different levels of immunogenicity, although a direct comparison between independent experiments is technically challenging due to batch differences of mice and histological stainings. While syngeneic transplants like AKP tumour organoids with FvB background transplanted into FvB mice are usually not rejected by immune cells [Trumble et al. 1993, Hwang et al. 2020], the presence of neoantigens due to *in vivo* evolution (AKP* organoids) or AOM induced mutagenesis increases immunogenicity and induces a selective pressure to escape immune responses in tumour cells [Picard et al. 2020, Marmorino et al. 2020]. In colorectal cancer, this often results in exclusion of immune cells from the tumour and thereby could explain the reduced number of infiltrating immune cells in the more immunogenic models.

While multiple phenotypes of immune evasion have been reported, immune cell exclusion or immune deserted phenotypes are often observed in colorectal cancer [Picard et al. 2020, Marmorino et al. 2020]. Although some reports indicate a direct involvement of epithelial cells [Spranger & Gajewski 2016], accumulating evidence hints towards a prominent role of CAFs in this process [Cohen et al. 2017, Zheng et al. 2021]. Especially TGFβ signaling was found to be essential for the exclusion of immune cells from different tumour entities [Tauriello et al. 2018, Mariathasan et al. 2018]. In this work, specific deletion of *Zeb1* in fibroblasts resulted in increased infiltration of immune cells into immune-evasive mutagenic tumours (AOM/DSS Figure 21, AOM/P53 Figure 29, AKP* orthotopic Figure 31). Of note, infiltration patterns varied between the different models with a characteristic increase of FoxP3 regulatory T cells in tumours of the AOM/DSS model [Vega et al. 2022]. However, all immunogenic models displayed increased infiltration of B cells and at least one T cell population together with upregulation of immune checkpoint molecules, demonstrating activation of an adaptive immune response. Together with the previously discussed role of Zeb1 in the induction of a myofibroblast phenotype, this hints towards differential roles of fibroblast subtypes in the regulation of immune infiltration. Inflammatory fibroblast subtypes are characterized by secretion of immune-modulatory cytokines, of which many play a role in immune cell chemotaxis and might be responsible for increased infiltration of immune cells after inhibition of myofibroblast activation [Sahai et al. 2020, Biffi & Tuveson 2021]. At the same time, extracellular matrix signatures have been found to correlate with immune cell infiltration [Salmon et al. 2012, Hartmann et al. 2014, Chakravarty et al. 2018, Qi et al. 2022]. With multiple studies reporting prominent involvement of myofibroblasts in the production and reorganization of ECM [Kinchen et al. 2018, Grauel et al. 2020, Biffi & Tuveson 2021, Feldmann et al. 2021], this might indicate an immuno-exclusive function of ECM producing myofibroblasts. Consistent with previous studies reporting a correlation between expression of Zeb1 and ECM

deposition in fibroblasts [Kinchen et al. 2018, Fu et al. 2019], reduced enrichment of ECM signatures was observed in *Zeb1* deleted fibroblasts of orthotopic AKP tumours (Figure 28). This was confirmed on protein level in the orthotopic model (Figure 31). Of note, mice in the AKP* model were fed with Tamoxifen diet 10 days earlier than mice in the AKP model. Since organoids were transplanted without fibroblasts and in an artificial collagen matrix, these initial days of fibroblast recruitment and matrix remodelling might be responsible for the difference compared to orthotopic AKP tumours, where collagen reduction was less prominent. The differences in barrier function observed in OT1 T cell cocultures (Figure 35) also pointed towards an involvement of the ECM. However, in this experimental setup ECM-related effects could not be discriminated from intercellular effects caused by changes in cell-cell adhesion or cell morphology. Additionally, the increased attraction of T cells towards Zeb1 depleted fibroblasts (Figure 35) hinted towards mixed effects of reduced barrier function and increased chemotaxis in tumours.

Overall, modulation of fibroblast phenotypes by recombination of *Zeb1* reduced the immuno-exclusive properties of CAFs, leading to an increased infiltration of immune cells into immunogenic tumours and consequent upregulation of immune checkpoint molecules in these models.

4.2.3 Context specific role for primary tumour growth

As discussed above, loss of Zeb1 resulted in very limited effects in the immuno-microenvironment of tumours from subcutaneous or orthotopic transplantation of AKP tumour organoids. Consequently, no differences in anti-tumour immune response or immune-checkpoint molecule expression were observed in these models. Direct pro- or anti-tumourigenic effects of altered fibroblast subpopulations on primary tumour growth appeared to balance each other out [Biffi & Tuveson 2021, Wang et al. 2021a], resulting in similar primary tumour sizes in both genotypes (Figure 19, Figure 23).

In the AOM/DSS model, deletion of stromal *Zeb1* resulted in a more inflammatory TME and increased immune infiltration. As in previous studies, the resulting pro-inflammatory microenvironment resulted in increased primary tumour sizes (Figure 21) [Hu et al. 2010, Shukla et al. 2016, Jin et al. 2020, Vega et al. 2022]. To avoid anti-tumour immune responses, simultaneous upregulation of immune checkpoint molecules (PD-L1, CTLA-4) was observed, consistent with observations of previous reports [Yassin et al. 2019, Mager et al. 2020, Kang et al. 2021].

Although depletion of stromal Zeb1 resulted in increased infiltration of immune cells into tumours from orthotopic transplantation of AKP* organoids, this did not affect the primary tumour size (Figure 30). While anti-tumour immune responses might have been suppressed by upregulation of immune-checkpoint molecules (Figure 31), the short duration of the model and the progressed state at the time of transplantation might also diminish effects on the tumour size.

Interestingly, in the AOM/P53 model, stromal deletion of *Zeb1* resulted in not only increased immune infiltration but also reduced primary tumour size and invasiveness (Figure 29). Generally, little is known about tumours from this model, which makes interpretation of these results more speculative. However, the difference between orthotopic transplantation of AKP* organoids and AOM/P53 model might be explained by the progression level of the model. While in the orthotopic model full-blown tumour cells are transplanted [Bürtin et al. 2020], the tumour initiating cells in the AOM/P53 model may show distinct growth characteristics. However, contrary to the AOM/DSS model, an inflammatory TME develops after tumour initiation and is not required for tumour development [Schwitalla et al. 2013]. In this early state, an increased immuno-surveillance in stromal *Zeb1* KO mice might put selective pressure on tumours to develop immune-evasion mechanisms earlier than in WT mice. This could delay tumour growth, which would explain both, the reduced size and the reduction in invasiveness of primary tumours. Contrasting this hypothesis, no increase in expression of immune-checkpoint molecule PD-L1 was observed in epithelial cells after deletion of stromal *Zeb1*. However, PD-L1 expression was elevated in stromal cells from KO mice (Figure 29). This could compensate for the lack of expression in tumour cells [Gorchs et al. 2019]. Alternatively, other mechanisms like downregulation of MHC class I molecules might be responsible for immune evasion in this model [Maleno et al. 2004, Shukla et al 2015] and a more thorough analysis of the AOM/P53 tumours should provide further insights into the mechanisms underlying the observations of this work.

In summary, deletion of stromal *Zeb1* enhanced inflammation of the TME. In the inflammation driven and immune-adapted AOM/DSS model, this accelerated tumour growth. In contrast, in immunogenic models of sporadic CRC, the increased immune infiltration required tumour cells to adapt (e.g. by upregulation of inhibitory ligands), which in the AOM/P53 model appeared to delay initial tumour growth.

4.3 Stromal Zeb1 promotes tumour cell invasion and metastasis

Mice after subcutaneous transplantation or after AOM/DSS treatment usually succumb to primary tumour load before reaching invasive tumour stages. At the same time, the orthotopic model represents a state of invasive carcinoma growth already at the start of the model [Bürtin et al. 2020]. Thus, in this work only the AOM/P53 model allows examination of stromal Zeb1 during cancer cell invasion. In mice with fibroblast specific deletion of *Zeb1*, less invasive tumours were observed compared to control mice (Figure 29). This could be due to either a delay in tumour initiation caused by increased immuno-surveillance (see above) or direct effects of the loss of Zeb1 in fibroblasts. In contrast to the observations in this work, previous studies reported increased induction of EMT and enhanced tumour cell invasion due to the presence of inflammatory fibroblast subtypes in colorectal

cancer [Mosa et al. 2020, Zhong et al. 2021]. At the same time, contractility and matrix stiffness (both traits of myofibroblasts) have been shown to induce invasion in other cancer entities [Pathak & Kumar 2012, Navab et al. 2016, Labernadie et al. 2017, Gkretsi & Stylianopoulos 2018]. In addition, production and remodelling of ECM by CAFs has been shown to induce invasion and CAF migration can serve as scaffold for the migration and invasion of tumour cells [Gaggioli et al. 2007, Lee et al. 2011, Pickup et al. 2013, Miyazaki et al. 2019]. Further investigation is required to dissect which of these mechanisms is responsible for the reduced invasion observed in the AOM/P53 model.

Many steps of the metastatic process are influenced by fibroblasts. CAFs can induce EMT and invasion in tumour cells [Mosa et al. 2020, Zhong et al. 2021] and facilitate the dissemination of tumour cells from the primary tumours either as single cells or as homo- or heterotypic clusters [Gaggioli et al. 2007, Matsumura et al. 2019, Hurtado et al. 2020]. At the same time, they release factors that support intravasation [Han et al. 2016, Sznurkowska and Aceto 2021], protect circulating tumour cells in the vasculature [Duda et al. 2010, Hou et al. 2012], help establishing a pre-metastatic niche [Nielsen et al. 2016, Ji et al. 2020] and contribute to secondary tumour growth and immune evasion at metastatic sites [Monteran and Erez 2019]. Although some inhibitory functions (e.g. ECM barrier secretion by myofibroblasts [Feldmann et al. 2021, Bhattacharjee et al. 2021]) have been reported, cancer-associated fibroblasts are generally considered a metastasis-promoting factor [Hurtado et al. 2020]. Since the AOM/P53 model does not progress past lymph node metastasis [Schwitalla et al. 2013], only the orthotopic model qualified for the analysis of distant organ metastasis in this work. After transplantation of both, AKP and AKP* organoids, stromal *Zeb1* deletion reduced the incidence of liver metastasis (Figure 25, Figure 32). However, the number and size of metastases in the few KO mice that did develop liver metastasis after transplantation of AKP organoids was comparable to the WT. This indicated that the reduced incidence was not mainly driven by a reduced number of disseminating cells and that acquisition of another escape mechanism could overcome the effects of stromal Zeb1 loss. Interestingly, after transplantation of both organoid lines, immune-related changes could be observed. For AKP organoids, immune cell exclusion from metastases was observed exclusively in WT mice, while metastases in KO mice were infiltrated (Figure 25). For AKP* organoids, an increased number of immune cell accumulations were observed in the livers of KO mice which might be remainders of successful clearance of early metastases by the immune system (Figure 32). This indicated that myofibroblasts in metastases have a similar immuno-exclusive effect as in the primary tumours and that this effect is already important during the establishment of early metastases. This is in line with immune cell mediated clearing of metastases after TGFβ inhibition [Tauriello et al. 2018] and with increased metastatic burden in immuno-deficient mouse models [Leibold et al. 2022]. However, liver colonization was also impaired after TGFβ inhibition in immuno-compromised mice [Tan et al. 2019], indicating an additional immune-independent metastasis promoting effect of myofibroblasts. With

increasing evidence of the importance of ECM modulation in the (pre-) metastatic niche [Kaplan et al. 2005, Malanchi et al. 2012, Cox et al. 2012], it is possible that changes in ECM deposition like in the primary tumours (see above) also play a role in mediating metastatic effects of stromal Zeb1. However, recently contractile myofibroblasts rather than ECM myofibroblasts were associated with metastasis, indicating that tissue stiffness might also have an effect independent of ECM modulation [Pelon et al. 2020].

Overall, inhibition of the myofibroblast phenotype by stromal recombination of *Zeb1* could block metastasis by both the lack of a suitable pre-metastatic environment for colonization and reduced protection of metastases from immuno-surveillance. Additional experiments like colonization assays with co-injection of fibroblasts and tumour cells or experiments in immuno-compromised mice could be performed to further examine the pro-metastatic role of Zeb1 in fibroblasts.

4.4 Zeb1 loss creates an opportunity to increase response to immunotherapy

As knowledge about CAFs increased, they also became targets of cancer therapies. However, general ablation of CAFs not only had no beneficial effects but even worsened prognosis in preclinical models of pancreatic cancer [Rhim et al. 2014, Özdemir et al. 2014]. Thus, novel approaches targeting specific pro-tumourigenic subpopulations are centre of investigation in addition to combinations with other therapies. Depletion of specific CAF subpopulations (most prominently FAP^+ CAFs) yielded promising results in preclinical models but could not be translated into clinically beneficial applications yet [Pereira et al. 2019, Wang et al. 2021]. Other promising approaches are the reprogramming of CAFs into other clinically beneficial subpopulations and targeting the interactions of fibroblasts with other cells in the TME [Pereira et al. 2019, Barrett & Puré 2020, Wang et al. 2021]. In this work, ICB reduced liver metastasis and also strongly reduced primary tumour size in the AOM/DSS model. The shift in CAF populations induced by loss of stromal Zeb1 resulted in enhanced response to immune checkpoint inhibition in the AOM/DSS (Figure 34) and the orthotopic transplantation model (Figure 33). This is in line with previous publications showing correlation of myofibroblasts with resistance to immune checkpoint inhibition in multiple cancer entities [Costa et al. 2018, Chen et al. 2019, Ford et al. 2020, Dominguez et al. 2020]. Together with the observation that knockdown of *ZEB1* had similar effects in human fibroblasts as knockout in murine cells (although to a lesser extent because of residual ZEB1 activity, Figure 36), this might offer a potential target for future cancer therapies. Currently, clinical approaches are testing enhanced infiltration of immune cells by inhibition of TGFβ signaling in combination with immune checkpoint inhibition. However, the outcome of these studies was very heterogeneous, matching contrary results in preclinical models based on the immunogenicity of tumours [Sow et al. 2019] and some side effects were observed due to the broad effects of TGFβ

inhibition on homeostasis [Huynh et al. 2019, Teixeira et al. 2020]. Instead, targeting Zeb1 as a downstream target of TGFβ might reduce some of the side effects and selection of patients with immunogenic tumours based on pre-screening might increase clinical efficacy. In addition, expression of Zeb1 in tumour cells is also associated with malignant progression and therapy resistance (see above). Consequently, targeting Zeb1 not only in CAFs but also in tumour cells might have cumulative effects. So far, only the histone deacetylase inhibitor Mocetinostat has been published to inhibit Zeb1 expression and functionality [Meidhof et al. 2015]. Since these epigenetic modifiers can have many different effects, screenings for compounds more specifically targeting Zeb1 would be necessary before clinical application. Alternatively, the design of proteolysis targeting chimeras (PROTACs) or RNA interference (RNAi) against *ZEB1* could represent an interesting therapeutic option for CRC patients.

4.5 Conclusions

In summary, data in this work indicated that loss of Zeb1 prevented fibroblasts from acquiring a contractile and ECM producing myofibroblast phenotype. In the presence of inflammatory stimuli, this resulted in an inflammatory phenotype of the fibroblasts, which increased immune cell infiltration into immunogenic tumours. While increased infiltration and inflammation accelerated tumour growth in the inflammatory AOM/DSS model, it reduced tumour growth and metastasis in models of sporadic cancer. Stromal Zeb1 loss induced upregulation of immune checkpoint molecules, which could be used to enhance response to immune checkpoint inhibition in inflammation driven and sporadic cancer models (Figure 37). Thus, targeting fibroblast plasticity is a promising target for future cancer therapies. However, whether Zeb1 is a suitable target for clinical testing requires further mechanistic clarification, characterization of long-term effects and development of specific inhibitors.

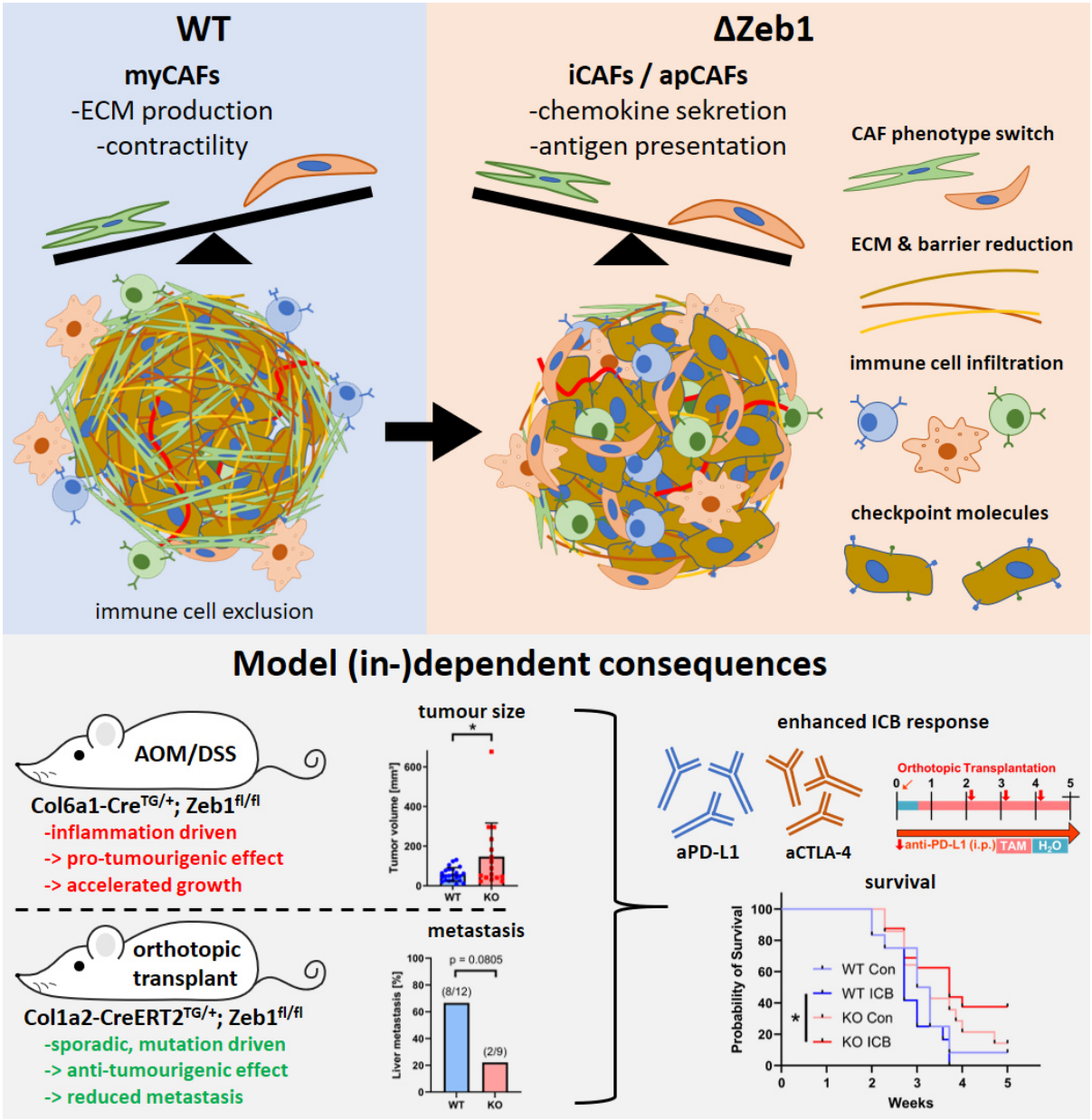

Figure 37: Graphical abstract of the main findings

Loss of Zeb1 induced an inflammatory fibroblast phenotype with model dependent consequences *in vivo*. Increased immune infiltration could be used to enhance immune checkpoint blockade. For details, see text.

5. Bibliography

5.1 Journal Articles

Ahlmann-Eltze, C. & Huber, W. glmGamPoi: fitting Gamma-Poisson generalized linear models on single cell count data. *Bioinformatics* **36**, 5701-5702 (2020). doi: /10.1093/bioinformatics/btaa1009

Aigner, K. *et al*. The transcription factor ZEB1 (dEF1) promotes tumour cell dedifferentiation by repressing master regulators of epithelial polarity. *Oncogene* **26**, 6979-6988 (2007). doi: 10.1038/sj.onc.1210508

Apte, U. *et al*. Activation of Wnt/'-Catenin Pathway During Hepatocyte Growth Factor–Induced Hepatomegaly in Mice. *Hepatology* **44**, 992-1002 (2006). doi: 10.1002/hep.21317

Arnold, M. *et al*. Global patterns and trends in colorectal cancer incidence and mortality. *Gut* **66,** 683-691 (2017). doi: 10.1136/gutjnl-2015-310912

Arumugam, T. *et al*. Epithelial to Mesenchymal Transition Contributes to Drug Resistance in Pancreatic Cancer. *Cancer Res* **69**, 5820-5828 (2009). doi: 10.1158/0008-5472.CAN-08-2819

Ashburner, M. *et al*. Gene Ontology: tool for the unification of biology. *Nat Genet* **25**, 25-29 (2000). doi: 10.1038/75556

Avery, D. *et al*. Extracellular matrix directs phenotypic heterogeneity of activated fibroblasts. *Matrix Biol* **67**, 90-106 (2018). doi: 10.1016/j.matbio.2017.12.003

Baisse, B., Bouzourene, H., Saraga, E.P., Bosman, F.T. & Benhattar, J. Intratumor genetic heterogeneity in advanced human colorectal adenocarcinoma. *Int J Cancer* **93**, 346-352 (2001). doi: 10.1002/ijc.1343

Barrett, R.L. & Puré, E. Cancer-associated fibroblasts and their influence on tumor immunity and immunotherapy. *eLife* **9**, e57243 (2020). doi: 10.7554/eLife.57243

Bartoschek, M. *et al*. Spatially and functionally distinct subclasses of breast cancer-associated fibroblasts revealed by single cell RNA sequencing. *Nat Commun* **9**, 5150 (2018). doi: 10.1038/s41467-018-07582-3

Beerling, E. *et al*. Plasticity between Epithelial and Mesenchymal States Unlinks EMT from Metastasis-Enhancing Stem Cell Capacity. *Cell Rep* **14**, 2281-2288 (2016). doi: 10.1016/j.celrep.2016.02.034

Bhattacharjee, S. et al. Tumor restriction by type I collagen opposes tumor-promoting effects of cancer-associated fibroblasts. J Clin Invest 131, e146987 (2021). doi: 10.1172/JCI146987

Biffi, G. *et al*. IL1-Induced JAK/STAT Signaling Is Antagonized by TGFa to Shape CAF Heterogeneity in Pancreatic Ductal Adenocarcinoma. *Cancer Discov* **9**, 282-301 (2019). doi: 10.1158/2159-8290.CD-18-0710

Biffi, G. & Tuveson, D.A. Diversity and biology of cancer-associated fibroblasts. *Physiol Rev* **101**, 147-176 (2021). doi: 10.1152/physrev.00048.2019

Boland, C.R. & Goel, A. Microsatellite Instability in Colorectal Cancer. *Gastroenterology* **138**, 2073-2087 (2010). doi: 10.1053/j.gastro.2009.12.064

Botteri, E. *et al*. Smoking and colorectal cancer: a meta-analysis. *JAMA* **300**, 2765-78 (2008). doi: 10.1001/jama.2008.839

Brabletz, T. *et al*. Variable β-catenin expression in colorectal cancers indicates tumor progression driven by the tumor environment. *PNAS* **98**, 10356-10361 (2001). doi: 10.1073/pnas.171610498

Brabletz, S. *et al*. Generation and characterization of mice for conditional inactivation of Zeb1. *Genesis* **55**, e23024 (2017). doi: 10.1002/dvg.23024

Bracken, C.P. *et al*. A Double-Negative Feedback Loop between ZEB1-SIP1 and the microRNA-200 Family Regulates Epithelial-Mesenchymal Transition. *Cancer Res* **68**, 7846-7854 (2008). doi: 10.1158/0008-5472.CAN-08-1942

Bramsen J.B. *et al*. Molecular-Subtype-Specific Biomarkers Improve Prediction of Prognosis in Colorectal Cancer. *Cell Rep* **19**, 1268-1280 (2017). doi: 10.1016/j.celrep.2017.04.045

Bray, F. *et al*. Global Cancer Statistics 2018: GLOBOCAN Estimates of Incidence and Mortality Worldwide for 36 Cancers in 185 Countries. *CA Cancer J Clin* **68**, 394-424 (2018). doi: 10.3322/caac.21492

Bronsert, P. *et al.* Prognostic significance of Zinc finger E-box binding homeobox 1 (ZEB1) expression in cancer cells and cancer-associated fibroblasts in pancreatic head cancer. *Surgery* **156**, 97-108 (2014). doi: 10.1016/j.surg.2014.02.018

Brunelli, L. & Caiola, E. *et al*. Capturing the metabolomic diversity of KRAS mutants in non- small-cell lung cancer cells. *Oncotarget* **5**, 4722-4731 (2014). doi: 10.18632/oncotarget.1958

Burgenske, D.M. *et al*. Establishment of genetically diverse patient-derived xenografts of colorectal cancer. *Am J Cancer Res* **4**, 824-837 (2014).

Burk, U., Schubert, J., Wellner, U. *et al*. A reciprocal repression between ZEB1 and members of the miR-200 family promotes EMT and invasion in cancer cells. *EMBO Rep* **9**, 582-589 (2008). doi: 10.1038/embor.2008.74

Burt, R. Inheritance of colorectal cancer. *Drug Discov Today Dis Mech* **4**, 293-300 (2007). doi: 10.1016/j.ddmec.2008.05.004

Bürtin, F., Mullins, C.S., & Linnebacher, M. Mouse models of colorectal cancer: Past, present and future perspectives. *World J Gastroenterol* **26**, 1394-1426 (2020). doi: 10.3748/wjg.v26.i13.1394

Butler, A., Hoffman, P., Smibert, P., Papalexi, E. & Satija, R. Integrating single-cell transcriptomic data across different conditions, technologies, and species. *Nat Biotechnol* **36**, 411-420 (2018). doi: 10.1038/nbt.4096

Cai, S., Li, Y., Ding, Y., Chen, K. & Jin, M. Alcohol drinking and the risk of colorectal cancer death: a meta-analysis. *Eur J Cancer Prev* **23**, 532-539 (2014). doi: 10.1097/CEJ.0000000000000076

Calon, A. *et al*. Stromal gene expression defines poor-prognosis subtypes in colorectal cancer. *Nat Genet* **47**, 320-329 (2015). doi: 10.1038/ng.3225

Carmeliet, P. & Jain, R.K. Angiogenesis in cancer and other diseases. *Nature* **407**, 249-257 (2000). doi: 10.1038/35025220

Chakravarthy, A., Khan, L., Bensler, N.P., Bose, P. & De Carvalho, D.D. TGF-β-associated extracellular matrix genes link cancer-associated fibroblasts to immune evasion and immunotherapy failure. *Nat Commun* **9**, 4692 (2018). doi: 10.1038/s41467-018-06654-8

Chan, D.S.M. *et al*. Red and Processed Meat and Colorectal Cancer Incidence: Meta-Analysis of Prospective Studies. *PLoS One* **6**, e20456 (2011). doi: 10.1371/journal.pone.0020456

Chan, T.A. *et al*. Development of tumor mutation burden as an immunotherapy biomarker: utility for the oncology clinic. *Ann Oncol* **30**, 44-56 (2019). doi: 10.1093/annonc/mdy495

Chang, T.-H. *et al*. Slug Confers Resistance to the Epidermal Growth Factor Receptor Tyrosine Kinase Inhibitor. *Am J Respir Crit Care Med* **183**, 1071-1079 (2011). doi: 10.1164/rccm.201009-1440OC

Chen, I.X. *et al*. Blocking CXCR4 alleviates desmoplasia, increases T-lymphocyte infiltration, and improves immunotherapy in metastatic breast cancer. *Proc Natl Acad Sci U S A* **116**, 4558-4566 (2019). doi: 10.1073/pnas.1815515116

Clevers, H. The Intestinal Crypt, A Prototype Stem Cell Compartment. *Cell* **154**, 274-284 (2013). doi: 10.1016/j.cell.2013.07.004

Cohen, N. *et al*. Fibroblasts drive an immunosuppressive and growth-promoting microenvironment in breast cancer via secretion of Chitinase 3-like 1. *Oncogene* **36**, 4457-4468 (2017). doi: 10.1038/onc.2017.65

Conant, D., Hsiau, T. *et al*. Inference of CRISPR Edits from Sanger Trace Data. *CRISPR J* **5**, 123-130 (2022). doi: 10.1089/crispr.2021.0113

Condeelis, J. & Pollard, J.W. Macrophages: Obligate Partners for Tumor Cell Migration, Invasion, and Metastasis. *Cell* **124**, 263-266 (2006). doi: 10.1016/j.cell.2006.01.007

Contardi, E. *et al*. CTLA-4 is constitutively expressed on tumor cells and can trigger apoptosis upon ligand interaction. *Int J Cancer* **117**, 538-550 (2005). doi: 10.1002/ijc.21155

Cosin-Roger, J. Ortiz-Masià, M.D. & Barrachina, M.D. Macrophages as an Emerging Source of Wnt Ligands: Relevance in Mucosal Integrity. *Front Immunol* **10**, 2297 (2019). doi: 10.3389/fimmu.2019.02297

Costa, A. *et al*. Fibroblast Heterogeneity and Immunosuppressive Environment in Human Breast Cancer. *Cancer Cell* **33**, 463-479 (2018). doi: 10.1016/j.ccell.2018.01.011

Cox, T.R. *et al*. LOX-Mediated Collagen Crosslinking Is Responsible for Fibrosis-Enhanced Metastasis. *Cancer Res* **73**, 1721-1732 (2013). doi: 10.1158/0008-5472.CAN-12-2233

Dang, H., Harryvan, T.J. & Hawinkels, L.J.A.C. Fibroblast Subsets in Intestinal Homeostasis, Carcinogenesis, Tumor Progression, and Metastasis. *Cancers* **13**, 183 (2021). doi: 10.3390/ cancers13020183

Darvin, P., Toor, S.M., Nair, V.S. & Elkord, E. Immune checkpoint inhibitors: recent progress and potential biomarkers. *Exp Mol Med* **50**, 1-11 (2018). doi: 10.1038/s12276-018-0191-1

Date, S. & Sato, T. Mini-Gut Organoids: Reconstitution of the Stem Cell Niche. *Annu Rev Cell Dev Biol* **31**, 269-289 (2015). doi: 10.1146/annurev-cellbio-100814-125218

De Craene, B. *et al*. Epidermal Snail expression drives skin cancer initiation and progression through enhanced cytoprotection, epidermal stem/progenitor cell expansion and enhanced metastatic potential. *Cell Death Differ* **21**, 310-320 (2014). doi: 10.1038/cdd.2013.148

De Filippo, C. *et al*. Mutations of the Apc gene in experimental colorectal carcinogenesis induced by azoxymethane in F344 rats. *Br J Cancer* **77**, 2148-2151 (1998). doi: 10.1038/bjc.1998.359

De Rosa, M. *et al*. Genetics, diagnosis and management of colorectal cancer (Review). *Oncol Rep* **34**, 1087-1096 (2015). doi: 10.3892/or.2015.4108

de Sousa e Melo, F. *et al*. A distinct role for Lgr5+ stem cells in primary and metastatic colon cancer. *Nature* **543**, 676-680 (2017). doi: 10.1038/nature21713

Dekker, E., Tanis, P.J., Vleugels, J.L.A., Kasi, P.M. & Wallace, M.B. Colorectal cancer. *Lancet* **394**, 1467-1480 (2019). doi: 10.1016/S0140-6736(19)32319-0

Deng, F. *et al*. YAP triggers the Wnt/β-catenin signalling pathway and promotes enterocyte self-renewal, regeneration and tumorigenesis after DSS-induced injury. *Cell Death Dis* **9**, 153 (2018). doi: 10.1038/s41419-017-0244-8

Dobin, A. *et al*. STAR: ultrafast universal RNA-seq aligner. *Bioinformatics* **29**, 15-21 (2013). doi: 10.1093/bioinformatics/bts635

Dominguez, C.X. *et al*. Single-Cell RNA Sequencing Reveals Stromal Evolution into LRRC15+ Myofibroblasts as a Determinant of Patient Response to Cancer Immunotherapy. *Cancer Discov* **10**, 232-253 (2020). doi: 10.1158/2159-8290.CD-19-0644

Drost, J. *et al*. Sequential cancer mutations in cultured human intestinal stem cells. *Nature* **521**, 43-47 (2015). doi: 10.1038/nature14415

Duda, D.G., Duyverman, A.M.M.J., Kohno, M. *et al*. Malignant cells facilitate lung metastasis by bringing their own soil. *Proc Natl Acad Sci U S A* **107**, 21677-21682 (2010). doi: 10.1073/pnas.1016234107

Dulai, P.S., Sandborn, W.J. & Gupta, S. Colorectal Cancer and Dysplasia in Inflammatory Bowel Disease: A Review of Disease Epidemiology, Pathophysiology, and Management. *Cancer Prev Res (Phila)* **9**, 887-894 (2016). doi: 10.1158/1940-6207.CAPR-16-0124

East, J.E. *et al*. British Society of Gastroenterology position statement on serrated polyps in the colon and rectum. *Gut* **66**, 1181-1196 (2017). doi: 10.1136/gutjnl-2017-314005

Eichele, D.D. & Kharbanda, K.K. Dextran sodium sulfate colitis murine model: An indispensable tool for advancing our understanding of inflammatory bowel diseases pathogenesis. *World J Gastroenterol* **23**, 6016-6029 (2017). doi: 10.3748/wjg.v23.i33.6016

Eischen, C.M. Genome Stability Requires p53. *Cold Spring Harb Perspect Med* **6**, a026096 (2016). doi: 10.1101/cshperspect.a026096

Elyada E., *et al*. Cross-species single-cell analysis of pancreatic ductal adenocarcinoma reveals antigen-presenting cancer-associated fibroblasts. *Cancer Discov* **9**, 1102-1123 (2019). doi: 10.1158/2159-8290.CD-19-0094

Erdman, S.H., Wu, H.D., Hixson, L.J., Ahnen, D.J. & Gerner, E.W. Assessment of Mutations in Ki-ras and p53 in Colon Cancers From Azoxymethane- and Dimethylhydrazine-Treated Rats. *Mol Carcinog* **19**, 137-144 (1997). doi: 10.1002/(sici)1098-2744(199707)19:2<137::aid-mc8>3.0.co;2-c

Farin, H.F., Van Es, J.H. & Clevers, H. Redundant Sources of Wnt Regulate Intestinal Stem Cells and Promote Formation of Paneth Cells. *Gastroenterology* **143**, 1518-1529 (2012). doi: 10.1053/j.gastro.2012.08.031

Fearon, E.R. & Vogelstein, B. A Genetic Model for Colorectal Tumorigenesis. *Cell* **61**, 759-767 (1990). doi: 10.1016/0092-8674(90)90186-i

Feldmann, K. *et al*. Mesenchymal Plasticity Regulated by Prrx1 Drives Aggressive Pancreatic Cancer Biology. *Gastroenterology* **160**, 346-385 (2021). doi: 10.1053/j.gastro.2020.09.010

Fischer, K.R. *et al*. Epithelial-to-mesenchymal transition is not required for lung metastasis but contributes to chemoresistance. *Nature* **527**, 472-476 (2015). doi: 10.1038/nature15748

Fleming, M., Ravula, S., Tatishchev, S.F. & Wang, H.L. Colorectal carcinoma: Pathologic aspects. *J Gastrointest Oncol* **3**, 153-173 (2012). doi: 10.3978/j.issn.2078-6891.2012.030

Ford, K. *et al*. NOX4 Inhibition Potentiates Immunotherapy by Overcoming Cancer-Associated Fibroblast-Mediated CD8 T-cell Exclusion from Tumors. *Cancer Res* **80**, 1846-1860 (2020). doi: 10.1158/0008-5472.CAN-19-3158

Fouani, L. *et al*. During mitosis ZEB1 "switches" from being a chromatin-bound epithelial gene repressor, to become a microtubule-associated protein. *Biochim Biophys Acta Mol Cell Res* **1867**, 118673 (2020). doi: 10.1016/j.bbamcr.2020.118673

Fu, R., Han, C.-F., Ni, T. & Di, L. *et al*. A ZEB1/p53 signaling axis in stromal fibroblasts promotes mammary epithelial tumours. *Nat Commun* **10**, 3210 (2019). doi: 10.1038/s41467-019-11278-7

Fujii, M. & Shimokawa, M. *et al*. A Colorectal Tumor Organoid Library Demonstrates Progressive Loss of Niche Factor Requirements during Tumorigenesis. *Cell Stem Cell* **18**, 827-838 (2016). doi: 10.1016/j.stem.2016.04.003

Fumagalli, A. & Drost, J. *et al*. Genetic dissection of colorectal cancer progression by orthotopic transplantation of engineered cancer organoids. *Proc Natl Acad Sci U S A* **114**, E2357-E2364 (2017). doi: 10.1073/pnas.1701219114

Fumagalli, A. *et al*. A surgical orthotopic organoid transplantation approach in mice to visualize and study colorectal cancer progression. *Nat Protoc* **13**, 235-247 (2018). doi: 10.1038/nprot.2017.137

Gabrilovich, D.I. & Nagaraj, S. Myeloid-derived suppressor cells as regulators of the immune system. *Nat Rev Immunol* **9**, 162-174 (2009). doi: 10.1038/nri2506

Gaggioli, C. *et al*. Fibroblast-led collective invasion of carcinoma cells with differing roles for RhoGTPases in leading and following cells. *Nat Cell Biol* **9**, 1392-1400 (2007). doi: 10.1038/ncb1658

Gallimore, A.M. & Simon, A.K. Positive and negative influences of regulatory T cells on tumour immunity. *Oncogene* **27**, 5886-5893 (2008). doi: 10.1038/onc.2008.269

Galon, J. *et al.* Type, Density, and Location of Immune Cells Within Human Colorectal Tumors Predict Clinical Outcome. *Science* **313**, 1960-1964 (2006). doi: 10.1126/science.1129139

Galon, J. & Lanzi, A. Immunoscore and its introduction in clinical practice. *Q J Nucl Med Mol Imaging* **64**, 152-161 (2020). doi: 10.23736/S1824-4785.20.03249-5

Gavin, P.G. *et al*. Mutation Profiling and Microsatellite Instability in Stage II and III Colon Cancer: An Assessment of Their Prognostic and Oxaliplatin Predictive Value. *Clin Cancer Res* **18**, 6531-6541 (2012). doi: 10.1158/1078-0432.CCR-12-0605

Gerlitz, O. & Basler, K. Wingful, an extracellular feedback inhibitor of Wingless. *Genes Dev* **16**, 1055-1059 (2002). doi: 10.1101/gad.991802

Giannakis, M., Mu, X.J. & Shukla, S.A. *et al*. Genomic Correlates of Immune-Cell Infiltrates in Colorectal Carcinoma. *Cell Rep* **15**, 857-865 (2016). doi: 10.1016/j.celrep.2016.03.075

Giráldez, A.J., Copley, R.R. & Cohen, S.M. HSPG Modification by the Secreted Enzyme Notum Shapes the Wingless Morphogen Gradient. *Dev Cell* **2**, 667-676 (2002). doi: 10.1016/s1534-5807(02)00180-6

Giraldo, N.A. *et al*. The clinical role of the TME in solid cancer. *Br J Cancer* **120**, 45-53 (2019). doi: 10.1038/s41416-018-0327-z

Gkretsi, V. & Stylianopoulos, T. Cell Adhesion and Matrix Stiffness: Coordinating Cancer Cell invasion and Metastasis. *Front Oncol* **8**, 145 (2018). doi: 10.3389/fonc.2018.00145

Gorchs, L. *et al*. Human Pancreatic Carcinoma-Associated Fibroblasts Promote Expression of Co-inhibitory Markers on CD4+ and CD8+ T-Cells. *Front Immunol* **10**, 847 (2019). doi: 10.3389/fimmu.2019.00847

Grauel, A.L. & Nguyen, B. *et al*. TGFβ-blockade uncovers stromal plasticity in tumors by revealing the existence of a subset of interferon-licensed fibroblasts. *Nat Commun* **11**, 6315 (2020). doi: 10.1038/s41467-020-19920-5

Gregory, P.A. *et al*. The miR-200 family and miR-205 regulate epithelial to mesenchymal transition by targeting ZEB1 and SIP1. *Nat Cell Biol* **10**, 593-601 (2008). doi: 10.1038/ncb1722

Grill, J.I. *et al*. Dro1/Ccdc80 inactivation promotes AOM/DSS-induced colorectal carcinogenesis and aggravates colitis by DSS in mice. *Carcinogenesis* **39**, 1176-1184 (2018). doi: 10.1093/carcin/bgy077

Grivennikov, S.I., Greten, F.R. & Karin, M. Immunity, Inflammation, and Cancer. *Cell* **140**, 883-899 (2010). doi: 10.1016/j.cell.2010.01.025

Grivennikov, S.I. Inflammation and colorectal cancer: colitis-associated neoplasia. *Semin Immunopathol* **35**, 229-244 (2013). doi: 10.1007/s00281-012-0352-6

Guinney, J., Dienstmann, R., Wang, X., de Reyniès, A., Schlicker, A., Soneson, C., Marisa, L., Roepman, P. & Nyamundanda, G. *et al*. The consensus molecular subtypes of colorectal cancer. *Nat Med* **21**, 1350-1356 (2015). doi: 10.1038/nm.3967

Guo, C. *et al*. ZEB1 Promotes Oxaliplatin Resistance through the Induction of Epithelial - Mesenchymal Transition in Colon Cancer Cells. *J Cancer* **8**, 3555-3566 (2017). doi: 10.7150/jca.20952

Hadac, J.N. *et al*. Colon Tumors with the Simultaneous Induction of Driver Mutations in APC, KRAS, and PIK3CA Still Progress through the Adenoma-to-carcinoma Sequence. *Cancer Prev Res (Phila)* **8**, 952-961 (2015). doi: 10.1158/1940-6207.CAPR-15-0003

Haddad, Y., Choi, W. & McConkey, D.J. Delta-Crystallin Enhancer Binding Factor 1 Controls the Epithelial to Mesenchymal Transition Phenotype and Resistance to the Epidermal Growth Factor Receptor Inhibitor Erlotinib in Human Head and Neck Squamous Cell Carcinoma Lines. *Clin Cancer Res* **15**, 532-542 (2009). doi: 10.1158/1078-0432.CCR-08-1733

Haensel, D. & Dai, X. Epithelial-to-mesenchymal transition in cutaneous wound healing: where we are and where we are heading. *Dev Dyn* **247**, 473-480 (2018). doi: 10.1002/dvdy.24561

Hafemeister, C. & Satija, R. Normalization and variance stabilization of single-cell RNA-seq data using regularized negative binomial regression. *Genome Biol* **20**, 296 (2019). doi: 10.1186/s13059-019-1874-1

Halberg, R.B. *et al*. Tumorigenesis in the multiple intestinal neoplasia mouse: Redundancy of negative regulators and specificity of modifiers. *Proc Natl Acad Sci U S A* **97**, 3461-3466 (2000). doi: 10.1073/pnas.97.7.3461

Han, W. *et al*. Oriented collagen fibers direct tumor cell intravasation. *Proc Natl Acad Sci U S A* **113**, 11208-11213 (2016). doi: 10.1073/pnas.1610347113

Hao, Y. & Hao, S. *et al*. Integrated analysis of multimodal single-cell data. *Cell* **184**, 3573-3587 (2021). doi: 10.1016/j.cell.2021.04.048

Hartmann, N. *et al*. Prevailing Role of Contact Guidance in Intrastromal T-cell Trapping in Human Pancreatic Cancer. *Clin Cancer Res* **20**, 3422-3433 (2014). doi: 10.1158/1078-0432.CCR-13-2972

Havel, J.J., Chowell, D. & Chan, T.A. The evolving landscape of biomarkers for checkpoint inhibitor immunotherapy. *Nat Rev Cancer* **19**, 133-150 (2019). doi: 10.1038/s41568-019-0116-x

Henke, E. Nandigama, R. & Ergün, S. Extracellular Matrix in the Tumor Microenvironment and Its Impact on Cancer Therapy. *Front Mol Biosci* **6**, 160 (2020). doi: 10.3389/fmolb.2019.00160

Herrinton, L.J. *et al.* Incidence and Mortality of Colorectal Adenocarcinoma in Persons With Inflammatory Bowel Disease From 1998 to 2010. *Gastroenterology* **143**, 382-389 (2012). doi: 10.1053/j.gastro.2012.04.054

Heuberger, J. & Birchmeier, W. Interplay of Cadherin-Mediated Cell Adhesion and Canonical Wnt Signaling. *Cold Spring Harb Perspect Biol* **2**, a002915 (2010). doi: 10.1101/cshperspect.a002915

Hogquist, K.A. *et al*. T cell receptor antagonist peptides induce positive selection. *Cell* **76**, 17-27 (1994). doi: 10.1016/0092-8674(94)90169-4

Hou, J.-M. *et al*. Clinical Significance and Molecular Characteristics of Circulating Tumor Cells and Circulating Tumor Microemboli in Patients With Small-Cell Lung Cancer. *J Clin Oncol* **30**, 525-532 (2012). doi: 10.1200/JCO.2010.33.3716

Hu, B. & Elinav, E. *et al*. Inflammation-induced tumorigenesis in the colon is regulated by caspase-1 and NLRC4. *Proc Natl Acad Sci U S A* **107**, 21635-21640 (2010). doi: 10.1073/pnas.1016814108

Huang, X. *et al*. Matrix Stiffness–Induced Myofibroblast Differentiation Is Mediated by Intrinsic Mechanotransduction. *Am J Respir Cell Mol Biol* **47**, 340-348 (2012). doi: 10.1165/rcmb.2012-0050OC

Huang, R.Y.-J., Guilford, P. & Thiery, J.P. Early events in cell adhesion and polarity during epithelial mesenchymal transition. *J Cell Sci* **125**, 4417-4422 (2012a). doi: 10.1242/jcs.099697

Huang, Y. *et al*. Improving immune-vascular crosstalk for cancer immunotherapy. *Nat Rev Immunol* **18**, 195-203 (2018). doi: 10.1038/nri.2017.145

Huang, H. *et al*. Mesothelial cell-derived antigen-presenting cancer-associated fibroblasts induce expansion of regulatory T cells in pancreatic cancer. *Cancer Cell* **40**, 656-673 (2022). doi: 10.1016/j.ccell.2022.04.011

Hurtado, P., Martínez-Pena, I. & Piñeiro, R. Dangerous Liaisons: Circulating Tumor Cells (CTCs) and Cancer-Associated Fibroblasts (CAFs). *Cancers (Basel)* **12**, 2861 (2020). doi: 10.3390/cancers12102861

Huynh, L.K., Hipolito, C.J. & ten Dijke, P. A Perspective on the Development of TGF-Inhibitors for Cancer Treatment. *Biomolecules* **9**, 743 (2019). doi: 10.3390/biom9110743

Hwang, J.W. & Lee, N. K. *et al*. A Comparison of Immune Responses Exerted Following Syngeneic, Allogeneic, and Xenogeneic Transplantation of Mesenchymal Stem Cells into the Mouse Brain. *Int J Mol Sci* **21**, 3052 (2020). doi: 10.3390/ijms21093052

Isella, C. *et al*. Stromal contribution to the colorectal cancer transcriptome. *Nat Genet* **47**, 312-319 (2015). doi: 10.1038/ng.3224

Ishikawa, T.-o & Herschman, H.R. Tumor formation in a mouse model of colitis-associated colon cancer does not require COX-1 or COX-2 expression. *Carcinogenesis* **31**, 729-736 (2010). doi: 10.1093/carcin/bgq002

Jackson, E.L. *et al*. Analysis of lung tumor initiation and progression using conditional expression of oncogenic K-ras. *Genes Dev* **15**, 3243-3248 (2001). doi: 10.1101/gad.943001

Jackstadt, R. *et al*. Epithelial NOTCH Signaling Rewires the Tumor Microenvironment of Colorectal Cancer to Drive Poor-Prognosis Subtypes and Metastasis. *Cancer Cell* **36**, 319-336 (2019). doi: 10.1016/j.ccell.2019.08.003

Jesnowski, R. *et al*. Immortalization of pancreatic stellate cells as an in vitro model of pancreatic fibrosis: deactivation is induced by matrigel and N-acetylcysteine. *Lab Invest* **85**, 1276-1291 (2005). doi: 10.1038/labinvest.3700329

Ji, Q. *et al*. Primary tumors release ITGBL1-rich extracellular vesicles to promote distal metastatic tumor growth through fibroblast-niche formation. *Nat Commun* **11**, 1211 (2020). doi: 10.1038/s41467-020-14869-x

Jin, B.-R., Chung, K.-S-, Lee, M. & An, H.-J. High-Fat Diet Propelled AOM/DSS-Induced Colitis-Associated Colon Cancer Alleviated by Administration of Aster glehni via STAT3 Signaling Pathway. *Biology (Basel)* **9**, 24 (2020). doi: 10.3390/biology9020024

Joseph, J.V. *et al*. TGF-β is an inducer of ZEB1-dependent mesenchymal transdifferentiation in glioblastoma that is associated with tumor invasion. *Cell Death Dis* **5**, e1443 (2014). doi: 10.1038/cddis.2014.395

Kalluri, R. The biology and function of fibroblasts in cancer. *Nat Rev Cancer* **16**, 582-598 (2016). doi: 10.1038/nrc.2016.73

Kalyan, A., Kircher, S., Shah, H. Mulcahy, M. & Benson, A. Updates on immunotherapy for colorectal cancer. *J Gastrointest Oncol* **9**, 160-169 (2018). doi: 10.21037/jgo.2018.01.17

Kang, C. & Song, C.-H. *et al*. The Enhanced Inhibitory Effect of Estrogen on PD-L1 Expression Following Nrf2 Deficiency in the AOM/DSS Model of Colitis-Associated Cancer. *Front Oncol* **11**, 679324 (2021). doi: 10.3389/fonc.2021.679324

Kaplan, R.N., Riba, R.D. & Zacharoulis, S. *et al*. VEGFR1-positive haematopoietic bone marrow progenitors initiate the pre-metastatic niche. *Nature* **438**, 820-827 (2005). doi: 10.1038/nature04186

Karlsson, K. & Przybilla, M. *et al*. Experimental evolution in TP53 deficient gastric organoids recapitulates tumorigenesis. Preprint at *www.biorxiv.org/content/ 10.1101/2022.04.09.487529v2* (2022).

Karpus, O.N. & Westendorp, B.F. *et al*. Colonic CD90+ Crypt Fibroblasts Secrete Semaphorins to Support Epithelial Growth. *Cell Rep* **26**, 3698-3708 (2019). doi: 10.1016/j.celrep.2019.02.101

Katsura A. & Tamura, Y. *et al*. ZEB1-regulated inflammatory phenotype in breast cancer cells. *Mol Oncol* **11**, 1241-1262 (2017). doi: 10.1002/1878-0261.12098

Ke, X. & Shen, L. Molecular targeted therapy of cancer: The progress and future prospect. *Frontiers in Laboratory Medicine* **1**, 69-75 (2017). doi: 10.1016/j.flm.2017.06.001

Khaliq, A.M. *et al*. Refining colorectal cancer classification and clinical stratification through a single-cell atlas. *Genome Biol* **23**, 113 (2022). doi: 10.1186/s13059-022-02677-z

Kim, D.H. & Xing, T. *et al*. Epithelial Mesenchymal Transition in Embryonic Development, Tissue Repair and Cancer: A Comprehensive Overview. *J Clin Med* **7**, 1 (2017). doi: 10.3390/jcm7010001

Kim, S.Y. & Kim, T.I. Serrated neoplasia pathway as an alternative route of colorectal cancer carcinogenesis. *Intest Res* **16**, 358-365 (2018). doi: 10.5217/ir.2018.16.3.358

Kim, J.K., Wu, C., Del Latto, M. & Gao, Y. *et al*. An immunocompetent rectal cancer model to study radiation therapy. *Cell Rep Methods* **2**, 100353 (2022). doi: 10.1016/j.crmeth.2022.100353

Kinchen, J., Chen, H.H. & Parikh, K. *et al*. Structural Remodeling of the Human Colonic Mesenchyme in Inflammatory Bowel Disease. *Cell* **175**, 372-386 (2018). doi: 10.1016/j.cell.2018.08.067

Kishimoto, H. *et al*. Development of a Clinically-Precise Mouse Model of Rectal Cancer. *PLoS One* **8**, e79453 (2013). doi: 10.1371/journal.pone.0079453

Klose, J. *et al*. Salinomycin inhibits metastatic colorectal cancer growth and interferes with Wnt/β-catenin signaling in CD133+ human colorectal cancer cells. *BMC Cancer* **16**, 896 (2016). doi: 10.1186/s12885-016-2879-8

Kobayashi, H. *et al.* Cancer-associated fibroblasts in gastrointestinal cancer. *Nat Rev Gastroenterol Hepatol* **16**, 282-295 (2019). doi: 10.1038/s41575-019-0115-0

Koo, B.-K., Sasselli, V. & Clevers, H. Retroviral Gene Expression Control in Primary Organoid Cultures. *Curr Protoc Stem Cell Biol* **27**, Unit 5A.6 (2013). doi: 10.1002/9780470151808.sc05a06s27

Korpal, M., Lee, E.S., Hu, G. & Kang, Y. The miR-200 Family Inhibits Epithelial-Mesenchymal Transition and Cancer Cell Migration by Direct Targeting of E-cadherin Transcriptional Repressors ZEB1 and ZEB2. *J Biol Chem* **283**, 14910-14914 (2008). doi: 10.1074/jbc.C800074200

Krebs, A.M. *et al*. The EMT-activator Zeb1 is a key factor for cell plasticity and promotes metastasis in pancreatic cancer. *Nat Cell Biol* **19**, 518-529 (2017). doi: 10.1038/ncb3513

Kretzschmar, K. Cancer research using organoid technology. *J Mol Med (Berl)* **99**, 501-515 (2021). doi: 10.1007/s00109-020-01990-z

Kucherlapati, M.H. *et al*. An Msh2 Conditional Knockout Mouse for Studying Intestinal Cancer and Testing Anticancer Agents. *Gastroenterology* **138**, 993-1002 (2010). doi: 10.1053/j.gastro.2009.11.009

Kuzet, S.-E. & Gaggioli, C. Fibroblast activation in cancer: when seed fertilizes soil. *Cell Tissue Res* **365**, 607-619 (2016). doi: 10.1007/s00441-016-2467-x

Kwong, T.N.Y. & Wang, X. *et al*. Association Between Bacteremia From Specific Microbes and Subsequent Diagnosis of Colorectal Cancer. *Gastroenterology* **155**, 383-390 (2018). doi: 10.1053/j.gastro.2018.04.028

Kyrgiou, M. *et al*. Adiposity and cancer at major anatomical sites: umbrella review of the literature. *BMJ* **356**, j477 (2017). doi: 10.1136/bmj.j477

Labernadie, A. *et al*. A mechanically active heterotypic E-cadherin/N-cadherin adhesion enables fibroblasts to drive cancer cell invasion. *Nat Cell Biol* **19**, 224-237 (2017). doi: 10.1038/ncb3478

Lahar, N. *et al*. Intestinal Subepithelial Myofibroblasts Support in vitro and in vivo Growth of Human Small Intestinal Epithelium. *PLoS One* **6**, e26898 (2011). doi: 10.1371/journal.pone.0026898

Lambrechts, D. *et al*. Phenotype molding of stromal cells in the lung tumor microenvironment. *Nat Med* **24**, 1277-1289 (2018). doi: 10.1038/s41591-018-0096-5

Lamouille, S., Xu, J. & Derynck, R. Molecular mechanisms of epithelial–mesenchymal transition. *Nat Rev Mol Cell Biol* **15**, 178-196 (2014). doi: 10.1038/nrm3758

Lavin, M.F. & Gueven, N. The complexity of p53 stabilization and activation. *Cell Death Differ* **13**, 941-950 (2006). doi: 10.1038/sj.cdd.4401925

Le, D.T. *et al.* PD-1 Blockade in Tumors with Mismatch-Repair Deficiency. *N Engl J Med* **372**, 2509-2520 (2015). doi: 10.1056/NEJMoa1500596

Le, D.T. *et al*. Mismatch repair deficiency predicts response of solid tumors to PD-1 blockade. *Science* **357**, 409-413 (2017). doi: 10.1126/science.aan6733

Lee, H.-O. *et al*. FAP-overexpressing fibroblasts produce an extracellular matrix that enhances invasive velocity and directionality of pancreatic cancer cells. *BMC Cancer* **11**, 245 (2011). doi: 10.1186/1471-2407-11-245

Lehmann, W. *et al*. ZEB1 turns into a transcriptional activator by interacting with YAP1 in aggressive cancer types. *Nat Commun* **7**, 10498 (2016). doi: 10.1038/ncomms10498

Leibold, J., Amor, C. & Tsanov, K.M. *et al*. Somatic mouse models of gastric cancer reveal genotype-specific features of metastatic disease. Preprint at *www.biorxiv.org/content/ 10.1101/2022.06.15.494941v1* (2022).

Li, H. & Courtois, E.T. *et al*. Reference component analysis of single-cell transcriptomes elucidates cellular heterogeneity in human colorectal tumors. *Nat Genet* **49**, 708-718 (2017). doi: 10.1038/ng.3818

Liberzon, A. *et al*. The Molecular Signatures Database Hallmark Gene Set Collection. *Cell Syst* **1**, 417-425 (2015). doi: 10.1016/j.cels.2015.12.004

Liu, Y., El-Naggar, S., Darling, D.S., Higashi, Y. & Dean, D.C. Zeb1 links epithelial-mesenchymal transition and cellular senescence. *Development* **135**, 579-588 (2008). doi: 10.1242/dev.007047

Liu, F. *et al*. Mechanosignaling through YAP and TAZ drives fibroblast activation and fibrosis. *Am J Physiol Lung Cell Mol Physiol* **308**, L344-357 (2015). doi: 10.1152/ajplung.00300.2014

Liu, T., Han, C. & Wang, S. *et al*. Cancer-associated fibroblasts: an emerging target of anti-cancer immunotherapy. *J Hematol Oncol* **12**, 86 (2019). doi: 10.1186/s13045-019-0770-1

Liu, C., Pei, H. & Tan, F. Matrix Stiffness and Colorectal Cancer. *Onco Targets Ther* **13**, 2747-2755 (2020). doi: 10.2147/OTT.S231010

Loonstra, A. *et al*. Growth inhibition and DNA damage induced by Cre recombinase in mammalian cells. *Proc Natl Acad Sci U S A* **98**, 9209-9214 (2001). doi: 10.1073/pnas.161269798

Love, M. I., Huber, W. & Anders, S. Moderated estimation of fold change and dispersion for RNA-seq data with DESeq2. *Genome Biol* **15**, 550 (2014). doi: 10.1186/s13059-014-0550-8

Lu, Y.-X. *et al*. Regulation of Colorectal Carcinoma Stemness, Growth, and Metastasis by an miR-200c-Sox2–Negative Feedback Loop Mechanism. *Clin Cancer Res* **20**, 2631-2642 (2014). doi: 10.1158/1078-0432.CCR-13-2348

Lu, W. & Kang, Y. Epithelial-Mesenchymal Plasticity in Cancer Progression and Metastasis. *Dev Cell* **49**, 361-374 (2019). doi: 10.1016/j.devcel.2019.04.010

Madisen, L. *et al*. A robust and high-throughput Cre reporting and characterization system for the whole mouse brain. *Nat Neurosci* **13**, 133-140 (2010). doi: 10.1038/nn.2467

Mager, L.F. *et al*. Microbiome-derived inosine modulates response to checkpoint inhibitor immunotherapy. *Science* **369**, 1481-1489 (2020). doi: 10.1126/science.abc3421

Mah, A.T., Yan, K.S. & Kuo, C.J. Wnt pathway regulation of intestinal stem cells. *J Physiol* **594**, 4837-4847 (2016). doi: 10.1113/JP271754

Maitra, R. *et al*. Development and Characterization of a Genetic Mouse Model of KRAS Mutated Colorectal Cancer. *Int J Mol Sci* **20**, 5677 (2019). doi: 10.3390/ijms20225677

Malanchi, I. & Santamaria-Martínez, A. *et al*. Interactions between cancer stem cells and their niche govern metastatic colonization. *Nature* **481**, 85-89 (2012). doi: 10.1038/nature10694

Maleno, I. *et al*. Distribution of HLA class I altered phenotypes in colorectal carcinomas: high frequency of HLA haplotype loss associated with loss of heterozygosity in chromosome region 6p21. *Immunogenetics* **56**, 244-253 (2004). doi: 10.1007/s00251-004-0692-z

Mali, P. & Yang, L. *et al*. RNA-Guided Human Genome Engineering via Cas9. *Science* **339**, 823-826 (6121). doi: 10.1126/science.1232033

Mani, S.A., Guo, W. & Liao, M.-J. *et al*. The Epithelial-Mesenchymal Transition Generates Cells with Properties of Stem Cells. *Cell* **133**, 704-715 (2008). doi: 10.1016/j.cell.2008.03.027

Mariathasan, S., Turley, S.J. & Nickles, D. *et al*. TGFβ attenuates tumour response to PD-L1 blockade by contributing to exclusion of T cells. *Nature* **554**, 544-548 (2018). doi: 10.1038/nature25501

Marisa, L. *et al*. Gene Expression Classification of Colon Cancer into Molecular Subtypes: Characterization, Validation, and Prognostic Value. *PLoS Med* **10**, e1001453 (2013). doi: 10.1371/journal.pmed.1001453

el Marjou, F. *et al*. Tissue-Specific and Inducible Cre-Mediated Recombination in the Gut Epithelium. *Genesis* **39**, 186-193 (2004). doi: 10.1002/gene.20042

Marmorino F., Boccaccino, A., Germani, M.M., Falcone, A. & Cremolini, C. Immune Checkpoint Inhibitors in pMMR Metastatic Colorectal Cancer: A Tough Challenge. *Cancers (Basel)* **12**, 2317 (2020). doi: 10.3390/cancers12082317

Matano, M., Date, S., Shimokawa, M. & Takano, A. *et al*. Modeling colorectal cancer using CRISPR-Cas9–mediated engineering of human intestinal organoids. *Nat Med* **21**, 256-262 (2015). doi: 10.1038/nm.3802

Matsumura, Y. *et al*. Stromal fibroblasts induce metastatic tumor cell clusters via epithelial–mesenchymal plasticity. *Life Sci Alliance* **2**, e20190425 (2019). doi: 10.26508/lsa.201900425

McCauley, H.A. & Wells, J.M. Pluripotent stem cell-derived organoids: using principles of developmental biology to grow human tissues in a dish. *Development* **144**, 958-962 (2017). doi: 10.1242/dev.140731

McQuin, C., Goodman, A., Chernyshev, V., Kamentsky, L., Cimini, B.A., Karhohs, K.W. *et al.* CellProfiler 3.0: Next-generation image processing for biology. *PLoS Biol* **16**, e2005970 (2018). doi: org/10.1371/journal.pbio.2005970

Meidhof, S. & Brabletz, S. *et al*. ZEB1-associated drug resistance in cancer cells is reversed by the class I HDAC inhibitor mocetinostat. *EMBO Mol Med* **7**, 831-847 (2015). doi: 10.15252/emmm.201404396

Meira, L.B. *et al*. DNA damage induced by chronic inflammation contributes to colon carcinogenesis in mice. *J Clin Invest* **118**, 2516-2525 (2008). doi: 10.1172/JCI35073

Menche, C. & Farin, H.F. Strategies for genetic manipulation of adult stem cell-derived organoids. *Exp Mol Med* **53**, 1483-1494 (2021). doi: 10.1038/s12276-021-00609-8

Meran, L., Baulies, A. & Li, V.S.W. Intestinal Stem Cell Niche: The Extracellular Matrix and Cellular Components. *Stem Cells Int* **2017**, 7970385 (2017). doi: 10.1155/2017/7970385

Miyazaki, K. *et al*. Cancer cell migration on elongate protrusions of fibroblasts in collagen matrix. *Sci Rep* **9**, 292 (2019). doi: 10.1038/s41598-018-36646-z

Molinari, C. *et al*. Heterogeneity in Colorectal Cancer: A Chellange for Personalized Medicine? *Int J Mol Sci* **19**, 3733 (2018). doi: 10.3390/ijms19123733

Møllersen, L., Paulsen, J.E. & Alexander, J. Loss of Heterozygosity and Nonsense Mutation in Apc in Azoxymethane-induced Colonic Tumours in Min Mice. *Anticancer Res* **24**, 2595-2599 (2004).

Monga, S.P.S. *et al*. Hepatocyte growth factor induces Wnt-independent nuclear translocation of beta-catenin after Met-beta-catenin dissociation in hepatocytes. *Cancer Res* **62**, 2064-2071 (2002).

Monteran, L. & Erez, N. The Dark Side of Fibroblasts: Cancer-Associated Fibroblasts as Mediators of Immunosuppression in the Tumor Microenvironment. *Front Immunol* **10**, 1835 (2019). doi: 10.3389/fimmu.2019.01835

Mooi, J.K. *et al*. The prognostic impact of consensus molecular subtypes (CMS) and its predictive effects for bevacizumab benefit in metastatic colorectal cancer: molecular analysis of the AGITG MAX clinical trial. *Ann Oncol* **29**, 2240-2246 (2018). doi: 10.1093/annonc/mdy410

Mootha, V.K. & Lindgren, C.M. *et al*. PGC-1α-responsive genes involved in oxidative phosphorylation are coordinately downregulated in human diabetes. *Nat Genet* **34**, 267-273 (2003). doi: 10.1038/ng1180

Mosa, M.H. *et al*. A Wnt-Induced Phenotypic Switch in Cancer-Associated Fibroblasts Inhibits EMT in Colorectal Cancer. *Cancer Res* **80**, 5569-5582 (2020). doi: 10.1158/0008-5472.CAN-20-0263

Moser, A.R., Pitot, H.C. & Dove, W.F. A dominant mutation that predisposes to multiple intestinal neoplasia in the mouse. *Science* **247**, 322-324 (1990). doi: 10.1126/science.2296722

Moser, A.R. *et al*. Homozygosity for the Min Allele of Apc Results in Disruption of Mouse Development Prior to Gastrulation. *Dev Dyn* **203**, 422-433 (1995). doi: 10.1002/aja.1002030405

Mullins, C.S. *et al*. Integrated Biobanking and Tumor Model Establishment of Human Colorectal Carcinoma Provides Excellent Tools for Preclinical Research. *Cancers (Basel)* **11**, 1520 (2019). doi: 10.3390/cancers11101520

Muraro, M.J. & Dharmadhikari, G. *et al*. A Single-Cell Transcriptome Atlas of the Human Pancreas. *Cell Syst* **3**, 385-394 (2016). doi: 10.1016/j.cels.2016.09.002

Muzumdar, M.D., Tasic, B., Miyamichi, K., Li, L. & Luo, L. A Global Double-Fluorescent Cre Reporter Mouse. *Genesis* **45**, 593-605 (2007). doi: 10.1002/dvg.20335

Nakatsu, G., Li, X., Zhou, H. Sheng, J. Wong, S.H. & Wu, W.K.K. *et al*. Gut mucosal microbiome across stages of colorectal carcinogenesis. *Nat Commun* **6**, 8727 (2015). doi: 10.1038/ncomms9727

Nambiar, P.R. *et al*. Preliminary analysis of azoxymethane induced colon tumors in inbred mice commonly used as transgenic/knockout progenitors. *Int J Oncol* **22**, 145-150 (2003). doi: 10.3892/ijo.22.1.145

Navab, R. *et al*. Integrin α11β1 regulates cancer stromal stiffness and promotes tumorigenicity and metastasis in non-small cell lung cancer. *Oncogene* **35**, 1899-1908 (2016). doi: 10.1038/onc.2015.254

Neufert, C. Becker, C. & Neurath, M.F. An inducible mouse model of colon carcinogenesis for the analysis of sporadic and inflammation-driven tumor progression. *Nat Protoc* **2**, 1998-2004 (2007). doi: 10.1038/nprot.2007.279

Nielsen, S.R. *et al*. Macrophage-secreted granulin supports pancreatic cancer metastasis by inducing liver fibrosis. *Nat Cell Biol* **18**, 549-560 (2016). doi: 10.1038/ncb3340

Nik, A.M., Reyahi, A., Pontén, F. & Carlsson, P. Foxf2 in Intestinal Fibroblasts Reduces Numbers of Lgr5 Stem Cells and Adenoma Formation by Inhibiting Wnt Signaling. *Gastroenterology* **144**, 1001-1011 (2013). doi: 10.1053/j.gastro.2013.01.045

Ohaegbulam, K.C., Assal, A., Lazar-Molnar, E., Yao, Y. & Zang, X. Human cancer immunotherapy with antibodies to the PD-1 and PD-L1 pathway. *Trends Mol Med* **21**, 24-33 (2015). doi: 10.1016/j.molmed.2014.10.009

Ohashi, S. *et al*. Epidermal Growth Factor Receptor and Mutant p53 Expand an Esophageal Cellular Subpopulation Capable of Epithelial-to-Mesenchymal Transition through ZEB Transcription Factors. *Cancer Res* **70**, 4174-4184 (2010). doi: 10.1158/0008-5472.CAN-09-4614

Öhlund, D., Handly-Santana, A., Biffi, G. & Elyada, E. *et al*. Distinct populations of inflammatory fibroblasts and myofibroblasts in pancreatic cancer. *J Exp Med* **214**, 579-596 (2017). doi: 10.1084/jem.20162024

Olsen, A.L. & Bloomer, S.A. *et al*. Hepatic stellate cells require a stiff environment for myofibroblastic differentiation. *Am J Physiol Gastrointest Liver Physiol* **301**, G110-118 (2011). doi: 10.1152/ajpgi.00412.2010

O'Rourke, K.P. *et al*. Transplantation of engineered organoids enables rapid generation of metastatic mouse models of colorectal cancer. *Nat Biotechnol* **35**, 577-582 (2017). doi: 10.1038/nbt.3837

Ouakrim, D.A. *et al*. Trends in colorectal cancer mortality in Europe: retrospective analysis of the WHO mortality database. *BMJ* **351**, h4970 (2015). doi: 10.1136/bmj.h4970

Özdemir, B.C. *et al*. Depletion of Carcinoma-Associated Fibroblasts and Fibrosis Induces Immunosuppression and Accelerates Pancreas Cancer with Reduced Survival. *Cancer Cell* **25**, 719-734 (2014). doi: 10.1016/j.ccr.2014.04.005

Palagani, V. *et al*. Epithelial Mesenchymal Transition and Pancreatic Tumor Initiating CD44+/EpCAM+ Cells Are Inhibited by c-Secretase Inhibitor IX. *PLoS One* **7**, e46514 (2012). doi: 10.1371/journal.pone.0046514

Pallangyo, C.K., Ziegler, P.K. & Greten, F.R. IKKβ acts as a tumor suppressor in cancer-associated fibroblasts during intestinal tumorigenesis. *J Exp Med* **212**, 2253-2266 (2015). doi: 10.1084/jem.20150576

Pan, Q. *et al*. Genomic variants in mouse model induced by azoxymethane and dextran sodium sulfate improperly mimic human colorectal cancer. *Sci Rep* **7**, 25 (2017). doi: 10.1038/s41598-017-00057-3

Papanikolaou, A., Wang, Q.-S., Papanikolaou, D., Whiteley, H.E. & Rosenberg, D.W. Sequential and morphological analyses of aberrant crypt foci formation in mice of differing susceptibility to azoxymethane-induced colon carcinogenesis. *Carcinogenesis* **21**, 1567-1572 (2000).

Pathak, A. & Kumar, S. Independent regulation of tumor cell migration by matrix stiffness and confinement. *Proc Natl Acad Sci U S A* **109**, 10334-10339 (2012). doi: 10.1073/pnas.1118073109

Pei, D., Shu, X., Gassama-Diagne, A. & Thiery, J.P. Mesenchymal–epithelial transition in development and reprogramming. *Nat Cell Biol* **21**, 44-53 (2019). doi: 10.1038/s41556-018-0195-z

Pelon, F. *et al*. Cancer-associated fibroblast heterogeneity in axillary lymph nodes drives metastases in breast cancer through complementary mechanisms. *Nat Commun* **11**, 404 (2020). doi: 10.1038/s41467-019-14134-w

Pereira, E.R. *et al*. Lymph node metastases can invade local blood vessels, exit the node, and colonize distant organs in mice. *Science* **359**, 1403-1407 (2018). doi: 10.1126/science.aal3622

Pereira, B.A. & Vennin, C. *et al*. CAF Subpopulations: A New Reservoir of Stromal Targets in Pancreatic Cancer. *Trends Cancer* **5**, 724-741 (2019). doi: 10.1016/j.trecan.2019.09.010

Picard, E., Verschoor, C.P., Ma, G.W. & Pawelec, G. Relationships Between Immune Landscapes, Genetic Subtypes and Responses to Immunotherapy in Colorectal Cancer. *Front Immunol* **11**, 369 (2020). doi: 10.3389/fimmu.2020.00369

Piccinin, S. & Tonin, E. *et al*. A ‘‘Twist box’’ Code of p53 Inactivation: Twist box:p53 Interaction Promotes p53 Degradation. *Cancer Cell* **22**, 404-415 (2012). doi: 10.1016/j.ccr.2012.08.003

Pickup, M.W. *et al*. Stromally Derived Lysyl Oxidase Promotes Metastasis of Transforming Growth Factor-b–Deficient Mouse Mammary Carcinomas. *Cancer Res* **73**, 5336-5346 (2013). doi: 10.1158/0008-5472.CAN-13-0012

Pino, M.S. & Chung, D.C. The Chromosomal Instability Pathway in Colon Cancer. *Gastroenterology* **138**, 2059-2072 (2010). doi: 10.1053/j.gastro.2009.12.065

Postigo, A.A. & Dean, D.C. ZEB represses transcription through interaction with the corepressor CtBP. *Proc Natl Acad Sci U S A* **96**, 6683-6688 (1999). doi: 10.1073/pnas.96.12.6683

Postigo, A.A. Opposing functions of ZEB proteins in the regulation of the TGFβ/BMP signaling pathway. *EMBO J* **22**, 2443-2452 (2003). doi: 10.1093/emboj/cdg225

Postigo, A.A., Depp, J.L., Taylor, J.J. & Kroll, K.L. Regulation of Smad signaling through a differential recruitment of coactivators and corepressors by ZEB proteins. *EMBO J* **22**, 2453-2462 (2003a). doi: 10.1093/emboj/cdg226

Puisieux, A., Brabletz, T. & Caramel, J. Oncogenic roles of EMT-inducing transcription factors. *Nat Cell Biol* **16**, 488-494 (2014). doi: 10.1038/ncb2976

Qi, J. *et al*. Single-cell and spatial analysis reveal interaction of FAP+ fibroblasts and SPP1+ macrophages in colorectal cancer. *Nat Commun* **13**, 1742 (2022). doi: 10.1038/s41467-022-29366-6

Radulovic, S., Miller, G. & Schally, A.V. Inhibition of Growth of HT-29 Human Colon Cancer Xenografts in Nude Mice by Treatment with Bombesin/Gastrin Releasing Peptide Antagonist (RC-3095). *Cancer Res* **51**, 6006-6009 (1991).

Raz, Y. & Cohen, N. *et al*. Bone marrow–derived fibroblasts are a functionally distinct stromal cell population in breast cancer. *J Exp Med* **215**, 3075-3093 (2018). doi: 10.1084/jem.20180818

Rebersek, M. Consensus molecular subtypes (CMS) in metastatic colorectal cancer - personalized medicine decision. *Radiol Oncol* **54**, 272-277 (2020). doi: 10.2478/raon-2020-0031

Rhim, A.D., Oberstein, P.E., Thomas, D.H. *et al*. Stromal Elements Act to Restrain, Rather Than Support, Pancreatic Ductal Adenocarcinoma. *Cancer Cell* **25**, 735-747 (2014). doi: 10.1016/j.ccr.2014.04.021

Rieder, F., Brenmoehl, J., Leeb, S., Schölmerich, J. & Rogler, G. Wound healing and fibrosis in intestinal disease. *Gut* **56**, 130-139 (2007). doi: 10.1136/gut.2006.090456

Riihimäki, M., Hemminki, A., Sundquist, J. & Hemminki, K. Patterns of metastasis in colon and rectal cancer. *Sci Rep* **6**, 29765 (2016). doi: 10.1038/srep29765

Roche, J. *et al*. Global Decrease of Histone H3K27 Acetylation in ZEB1-Induced Epithelial to Mesenchymal Transition in Lung Cancer Cells. *Cancers (Basel)* **5**, 334-356 (2013). doi: 10.3390/cancers5020334

Rohaan, M.W., Wilgenhof, S. & Haanen, J.B.A.G. Adoptive cellular therapies: the current landscape. *Virchows Arch* **474**, 449-461 (2019). doi: 10.1007/s00428-018-2484-0

Roper, J. *et al*. Colonoscopy-based colorectal cancer modeling in mice with CRISPR-Cas9 genome editing and organoid transplantation. *Nat Protoc* **13**, 217-234 (2018). doi: 10.1038/nprot.2017.136

Rosenberg, D.W., Giardina, C. & Tanaka, T. Mouse models for the study of colon carcinogenesis. *Carcinogenesis* **30**, 183-196 (2009). doi: 10.1093/carcin/bgn267

Rothenberg, M.E. *et al*. Identification of a cKit Colonic Crypt Base Secretory Cell That Supports Lgr5+ Stem Cells in Mice. *Gastroenterology* **142**, 1195-1205 (2012). doi: 10.1053/j.gastro.2012.02.006

Roulis, M. *et al*. Paracrine orchestration of intestinal tumorigenesis by a mesenchymal niche. *Nature* **580**, 524–529 (2020). doi: 10.1038/s41586-020-2166-3

Rueden, C.T. *et al*. ImageJ2: ImageJ for the next generation of scientific image data. *BMC Bioinformatics* **18**, 529 (2017). doi: 10.1186/s12859-017-1934-z

Saam, J.R. & Gordon, J.I. Inducible Gene Knockouts in the Small Intestinal and Colonic Epithelium. *J Biol Chem* **274**, 38071-38082 (1999). doi: 10.1074/jbc.274.53.38071

Sadanandam, A. *et al*. A colorectal cancer classification system that associates cellular phenotype and responses to therapy. *Nat Med* **19**, 619-625 (2013). doi: 10.1038/nm.3175

Sahai, E. *et al*. A framework for advancing our understanding of cancer- associated fibroblasts. *Nat Rev Cancer* **20**, 174-186 (2020). doi: 10.1038/s41568-019-0238-1

Salmon, H. *et al*. Matrix architecture defines the preferential localization and migration of T cells into the stroma of human lung tumors. *J Clin Invest* **122**, 899-910 (2012). doi: 10.1172/JCI45817

Samstein, R.M., Lee, C.-H., Shoushtari, A.N. & Hellmann, M.D. *et al*. Tumor mutational load predicts survival after immunotherapy across multiple cancer types. *Nat Genet* **51**, 202-206 (2019). doi: 10.1038/s41588-018-0312-8

Sánchez-Tilló, E. *et al*. ZEB1 represses E-cadherin and induces an EMT by recruiting the SWI/SNF chromatin-remodeling protein BRG1. *Oncogene* **29**, 3490-3500 (2010). doi: 10.1038/onc.2010.102

Sanjana, N.E., Shalem, O. & Zhang, F. Improved vectors and genome-wide libraries for CRISPR screening. *Nat Methods* **11**, 783-784 (2014). doi: 10.1038/nmeth.3047

Sansom, O.J. *et al*. Loss of Apc in vivo immediately perturbs Wnt signaling, differentiation, and migration. *Genes Dev* **18**, 1385-1390 (2004). doi: 10.1101/gad.287404

Sansom, O.J. *et al*. Loss of Apc allows phenotypic manifestation of the transforming properties of an endogenous K-ras oncogene in vivo. *Proc Natl Acad Sci U S A* **103**, 14122-14127 (2006). doi: 10.1073/pnas.0604130103

Satija, R., Farrell, J.A., Gennert, D., Schier, A.F. & Regev, A. Spatial reconstruction of single-cell gene expression data. *Nat Biotechnol* **33**, 495-502 (2015). doi: 10.1038/nbt.3192

Sato, T. *et al*. Single Lgr5 stem cells build crypt–villus structures in vitro without a mesenchymal niche. *Nature* **459**, 262-265 (2009). doi: 10.1038/nature07935

Sato, T. *et al*. Paneth cells constitute the niche for Lgr5 stemcells in intestinal crypts. *Nature* **469**, 415-418 (2011). doi: 10.1038/nature09637

Sato, T. *et al*. Long-term Expansion of Epithelial Organoids From Human Colon, Adenoma, Adenocarcinoma, and Barrett's Epithelium. *Gastroenterology* **141**, 1762-1772 (2011a). doi: 10.1053/j.gastro.2011.07.050

Scheel, C. *et al*. Paracrine and Autocrine Signals Induce and Maintain Mesenchymal and Stem Cell States in the Breast. *Cell* **145**, 926-940 (2011). doi: 10.1016/j.cell.2011.04.029

Scheel, C. & Weinberg, R.A. Phenotypic plasticity and epithelial-mesenchymal transition in cancer and normal stem cells? *Int J Cancer* **129**, 2310-2314 (2011). doi: 10.1002/ijc.26311

Schindelin, J. *et al*. Fiji: an open-source platform for biological-image analysis. *Nat Methods* **9**, 676-682 (2012). doi: 10.1038/nmeth.2019

Schindelin, J., Rueden, C.T., Hiner, M.C. & Eliceiri, K.W. The ImageJ Ecosystem: An Open Platform for Biomedical Image Analysis. *Mol Reprod Dev* **82**, 519-529 (2015). doi: 10.1002/mrd.22489

Schnalzger, T.E. *et al*. 3D model for CAR-mediated cytotoxicity using patient-derived colorectal cancer organoids. *EMBO J* **38**, e100928 (2019). doi: 10.15252/embj.2018100928

Schwank, G., Andersson-Rolf, A., Koo, B.-K., Sasaki, N. & Clevers, H. Generation of BAC Transgenic Epithelial Organoids. *PLoS One* **8**, e76871 (2013). doi: 10.1371/journal.pone.0076871

Schwank, G., Koo, B.-K. *et al*. Functional Repair of CFTR by CRISPR/Cas9 in Intestinal Stem Cell Organoids of Cystic Fibrosis Patients. *Cell Stem Cell* **13**, 653-658 (2013a). doi: 10.1016/j.stem.2013.11.002

Schwitalla, S. *et al*. Loss of p53 in Enterocytes Generates an Inflammatory Microenvironment Enabling Invasion and Lymph Node Metastasis of Carcinogen-Induced Colorectal Tumors. *Cancer Cell* **23**, 93-106 (2013). doi: 10.1016/j.ccr.2012.11.014

Sheppard, D. Integrin-mediated activation of latent transforming growth factor β. *Cancer Metastasis Rev* **24**, 395-402 (2005). doi: 10.1007/s10555-005-5131-6

Shoshkes-Carmel, M. *et al.* Subepithelial telocytes are an important source of Wnts that supports intestinal crypts. *Nature* **557**, 242-246 (2018). doi: 10.1038/s41586-018-0084-4

Shukla, S.A. *et al*. Comprehensive analysis of cancer-associated somatic mutations in class I HLA genes. *Nat Biotechnol* **33**, 1152-1158 (2015). doi: 10.1038/nbt.3344

Shukla, P.K. *et al*. Chronic ethanol feeding promotes azoxymethane and dextran sulfate sodiuminduced colonic tumorigenesis potentially by enhancing mucosal inflammation. *BMC Cancer* **16**, 189 (2016). doi: 10.1186/s12885-016-2180-x

Siegel, R.L., Miller, K.D. & Jemal, A. Cancer Statistics, 2015. *CA Cancer J Clin* **65**, 5-29 (2015). doi: 10.3322/caac.21254

Smyth, M.J., Dunn, G.P. & Schreiber, R.D. Cancer Immunosurveillance and Immunoediting: The Roles of Immunity in Suppressing Tumor Development and Shaping Tumor Immunogenicity. *Adv Immunol* **90**, 1-15 (2006). doi: 10.1016/S0065-2776(06)90001-7

Somers, A. *et al*. Generation of transgene-free lung disease-specific human iPS cells using a single excisable lentiviral stem cell cassette. *Stem Cells* **28**, 1728-1740 (2010). doi: 10.1002/stem.495

Son, J. & Lyssiotis, C.A. *et al*. Glutamine supports pancreatic cancer growth through a KRAS-regulated metabolic pathway. *Nature* **496**, 101-105 (2013). doi: 10.1038/nature12040

Song, J. EMT or apoptosis: a decision for TGF-β. *Cell Res* **17**, 289-290 (2007). doi: 10.1038/cr.2007.25

Sow, H.S., Ren, J., Camps, M., Ossendorp, F. & ten Dijke, P. Combined Inhibition of TGF-β Signaling and the PD-L1 Immune Checkpoint Is Differentially Effective in Tumor Models. *Cells* **8**, 320 (2019). doi: 10.3390/cells8040320

Spaderna, S. *et al*. A Transient, EMT-Linked Loss of Basement Membranes Indicates Metastasis and Poor Survival in Colorectal Cancer. *Gastroenterology* **131**, 830-840 (2006). doi: 10.1053/j.gastro.2006.06.016

Spranger, S. & Gajewski, T.F. Tumor-intrinsic oncogene pathways mediating immune avoidance. *Oncoimmunology* **5**, e1086862 (2016). doi: 10.1080/2162402X.2015.1086862

Stintzing, S. *et al*. Consensus molecular subgroups (CMS) of colorectal cancer (CRC) and first-line efficacy of FOLFIRI plus cetuximab or bevacizumab in the FIRE3 (AIO KRK-0306) trial. *Ann Oncol* **30**, 1796-1803 (2019). doi: 10.1093/annonc/mdz387

Stuart, T. & Butler, A. *et al*. Comprehensive Integration of Single-Cell Data. *Cell* **177**, 1888-1902 (2019). doi: 10.1016/j.cell.2019.05.031

Su, S., Chen, J. & Yao, H. *et al*. CD10+GPR77+ Cancer-Associated Fibroblasts Promote Cancer Formation and Chemoresistance by Sustaining Cancer Stemness. *Cell* **172**, 841-856 (2018). doi: 10.1016/j.cell.2018.01.009

Subramanian, A. *et al*. Gene set enrichment analysis: A knowledge-based approach for interpreting genome-wide expression profiles. *Proc Natl Acad Sci U S A* **102**, 15545-15550 (2005). doi: 10.1073/pnas.0506580102

Sugimoto, S. *et al*. Reconstruction of the Human Colon Epithelium In Vivo. *Cell Stem Cell* **22**, 171-176 (2018). doi: 10.1016/j.stem.2017.11.012

Sun, M.-c. *et al*. Lactobacillus reuteri F-9-35 Prevents DSS-Induced Colitis by Inhibiting Proinflammatory Gene Expression and Restoring the Gut Microbiota in Mice. *J Food Sci* **83**, 2645-2652 (2018). doi: 10.1111/1750-3841.14326

Suzuki, R., Kohno, H., Sugie, S., Nakagama, H. & Tanaka, T. Strain differences in the susceptibility to azoxymethane and dextran sodium sulfate-induced colon carcinogenesis in mice. *Carcinogenesis* **27**, 162-169 (2006). doi: 10.1093/carcin/bgi205

Sznurkowska, M.K. & Aceto, N. The gate to metastasis: key players in cancer cell intravasation. *FEBS J* **289**, 4336-4354 (2022). doi: 10.1111/febs.16046

Takaku, K. *et al*. Intestinal Tumorigenesis in Compound Mutant Mice of both Dpc4 (Smad4) and Apc Genes. *Cell* **92**, 645-656 (1998). doi: 10.1016/s0092-8674(00)81132-0

Tan, H.-X. *et al*. CXCR4/TGF-β1 mediated hepatic stellate cells differentiation into carcinoma-associated fibroblasts and promoted liver metastasis of colon cancer. *Cancer Biol Ther* **21**, 258-268 (2020). doi: 10.1080/15384047.2019.1685157

Tanaka, T. *et al*. A novel inflammation-related mouse colon carcinogenesis model induced by azoxymethane and dextran sodium sulfate. *Cancer Sci* **94**, 965-973 (2003). doi: 10.1111/j.1349-7006.2003.tb01386.x

Tauriello, D.V.F. *et al*. TGFβ drives immune evasion in genetically reconstituted colon cancer metastasis. *Nature* **554**, 538-543 (2018). doi: 10.1038/nature25492

The Cancer Genome Atlas Network. Comprehensive molecular characterization of human colon and rectal cancer. *Nature* **487**, 330–337 (2012). doi: 10.1038/nature11252

Teixeira, A.F., ten Dijke, P. & Zhu, H.-J. On-Target Anti-TGF-b Therapies Are Not Succeeding in Clinical Cancer Treatments: What Are Remaining Challenges? *Front Cell Dev Biol* **8**, 605 (2020). doi: 10.3389/fcell.2020.00605

Tetteh, P.W. *et al*. Generation of an inducible colon-specific Cre enzyme mouse line for colon cancer research. *Proc Natl Acad Sci U S A* **113**, 11859-11864 (2016). doi: 10.1073/pnas.1614057113

The Gene Ontology Consortium. The Gene Ontology resource: enriching a GOld mine. *Nucleic Acids Res* **49**, D325-D334 (2021). doi: 10.1093/nar/gkaa1113

Thiery, J.P., Acloque, H., Huang, R.Y.J. & Nieto, M.A. Epithelial-Mesenchymal Transitions in Development and Disease. *Cell* **139**, 871-890 (2009). doi: 10.1016/j.cell.2009.11.007

Tran, H.D. *et al*. Transient SNAIL1 Expression Is Necessary for Metastatic Competence in Breast Cancer. *Cancer Res* **74**, 6330-6340 (2014). doi: 10.1158/0008-5472.CAN-14-0923

Trumble, T., Gunlikson, R. & Parvin, D. A Comparison of Immune Response to Nerve and Skin Allografts. *J Reconstr Microsurg* **9**, 367-372 (1993). doi: 10.1055/s-2007-1006744

Tryndyak, V.P., Beland, F.A. & Pogribny, I.P. E-cadherin transcriptional down-regulation by epigenetic and microRNA-200 family alterations is related to mesenchymal and drug-resistant phenotypes in human breast cancer cells. *Int J Cancer* **126**, 2575-2583 (2010). doi: 10.1002/ijc.24972

Tsai, J.H., Donaher, J.L., Murphy, D.A., Chau, S. & Yang, J. Spatiotemporal Regulation of Epithelial-Mesenchymal Transition Is Essential for Squamous Cell Carcinoma Metastasis. *Cancer Cell* **22**, 725-736 (2012). doi: 10.1016/j.ccr.2012.09.022

Uhlitz, F., Bischoff, P. & Peidli, S. *et al*. Mitogen-activated protein kinase activity drives cell trajectories in colorectal cancer. *EMBO Mol Med* **13**, e14123 (2021). doi: 10.15252/emmm.202114123

Valcz, G. *et al*. Myofibroblast-Derived SFRP1 as Potential Inhibitor of Colorectal Carcinoma Field Effect. *PLoS One* **9**, e106143 (2014). doi: 10.1371/journal.pone.0106143

van de Wetering, M., Francies, H.E. & Francis, J.M. *et al*. Prospective Derivation of a Living Organoid Biobank of Colorectal Cancer Patients. *Cell* **161**, 933-945 (2015). doi: 10.1016/j.cell.2015.03.053

Vega, P.N. *et al*. Cancer-Associated Fibroblasts and Squamous Epithelial Cells Constitute a Unique Microenvironment in a Mouse Model of Inflammation-Induced Colon Cancer. *Front Oncol* **12**, 878920 (2022). doi: 10.3389/fonc.2022.878920

Velázquez, K.T. *et al*. Weight loss following diet-induced obesity does not alter colon tumorigenesis in the AOM mouse model. *Am J Physiol Gastrointest Liver Physiol* **311**, G699-G712 (2016). doi: 10.1152/ajpgi.00207.2016

Venkatesan, S., Swanton, C., Tayler, B.S. & Costello, J.F. Treatment-Induced Mutagenesis and Selective Pressures Sculpt Cancer Evolution. *Cold Spring Harb Perspect Med* **7**, a026617 (2017). doi: 10.1101/cshperspect.a026617

Wang, Z. & Liu, J. *et al*. Metastasis-associated fibroblasts: an emerging target for metastatic cancer. *Biomark Res* **9**, 47 (2021). doi: 10.1186/s40364-021-00305-9

Wang, Z. *et al*. Cancer-Associated Fibroblasts Suppress Cancer Development: The Other Side of the Coin. *Front Cell Dev Biol* **9**, 613534 (2021). doi: 10.3389/fcell.2021.613534

Wellner, U. & Schubert, J. *et al*. The EMT-activator ZEB1 promotes tumorigenicity by repressing stemness-inhibiting microRNAs. *Nat Cell Biol* **11**, 1487-1495 (2009). doi: 10.1038/ncb1998

Winkler, J., Abisoye-Ogunniyan, A., Metcalf, K.J. & Werb, Z. Concepts of extracellular matrix remodelling in tumour progression and metastasis. *Nat Commun* **11**, 5120 (2020). doi: 10.1038/s41467-020-18794-x

Witta, S.E. *et al*. Restoring E-Cadherin Expression Increases Sensitivity to Epidermal Growth Factor Receptor Inhibitors in Lung Cancer Cell Lines. *Cancer Res* **66**, 944-950 (2006). doi: 10.1158/0008-5472.CAN-05-1988

Wu, S.Z., Al-Eryani, G. & Roden, D.L. *et al*. A single-cell and spatially resolved atlas of human breast cancers. *Nat Genet* **53**, 1334-1347 (2021). doi: 10.1038/s41588-021-00911-1

Xu, Y. & Lee, D.-K. *et al*. Breast tumor cell-specific knockout of Twist1 inhibits cancer cell plasticity, dissemination, and lung metastasis in mice. *Proc Natl Acad Sci U S A* **114**, 11494-11499 (2017). doi: 10.1073/pnas.1618091114

Yan, N. & Chen, Z.J. Intrinsic antiviral immunity. *Nat Immunol* **13**, 214-222 (2012). doi: 10.1038/ni.2229

Yang, Y. *et al*. Autophagy in PDGFRα+ mesenchymal cells is essential for intestinal stem cell survival. *Proc Natl Acad Sci U S A* **119**, e2202016119 (2022). doi: 10.1073/pnas.2202016119

Yassin, M. *et al*. Upregulation of PD-1 follows tumour development in the AOM/DSS model of inflammation-induced colorectal cancer in mice. *Immunology* **158**, 35-46 (2019). doi: 10.1111/imm.13093

Ye, J. *et al*. Primer-BLAST: A tool to design target-specific primers for polymerase chain reaction. *BMC Bioinformatics* **13**, 134 (2012). doi: 10.1186/1471-2105-13-134

Yilmaz, M. & Christofori, G. EMT, the cytoskeleton, and cancer cell invasion. *Cancer Metastasis Rev* **28**, 15-33 (2009). doi: 10.1007/s10555-008-9169-0

Zackular, J.P., Baxter, N.T., Chen, G.Y. & Schloss, P.D. Manipulation of the Gut Microbiota Reveals Role in Colon Tumorigenesis. *mSphere* **1**, e00001-15 (2015). doi: 10.1128/mSphere.00001-15

Zaytseva, Y.Y. *et al*. Cancer cell-associated fatty acid synthase activates endothelial cells and promotes angiogenesis in colorectal cancer. *Carcinogenesis* **35**, 1341-1351 (2014). doi: 10.1093/carcin/bgu042

Zhang, L. *et al*. Hypoxia induces epithelial-mesenchymal transition via activation of SNAI1 by hypoxia-inducible factor -1α in hepatocellular carcinoma. *BMC Cancer* **13**, 108 (2013). doi: 10.1186/1471-2407-13-108

Zhang, P., Sun, Y. & Ma, L. ZEB1: At the crossroads of epithelial-mesenchymal transition, metastasis and therapy resistance. *Cell Cycle* **14**, 481-487 (2015). doi: 10.1080/15384101.2015.1006048

Zheng, B., Zhang, Z., Black, C.M., de Crombrugghe, B. & Denton, C.P. Ligand-dependent genetic recombination in fibroblasts : a potentially powerful technique for investigating gene function in fibrosis. *Am J Pathol* **160**, 1609-1617 (2002). doi: 10.1016/S0002-9440(10)61108-X

Zheng, X. & Carstens, J.L. *et al*. Epithelial-to-mesenchymal transition is dispensable for metastasis but induces chemoresistance in pancreatic cancer. *Nature* **527**, 525-530 (2015). doi: 10.1038/nature16064

Zheng, X. *et al*. Identification of immune-related subtypes of colorectal cancer to improve antitumor immunotherapy. *Sci Rep* **11**, 19432 (2021). doi: 10.1038/s41598-021-98966-x

Zhong, B. & Cheng, B. *et al*. Colorectal cancer-associated fibroblasts promote metastasis by up-regulating LRG1 through stromal IL-6/STAT3 signaling. *Cell Death Dis* **13**, 16 (2022). doi: 10.1038/s41419-021-04461-6

Zhu, A., Ibrahim, J.G. & Love, M.I. Heavy-tailed prior distributions for sequence count data: removing the noise and preserving large differences. *Bioinformatics* **35**, 2084-2092 (2019). doi: 10.1093/bioinformatics/bty895

Zhu, K., Cai, L., Cui, C., de los Toyos, J.R. & Anastassiou, D. Single-cell analysis reveals the pan-cancer invasiveness-associated transition of adiposederived stromal cells into COL11A1-expressing cancer-associated fibroblasts. *PLoS Comput Biol* **17**, e1009228 (2021). doi: 10.1371/journal.pcbi.1009228

Ziani,L. Chouaib, S. & Thiery, J. Alteration of the Antitumor immune Response by Cancer-Associated Fibroblasts. *Front Immunol* **9**, 414 (2018). doi: 10.3389/fimmu.2018.00414

Zigmond, E. *et al*. Utilization of Murine Colonoscopy for Orthotopic Implantation of Colorectal Cancer. *PLoS One* **6**, e28858 (2011). doi: 10.1371/journal.pone.0028858

5.2 Books:

H. Wickham. ggplot2: Elegant Graphics for Data Analysis*. Springer-Verlag New York*, 2016.

5.3 Web sources:

Cancer Facts & Figures 2020, downloaded 15.01.2021 from: https://www.cancer.org/content/dam/cancer-org/research/cancer-facts-and-statistics/annual-cancer-facts-and-figures/2020/cancer-facts-and-figures-2020.pdf

CCA Treatment, downloaded 15.01.2021 from: https://www.ccalliance.org/pdfs/resources/CCA_Treatment_42816.pdf

UniProt Information on Zeb1, obtained 01.03.2022 from: https://www.uniprot.org/uniprot/P37275

R for Windows: R Core Team (2021). R: A language and environment for statistical computing. R Foundation for Statistical Computing, Vienna, Austria. URL: https://www.R-project.org/.

R package xlsx: Adrian Dragulescu and Cole Arendt (2020). xlsx: Read, Write, Format Excel 2007 and Excel 97/2000/XP/2003 Files. R package version 0.6.5. https://CRAN.R-project.org/package=xlsx

R package dplyr: Hadley Wickham, Romain François, Lionel Henry and Kirill Müller (2022). dplyr: A Grammar of Data Manipulation. R package version 1.0.8. https://CRAN.R-project.org/package=dplyr

R package ggpubr: Alboukadel Kassambara (2020). ggpubr: 'ggplot2' Based Publication Ready Plots. R package version 0.4.0. https://CRAN.R-project.org/package=ggpubr

R package tidyr: Hadley Wickham and Maximilian Girlich (2022). tidyr: Tidy Messy Data. R package version 1.2.0. https://CRAN.R-project.org/package=tidyr

Abbreviations

4OHT	4-hydroxy-tamoxifen
Acta2	Gene Symbol: actin alpha 2
apCAF	Antigen presenting CAF
AOM	Azoxymethane
APC	Gene Symbol: Adenomatous polyposis coli
aSMA	Alpha smooth muscle actin
BMP	Bone morphogenic protein
BRAF	v-raf murine sarcoma viral oncogene homolog B1
CAF	Cancer-associated fibroblast
Cas9	CRISPR associated 9
Ccl9	Gene Symbol: C-C motif ligand 9
CD3e/4/8/14/31/45/79b/326	Cluster of differentiation 3e/4/8/14/31/45/79b/326
CIMP	CpG island methylation phenotype
CIN	Chromosomal instability
cl. Casp. 3	Cleaved Caspase 3
Clec3b	Gene Symbol: C-Type Lectin Domain Family 3 Member B
CMS	Consensus molecular subtype
Col1a2/4a1/4a2/6a1	Gene Symbol: Collagen Type 1/4/6 Apha 1/2 Chain
CRC	Colorectal cancer
Cre-LV	Cre-Lentivirus
CRISPR	Clustered regularly interspaced short palindromic repeats
CtBP	C-terminal Binding Proteins
CTLA-4	Gene Symbol: cytotoxic T-lymphocyte-associated protein 4
CXCL1/12	Gene Symbol: C-X-C motif ligand 1/12
DAPI	4',6-diamidino-2-phenylindole
DMSO	Dimethyl sulfoxide
DSS	Dextran sodium sulfate
Ecad	E-cadherin
ECM	Extracellular matrix
EDTA	Ethylenediaminetetraacetic acid
(h)EGF	(human) Epidermal growth factor
EGFR	Gene Symbol: Epidermal growth factor receptor
(p)EMT	(partial) Epithelial-mesenchymal-transition
Epcam	Gene Symbol: Epithelial cellular adhesion molecule
FAP (disease)	Familial adenomatous polyposis
FAP (gene)	Gene Symbol: Fibroblast activation protein
FCS	Fetal calf serum
FFPE	Formalin fixed paraffin embedded
FGF	Fibroblast growth factor
FoxP3	Gene Symbol: Forkhead box P3
gDNA	Genomic DNA
(e)GFP	(enhanced) Green fluorescent protein
GSEA	Gene set enrichment analysis
HDI	Human development index
HPRT	Gene Symbol: Hypoxanthine phosphoribosyltransferase 1
HNPCC	Hereditary non-polyposis colorectal cancer
IBD	Intestinal bowel disease
iCAF	Inflammatory cancer-associated fibroblast
Icam1	Gene Symbol: Intercellular Adhesion Molecule 1
ICB	Immune checkpoint blockade
IgG	Immunoglobulin G
IL-1	Interleukin-1
IL6	Gene Symbol: Interleukin 6
Itgax	Gene Symbol: Integrin Subunit Alpha X
KO	Knockout
KRAS	Gene Symbol: Kirsten rat sarcoma virus

LB	Lysogeny broth
Lif	Gene Symbol: Leukemia inhibitory factor
LOH	Loss of heterozygocity
MET	Mesenchymal-epithelial-transition
MHC	Major Histocompatibility complex
miR	microRNA
MLH1/3	Gene Symbol: MutL protein homolog 1/3
MSH2/3/6	Gene Symbol: MutS homolog 2/3/6
MSI	Microsatellite instability
MSS	Microsatellite stable
myCAF	myofibroblastic cancer-associated fibroblast
NICD	Notch intracellular domain
NK cell	Natural killer cell
Nkain4	Gene Symbol: Sodium/potassium transporting ATPase interacting 4
OVA	Ovalbumin
PBS	Phosphate buffered saline
(qRT-)PCR	(quantitative real-time) Polymerase chain reaction
PD-L1	Programmed death-ligand 1
Pdgfra/b	Gene Symbol: Platelet-derived growth factor receptor alpha / beta
PDTO	Patient derived tumour organoid
PFA	Paraformaldehyde
Pik3a	Phosphatidylinositol 3 kinase 3a
PMS2	Gene Symbol: PMS1 homolog 2
Ptprc	Gene Symbol: Protein Tyrosine Phosphatase Receptor Type C
Saa3	Gene Symbol: Serum amyloid A 3
SCNA	Somatic copy number alteration
SCT	Subcutaneous transplantation
SD	Standard deviation
SDS	Sodium dodecyl sulfate
SFCA	Surfactant-free cellulose acetate
sgRNA	Small guide RNA
shRNA	Short hairpin RNA
Smad4	Gene Symbol: SMAD family member 4
Snai1/2	Gene Symbol: Snail family transcriptional repressor 1/2
Tagln	Gene Symbol: Transgelin
TBS(T)	Tris buffered salin (+ Tween 20)
TEMED	Tetramethylethylenediamine
TF	Transcription factor
TME	Tumour microenvironment
Tnc	Gene Symbol: Tenascin C
(h)TGFβ	(human) Transforming growth factor beta
Tgfbr2	Gene Symbol: Transforming growth factor beta receptor 2
TP53	Gene Symbol: Tumor protein P53
Twist1	Gene Symbol: Twist family bHLH transcription factor 1
UMI	Unique molecular identifier
VEGF	Vascular endothelial growth factor
WT	Wildtype
YAP1	Gene Symbol: Yes-associated protein 1
Zeb1/2	Gene Symbol: Zinc finger E-box binding homeobox 1/2

Common abbreviations like units of measurement are not listed.
Abbreviations for tumour organoid genotypes are listed in Figure 15.

List of Figures

List of Tables

R Code Attachments

R Code for DESeq2 analysis of bulk RNA sequencing data

```
sample298015 <- read.csv(file = './Zeb1_BulkSeq/298015.tab', sep = '\t', skip = 4)
sample298015 <- sample298015[,-(2:3)]
colnames(sample298015) <- c('GeneID', '298015')

sample298016 <- read.csv(file = './Zeb1_BulkSeq/298016.tab', sep = '\t', skip = 4)
sample298016 <- sample298016[,-(2:3)]
colnames(sample298016) <- c('GeneID', '298016')

sample298017 <- read.csv(file = './Zeb1 BulkSeq/298017.tab', sep = '\t', skip = 4)
sample298017 <- sample298017[,-(2:3)]
colnames(sample298017) <- c('GeneID', '298017')

sample298018 <- read.csv(file = './Zeb1_BulkSeq/298018.tab', sep = '\t', skip = 4)
sample298018 <- sample298018[,-(2:3)]
colnames(sample298018) <- c('GeneID', '298018')

sample298019 <- read.csv(file = './Zeb1_BulkSeq/298019.tab', sep = '\t', skip = 4)
sample298019 <- sample298019[,-(2:3)]
colnames(sample298019) <- c('GeneID', '298019')

sample298020 <- read.csv(file = './Zeb1_BulkSeq/298020.tab', sep = '\t', skip = 4)
sample298020 <- sample298020[,-(2:3)]
colnames(sample298020) <- c('GeneID', '298020')

sample298021 <- read.csv(file = './Zeb1_BulkSeq/298021.tab', sep = '\t', skip = 4)
sample298021 <- sample298021[,-(2:3)]
colnames(sample298021) <- c('GeneID', '298021')

sample298022 <- read.csv(file = './Zeb1_BulkSeq/298022.tab', sep = '\t', skip = 4)
sample298022 <- sample298022[,-(2:3)]
colnames(sample298022) <- c('GeneID', '298022')

sample298023 <- read.csv(file = './Zeb1_BulkSeq/298023.tab', sep = '\t', skip = 4)
sample298023 <- sample298023[,-(2:3)]
colnames(sample298023) <- c('GeneID', '298023')

sample298024 <- read.csv(file = './Zeb1 BulkSeq/298024.tab', sep = '\t', skip = 4)
sample298024 <- sample298024[,-(2:3)]
colnames(sample298024) <- c('GeneID', '298024')

sample298015 <- sample298015[-which(sample298015$`298015` == 0),]
sample298016 <- sample298016[-which(sample298016$`298016` == 0),]
sample298017 <- sample298017[-which(sample298017$`298017` == 0),]
sample298018 <- sample298018[-which(sample298018$`298018` == 0),]
sample298019 <- sample298019[-which(sample298019$`298019` == 0),]
sample298020 <- sample298020[-which(sample298020$`298020` == 0),]
sample298021 <- sample298021[-which(sample298021$`298021` == 0),]
sample298022 <- sample298022[-which(sample298022$`298022` == 0),]
sample298023 <- sample298023[-which(sample298023$`298023` == 0),]
sample298024 <- sample298024[-which(sample298024$`298024` == 0),]

genenames <- read.csv('./mart export all.txt', sep = '\t', header = TRUE)

sample298015 <- merge(genenames, sample298015, all.y = TRUE, by.x = 'Gene.stable.ID', by.y = 'GeneID')
sample298016 <- merge(genenames, sample298016, all.y = TRUE, by.x = 'Gene.stable.ID', by.y = 'GeneID')
sample298017 <- merge(genenames, sample298017, all.y = TRUE, by.x = 'Gene.stable.ID', by.y = 'GeneID')
sample298018 <- merge(genenames, sample298018, all.y = TRUE, by.x = 'Gene.stable.ID', by.y = 'GeneID')
sample298019 <- merge(genenames, sample298019, all.y = TRUE, by.x = 'Gene.stable.ID', by.y = 'GeneID')
sample298020 <- merge(genenames, sample298020, all.y = TRUE, by.x = 'Gene.stable.ID', by.y = 'GeneID')
sample298021 <- merge(genenames, sample298021, all.y = TRUE, by.x = 'Gene.stable.ID', by.y = 'GeneID')
sample298022 <- merge(genenames, sample298022, all.y = TRUE, by.x = 'Gene.stable.ID', by.y = 'GeneID')
sample298023 <- merge(genenames, sample298023, all.y = TRUE, by.x = 'Gene.stable.ID', by.y = 'GeneID')
sample298024 <- merge(genenames, sample298024, all.y = TRUE, by.x = 'Gene.stable.ID', by.y = 'GeneID')

sample298015 <- sample298015[,-1]
sample298016 <- sample298016[,-1]
sample298017 <- sample298017[,-1]
sample298018 <- sample298018[,-1]
sample298019 <- sample298019[,-1]
sample298020 <- sample298020[,-1]
sample298021 <- sample298021[,-1]
sample298022 <- sample298022[,-1]
sample298023 <- sample298023[,-1]
sample298024 <- sample298024[,-1]

merge <- Reduce(function(x,y) merge (x = x, y = y, by = 'Gene.name', all = TRUE), list(sample298015,
         sample298016, sample298017, sample298018, sample298019, sample298020, sample298021,
         sample298022, sample298023, sample298024))
merge <- merge[order(merge$Gene.name),]
merge[is.na(merge)] <- 0
```

```
merge <- merge[grep('Aldoa', merge$Gene.name, fixed = TRUE, value = FALSE, invert = TRUE),]
merge <- merge[grep('Gcat', merge$Gene.name, fixed = TRUE, value = FALSE, invert = TRUE),]
merge <- merge[grep('St6galnac2', merge$Gene.name, fixed = TRUE, value = FALSE, invert = TRUE),]
merge <- merge[grep('Gm16499', merge$Gene.name, fixed = TRUE, value = FALSE, invert = TRUE),]
merge <- merge[grep('Gm16701', merge$Gene.name, fixed = TRUE, value = FALSE, invert = TRUE),]
merge <- merge[grep('Gm35558', merge$Gene.name, fixed = TRUE, value = FALSE, invert = TRUE),]
merge <- merge[grep('Gm36638', merge$Gene.name, fixed = TRUE, value = FALSE, invert = TRUE),]
merge <- merge[grep('Gm4430', merge$Gene.name, fixed = TRUE, value = FALSE, invert = TRUE),]
merge <- merge[grep('Gm5089', merge$Gene.name, fixed = TRUE, value = FALSE, invert = TRUE),]

merge <- merge[grep('Snhg4', merge$Gene.name, fixed = TRUE, value = FALSE, invert = TRUE),]
merge <- merge[grep('Zkscan7', merge$Gene.name, fixed = TRUE, value = FALSE, invert = TRUE),]

rownames(merge) <- c()
merge <- tibble::column_to_rownames(merge, var = 'Gene.name')

coldata <- read.csv(file = './MetaData.txt', sep = '\t', header = TRUE, row.names = 1)

library(DESeq2)
library(xlsx)

CountTable <- DESeqDataSetFromMatrix(countData = merge, colData = coldata, design = ~ Genotype)

CountTable$Genotype <- relevel(CountTable$Genotype, 'WT')
CountTable <- DESeq(CountTable, )
res <- results(CountTable)
DFres <- as.data.frame(res)
DFres <- DFres[order(DFres$log2FoldChange, decreasing = TRUE),]

## Exporting ranked list of genes for GSEA
DFresExp <- tibble::rownames_to_column(DFres)
colnames(DFresExp)[1] <- 'Name'
DFresExp <- DFresExp[,-c(2,4,5,6,7)]
# colnames(DFresExp)[2] <- ''
write.xlsx(x = DFresExp, file = './DESeq-Export.xlsx', row.names = FALSE, append = TRUE)

resultsNames(CountTable)
CountTable <- lfcShrink(CountTable, coef = 'Genotype_KO_vs_WT')

plotMA(CountTable, ylim = c(-2, 5), colSig = 'red', colNonSig = 'gray40',
       colLine = 'black', xlim = c(1,100000), alpha = 0.05, cex = 1)
```

R Code for Seurat analysis of single cell RNA sequencing data

```
library(Seurat)
library(sctransform)
library(ggplot2)
library(dplyr)
library(xlsx)
library(ggpubr)
library(tidyr)

#### Step 1: Preprocessing of Input data for Seurat ####
PlateInfo <- read.csv('./Input/PlateInfo.txt', sep = '\t', header = TRUE, colClasses = 'character')
plates <- PlateInfo$Plate
barcodes <- read.csv('./Input/cel-seq2_barcodes.csv', sep ='\t', colClasses = 'character')
colnames(barcodes) <- c('Cell_ID', 'Barcode')
genenames <- read.csv('./Input/mart_export_allGenes_m39.txt', sep = '\t', header = TRUE)
layout <- read.csv('./Input/PlateLayout.tsv', sep = '\t', header = FALSE)
rownames(layout) <- 'CellType'

## Processing of Input data per plate
for (i in plates) {
    path <- paste0('./Input/STARsolo/m39 Genome/FFM_', i)
    reads <- ReadMtx(mtx = paste0(path, '/UniqueAndMult-EM.mtx'),
                     cells = paste0(path, '/barcodes.tsv'),
                     features = paste0(path, '/features.tsv'))
    reads <- as.data.frame(reads)
    columns <- c(1:length(colnames(reads)))

    for (j in columns){
        barcode <- colnames(reads)[j]
        cellID <- barcodes[barcodes$Barcode == barcode, 'Cell_ID']
        colnames(reads)[j] <- paste(i, cellID, sep = ' ')
    }

    reads <- reads[ , order(colnames(reads))]
    reads <- reads[order(rownames(reads)) , ]
    assign(paste0('reads', i), reads)

    ## Processing of flow data
    flowdata <- read.csv(paste0('./Input/FlowData/flow', i, '.tsv'), sep = '\t', header = TRUE)
    flowdata <- as.data.frame(t(flowdata[ ,c('PE.A', 'APC.A', 'PE.Cy7.A',
                                             'Pacific.Blue.A', 'APC.eF780.A')]))
    flowdata[flowdata < 0] <- 0
    colnames(flowdata) <- colnames(reads)
    assign(paste0('flow', i), flowdata)

    ## Processing of Metadata
    metadata <- layout
    colnames(metadata) <- colnames(reads)
    metadata['Genotype',] <- PlateInfo[PlateInfo$Plate == i, 'Genotype']
    metadata['Platenumber', ] <- i
    assign(paste0('metadata', i), metadata)
}

## Combine all plates into one matrix and transpose for Seurat input
Reads <- cbind(reads002, reads003, reads004, reads005, reads006, reads007, reads009, reads010)
Flow <- cbind(flow002, flow003, flow004, flow005, flow006, flow007, flow009, flow010)
Metadata <- cbind(metadata002, metadata003, metadata004, metadata005,
                  metadata006, metadata007, metadata009, metadata010)
Metadata <- as.data.frame(t(Metadata))

#### Step 2: Plotting QC Data and filtering rules ####
SeuFiltering <- CreateSeuratObject(counts = Reads, min.cells = 5, min.features = 0)
SeuFiltering <- AddMetaData(SeuFiltering, Metadata, col.name = c('CellType', 'Genotype', 'Platenumber'))

## Calculate percentage of mitochondrial genes (starting with 'mt-') and ERCC genes (starting with 'ERCC-')
SeuFiltering[['percentMt']] <- PercentageFeatureSet(SeuFiltering, pattern = '^mt-')
SeuFiltering[['percentERCC']] <- PercentageFeatureSet(SeuFiltering, pattern = '^ERCC-')
SeuFiltering[['log10GenesPerUMI']] <- log10(SeuFiltering$nFeature_RNA) / log10(SeuFiltering$nCount_RNA)

## Plot QC Data as ViolinPlots
Plot <- VlnPlot(SeuFiltering, features = c('nFeature_RNA', 'nCount_RNA', 'percentMt', 'percentERCC',
                              'log10GenesPerUMI'),pt.size = 0.1, ncol = 1, group.by = 'Platenumber')
ggsave('./Output/Filtering/QC-Violin.tiff', Plot, device = 'tiff', dpi = 300, height = 13.5, width = 3, )

## Normalizing Data, Performing PCA, Clustering and UMAP
SeuFiltering <- SCTransform(SeuFiltering, method = 'glmGamPoi')
SeuFiltering <- RunPCA(SeuFiltering, features = VariableFeatures(object = SeuFiltering), verbose = FALSE)
SeuFiltering <- FindNeighbors(SeuFiltering, dims = 1:30)
SeuFiltering <- FindClusters(SeuFiltering, resolution = 0.8)
SeuFiltering <- RunUMAP(SeuFiltering, dims = 1:30)

## Plotting Cells after applying filtering rules
SeuTest <- subset(SeuFiltering, subset = (CellType == 'Immune' & nCount_RNA > 1300 &
log10GenesPerUMI > 0.78 & log10GenesPerUMI < 0.92 & percentMt <12 & percentERCC < 38) |
  (CellType == 'Epithelial' & nCount_RNA > 7700 & nFeature_RNA > 2000 & percentMt < 47 &
  log10GenesPerUMI < 0.9 & log10GenesPerUMI > 0.78) | (CellType == 'Fibroblast' & nCount_RNA > 3000 &
  percentERCC < 12 & log10GenesPerUMI < 0.9))
```

```
Plot1 <- DimPlot(SeuFiltering, reduction = 'umap', pt.size = 1.5) +
         ggtitle('Cells before filtering') +NoLegend()
Plot2 <- DimPlot(SeuTest, reduction = 'umap', pt.size = 1.5) +ggtitle('Cells after filtering') +NoLegend()
Plot <- Plot1 + Plot2

ggsave('./Output/Filtering/Cluster-Filt.tiff', Plot, device = 'tiff', dpi = 300, height = 6, width = 12)

#### Step 3: Seurat analysis after applying filtering rules ####
SeuAll <- CreateSeuratObject(counts = Reads, min.cells = 5, min.features = 0)
SeuAll <- AddMetaData(SeuAll, Metadata, col.name = c('CellType', 'Genotype', 'Platenumber'))
SeuAll[['percentMt']] <- PercentageFeatureSet(SeuAll, pattern = '^mt-')
SeuAll[['percentERCC']] <- PercentageFeatureSet(SeuAll, pattern = '^ERCC-')
SeuAll[['log10GenesPerUMI']] <- log10(SeuAll$nFeature_RNA) / log10(SeuAll$nCount_RNA)
SeuAll[['FLOW']] <- CreateAssayObject(counts = Flow)

## Subset Cells based on QC parameters
SeuAll <- subset(SeuAll, subset = (CellType == 'Immune' & nCount_RNA > 1300 &
  log10GenesPerUMI > 0.78 & log10GenesPerUMI < 0.92 & percentMt <12 & percentERCC < 38) |
  (CellType == 'Epithelial' & nCount_RNA > 7700 & nFeature_RNA > 2000 & percentMt < 47 &
  log10GenesPerUMI < 0.9 & log10GenesPerUMI > 0.78) | (CellType == 'Fibroblast' &
  nCount_RNA > 3000 & percentERCC < 12 & log10GenesPerUMI < 0.9))

SeuAll <- NormalizeData(SeuAll, assay = 'FLOW', normalization.method = 'CLR')
SeuAll <- ScaleData(SeuAll, assay = 'FLOW')
SeuAll <- SCTransform(SeuAll, method = 'glmGamPoi', return.only.var.genes = FALSE)
SeuAll <- RunPCA(SeuAll, features = VariableFeatures(object = SeuAll), verbose = FALSE)
SeuAll <- FindNeighbors(SeuAll, dims = 1:30, k.param = 10)
SeuAll <- FindClusters(SeuAll, resolution = 0.8)
SeuAll <- RunUMAP(SeuAll, dims = 1:30)
SeuAll$Cluster <- Idents(SeuAll)

## Plot UMAP Neighbouring
Plot <- DimPlot(SeuAll, reduction = 'umap', label = TRUE, pt.size = 1.2, group.by = 'Cluster', ) +
NoLegend()
ggsave('./Output/All/UMAP-Cluster-NL.tiff', Plot, device = 'tiff', dpi = 300, height = 6, width = 6)
Plot <- DimPlot(SeuAll, reduction = 'umap', label = FALSE, pt.size = 1.2, split.by = 'Genotype',
  group.by = 'Genotype', )
ggsave('./Output/All/UMAP-Cluster-GT.tiff', Plot, device = 'tiff', dpi = 300, height = 6, width = 12)

## Differential Gene Expression
SeuAll$Cluster.Geno <- paste(Idents(SeuAll), SeuAll$Genotype, sep = "_")
Idents(SeuAll) <- 'Cluster.Geno'
Clusters <- levels(SeuAll$Cluster)
Clusters <- as.numeric(Clusters)

## Comparing DE Genes between KO vs WT for all Clusters
for(i in Clusters){
    ident1 <- paste(i, 'KO', sep = ' ')
    ident2 <- paste(i, 'WT', sep = '_')

    DEG <- FindMarkers(SeuAll, ident.1 = ident1, ident.2 = ident2, min.pct = 0.2, logfc.threshold = 0.25)
    write.xlsx(DEG, file = paste0('./Output/All/Lists/C ', Clusters[i+1], '.xlsx'), append = TRUE, )
}

## Define function with plotting parameters for Violin Plots
Violin <- function(x) {
    Plot <- VlnPlot(SeuAll, features = x, pt.size = 0, group.by = 'Cluster') +
        theme(axis.text.x = element_text(size = 9), axis.text.y = element_text(size = 9),
              axis.title.y = element_text(size = 8, hjust = 0.7)) +NoLegend()
    return(Plot)
}

## Plot FACS marker expression as violin per cluster
Plot1 <- Violin('PE.Cy7.A')
Plot2 <- Violin('Pacific.Blue.A')
Plot <- ggarrange(Plot1, Plot2, ncol = 2)
ggsave('./Output/All/FACS-Violin.tiff', Plot, device = 'tiff', dpi = 300, height = 1.8, width = 10)

## Plot CD45 (Ptprc) and Epcam as violins to match FACS marker expression
Plot1 <- Violin('Ptprc')
Plot2 <- Violin('Epcam')
Plot <- ggarrange(Plot1, Plot2, ncol = 2)
ggsave('./Output/All/CD45-EpCAM-Violin.tiff', Plot, device = 'tiff', dpi = 300, height = 1.8, width = 10)

## Plot Myeloid Cells markers as violins per cluster
Plot1 <- Violin('Itgax')
Plot2 <- Violin('Cd14')
Plot <- ggarrange(Plot1, Plot2, ncol = 2)
ggsave('./Output/All/Myeloid-Violin.tiff', Plot, device = 'tiff', dpi = 300, height = 1.8, width = 10)

## Plot B Cell marker as violin per Cluster
Plot <- Violin('Cd79b')
ggsave('./Output/All/B Cell-Violin.tiff', Plot, device = 'tiff', dpi = 300, height = 1.8, width = 5)

## Plot Macrophage marker as violin per Cluster
Plot <- Violin('Ccl9')
ggsave('./Output/All/Macrophage-Violin.tiff', Plot, device = 'tiff', dpi = 300, height = 1.8, width = 5)
```

```
## Plot T Cell markers as violin per Cluster
Plot1 <- Violin('Cd3e')
Plot2 <- Violin('Ctla4')
Plot <- ggarrange(Plot1, Plot2, ncol = 2)
ggsave('./Output/All/TCell-Violin.tiff', Plot, device = 'tiff', dpi = 300, height = 1.8, width = 10)

## Plot iCAF markers as violin per Cluster
Plot1 <- Violin('Clec3b')

Plot2 <- Violin('Pdgfra')
Plot <- ggarrange(Plot1, Plot2, ncol = 2)
ggsave('./Output/All/iCAF-Violin.tiff', Plot, device = 'tiff', dpi = 300, height = 1.8, width = 10)

## Plot myCAF markers as violin per Cluster
Plot1 <- Violin('Tnc')
Plot2 <- Violin('Tagln')
Plot <- ggarrange(Plot1, Plot2, ncol = 2)
ggsave('./Output/All/myCAF-Violin.tiff', Plot, device = 'tiff', dpi = 300, height = 1.8, width = 10)

## Plot apCAF markers as violin per Cluster
Plot1 <- Violin('Saa3')
Plot2 <- Violin('Nkain4')
Plot <- ggarrange(Plot1, Plot2, ncol = 2)
ggsave('./Output/All/apCAF-Violin.tiff', Plot, device = 'tiff', dpi = 300, height = 1.8, width = 10)

## Plot Collagens as ECM CAF markers
Plot1 <- Violin('Col4a1')
Plot2 <- Violin('Col4a2')
Plot <- ggarrange(Plot1, Plot2, ncol = 2)
ggsave('./Output/All/Collagens-Violin.tiff', Plot, device = 'tiff', dpi = 300, height = 1.8, width = 10)

## Plot Zeb1 and Col1a2 as Violins
Plot1 <- Violin('Zeb1')
Plot2 <- Violin('Col1a2')
Plot <- ggarrange(Plot1, Plot2, ncol = 2)
ggsave('./Output/All/Zeb1+Col1a2-Violin.tiff', Plot, device = 'tiff', dpi = 300, height = 1.8, width = 10)
```